THREE-DIMENSIONAL MODELING OF UPPER MANTLE STRUCTURE AND ITS SIGNIFICANCE TO TECTONICS

Thesis by

Yu-Shen Zhang

In Partial Fulfillment of the Requirements

for the Degree of

Doctor of Philosophy

California Institute of Technology

Pasadena, California

1992

(Defended July 23, 1991)

Acknowledgements

I would like to thank the faculty of the Seismological Laboratory for offering me the opportunity to acquire an excellent education, and for giving me financial support throughout my stay at Caltech.

Professor Toshiro Tanimoto has exerted a profound influence on my education at the Seismo. Lab. Without his constant guidance and unwaivering support this thesis could not have been completed. For his inspiration, criticism and friendship I express my deep and lasting gratitude. I would like to thank particularly Professor Don L. Anderson for his extreme patience with me and for his continuing encouragement and enthusiasm for my work. His broad knowledge was my most valuable resource. I owe a great deal to Professors Hiroo Kanamori, Thomas Ahrens, Rob Clayton, David Harkrider, Peter Wyllie and Clarence Allen. Their support, patience and advice were important to my studies at Caltech.

I wish to thank particularly Tom Duffy, Monica Kohler and Cathy Smither, who read this thesis critically. I am indebted to many colleagues for their inspiration, cooperation and friendship during my stay, especially to Doug Dreger, Walter Kiefer, Scott King, Harold Magistrale, Jean-Paul Montagner, Kenji Satake, Richard Stead, Hong-Kie Tiao, David Wald, Shingo Watada, Joann Yoshimura, Jiajun Zhang, Hua-wei Zhou, and Lian-she Zhao.

I thank all of the staffs at the Seismo Lab and the Division for their help and friendship, especially Janet Fernandes and Dee Page. I thank GDSN and GEOSCOPE networks for providing data which made this study possible. This research was supported by NSF.

The completion of this thesis would have been impossible without the understanding and support of my wife, Xinxin, who always stood at my side. Her love, help, encouragement and tolerance were essential. I thank my father Xiqing Zhang for his infallible support. He fostered in me the interest in science even during "the Culture Revolution," the darkest days of China in the 1970's. Lastly, I thank my family for their wholehearted support over the years. I dedicate this thesis to my family.

Abstract

A global model was constructed for shear wave velocity structure, expanded up to degree and order 36 in spherical harmonic expansion, and down in 500 km of the Earth's upper mantle. The data set included about 18,000 seismograms associated with 971 events with magnitude larger than about 5.5.

Assuming that the errors in data space and model space are both Gaussian random distributed, we used the *Akaike Bayesian information criterion (ABIC)* method and the *Akaike information criterion (AIC)* method to determine the optimal damping parameters and the optimal regularization of the unknown continuous model, respectively. Both the spherical harmonic expansion and the block parametrization approaches have been tested. The equal area block regularization approach gave a more accurate result than the spherical harmonic expansion approach, and it was adopted.

Age-Love wave phase velocity variations were retrieved for the Pacific, Atlantic and Indian Oceans, respectively. Simple forward modeling showed that seismic phase velocity variation with a continuous thickening of lithosphere up to about 150 Ma fits the present observation, disagreeing with the conventional model, which changes the age-depth curve at about 60-80 Ma. The age-Love wave phase velocity variations in different oceans showed systematic differences at younger ages, and convergence beyond 100 Ma. Age-

seismic phase velocity relationships on each side of ridges were also examined and asymmetric velocity variations were found. The average age-phase velocity relations were subtracted from Love wave phase velocity variation maps and "residual" maps were produced. The results indicated broad, low velocity regions in the south Pacific (super-swell region), the south and west Indian Ocean, and high velocity regions east of the East Pacific Rise and in the north to northeast Indian Ocean.

In the S-wave velocity results under global mid-ocean ridges, low velocity anomalies were resolved but were limited in the 100 km below the surface. The minimum velocities were at depth about 50 km. The horizontal width of the low velocity anomaly, which crossed over ridges, increased with the spreading rate. The S-wave velocities under ridges were strongly correlated with spreading rates at shallow depth, but the correlation decreased for deeper results and almost disappeared at 100 km. Several major hotspots were associated with low-velocity anomalies of about 1-2 percent and diameters larger than 1000 km. But the depths of the low velocity anomalies were between 100-200 km, which were different from those of ridges and expressed the mechanism differences between ridges and hotspots. The velocity structures under the East African Rift Valley and the Baikal Rift Valley were inspected. An active mechanism was suggested with the East African Rift Valley, and a different mechanism was connected with the Baikal Rift Valley.

Table of Contents

Chapter 1

General Introduction

The research presented in this thesis utilizes digital data from GDSN (Peterson and Hutt, 1982) and GEOSCOPE (Romanowicz *et al.*, 1984) networks to study the three-dimensional structure of the upper mantle on a global scale, to investigate the relationship between seismology results and plate tectonics and to improve our understanding of the Earth's dynamics.

Seismological study over most of this century has led to a refined picture of the Earth under the assumption of spherical symmetry, such as the existence of the crust, the upper mantle, the lower mantle, the fluid outer core and the solid inner core, and also the detailed profiles of seismic wave velocities and density as a function of the radius (or depth) (*e.g.*, Jeffreys and Bullen, 1940; Anderson and Toksöz, 1963; Gilbert and Dziewonski, 1975; Dziewonski and Anderson, 1981; Kennett and Engdahl, 1991). Progress in a more thorough collection of the digital data and growing computer power in the last decade has led to three-dimensional image of the Earth's interior from the upper mantle (*e.g.*, Masters *et al.*, 1982; Nakanishi and Anderson, 1982, 1983, 1984; Nataf *et al.*, 1984, 1986; Woodhouse and Dziewonski, 1986; Tanimoto and Anderson, 1985; Tanimoto, 1986a,b; Montagner and Tanimoto, 1990; Zhang and

Tanimoto, 1991) to the lower mantle and the core (*e.g.*, Clayton and Comer, 1983; Dziewonski, 1984; Creager and Jordan, 1986; Woodhouse and Dziewonski, 1986; Morelli and Dziewonski, 1987; Giardini *et al.*, 1988; Ritzwoller *et al.*, 1988; Gudmundsson, 1989; Tanimoto, 1990; Li, 1990). These seismic tomographic inferences have already benefited other disciplines of the Earth sciences. Some geophysicists, for example, have employed these results to model mantle convection, plate motion, undulations of the core-mantle boundary and the geoid (Hager *et al.*, 1985; Hager and Clayton, 1988; Lay *et al.*, 1990; Forte and Peltier, 1991).

One of the shortcomings of previous tomography studies, however, is their restriction to low order spherical harmonic expansion or large wavelength anomalies (larger than 4,000 km). Previous upper mantle studies, such as Woodhouse and Dziewonski (1984), and Nataf *et al.* (1986) truncated expansion at spherical order (l) 8 and 6, respectively. The early data set did not justify expansions to orders higher than 6 (Nataf *et al.*, 1986, Nakanishi and Anderson, 1984). There were some attempts to increase the cutoff, for example, to $l=10$ by Tanimoto and Anderson (1985), and recently to $l=12$ by Wong (1989), but the data set did not warrant extension to higher order (at least not clearly to Tanimoto and Anderson). In order to correlate seismological results and tectonics, extending the analysis to higher spherical order and obtaining small scale feature are needed.

The object of this thesis is to obtain a detailed global, upper mantle structure, to correlate the seismological results with the plate tectonics, and to improve our understanding of the Earth's dynamics. This is possible because of the development of digital seismic networks, which has resulted in the accumulation of an unprecedented amount of high quality digital data in the last

decade, and has also improved spatial and azimuthal coverage. We have collected about 18,000 seismograms associated with 971 events with magnitude larger than about 5.5.

When solving an inversion problem, the unknown model (it is a continuous function) is always parameterized by the observer's preference, and the damping parameter (by using the Stochastic method or the Bayesian method) or the number of eigenvalues (by using the SVD method) are usually selected by observer's experience and *a priori* belief subjectively. In this study, we have solved these problems objectively with the statistic theory. The assumption we used is that the errors in data space and model space are both Gaussian random distributed. This is a reasonable assumption when the number of observations is large. The optimal regularization of the unknown function is determined by using the *Akaike information criterion (AIC)* (Akaike, 1974; Sakamoto *et al.* 1986), and the optimal damping parameter is determined by the *Akaike Bayesian information criterion (ABIC)* (Akaike, 1979, 1980), which are based upon the maximum likelihood of the inversion system.

Two most commonly used methods in present seismic tomography are the spherical harmonic expansion inversion (Dziewonski, 1984; Nataf *et al.*, 1984, 1986; Woodhouse and Dziewonski, 1984) and the block parametrization inversion (Aki *et al.*, 1976; Clayton and Comer, 1983; Suetsugu and Nakanishi, 1985; Zhang and Tanimoto, 1989). Theoretically, these two methods give equivalent results under uniform path coverage, but in a real situation, path coverage is nonuniform. In the thesis, we have examined these two methods by using a synthetic method associated with an optimal, constant damping parameter approach. We find that the equal area block parametrization inversion gives more accurate results than the spherical harmonic expansion

inversion does. The optimal truncated spherical angular order is about 18 for the spherical harmonic expansion, and is about 24 for the equivalent cutoff level of the equal-area block inversion. The spectral amplitudes for both methods have shown similar results.

The two-step inversion method has been used in this thesis. The first step is to measure the global phase velocity variation, the fundamental mode Love and Rayleigh wave variations are solved for periods ranging from 75 to 250 s, and the second step is the construction of the three-dimensional upper mantle S-wave velocity structure. A global model is constructed for shear wave velocity, expanded up to degree and order 36 (the optimal is about 24) in spherical harmonic expansion, and down in depth of 500 km of the Earth's mantle. The anisotropic terms are dropped, because on the basis of the data we have, the resolution is not good enough to convince us of the inversion result for the anisotropic parameters. The model presented in this thesis is consistent with previous global studies (*e.g.*, Nakanishi and Anderson, 1984; Woodhouse and Dziewonski, 1984; Tanimoto, 1986a,b; Wong, 1989) and local studies (*e.g.*, Grand and Helmberger, 1984; Grand, 1987; Zhang and Tanimoto, 1989). However, because of our smaller resolution scale, the present results contain much more detail than those of previous studies, which allows us to investigate the relationship between seismological results and plate tectonics.

Average Love wave phase velocities are obtained every 10 million years along oceanic plates, and then the age-Love wave phase velocity relations for the Pacific, Atlantic and Indian Oceans are established separately. One of the features for different oceans is that the phase velocity shows a smooth increase with plate age. Simple forward modeling shows that Love wave phase velocity variates with a continuous thickening of lithosphere up to about 150 Ma fit the

present observation, disagreeing with the model deduced from ocean depth data and heat flow data (Parsons and Sclater, 1977; Sclater *et al.*, 1980; Renkin and Sclater,1988), which change variation at about 60-80 Ma. Another important feature is that the age-phase velocity relation is different from one ocean to another, suggesting a violation of the universal scaling law derived in previous studies (Turcotte and Oxburgh, 1967; Parker and Oldenburg, 1973). In order to understand mantle heterogeneity that is unrelated to plates, we subtracted the average age-phase velocity relations from Love wave phase velocity maps and produced "residual" maps. In these "residual" maps, we find large-scale low velocity anomalies in the south Pacific, the so-called "superswell region" (Smith *et al.* 1989; McNutt and Judge, 1990), and southern parts of the Indian Ocean; high velocity anomalies east of the East Pacific Rise, and northeastern Indian Ocean.

Weissel and Hayes (1971) find asymmetric spreading along the South-East Indian Ocean Ridge, but other ridges, like the East Pacific Rise and Mid-Atlantic Ridge, are thought to exhibit symmetric spreading (*e.g.* Minster and Jordan, 1978; Vogt, 1986). A recent study by Hayes (1988) indicated asymmetric subsidence in the south-east Indian Ocean and the south Atlantic Ocean. We have examined the age-phase velocity relations on different sides and different ridges, and found asymmetric velocity variations. There are probably a wide variety of differences in the thermal state of the lithosphere, resulting perhaps in different lithosphere thickening rates.

The spreading of oceanic plates, the formation of new oceanic lithosphere at mid-ocean ridges, the hotspot distribution over the world and continental rifts are essential features of plate tectonics. The global mid-ocean ridge shows different morphology, bathymetry and gravity variations with spreading rates

(Macdonald, *et al.*, 1984; Macdonald, 1986; Small and Sandwell, 1989). In our seismological study, low velocity anomalies are associated with global mid-ocean ridges, but the low velocity anomalies are limited in the top 100 km, and the minimum velocity is shallower than 50 km. The width of the low velocity anomalies, which cross over ridges, increases with spreading rates. We also find that seismic velocities at shallow depth are strongly correlated with spreading rates under ridges, but the correlation decreases for deeper results and vanishes below 100 km.

There are many hotspots in the world (Morgan, 1972; Crough and Jurdy, 1980; Vogt, 1981; and Weinstein and Olson, 1989). The mantle plume hypothesis (*e.g.*, Morgan, 1972; Turcotte and Oxburgh, 1978; Courtney and White, 1986; White and McKenzie, 1989) gives a possible explanation of forming hotspots. In the present study, several major hotspots are associated with low-velocity anomalies with magnitudes of about 1-2 percent and diameters of more than 1000 km. But the depths of the low-velocity anomalies are between 100-200 km, which are different from those of ridges, and represent a different thermal (or volatile) structure and, perhaps, a mechanism difference between ridges and hotspots.

From the study of ridges and hotspots, we make a conjecture: The depth of the low velocity anomaly can serve as a criterion to distinguish between passive and active upwellings. A passive mechanism is suggested as associating with shallow, low velocity anomaly, while a deep anomaly suggests an active mechanism. The East African Rift Valley and the Baikal Rift Valley are studied. The East African Rift is associated with a deep low velocity anomaly. The shape of the low velocity anomaly indicates that the materials may be fed by hotspots at Afar and in north-east of African. And an active mechanism is

suggested there. The velocity under the Baikal Rift is clearly different from that of the African Rift Valley. It is associated with low velocity anomalies at a depth of about 100 km and does not penetrate deeply. The seismic result suggests that the Baikal Rift is connected with a passive rift.

This thesis is divided into five independent chapters in addition to this general introduction. Chapter 2, "Data and synthetic model tests," presents the data sets used in this thesis and the synthetic model tests for a different parametrization approach. Chapter 3, "The use of *ABIC* and *AIC* methods to resolve the linear inversion," outlines methods to solve the linear inversion problem associated with statistical consideration. And some examples are presented in this chapter. Chapter 4, "3-D modeling of upper mantle S-wave velocity structure," presents the results of shear wave velocity structure in the upper mantle to a depth of 500 km. The Love and Rayleigh wave phase velocity variations are also presented in Chapter 4. Chapter 5, "Oceanic lithosphere," discusses the possible oceanic lithosphere variation deduced from Love wave phase velocity variation. Chapter 6, "Ridges, Hotspots and Rifts," discusses differences between ridges and hotspots, the relationship of the shear wave velocity under ridges with the spreading rate, and the possible mechanisms associated with ridges, hotspots and rifts.

Chapter 2

Data and Synthetic Model Tests

2.1 Introduction

From the 1960s to the first half of the 1980s, most kinds of seismic studies were concentrated in local areas (*e.g.*, Dorman *et al.*, 1960; Kanamori, 1970; Forsyth, 1975, 1977; Schlue and Knopoff, 1977; Yu and Mitchell, 1979; Mitchell and Yu, 1980; Anderson and Regan, 1983; Regan and Anderson, 1984; Suetsugu and Nakanishi, 1985) due to data availability. There have been a lot of global studies after 1980 (*e.g.*, Masters *et al.*, 1982; Nakanishi and Anderson, 1982, 1983, 1984; Woodhouse and Dziewonski, 1984; Nataf *et al.*, 1984, 1986; Tanimoto and Anderson, 1985; Tanimoto, 1986a,b, 1988; Montagner and Tanimoto, 1990), because of the accumulated digital data. But all of these studies obtain only large scale features (larger then 4000 km), and it is difficult to correlate these results to detailed plate tectonic features. With the development of digital seismic networks, GDSN (Peterson and Hutt, 1982) and GEOSCOPE (Romanowicz *et al.*, 1984), there have resulted in an accumulation of a vast amount of high quality digital data in the last decade, and an improved spatial and azimuthal coverage. We have collected about 18,000 seismograms

associated with 971 events with magnitude larger than about 5.5. In order to keep the accuracy of the inversion results, we used only R1 and G1 phases in the present study. The phase velocities of fundamental mode Love and Rayleigh waves were first measured for periods ranging from 75 to 250 s, and then these data were solved for regional variation of phase velocity. The data process will be described in the first part of this chapter.

The two most commonly used methods in current seismic tomography are spherical harmonic expansion inversion (*e.g.*, Dziewonski, 1984; Nataf *et al.*, 1984, 1986; Woodhouse and Dziewonski, 1984; Tanimoto and Anderson, 1985) and block parametrization inversion (*e.g.*, Aki *et al.*, 1976; Clayton and Comer, 1983; Suetsugu and Nakanishi, 1985; Zhang and Tanimoto, 1989). There are other kind of approaches (Tarantola and Nercessian, 1984; Montagner, 1986); however, we will not discuss them here. Theoretically, the spherical harmonic expansion and the block parametrization method should give equivalent results under uniform path coverage; but, in a real situation, path coverage is nonuniform, because most of the earthquakes are in tectonically active areas, and many of the observation stations are in northern hemisphere continental areas. There has been no study to test these two methods with the same data set. It is important to know the possible bias effects and the errors associated with different methods before we do real data inversion; otherwise the reliability of the results will not be known. In the second part of this chapter, we will examine these two methods by using synthetic models, associated with a simple, constant damping parameter approach. We find that the equal area block parametrization inversion gives more accurate results than the spherical harmonic expansion inversion. This is probably due to the nonuniform path coverage and to the fact that the use of global basis functions, such as spherical

harmonics, requires a more intricate damping scheme to produce equivalent results.

2.2 Data Processing

The accumulated digital data from GDSN and GEOSCOPE networks in the last ten years are excellent data sources. The basic data set consists of long-period Love and Rayleigh waves (75-250 seconds). In this study, most of the data were collected from GDSN stations, but GEOSCOPE provided data from important stations in the southern hemisphere, which improved the spatial and azimuthal coverage of the Earth.

The distribution of the sources and stations is rather sparse, because most earthquakes cluster on plate boundaries and tectonic active areas, and most stations are in the northern hemisphere continental areas. In order to obtain detailed velocity structure, we should collect as much data as possible, and obtain the best path coverage. We divided the world map into $2^o \times 2^o$ cells, and selected one earthquake in each cell for which a sufficiently large event was available. Sometimes, if there were large, shallow, intermediate and deep events in a block, we selected more than one earthquake in that block. The raw data were chosen by using several overlapping criteria:

(1) The main phases used in this study are the minor-arc Love wave G_1 and Rayleigh wave R_1. The lower bound of magnitude is $M = 5.5$, since signals from smaller events are generally poor for the period range considered.

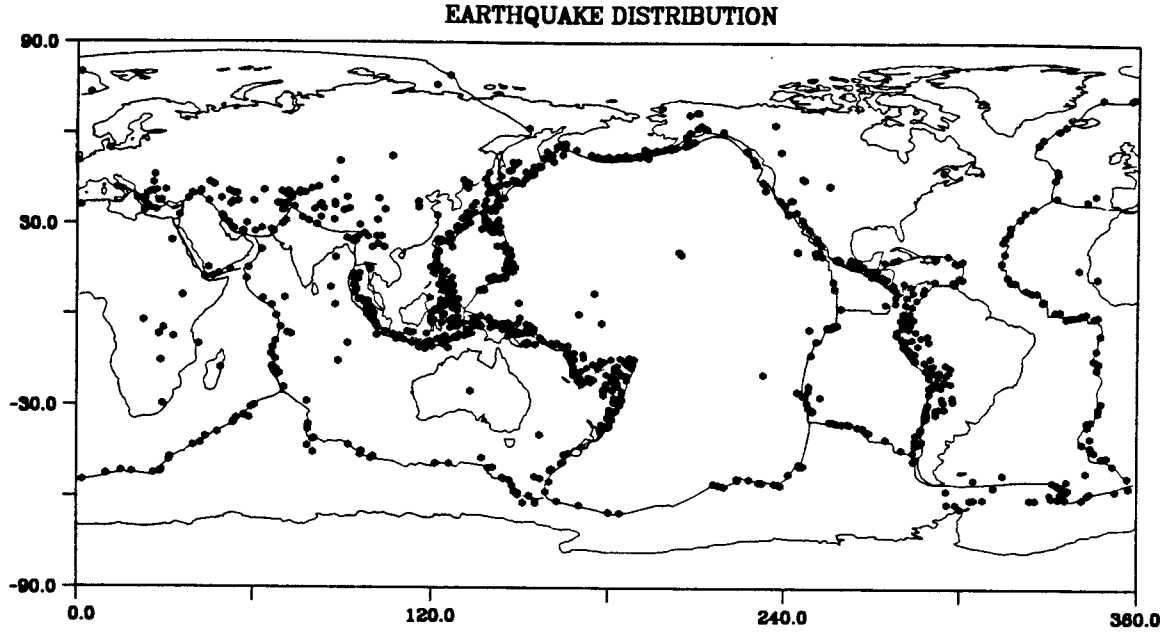

Figure 2.1, The location of earthquakes used in this study. Each star represents one event. Total number of events (with $M \geq 5.5$) is 971.

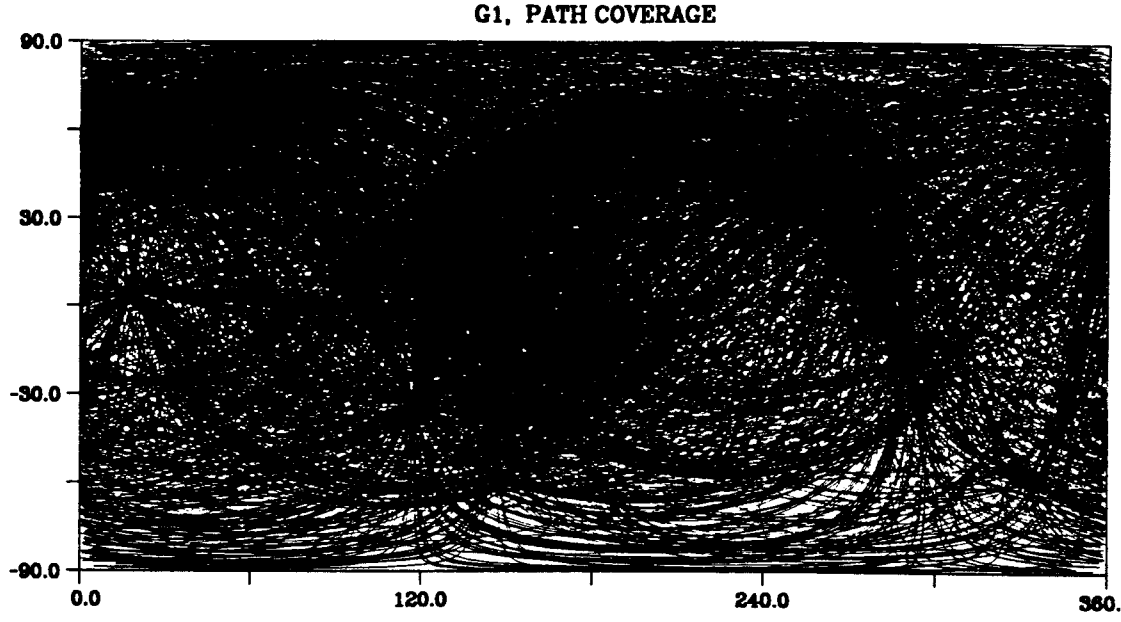

Figure 2.2, Path coverage of Love waves (G_1) used for inversion and synthetic tests. There are approximately 9000 paths collected from the GDSN and GEOSCOPE networks. One of the notable features is the unbalanced path coverage, which will affect the inversion results.

(2) The shortest distance range between source and station was set at 10^o. This avoided the complicated near-field effects, and allowed the surface wave to develop completely. Also, data from short distances often show non-linear instrument effects, which are apparent for some GDSN stations.

(3) The largest source-receiver distance was set at 165^0 to avoid possible interference between the minor-arc and the major-arc phases.

(4) For each observed seismogram, a synthetic seismogram was computed by following the normal mode theory (Gilbert and Dziewonski, 1975) and visually compared with the data. If a nonlinear response was apparent, the signal was too noisy, or the observed seismogram was very different from the synthetics, the data was rejected. If higher modes were well excited and interfered with the fundamental mode, the seismogram was also discarded.

(5) The phase velocity for each path was computed from the phase differences between the data and synthetics shown in the Fourier transform. If the phase velocity dispersion curve was irregular with rapid jumps, the data was thrown away.

The total number of earthquakes (with $M \geq 5.5$) collected in the present study was 971, spanning the years 1980 to 1987. The locations of these events are shown in Figure 2.1. The original, long-period transverse and vertical component seismograms were filtered for periods between 70 and 500 s and resampled every 10 seconds. Figure 2.2 shows the great circle path coverage for Love waves, which consists of about 9,000 paths collected from GDSN and GEOSCOPE networks. The path coverage for Rayleigh waves is mostly the same; we will not show it here. One significant feature of Figure 2.2 is the

nonuniform path coverage. There are more paths in the northern hemisphere than in the southern hemisphere, and many waves propagate along similar directions. This affected the inversion results, a point we discuss in later chapter. However, the present path coverage is much better than those in previous studies, and allows us to investigate detailed velocity structure.

We have made the following assumption in this study: (1) Love and Rayleigh waves propagate along great circle paths, and (2) the local velocity structure is determined by the local surface wave dispersion. Long path length data have been observed to contribute to problems caused by heterogeneity refraction effects (Lay and Kanamori, 1985; Jobert, 1986), but Schwartz and Lay (1987) and Um *et al.* (1991) conclude that the geometrical optics approximation appears to be valid for long-period, low-orbit surface waves. In the present study, we used only the minor arc phases, G_1 and R_1, with periods longer than 70 seconds, and thus the error that was due to lateral refraction was small and negligible.

In the past two decades, many researchers used the single-station method to obtain great circle phase velocity (*e.g.*, Brune *et al.*, 1960; Nakanishi and Anderson, 1984). In this study, we used a similar method, but we measured the phase in a slightly different way. The synthetic seismograms were first generated by following the normal mode theory (Gilbert and Dziewonski, 1975). For the source parameters (origin time, hypocenter, and moment tensor), the Harvard CMT (centroid moment tensor) solution (Dziewonski *et al.*, 1981; Dziewonski and Woodhouse, 1983) has been used. The ellipticity correction was also introduced; then using the Fourier transform, the phase differences between the observed and synthetic seismograms were measured.

$$\Delta\psi = \psi_0 - \psi_s, \tag{2.1}$$

where ψ_0 is the phase of the observed seismograms for a period, and ψ_s is the phase of the synthetic seismograms for the same period. Using the phase differences, we get the average phase velocity along the great circle,

$$\bar{v} = \frac{\Delta_{sr}}{\frac{\Delta_{sr}}{v_0} + \frac{\Delta\psi}{\omega}}, \tag{2.2}$$

where Δ_{sr} is the great circle distances from a source to a receiver, v_0 is the phase velocity for the reference earth model, ω is the angular phase velocity. A similar method was used by Suetsugu and Nakanishi (1985).

In this study, the group velocity window for each path was determined by visualizing the data and synthetic seismograms. The group velocity window was varied with different epicentral distance. By comparing the synthetic and observed seismograms, some bad data and possible noise can be easily eliminated; the accuracy of results is ensured.

2.3 Azimuthal Anisotropy

It has been shown that phase velocity has an azimuthal variation of about 1 percent (Tanimoto and Anderson, 1984; Nishimura and Forsyth, 1989; Montagner and Tanimoto, 1990). Azimuthal anisotropy is known to have 2λ and 4λ dependence (Smith and Dahlen, 1973; Tanimoto, 1986a), where λ is the azimuth. Observational studies of Forsyth (1975), Tanimoto and Anderson (1985), Nishimura and Forsyth (1989) and Montagner and Tanimoto (1990) show that the fastest Rayleigh wave direction coincides approximately with

plate motion but that the Love wave azimuthal variation is difficult to determine. The most recent work by Montagner and Tanimoto (1990) confirms that the azimuthal dependence of surface waves is rather small and that the inclusion of azimuthal terms affects velocity patterns very little. As a result, we have dropped the azimuthal terms.

2.4 Inversion Theory

The travel time of a phase at frequency ω from a source s to a station r is given by the simple equation

$$t = \int_s^r \frac{ds}{v(\theta, \phi)} , \tag{2.3}$$

and the travel time anomaly Δt is then given by

$$\Delta t = -\frac{1}{v_0} \int_s^r \frac{v_h}{v_0} ds , \tag{2.4}$$

where v_0 is the spherically averaged phase velocity and v_h is the deviation that is due to the heterogeneity. The integration is along the great circle and $| v_h | \ll v_0$.

To apply Equation (2.4), it is necessary to cast $\frac{v_h}{v_0}$ into a parameterized model. The two most widely used parametrization schemes in seismic tomography studies are the spherical harmonic expansion inversion (*e.g.*, Woodhouse and Dziewonski, 1984; Nataf *et al.*, 1986; Tanimoto and Anderson, 1985), and the block discretization inversion (*e.g.*, Aki *et al.*, 1976; Clayton and Comer, 1983; Suetsugu and Nakanishi, 1985; Zhang and Tanimoto, 1989, 1991).

For the block type inversion, the surface of the Earth is discretized into a number of small blocks, and $\frac{v_h}{v_o}$ in each block is assumed to be a constant. The travel time anomaly is thus,

$$\Delta t = \sum_i \left(\frac{v_h}{v_o} \right)_i S_i \ , \tag{2.5}$$

where

$$S_i = -\frac{1}{v_o} l_i \ ,$$

and l_i is the path length in each block. We solve for the velocity variation $(\frac{v_h}{v_o})_i$ in each block.

For the spherical harmonic expansion approach, $\frac{v_h}{v_0}$ is expanded into a spherical harmonic series,

$$\frac{v_h}{v_o} = \sum_l \sum_m \left\{ a_{lm} \cos(m\phi) + b_{lm} \sin(m\phi) \right\} P_l^m(\theta) \ , \tag{2.6}$$

where the coefficients a_{lm} and b_{lm} are the unknown parameters, and the spherical harmonics are fully normalized with

$$P_l^m(\theta) = \left[(2 - \delta_{m,0})(2l+1) \frac{(l-m)!}{(l+m)!} \right]^{1/2} p_l^m(\cos\theta) \ , \tag{2.7}$$

where the $p_l^m(\cos\theta)$) are the associated Legendre polynomials (*e.g.*, Stacey, 1977; Woodhouse and Dziewonski, 1984; Nataf *et al.*, 1986). Substituting (2.6) into (2.4) yields

$$\Delta t = -\sum_{l}\sum_{m}\left\{\int_{s}^{r}\frac{\cos(m\phi)P_l^m(\theta)}{v_o}ds\ a_{lm} + \int_{s}^{r}\frac{\sin(m\phi)P_l^m(\theta)}{v_o}ds\ b_{lm}\right\}. \quad (2.8)$$

For convenience in a later section, we write the system as

$$Y = AX, \quad (2.9)$$

where Y is made up by the travel time residual, vector X is composed of unknown parameters, and the elements of matrix A are given by S_i in Equation (2.5) or the great circle integral in Equation (2.8).

Theoretically, to describe exactly the $\frac{v_h}{v_0}$ needs the spherical harmonic expansion to infinite angular order, and the block size as small as possible. This is impossible under the present condition because of the limitation of the observation and computer capacity. In this chapter, we truncated the spherical harmonic expansion order to 36, and discretized the block size into $5^0 \times 5^0$ near the equator, and approximately an equal area at higher latitude. The Equation (2.9) is solved by the Stochastic method (Jackson, 1979; Aki and Richards, 1980). The other method will be discussed in Chapter 3.

$$\hat{X} = (A^T A + \alpha^2 I)^{-1} A^T Y, \quad (2.10)$$

where α^2 is a damping parameter and I is an identity matrix. We assumed that the covariance matrix of X is identity matrix. The resolution of X is given by

$$R = (A^T A + \alpha^2 I)^{-1} A^T A. \quad (2.11)$$

The error ΔX in the estimate of particular solutions because of the error ΔY in the data can be described by its covariance matrix

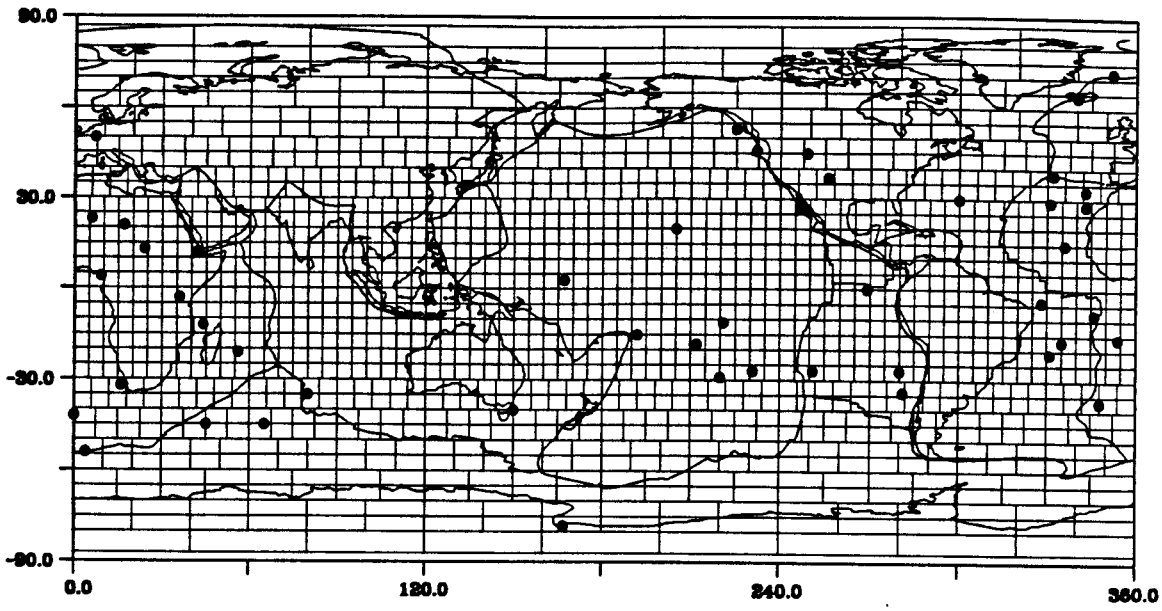

Figure 2.3, The surface distribution of blocks used in the inversion and synthetic tests. A total of 1628 blocks are used to cover the surface in an approximately equal area discretization. Cylindrical projection is used.

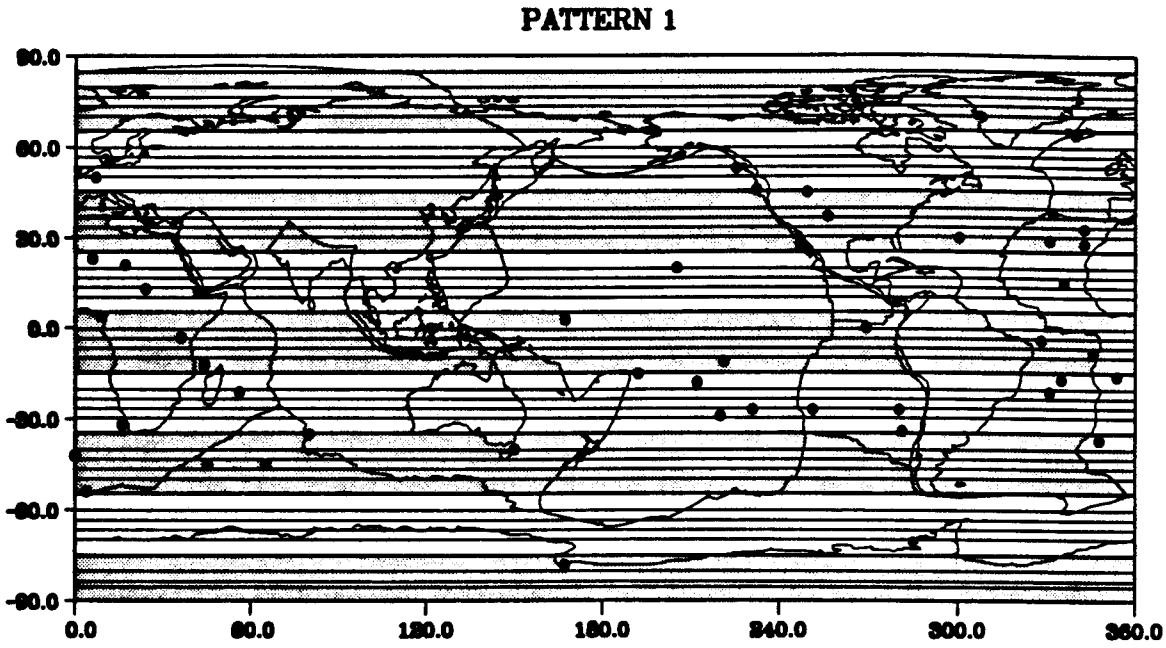

Figure 2.4, The first synthetic test velocity pattern. Velocity varies every 10 degrees in latitude. The shaded area represents a faster velocity anomaly than average, and the white area is a lower velocity anomaly. The contour interval is 0.5 percent.

$$<\Delta X\,\Delta X^T> =$$

$$= (A^T A + \alpha^2 I)^{-1} A^T <\Delta Y\,\Delta Y^T> A \left[(A^T A + \alpha^2 I)^{-1}\right]^T . \quad (2.12)$$

2.5 Synthetic model tests

With a uniform path coverage, the spherical harmonic expansion and block parametrization methods should give equivalent results. But the situation in the present study is complicated by clustering the earthquakes and stations. Before doing the real data inversion, an important question we would like to address is which approach produces more reliable result for a given data set. We performed two synthetic tests for our particular path coverage. In both cases, the spherical harmonic approach was expanded up to degree and order 36 and the block inversion discretized the surface of the Earth into 5 degrees by 5 degrees near the equator, and approximately equal area at higher latitude. This is equivalent to the spherical harmonic expansion up to $l = 36$. In the block discretization, we tried to keep the area in each block approximately the same. This would make the inversion results stable and reasonable. The block discretization is shown in Figure 2.3.

We used the stochastic method to solve the unknown parameters for both approaches. The damping constants were chosen at the same level as the real data inversion. The first test (Figure 2.4) had a striped pattern that changed velocity every 10 degrees in latitude. The shaded area represents faster velocity, and the white area represents lower velocity than average. The contour interval is 0.5 percent. Theoretical travel time anomalies were computed for the data set in Figure 2.2 and then inverted for velocity variation with various damping

parameters. Figures 2.5a and 2.5b show the spectral amplitude distribution as a function of angular order l for the block discretization approach and the spherical harmonic approach, respectively. The spectral amplitude for a particular angular order l is calculated by:

$$E(l) = \left[\frac{\sum_{m=0}^{l} (a_{lm}^2 + b_{lm}^2)}{2l + 1} \right]^{\frac{1}{2}} , \qquad (2.12)$$

where a_{lm} and b_{lm} are the spherical harmonic coefficients defined in Equation (2.6).

In the block discretization approach, the inversion results were expanded into spherical harmonics up to $l = 36$, and then the spectral amplitude as a function of angular order was computed. In Figures 2.5a and 2.5b, the spectral amplitude distributions of the original and three inversion cases, which correspond to different damping parameters, are presented.

Figure 2.5a, the spectral results of the block type inversion, shows that the general pattern of the original spectrum distribution was recovered, and there was not much difference even for the results associated with higher damping parameters. The amplitudes, however, were not faithfully retrieved. For the spherical harmonic expansion approach, Figure 2.5b shows that the pattern was recovered for a small damping parameter case but had much deviation from the original pattern for large damping parameters.

Figures 2.6a and 2.6b show the velocity inversion results for the block type inversion and the spherical harmonic expansion inversion, respectively. The original velocity patterns were generally reproduced. However, the block inversion results appear closer to the original patterns than the spherical harmonic expansion inversion results.

Figure 2.5, (a). Spectral amplitude distribution as a function of angular order l for the block inversion. Original and three inversion cases with different damping parameters are plotted (TAF means the damping parameter). The upper left is the original distribution. General patterns are recovered in these 3 cases. (b). Same as Fig. 2.5a, but for spherical harmonic expansion inversion. General patterns are recovered with only a small damping parameter. There are large deviations for a large damping parameter.

(a) SPECTRAL AMPLITUDE, PATTERN 1, EQUAL AREA BLOCK INVERSION

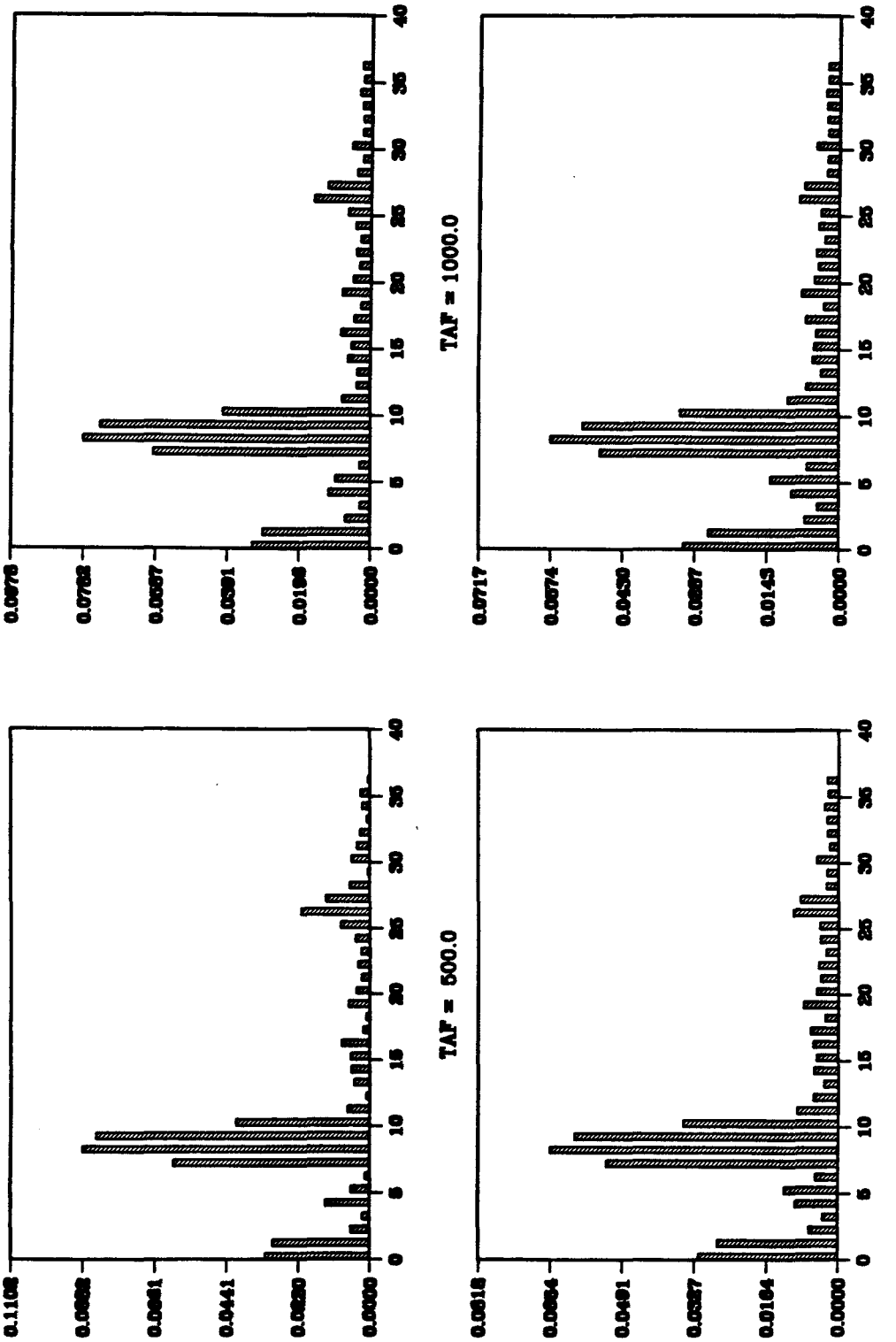

(b) SPECTRAL AMPLITUDE, PATTERN 1, SPHERICAL HARMONIC EXPANSION

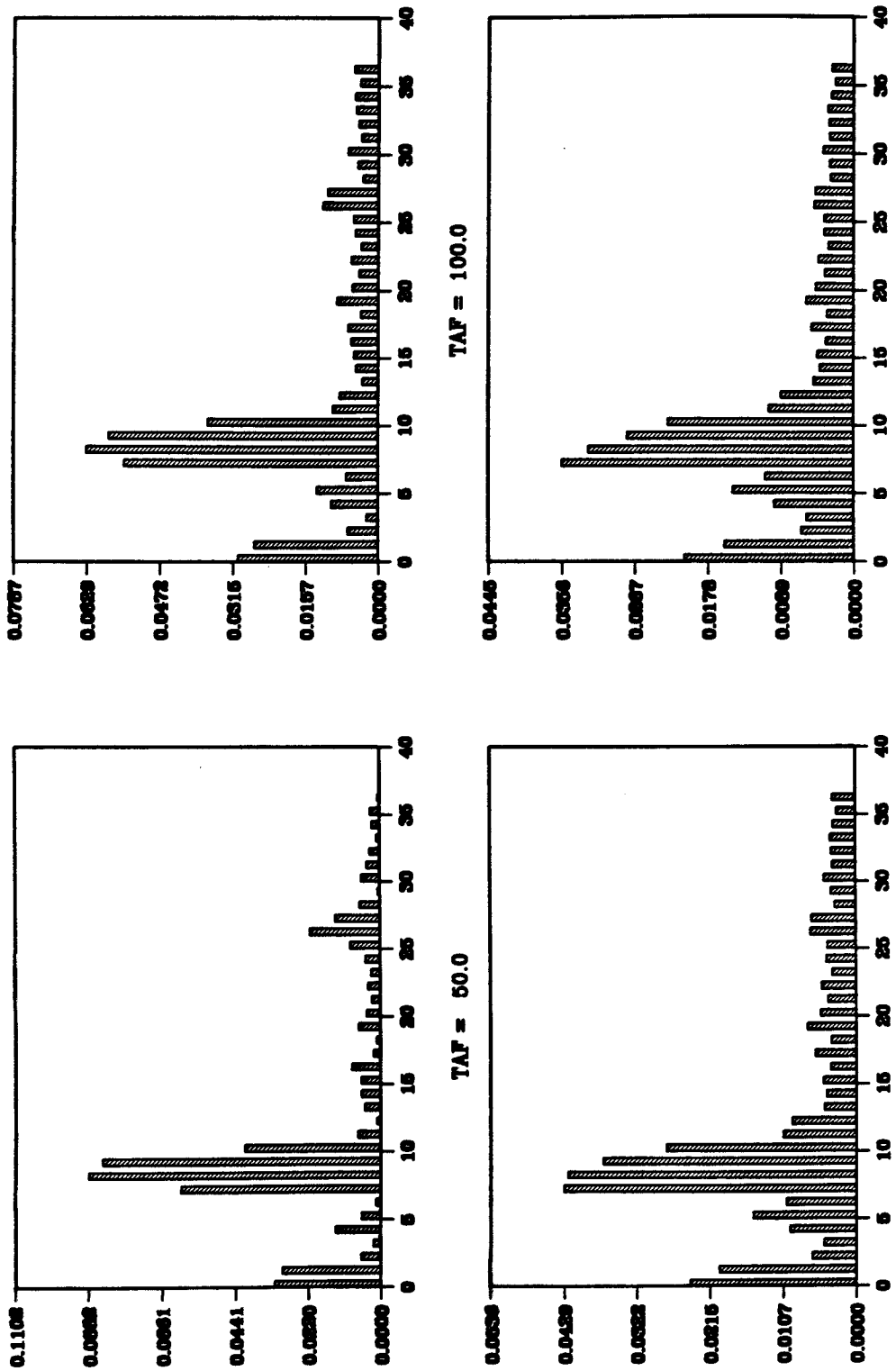

Figure 2.6, (a). Retrieved patterns by the equal area block inversion. (b). Retrieved patterns by the spherical harmonic expansion inversion. In both cases, we have used a constant damping parameter approach. The block inversion results are closer to the original than that of the spherical harmonic expansion inversion.

(a)

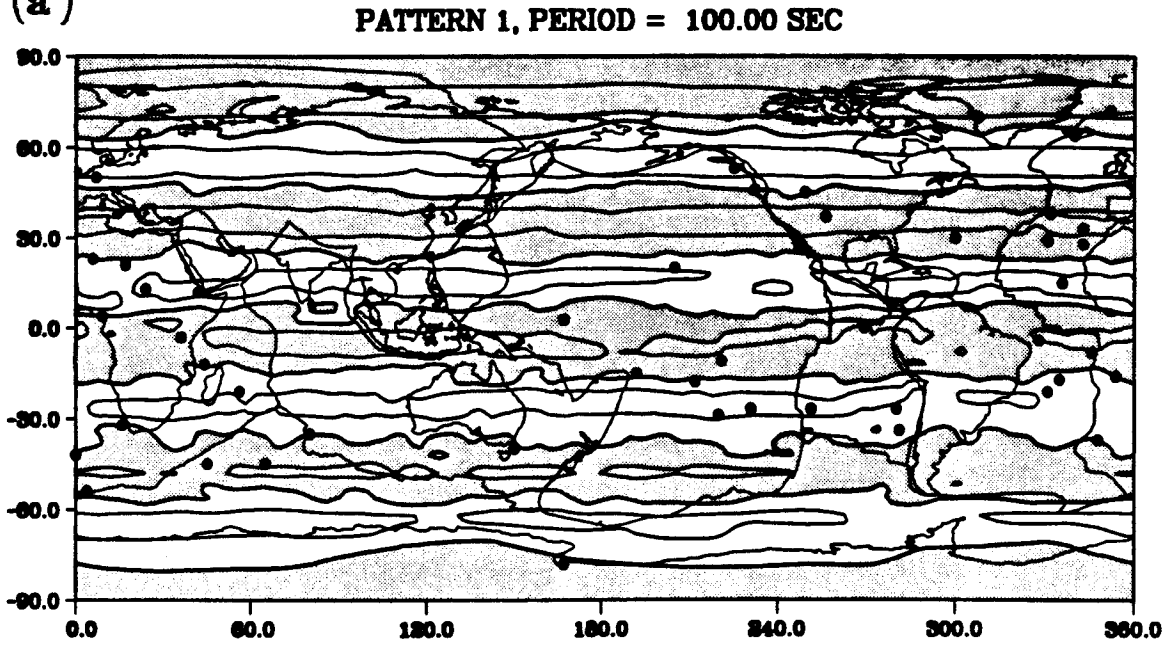
PATTERN 1, PERIOD = 100.00 SEC
90.0
60.0
30.0
0.0
-30.0
-60.0
-90.0
0.0
60.0
120.0
180.0
240.0
300.0
360.0
PHASE VEL. = 4.65 KM/SEC, TAF = 1.00e+03

(b)

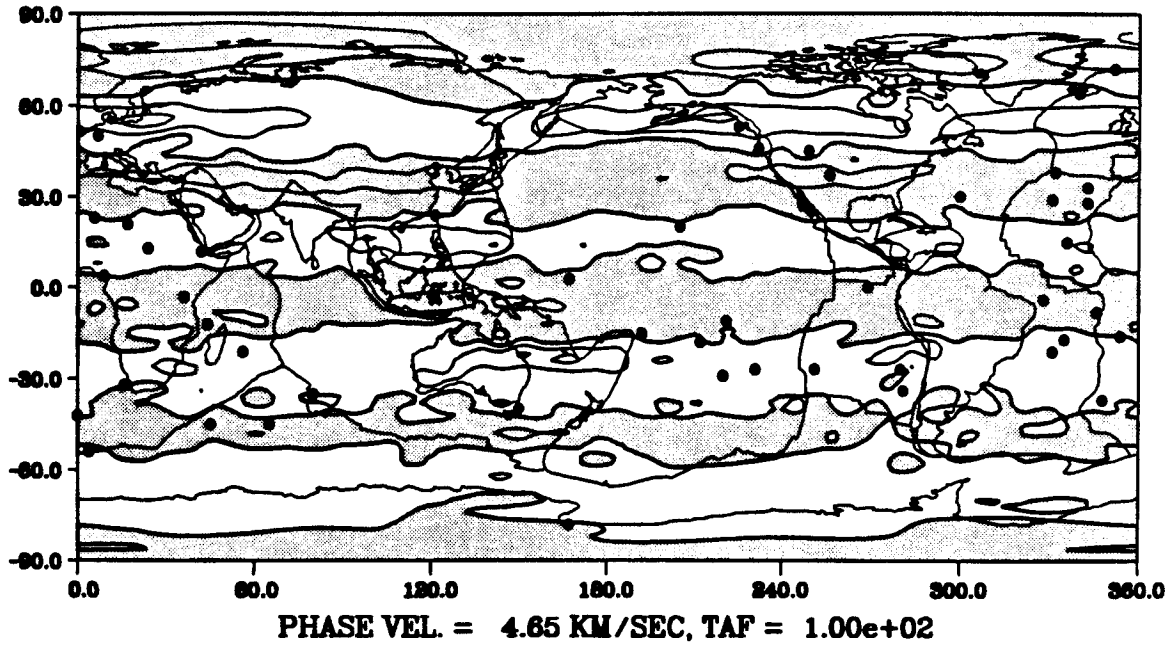
PATTERN 1, 0 <= L <= 36, PERIOD = 100.00 SEC
90.0
60.0
30.0
0.0
-30.0
-60.0
-90.0
0.0
60.0
120.0
180.0
240.0
300.0
360.0
PHASE VEL. = 4.65 KM/SEC, TAF = 1.00e+02

Since the first test did not provide longitudinal resolution, a second synthetic test was devised, which produced multicircular patterns shown in Figure 2.7, allowing longitudinal and latitudinal resolution to be tested simultaneously. This test produced the spectral peak at a completely different position; note that the peak occurred for $l = 9$ in the first test (Figures 2.5a and 2.5b) and for $l = 18$ in the second test (Figures 2.8a and 2.8b). Figures 2.8a and 2.8b show the spectral amplitude pattern, and Figure 2.9a and 2.9b show the velocity inversion results for the second test with the two different approaches respectively. The second test shows the same results as the first test. The equal area block type inversion obtained better results than the spherical harmonic expansion approach, in both the spectrum and spatial domains.

These two synthetic tests clearly demonstrate that the equal area block parametrization inversion gives better results than the spherical harmonic expansion inversion does. This was probably caused by the unbalanced path coverage of our data set. In the block inversion approach, the velocity variation at a particular block depended only upon the paths through that block. In the spherical harmonic expansion inversion, however, each coefficient was strongly dependent on the global path coverage, and the nonuniformly distributed paths became a problem. In order to obtain equivalent results, a more complicated damping scheme is probably needed for the spherical harmonic expansion inversion.

We also note that the southeast Pacific and other regions in the southern hemisphere are problematic. This is mainly caused by the sparse path coverage in these areas, thus interpretation of these regions must be carefully made. The second test showed that a spectral peak at angular order $l = 18$ was resolved for the block type approach (Figures 2.8a and 2.9a). This suggests

that the data set was good enough to allow resolution at a wavelength corresponding up to angular order $l = 18$, and most likely up to $l = 25$.

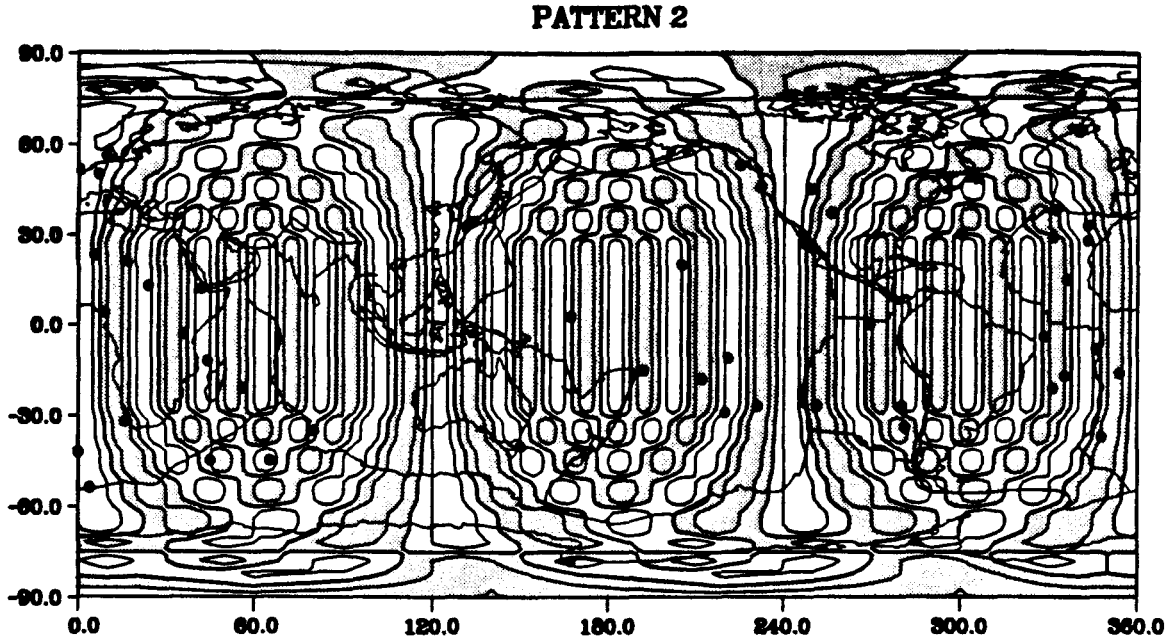

Figure 2.7, Velocity pattern for the second synthetic test. It is associated with velocity variation in latitude and longitude simultaneously, and has more power at higher angular order l than the first test.

Figure 2.8, (a). Spectral amplitude of the second synthetic test for the block inversion. A very strong peak at $l = 18$ is recovered. (b). Spectral amplitude of the second synthetic test for the spherical harmonic expansion inversion. The high angular order terms are much more sensitive to the damping parameter in this approach than in the block inversion.

(a) SPECTRAL AMPLITUDE, PATTERN 2, EQUAL AREA BLOCK INVERSION

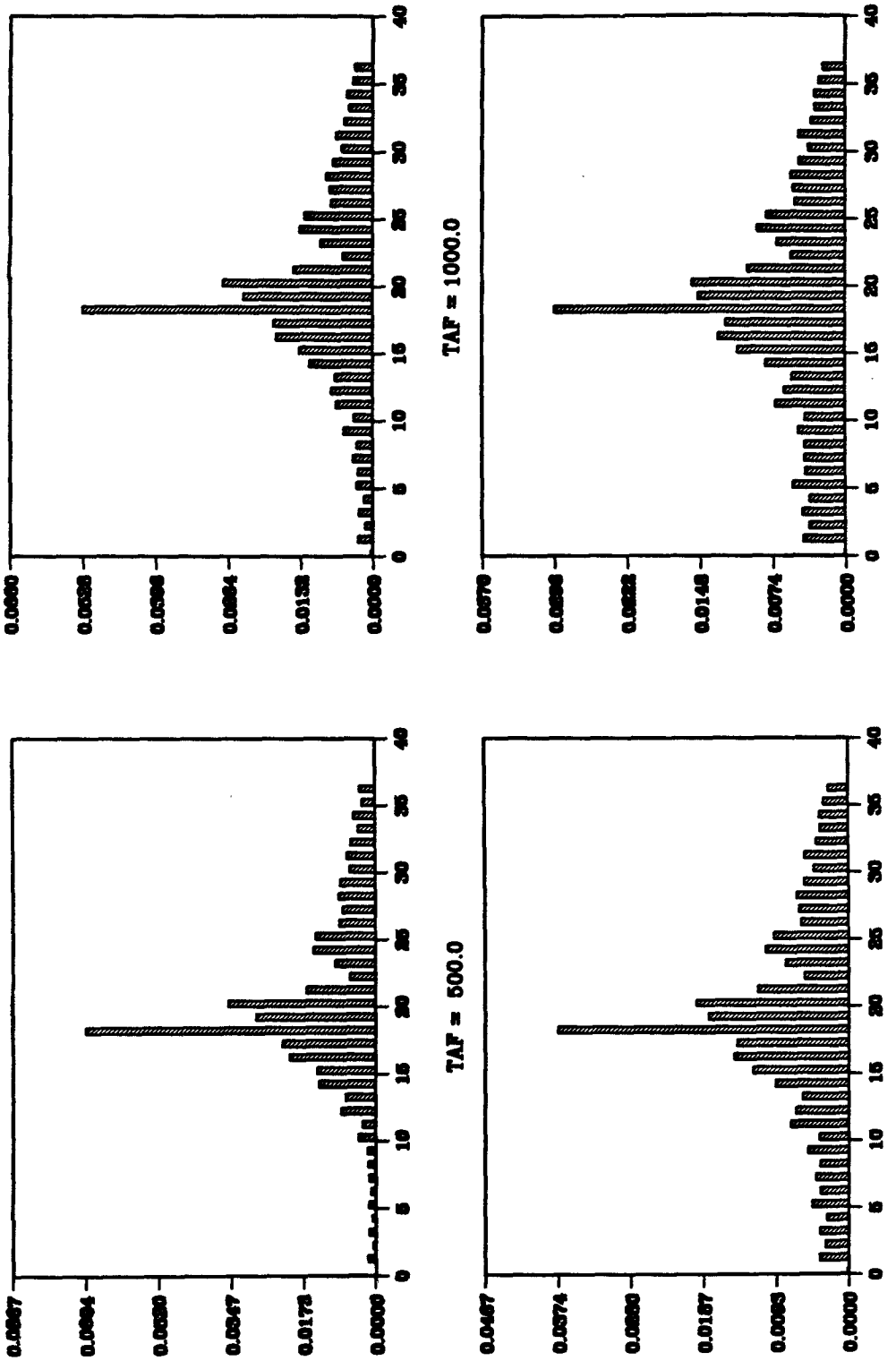

(b) SPECTRAL AMPLITUDE, PATTERN 2, SPHERICAL HARMONIC EXPANSION

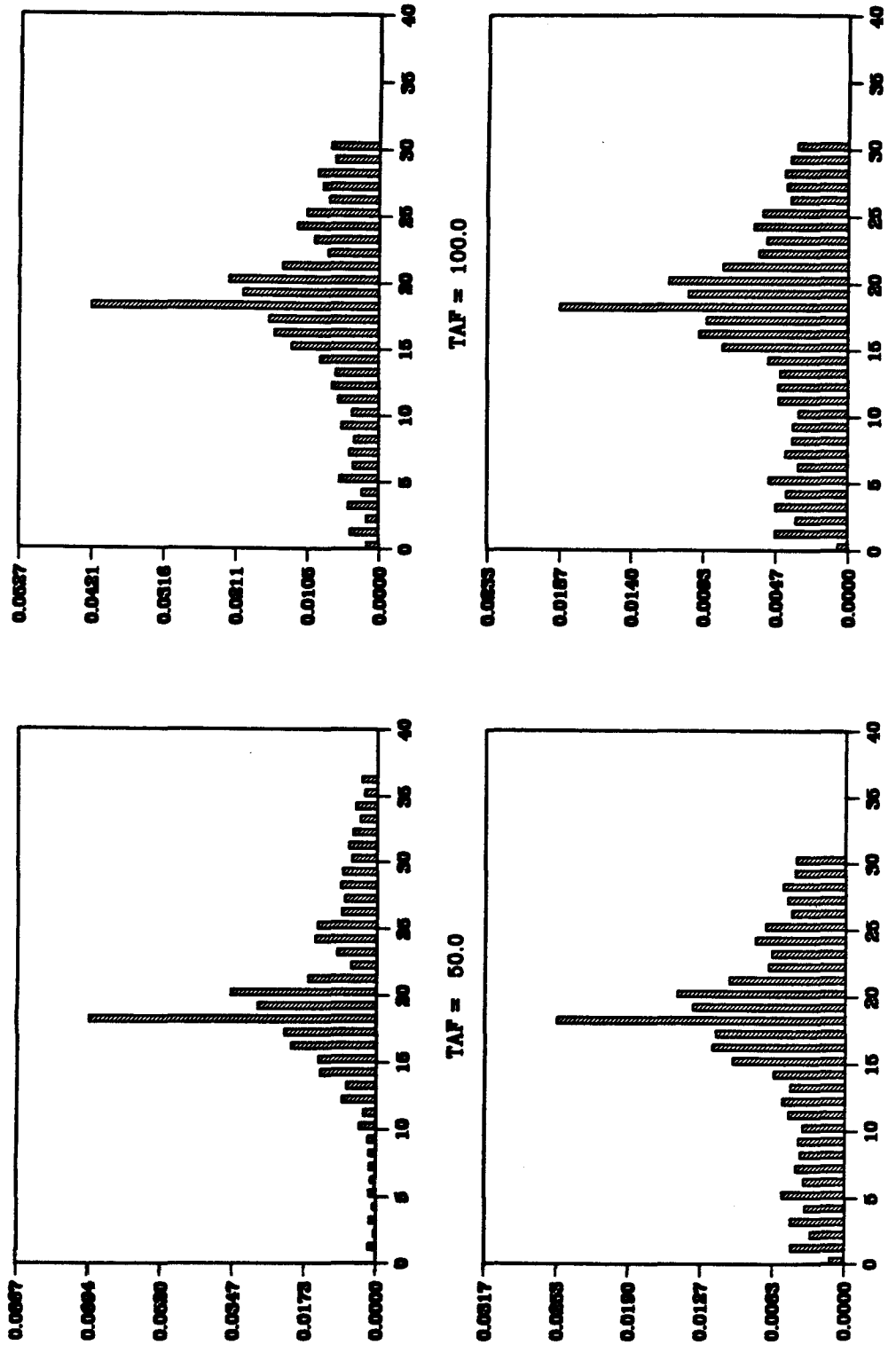

Figure 2.9, (a). Retrieved pattern for the second test by the equal area block inversion. (b). Retrieved pattern for the second test by the spherical harmonic expansion inversion.

(a)

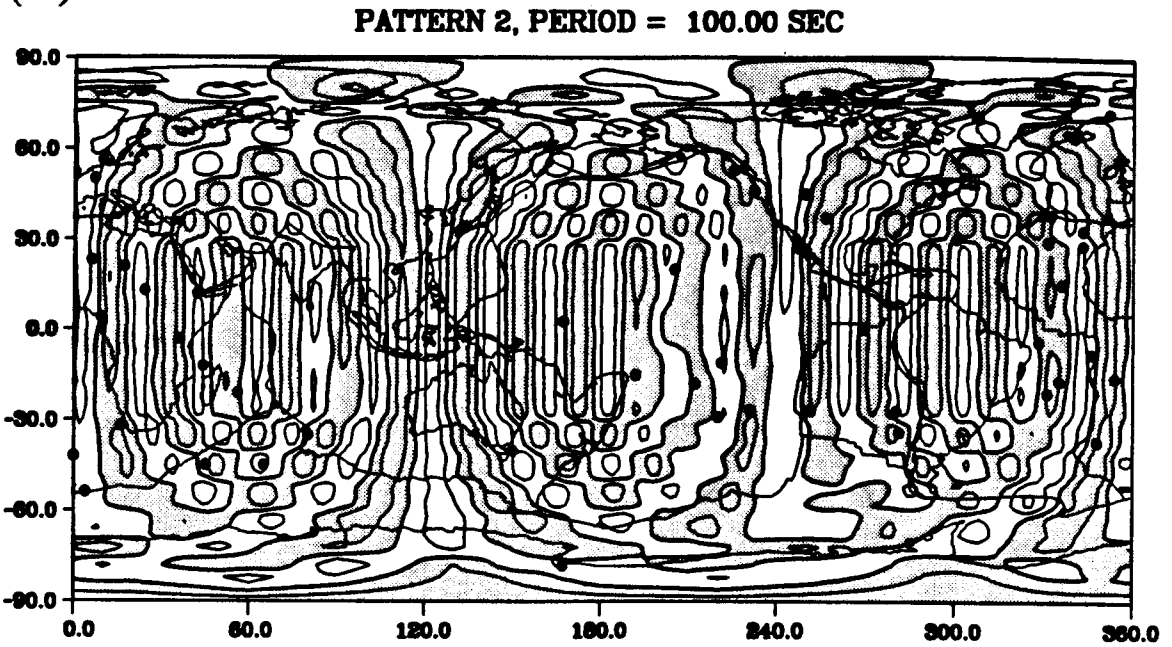
PATTERN 2, PERIOD = 100.00 SEC
90.0
60.0
30.0
0.0
-30.0
-60.0
-90.0
0.0
60.0
120.0
180.0
240.0
300.0
360.0
PHASE VEL. = 4.65 KM/SEC, TAF = 1.00e+02

(b)

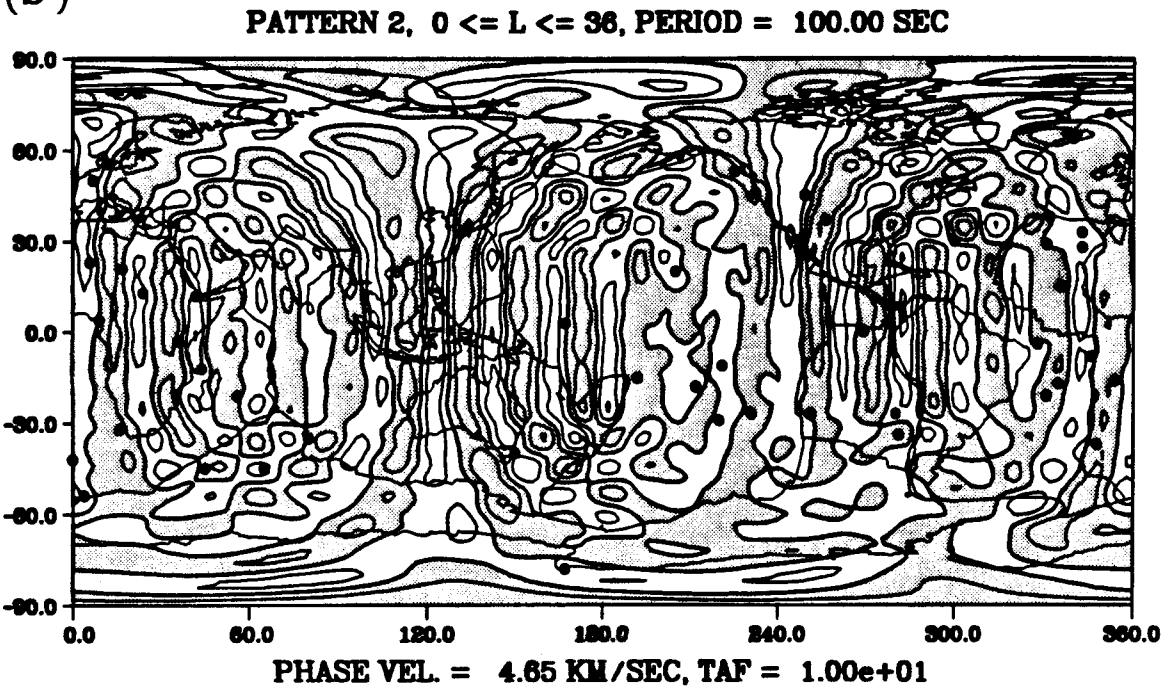
PATTERN 2, 0 <= L <= 36, PERIOD = 100.00 SEC
90.0
60.0
30.0
0.0
-30.0
-60.0
-90.0
0.0
60.0
120.0
180.0
240.0
300.0
360.0
PHASE VEL. = 4.65 KM/SEC, TAF = 1.00e+01

2.6 Summary

We have collected about 18,000 seismograms associated with 971 earthquakes with magnitude larger than about 5.5 from GDSN and GEOSCOPE networks. The path coverage is much better than previous upper mantle studies, which enable us to obtain small scale features.

Both the spherical harmonic expansion inversion and the equal area block parametrization inversion were tested. Without uniform path coverage, resolution of high angular order is problematic in the spherical harmonic expansion inversion, and the equal area block inversion seems to be a better approach. The synthetic tests showed that the present data set was allowed the resolution wave length in spherical angular order between $l = 18$ and 25 by using the equal area block approach. In order to improve the resolution, a more uniform and denser distributed network is needed, especially in the southern hemisphere. We adopted the equal area block parametrization inversion for this study.

Chapter 3

The Use of ABIC and AIC Methods to Resolve the Linear Inversion

3.1 Introduction

The goal of every inverse problem is to find at least one plausible model that fits the observations. In many such problems, the unknown continuous model is approximately presented by a finite number of elements; each element may be an expansion coefficient (*e.g.*, Nakanishi and Anderson, 1984; Woodhouse and Dziewonski, 1984; Tanimoto and Anderson, 1985; Nataf *et al.*, 1986), or an average of the unknown function over some narrow range (*e.g.*, Aki *et al.*, 1976; Clayton and Comer, 1983; Suetsugu and Nakanishi, 1985; Zhang and Tanimoto, 1989, 1991). The inverse problem may be expressed in the linear parametric form

$$Y = AX + \xi \,, \tag{3.1}$$

where Y is an n-element vector of observations, X is a vector of m unknown parameters, A is a known $n \times m$ matrix, and ξ is a vector of n random errors (in data space), presumed to have zero mean and variance σ^2.

Equation (3.1) can be solved by many different methods. The two most commonly used methods are Stochastic inversion and Bayesian inference inversion (*e.g.*, Jackson, 1979; Backus, 1988). Both methods use *a priori* information as constraints of the unknown model, and the estimated solution is

$$\hat{X} = (A^T A + \alpha^2 D^T D)^{-1} A^T Y \ , \tag{3.2}$$

where $(D^T D)^{-1}$ is proportional to the covariance matrix of vector X, and α^2 is a damping parameter. In such studies, the damping parameter α^2 is always subjectively selected by the observer's experience and an *a priori* belief. Obviously, solving an inverse problem is dependent upon accurate observations; but after getting good data, parameterizing the unknown continuous model and choosing the damping parameter for the inversion will be important for obtaining reliable results and avoiding possible bias effects.

Seismology provides a direct method to understanding the structure of the Earth. In the last decade, upper mantle studies have increased the truncated spherical angular order l from 2 to 12 (Masters *et al.*, 1982; Nakanishi and Anderson, 1984; Woodhouse and Dziewonski, 1984; Tanimoto and Anderson, 1985; Nataf *et al.*, 1986; Wong, 1989), and a lot of information has been obtained. But the Earth structure we obtained shows only long wavelength features (longer than 4,000 km), and we cannot explain many geological observations, for example, ridges, hotspots, rift valleys, *etc.* In order to understand the Earth, we should get Earth structure in as much detail as possible. The development of global networks of broad-band, digital seismographs (Peterson and Hutt, 1982; Romanowicz, 1984) has permitted the acquisition and processing of unprecedented amounts of seismic data. Under the present conditions, how much detail in velocity structure can we obtain? How do we avoid

possible bias effects? And which method is better to parameterize the three-dimensional velocity structure of the Earth? These questions are important for present and future study.

In Chapter 2, we discussed a special case: spherical harmonic expansion for $l_{max} = 36$ and equal area block parameterization ($5^o \times 5^o$ near the equator). The equal area block parameterization seems to be a better approach. We did not talk about the optimal truncation level and damping parameter for both methods. In this chapter, we are concerned with these problems associated with the same data set. We shall build up the likelihood function about the model with the statistic theory. The probability function for errors ξ (in data space) and ΔX (in model space) are both assumed to be Gaussian random functions. This is a reasonable assumption when the number of observations is large. The optimal damping parameter is determined by using "*Akaike Bayesian information criterion (ABIC)*" (Akaike, 1979, 1980), and the optimal regularization of the unknown function is determined by "*Akaike information criterion (AIC)*" (Akaike, 1974; Sakamoto *et al.*, 1986); both of the methods are based upon the maximum likelihood of the inversion system. We use global Love wave phase velocity inversion as an example in this chapter; the spherical harmonic expansion and the equal area block parameterizations are studied. Because of the non-uniform path coverage on the real world, we find that the equal area block parameterization gives a better approximation than the spherical harmonic expansion using the present data set. The optimal, truncated spherical angular order l is about 18 for the spherical harmonic expansion; the equivalent cutoff level for equal area block inversion is about 24. The spectral amplitudes for both methods have shown similar results.

In sections 3.2 and 3.3, we will discuss the *ABIC* and *AIC* methods. The example of global Love wave phase velocity inversion for a period of 100 s is shown in section 3.4. And the main conclusions are given in section 3.5.

3.2 ABIC method

Any phenomenon with uncertainty can be regarded as the realization of a random variable that follows a certain probability distribution. When solving Equation (3.1), a reasonable assumption associated with a large number of observations is that the error vector ξ (in data space) is Gaussian randomly distributed with the mean equal to zero. For the real inversion result X and variance σ^2 in inversion problems, the probability function is (*e.g.*, Box and Tiao, 1973)

$$p\,(Y\,|X,\sigma^2) = (2\pi\sigma^2)^{-\frac{n}{2}} \exp\left\{-\frac{1}{2\sigma^2}(Y-AX)^T\,(Y-AX)\right\}. \qquad (3.3)$$

There will be infinite solutions to satisfy Equation (3.1) because of the non-uniqueness of the inversion. Any possible inversion result $\hat{X}$ will be randomly drawn from the model space. Assuming that the real solution is X, then the error in model space will be $\Delta X = X - \hat{X}$. We suppose that the two random processes for ξ and ΔX are uncorrelated, and $\hat{Y} = A\hat{X}$; then, the probability function (3.3) is

$$p\,(Y\,|X,\sigma^2) = (2\pi\sigma^2)^{-\frac{n}{2}} \exp\left\{-\frac{1}{2\sigma^2}\left[(Y-\hat{Y})^T(Y-\hat{Y})\right.\right.$$

$$\left.\left.+(X-\hat{X})^T A^T A(X-\hat{X})\right]\right\}. \qquad (3.4)$$

Because of the uncertainty in solving an inversion problem and random error in data space, the exact model X may not be obtained, and the matrix A may be ill-conditioned. An *a priori* limitation for the model should be included when solving the inverse problem. Given a statistical description of the parameter X, we also consider that the error ΔX in model space is a Gaussian random variable, with zero mean and covariance matrix C_x. The prior distribution of ΔX for a possible damping parameter α^2 will be (*e.g.*, Box and Tiao, 1973)

$$\pi(X\,|\alpha) = (2\pi\sigma^2)^{-\frac{m}{2}}\,|\alpha^2 D^T D\,|^{\frac{1}{2}} \times$$

$$\exp\left\{-\frac{\alpha^2}{2\sigma^2}(X-\hat{X})^T D^T D(X-\hat{X})\right\}, \qquad (3.5)$$

where $(D^T D)^{-1}$ is proportional to the covariance matrix C_x. The normalization of probability function $\pi(X\,|\alpha)$ to 1 is considered in Equation (3.5).

By choosing a different damping parameter α^2, we can get many models. The possible range of X is $|X| < \infty$. Given the Bayesian inference, the marginal likelihood function (or the posterior distribution) of (α, σ^2) (Akaike, 1980; Berger, 1985) is

$$L\,(\alpha,\sigma^2) = \int_{-\infty}^{\infty} p\,(Y\,|X,\sigma^2)\,\pi(X\,|\alpha)\,dX$$

$$= (2\pi\sigma^2)^{-\frac{n}{2}}\,|\alpha^2 D^T D\,|^{\frac{1}{2}}\,|A^T A + \alpha^2 D^T D\,|^{-\frac{1}{2}} \exp\left\{-\frac{n}{2}\right\}. \qquad (3.6)$$

In the last equation, we have approximated $\sigma^2 = \frac{1}{n}(Y - \hat{Y})^T(Y - \hat{Y})$ when $n >> 0$ and $n >> m$.

Conventionally, we use that minus twice the log marginal likelihood function $(-2)logL(\alpha,\sigma^2)$, and try to minimize it. This is defined by Akaike (1980) as *"Akaike Bayesian information criterion (ABIC)."*

$$ABIC = n\log\sigma^2 - \log|\alpha^2 D^T D| + \log|A^T A + \alpha^2 D^T D| + const. \quad (3.7)$$

This is the equation we used to determine the optimal damping parameter α^2 in solving Equation (3.1). Because it is difficult to obtain an explicit formula for the damping parameter α^2, we consider a finite set of possible values of $(\alpha_1,\alpha_2,...,\alpha_t)$ and choose one that minimizes the *ABIC* value by using the graphic method.

3.3 AIC method

The unknown continuous model in the geophysical inversion problem is always regularized into a finite element presentation. The presentation maybe is expansion coefficients based upon some basis function, such as the Fourier function, the spherical harmonic function, and the Legendre function *etc.*, or average elements over small ranges. In both cases, we would require infinite coefficients or elements as small as possible to describe the unknown model exactly, but in the present seismological study, this would be impossible. One constraint is observation: we do not have enough data to describe the unknown model completely. Another constraint is the limitation of the computer capacity. We cannot increase the data and model parameters infinitely. The questions are: What are the optimal expansion limits, or the parts small enough to

best describe the unknown model under present observations? And which approach will give us a better approximation?

We believe that the true inversion result cannot be obtained without uncertainty. Supposing the observation Y is independent and identically distributed with a probability density function $f(Y|X)$, where X is a given model, the expected *log* likelihood of the distribution $f(Y|X)$ is defined by

$$l(X) = E(log\ f(Y|X)) = \int f(Y|X^*)\, log\ f(Y|X)\, dY\ , \tag{3.8}$$

where X^* is the true model. Around the true parameter, X^*, yields the approximation

$$l(X) = l(X^*) + (X - X^*)^T E\left[\frac{\partial log f(Y|X)}{\partial X}\right]_{X^*} + \frac{1}{2}(X - X^*)^T E\left[\frac{\partial^2 log f(Y|X)}{\partial X^2}\right]_{X^*}(X - X^*). \tag{3.9}$$

From the properties of the *Kullback-Leiber information quantity*, the maximum value of $l(X)$ occurs at $X = X^*$, and the second term of the right hand side vanishes. We assume that both Y and X are Gaussian random normal distributed with the true values Y^* and X^*. For a large number of observations, n,

$$(X - X^*)^T E\left[\frac{\partial^2 log f(Y|X)}{\partial X^2}\right]_{X^*}(X - X^*) \rightarrow -m\ ,$$

where m is the degrees of freedom of the model (Sakamoto *et al.*, 1986 (*pp25-26*)). Thus, for a large number of observations, we have

$$l(X) = l(X^*) - \frac{m}{2}. \tag{3.10}$$

The Taylor expansion of the *log* likelihood $g(X) = logf(Y|X)$ around the maximum likelihood estimate $\hat{X}$ yields the approximation

$$g(X) = g(\hat{X}) + (X - \hat{X})^T \left[\frac{\partial g}{\partial X}\right]_{\hat{X}} + \frac{1}{2}(X - \hat{X})^T \left[\frac{\partial^2 g}{\partial X^2}\right]_{\hat{X}} (X - \hat{X}). \tag{3.11}$$

Here, the second term on the right hand side vanishes when the *log* likelihood takes its maximum value at $\hat{X}$.

By the law of large numbers of observations,

$$(X - \hat{X})^T \left[\frac{\partial^2 g}{\partial X^2}\right]_{\hat{X}} (X - \hat{X}) \rightarrow (X - \hat{X})^T E\left[\frac{\partial^2 logf(Y|X)}{\partial X^2}\right]_{\hat{X}} (X - \hat{X}) = -m. \tag{3.12}$$

Substituting X^* for X in (3.11) and taking expectations of both sides, we have, therefore, for large n,

$$E[g(X^*)] = E[g(\hat{X})] - \frac{m}{2}, \tag{3.13}$$

and

$$l(X^*) = l(\hat{X}) - \frac{m}{2}. \tag{3.14}$$

Substituting (3.14) into (3.10), we obtain

$$l(X) = l(\hat{X}) - m. \tag{3.15}$$

We use that minus twice the above quantity (3.15), and try to minimize it. This is defined as "*Akaike information criterion (AIC)*" by Akaike (Akaike, 1974; Sakamoto *et al.*, 1986).

$$AIC = -2l(\hat{X}) + 2m \ . \tag{3.16}$$

The optimal regularization of the unknown continuous function is obtained with the smallest AIC value.

3.4 Example

The data we use here are the same as in Chapter 2. We want to invert for global, Love wave phase velocity and examine its lateral variation. In order to keep the accuracy, we have used only the minor arc phase G1 and checked all data with synthetic seismogram. The details of the selection of the data were described in Chapter 2. We will discuss both the spherical harmonic expansion method and the block parameterization method in this chapter.

For the spherical harmonic expansion approach, the relative velocity variation $\frac{v_h}{v_0}$ is expanded into a spherical harmonic series. The travel time residual is the Equation (2.8),

$$\Delta t = -\sum_l \sum_m \left\{ \int_s^r \frac{\cos(m\phi) P_l^m(\theta)}{v_o} ds \ a_{lm} + \int_s^r \frac{\sin(m\phi) P_l^m(\theta)}{v_o} ds \ b_{lm} \right\}. \tag{3.17}$$

Compared with Equation (3.1), Y is the travel time residual Δt, vector X is composed of the coefficients a_{lm} and b_{lm}, and the elements of matrix A are the integral along the great circle from source to receiver.

The usual assumption in the inversion problem is that the damping parameters for every element are constants; matrix $D^T D$ is chosen as an identity matrix. Then, Equation (3.7) is

Figure 3.1, *ABIC* curves vs. the damping parameters for different truncated l_{max}. These curves are for the spherical harmonic expansion regularization for Love waves at 100.0 seconds. The *ABIC* values are plotted in relative scale, and there is no unit on the vertical axis. As we change the truncated l_{max}, we can always find the optimal damping parameter associated with the minimum *ABIC* value.

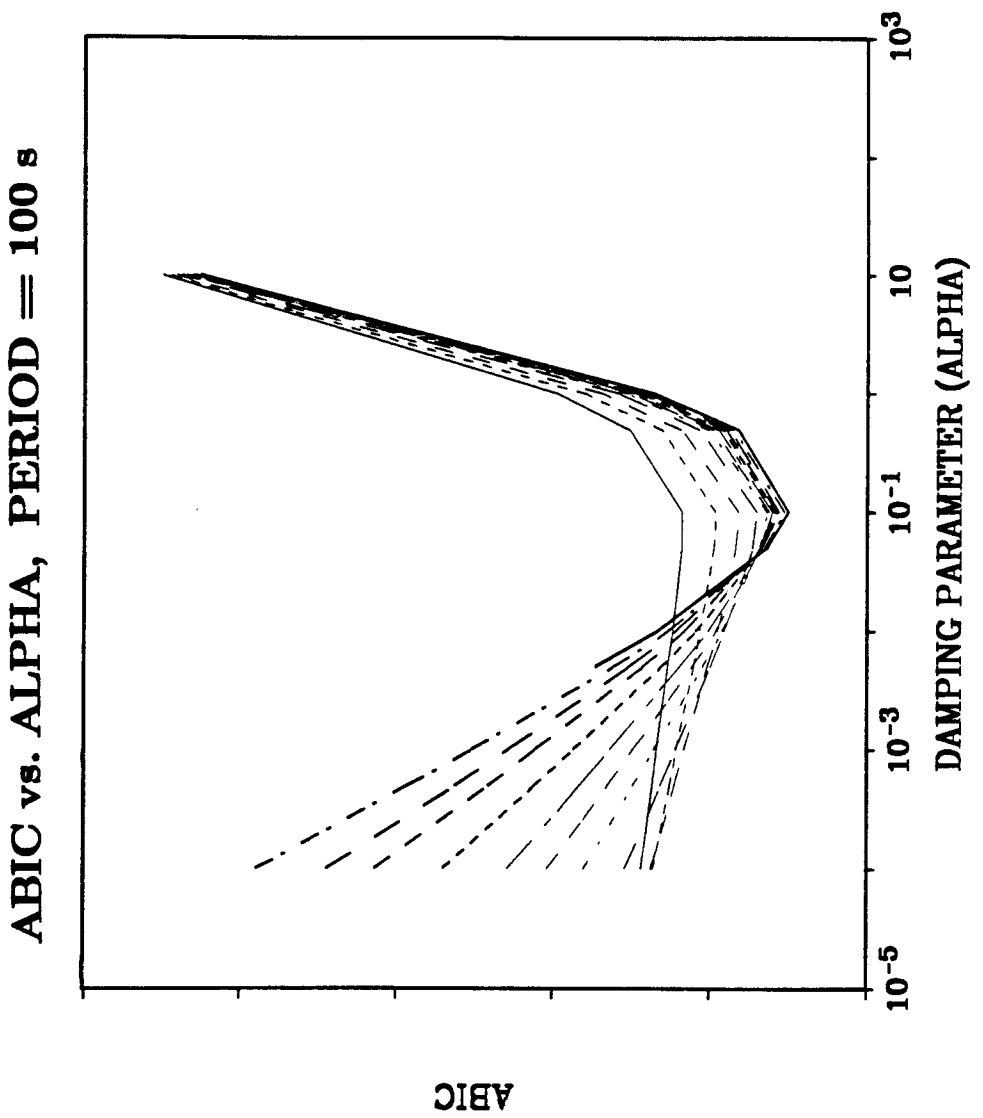
ABIC vs. ALPHA, PERIOD = 100 s
Lmax=8
Lmax=10
Lmax=12
Lmax=15
Lmax=18
Lmax=20
Lmax=22
Lmax=25
Lmax=28
Lmax=30
Lmax=33
Lmax=36
ABIC
10^{-5}
10^{-3}
10^{-1}
10
10^{3}
DAMPING PARAMETER (ALPHA)

Figure 3.2, (a). The spherical harmonic inversion results associated with $l_{max} = 12$ and optimal damping parameter. (b). Same as Figure 3.2a, but $l_{max} = 18$. (c). Same as Figure 3.2a, but $l_{max} = 20$. (d). Same as Figure 3.2a, but $l_{max} = 36$.

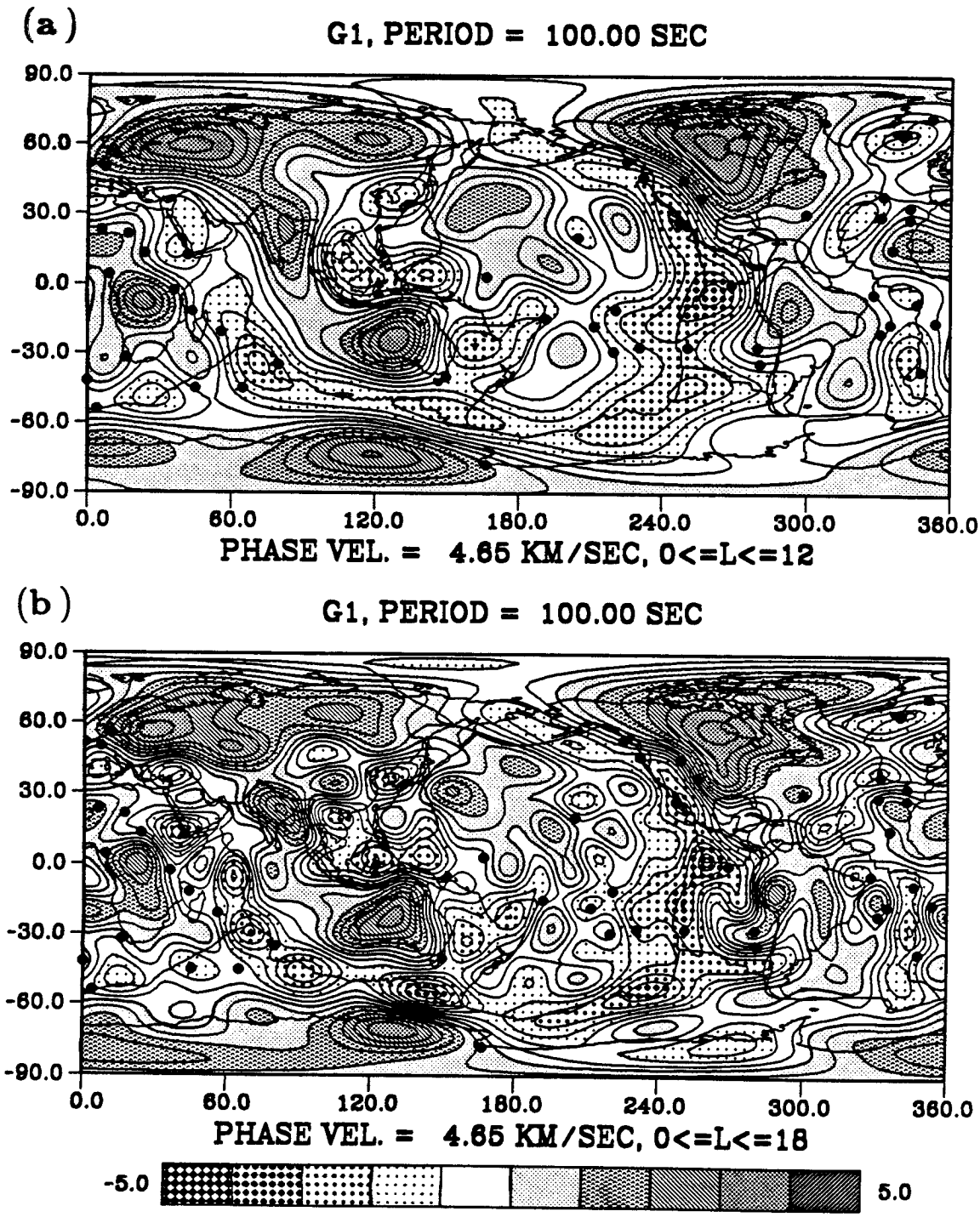
(a)
G1, PERIOD = 100.00 SEC
90.0
60.0
30.0
0.0
-30.0
-60.0
-90.0
0.0
60.0
120.0
180.0
240.0
300.0
360.0
PHASE VEL. = 4.65 KM/SEC, 0<=L<=12
(b)
G1, PERIOD = 100.00 SEC
90.0
60.0
30.0
0.0
-30.0
-60.0
-90.0
0.0
60.0
120.0
180.0
240.0
300.0
360.0
PHASE VEL. = 4.65 KM/SEC, 0<=L<=18
-5.0
5.0

(c)

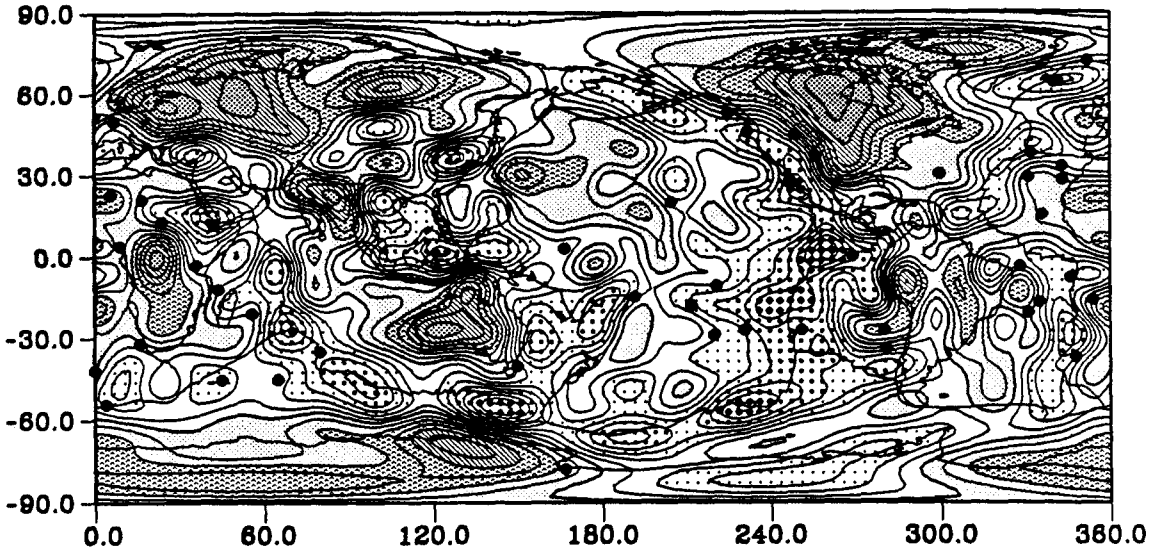
G1, PERIOD = 100.00 SEC
90.0
60.0
30.0
0.0
-30.0
-60.0
-90.0
0.0
60.0
120.0
180.0
240.0
300.0
360.0
PHASE VEL. = 4.65 KM/SEC, 0<=L<=20

(d)

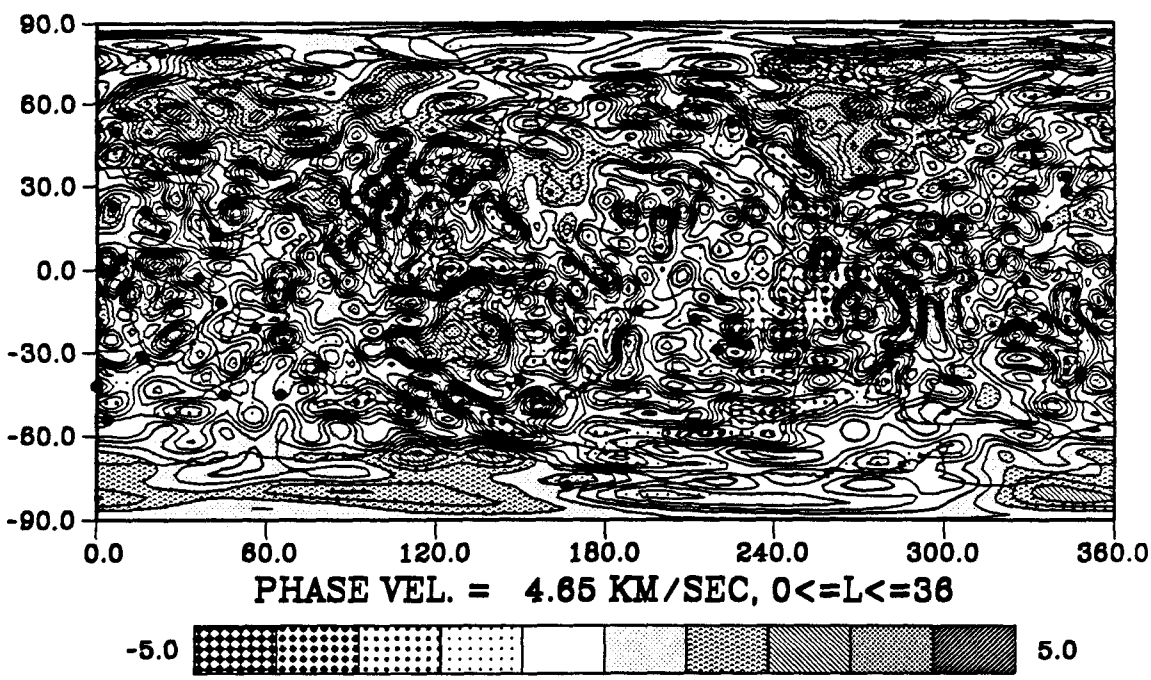
G1, PERIOD = 100.00 SEC
90.0
60.0
30.0
0.0
-30.0
-60.0
-90.0
0.0
60.0
120.0
180.0
240.0
300.0
360.0
PHASE VEL. = 4.65 KM/SEC, 0<=L<=36
-5.0
5.0

$$ABIC = n\log\sigma^2 - m\log\alpha^2 + \log|A^T A + \alpha^2 I| + const \ . \qquad (3.18)$$

We calculated the *ABIC* curves vs. damping parameters from the cutoff level $l_{max} = 8$ to $l_{max} = 36$ for Love wave at a period of 100 s. Figure 3.1 shows these curves. The *ABIC* values are presented in relative scale, and there is no unit on the vertical axis (this feature can also be found in other similar kinds of figures). Clearly, we can always find an optimal damping parameter for each truncated l_{max}. We also find that the optimal damping parameters for different l_{max} are always the same. For small l_{max}, there is no large variation in the *ABIC* curve when the damping parameters are less than the optimal damping parameter, and also the inversion results do not show much difference. The curve for large l_{max} is changed vastly, and the bias effect is clear in the results.

Figures 3.2a-d show the inversion results for $l_{max} = 12$, 18, 20 and 36 associated with the optimal damping parameter 0.1, respectively. General features of these results are the same. Figure 3.2b contains more detailed features than Figure 3.2a. The results appear to have improved with increasing the l_{max}. But after increasing l_{max} to 36, even if we use the optimal damping parameter, we find the results unacceptable. The bias effects are clear and large. For the present data set, these results show that we cannot increase the truncated level infinitely.

Using Equation (3.8), we have calculated the *AIC* curve vs. l_{max}, shown in Figure 3.3. The maximum likelihood of the model for each l_{max} is obtained with the optimal damping parameter. Figure 3.3 shows that the minimum *AIC* value is at about l_{max}=18.

Figure 3.4 shows the spectral amplitude distributions as a function of spherical angular order l on a logarithmic scale. The truncated l_{max} is equal to

12, 18, and 36, respectively. The spectral amplitude of a particular angular order l is calculated by using Equation (2.12). In Figure 3.4, we have plotted the topography spectral amplitude as a reference. The topography data were obtained from the National Geophysical Data Center in Boulder, Colorado, on a grid of 5 by 5 minutes. These spectral amplitudes are similar, and all of the curves decrease approximately to $\frac{1}{l}$ as l increases. But when l is larger than 18, the spectral curve flattens out. We think this is probably caused by the error or bias effects associated with the inversion. The truncated level for $l_{\max} = 18$ is about the optimal cutoff level. This is another evidence to prove that the *Akaike information criterion (AIC)* would give the optimal, truncated angular order level.

We also performed the same test for the block discretization. Because it is difficult to separate the surface of the Earth into any arbitrary sizes, we divided the Earth into only equal area blocks, $20^0 \times 20^0$, $15^0 \times 15^0$, $10^0 \times 10^0$, $9^0 \times 9^0$, $7.5^0 \times 7.5^0$ and $5^0 \times 5^0$ near the equator, respectively. They are equivalent to the spherical harmonic expansions of $l_{\max} = 9$, 12, 18, 20, 24 and 36, respectively.

For each block size, we calculated the *ABIC* and *AIC* values. Figure 3.5 shows the *ABIC* curve vs. damping parameter for the block-type inversion. We can always find the smallest value of *ABIC* for different block sizes. One difference from the spherical harmonic expansion is that the optimal damping parameter is not the same for different parameterizations. The smaller the block size, the smaller the optimal damping parameter. This is caused by the different parameterization. In the spherical harmonic expansion, as the truncated level increases, the lower l terms in matrix A are always the same, and

the optimal damping parameters are always the same. But in the block-type inversion, the matrix A is totally changed when we change the block size; thus the optimal damping parameter will be different.

Figure 3.6 shows the *AIC* test result for block-type inversion. The best block size is about $7.5^o \times 7.5^0$ degrees. The equivalent spherical harmonic expansion is about l_{max}=24. Figure 3.7 shows the spectrum amplitude distributions for the block-type inversion on a logarithmic scale. The block sizes are $9.0^0 \times 9^0$, $7.5^0 \times 7.5^0$ and $5^0 \times 5^0$, respectively. For the $5^0 \times 5^0$ size, shown here is the result with a damping parameter equal to the optimal damping parameter for the $7.5^0 \times 7.5^0$ block size. These curves follow the same trend as $\frac{1}{l}$, and more approximate to $\frac{1}{l}$ than in the spherical harmonic expansion case.

In Chapter 2, we did two synthetic tests for the similar data set and for both spherical harmonic expansion and block parameterization. The results show that the block-type inversion results are much better than those of the spherical harmonic expansion inversion. Figure 3.8 shows the spectral amplitudes of test 2 of Chapter 2 on a logarithmic scale. The maximum spherical angular order l is 36, and the block size is $5^0 \times 5^0$. The original power is at about angular order $l = 18$. There is a large deviation from the original power pattern for the spherical harmonic expansion in Figure 3.8. And the spectrum of the block-type inversion is much closer to the original pattern than the spherical harmonic expansion for higher angular order terms. This is more evidence to show that the block-type inversion can produce more detailed, reliable features than the spherical harmonic expansion inversion.

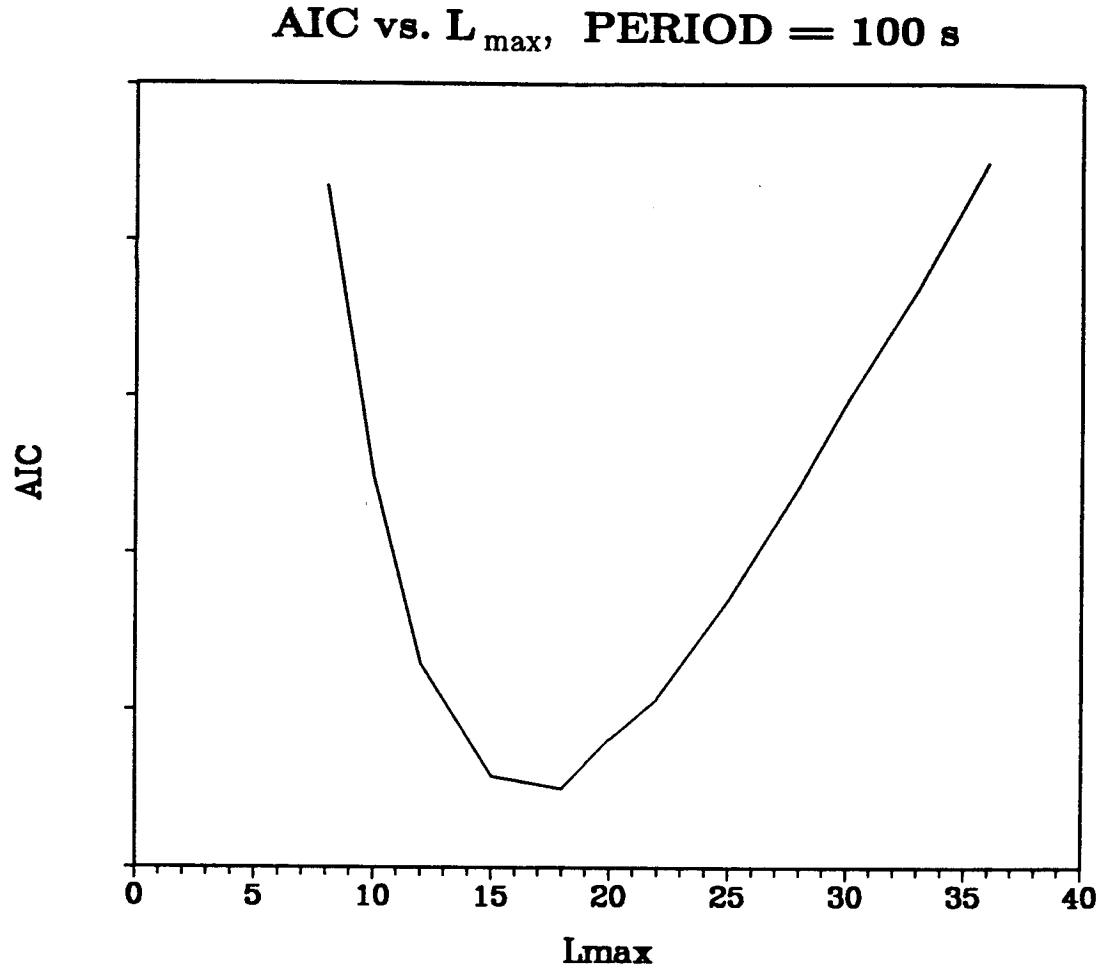

Figure 3.3, *AIC* curve vs. $l_{\max}$ for the spherical harmonic expansion inversion. The maximum likelihoods for different truncation levels are calculated with the optimal damping parameter. The *AIC* values are presented in relative scale, and there is no unit on the vertical axis. The minimum value of *AIC* is at about $l = 18$.

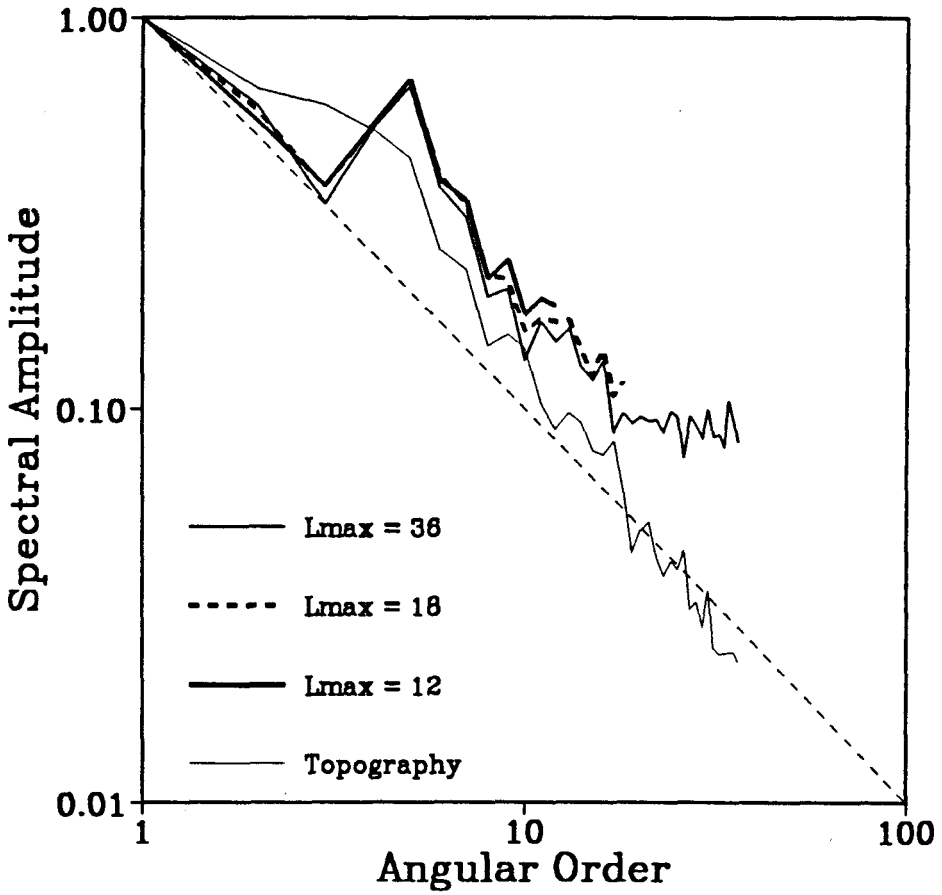

Figure 3.4, The spectral amplitude vs. the angular order for the spherical harmonic expansion inversion on a logarithmic scale. Plotted here are the spectral amplitudes at $l_{\max} = 12$, 18, and 36, respectively. The topography spectral amplitude is plotted for reference. All of the curves decrease approximately to $\frac{1}{l}$ as l increases.

Figure 3.5, Same as Figure 3.1, but for the block-type inversion. Plotted here are values associated with block sizes $20^o \times 20^o$, $15^o \times 15^o$, $10^o \times 10^o$, $9^o \times 9^o$, $7.5^o \times 7.5^o$ and $5^o \times 5^o$, respectively. The difference from the spherical harmonic expansion is that the optimal damping parameter changes as the block sizes change.

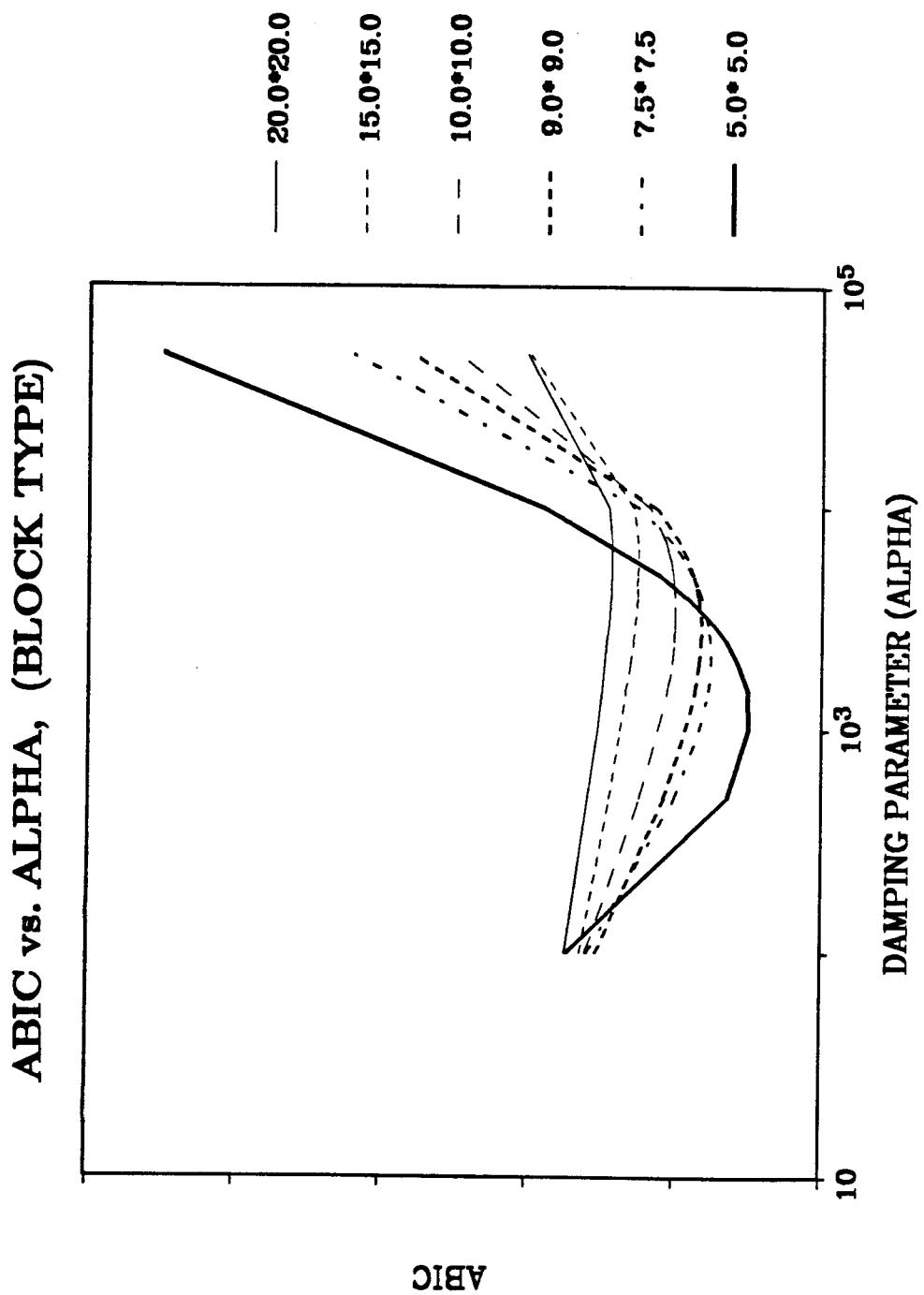
ABIC vs. ALPHA, (BLOCK TYPE)
20.0*20.0
15.0*15.0
10.0*10.0
8.0* 8.0
7.5* 7.5
5.0* 5.0
ABIC
10
10^3
10^5
DAMPING PARAMETER (ALPHA)

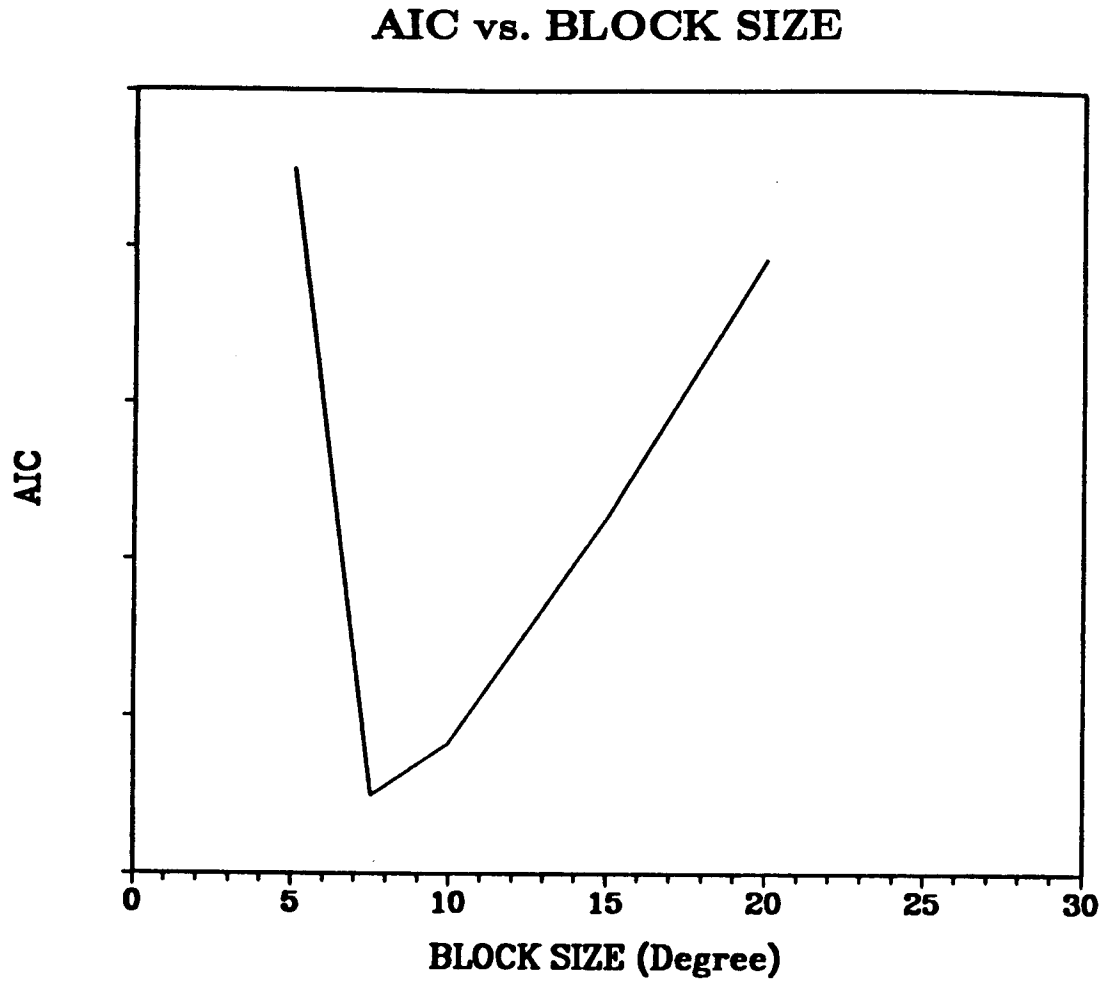

Figure 3.6, Same as Figure 3.3, except for the block-type inversion. The minimum value of *AIC* is at about block size $7.5^0 \times 7.5^0$. The equivalent spherical angular order is about 24.

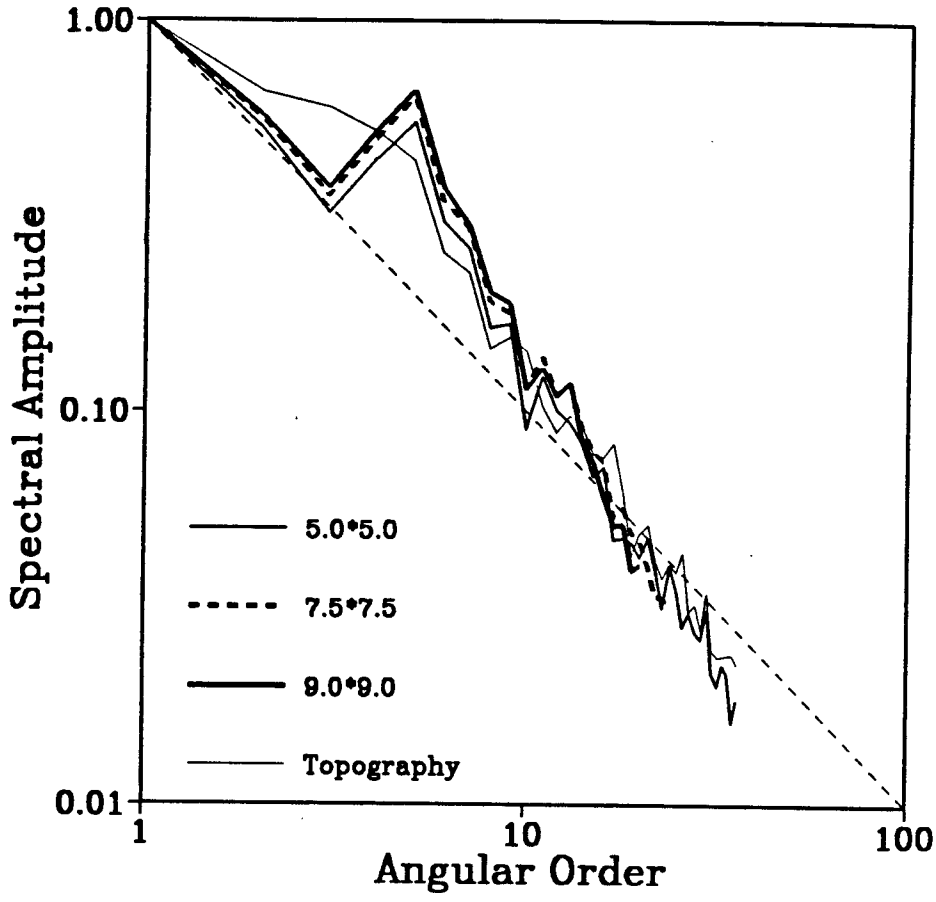

Figure 3.7, Same as Figure 3.4, except for the block-type inversion. Plotted here are values associated with block sizes $9^o \times 9^o$, $7.5^0 \times 7.5^o$ and $5^o \times 5^o$, respectively. For the $5^o \times 5^o$ size, we used the optimal damping parameter at $7.5^o \times 7.5^o$. These curves are more approximate to $\frac{1}{l}$ than the curves of the spherical expansion type.

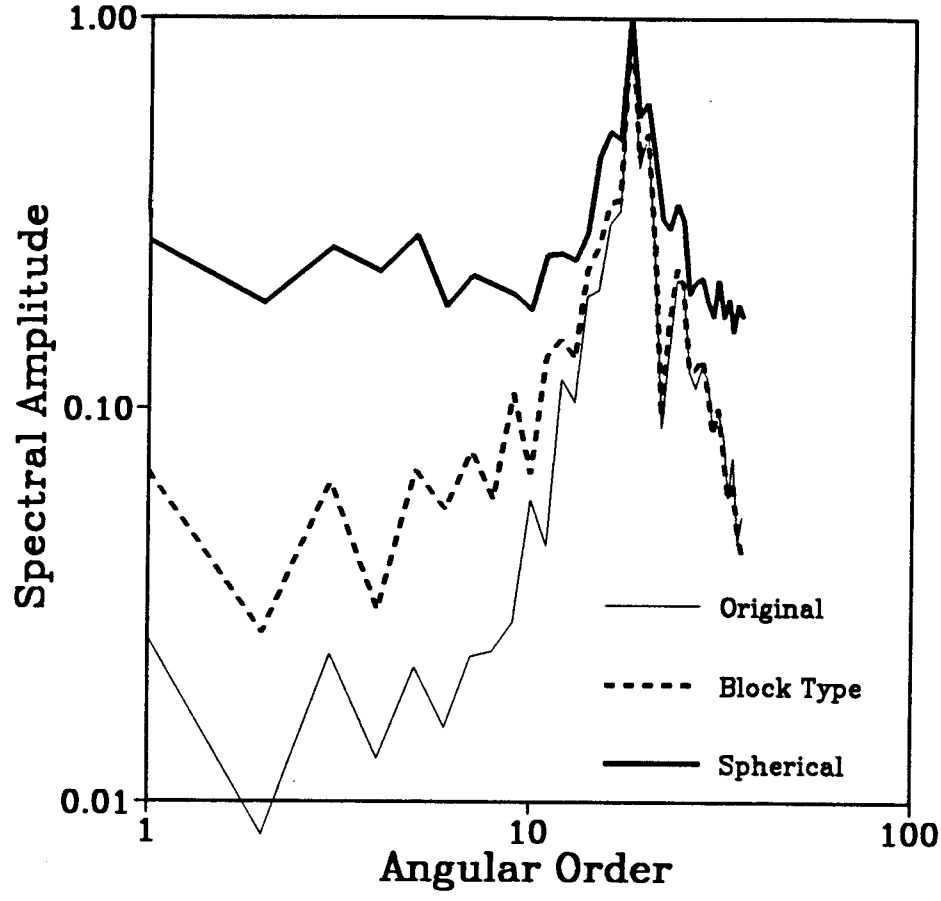

Figure 3.8, The spectral amplitudes for the synthetic test 2 in Chapter 2. The main power of the original pattern is at about $l = 18$. The maximum spherical angular order is 36, and the block size is $5^o \times 5^o$. The block-type inversion gives a better approximation than the spherical harmonic expansion inversion.

3.5 Summary

When solving a linear geophysical inverse problem, the parameterization of the unknown continuous model and the choice damping parameter in the inversion are always decided by researchers' experiences and prior beliefs. Thus, the inversion results are obtained subjectively. Assuming that the error ξ in the data space and the error ΔX in the model space are both Gaussian randomly distributed, and using Bayesian inference, the marginal likelihood function is built up. The optimal damping parameter α^2 is determined by using the *ABIC* method associated with the maximum likelihood.

An optimal regularization of the unknown continuous model is obtained by the *AIC* method, which is based upon the *K-L information quantity.* The *ABIC* and *AIC* methods provide a natural and systematic way of utilizing the information supplied by the likelihood function, which has a clearly defined objective meaning as the measure of the goodness of the model.

Applying the *ABIC* and *AIC* methods to the global Love phase velocity inversion, we find that the block-type inversion gives a better approximation than the spherical harmonic expansion does under the present data set. The spherical harmonic expansion method can provide a maximum spherical angular order up to 18. The equal area block-type inversion can provide the equivalent angular order up to about 24. The spectrum amplitudes of the inversion results are consistent with this conclusion.

Chapter 4

3-D Modeling of Upper Mantle S-Wave Velocity Structure

4.1 Introduction

The aim of this chapter is to investigate the three-dimensional structure of the Earth's upper mantle by using the information contained in long period Love and Rayleigh waves. We have collected about 18,000 seismograms associated with 971 events for Love and Rayleigh waves. The magnitudes of the events are larger than about 5.5. In order to maintain the accuracy of the results, we used only R1 and G1 phases. The period range is from 75 to 250 seconds. With this data set, it is possible to take a global perspective and to construct a reliable, three-dimensional earth structure model.

We have used a two-step inversion method in this study. The first step is to measure global phase velocity variation, and the second step is inversion of the S-wave velocity structure (Nakanishi and Anderson, 1984; Nataf *et al.*, 1986; Tanimoto, 1985, 1986a,b; Montagner and Tanimoto, 1990). The detailed methods for phase velocity determination and inversion are described in Chapters 2 and 3. For the S-wave velocity structure inversion, we used PREM

(Dziewonski and Anderson, 1981) as the starting model. The resolutions at different depth are improved by incorporating vertical component R-waves (Rayleigh waves) and transverse component G-waves (Love waves).

The model presented in this chapter is consistent with previous global studies (*e.g.*, Nakanishi and Anderson, 1984; Woodhouse and Dziewonski, 1984; Tanimoto, 1986a,b; Wong, 1989) and local surface wave and body wave studies (*e.g.* Grand and Helmberger, 1984; Grand, 1987; Zhang and Tanimoto, 1989). The present model contains many more detailed features than previous models, and it allows us to correlate the seismological results with tectonics, which is presented in this chapter, and in Chapters 5 and 6.

In Section 4.2, the seismic phase velocity variation results for Love wave and Rayleigh wave are shown. The three-dimensional S-wave velocity structure is presented in Section 4.3; main features of this model are also described. In Section 4.4, some discussions are presented. And the main conclusions are given in Section 4.5.

4.2 Global Phase Velocity Variations

4.2.1 Phase velocity maps

We selected the equal area block approach (See Chapter 2) and used *Akaike Bayesian information criterion (ABIC)*" (See Chapter 3) in the inversion. The set of parameters are the velocity variations $(\frac{v_h}{v_o})_i$ in every block, and the total number of parameters is 1628 (see Figure 2.3). We should mention that the optimal block size is about $7.5^o \times 7.5^o$ (Chapter 3), but in the present

study, we have used $5^o \times 5^o$ blocks and the optimal damping parameter for the $7.5^o \times 7.5^o$ block size. The reason for this is that we did the inversion study first, and the synthetic test later. We have shown that the spectral amplitudes for the $5^0 \times 5^0$ block size are similar to those of the $7.5^o \times 7.5^o$ block size when the damping parameter in both cases are the optimal damping parameter at $7.5^o \times 7.5^o$. We believe the present results are a good approximation but we can still improve them in the future.

Two experiments were performed regarding the phase velocity variation. The first experiment is to investigate global phase velocity variation without *a priori* regionalization. The topography and crustal thickness vary from one place to another in the Earth, and surface waves are sensitive to these variations (Nataf *et al.*, 1986; Woodhouse and Dziewonski, 1984; Tanimoto, 1986a,b). In order to obtain the velocity variations in the mantle, these effects should be removed. In the second experiment, we gave corrections for these effects. The shallower corrections are derived by the first order perturbation method. We have superimposed on PREM the difference between our present Moho and topography model and PREM. Topography was corrected to the average surface of the Earth, and Moho depth to 24.4 kilometer. The topography and bathymetry data are from the National Geophysical Data Center on a grid of 5 by 5 minutes, and the crustal structure data are obtained from Montagner (personal communication, 1988) on a grid of 5 by 5 degrees. Figure 4.1 shows the velocity perturbations that are due to the topography and crustal thickness effects at a period of 100 s for Love wave. The largest variation is about 2.5 and 2.0 percent for the Tibetan plateau and the Andes, respectively. Comparing the phase velocity inversion results with and without corrections, there are no clear differences in the general features, but at places with large

crustal thickness, the results vary by 1-2 percent. The preferred model of phase velocity variation is that with topography and crustal corrections. We will use our preferred model to investigate the global, upper mantle structure.

Figures 4.2a - 4.2b show Love wave phase velocity variations for periods at 100 s and 200 s. Figures 4.3a - 4.3b are Rayleigh wave phase velocity variations at 100 s and 200 s, respectively. All of results shown here include topography and Moho depth corrections. We will present more results with and without corrections in Appendix 4.1 and 4.2 for Love and Rayleigh waves respectively. The black dots in the maps are 47 active hotspots from Crough and Jurdy (1980), and Richards *et al.* (1988), and the average phase velocity is given at the bottom. The contours are at 0.5 percent intervals and patterns change at every percent. These results are smoothed representation of lateral heterogeneity with a resolution wavelength of about 1000 kilometers. Fast velocities are centered on stable shield areas (Canadian, South American, Antarctic, Australian, South African and Baltic) and old oceanic regions (northwest Pacific Ocean, east and west of the central Atlantic Ocean, southwest Atlantic Ocean, and the Wharton basin in the Indian Ocean); low velocities occur in younger oceans near the ridges (East Pacific Rise, Chile Rise, Mid-Atlantic Ridge, Mid-Indian Ocean Ridge, and Southeast Indian Ocean Ridge). Other low velocity anomalies are associated with tectonically active continental regions, back-arc basins and subduction zones, such as western North American, Peru-Chile trench, Aleutian trench, Japan trench, Philippine trench, Tonga trench, Java trench, Red Sea and Gulf of Aden. The variance reductions in this study are about 60 percent at 100 s period and decrease to about 50 percent at 200 s, which is comparable with previous studies.

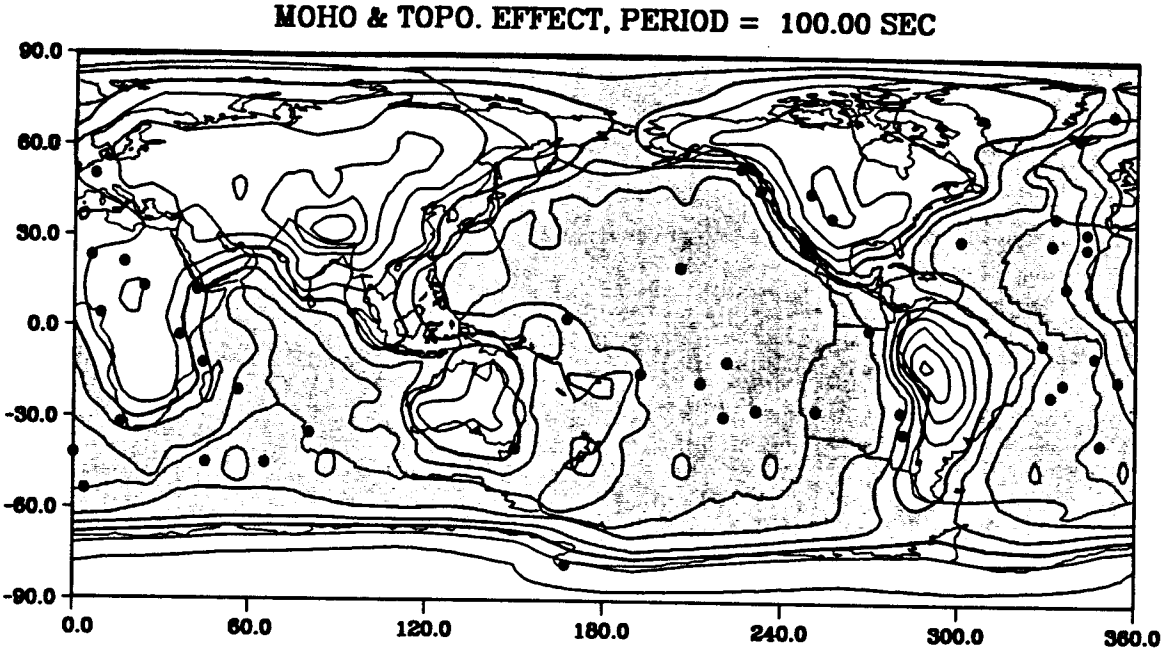

Figure 4.1, Love wave phase velocity perturbation that is due to Moho depth and topography variation at a period of 100 seconds. Dark regions are faster than average and contours are drawn at every 0.5 percent. We have corrected the topography to the surface of the Earth, and Moho depth to 24.4 km.

Figure 4.2, Love wave phase velocity variation at periods of 100 and 200 s. The contours are drawn at every 0.5 percent, and the patterns change every percent. Black dots are hotspots. Average velocity is given at the bottom. These maps include the topography and Moho depth correction. (a). Period at 100 s; (b). Period at 200 s.

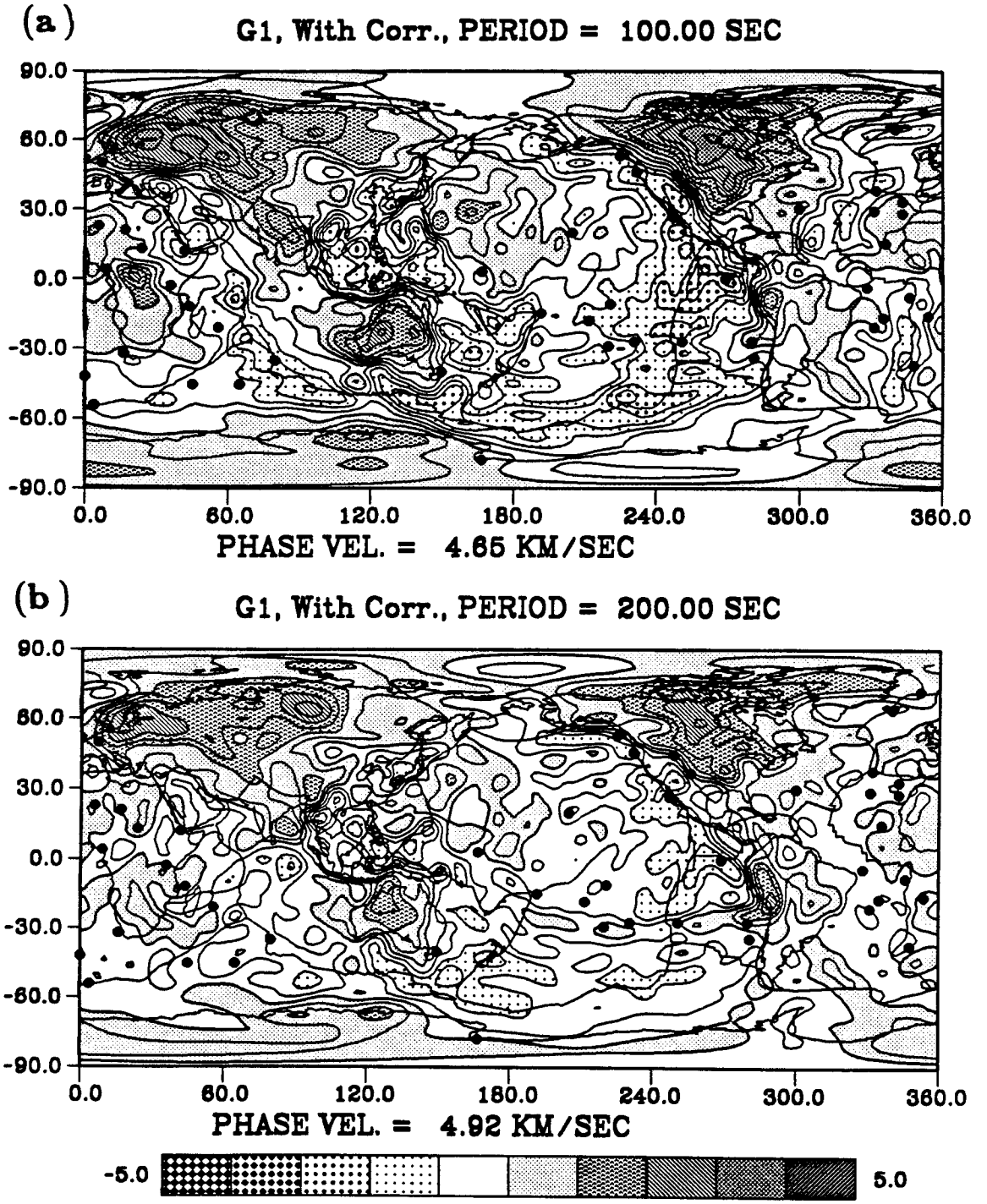
(a)
G1, With Corr., PERIOD = 100.00 SEC
90.0
60.0
30.0
0.0
-30.0
-60.0
-90.0
0.0
60.0
120.0
180.0
240.0
300.0
360.0
PHASE VEL. = 4.65 KM/SEC
(b)
G1, With Corr., PERIOD = 200.00 SEC
90.0
60.0
30.0
0.0
-30.0
-60.0
-90.0
0.0
60.0
120.0
180.0
240.0
300.0
360.0
PHASE VEL. = 4.92 KM/SEC
-5.0
5.0

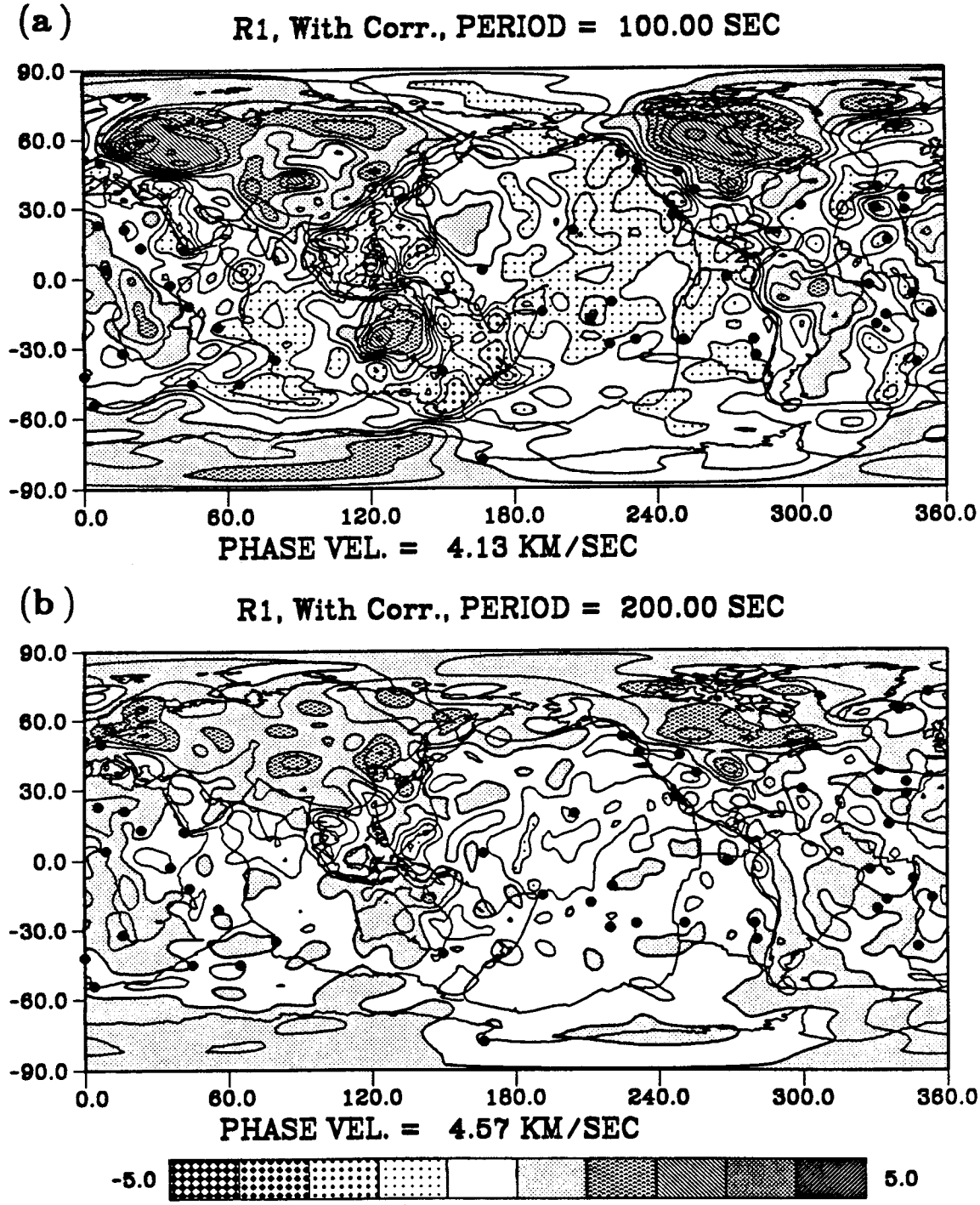

Figure 4.3, Same as Figure 4.2 but for Rayleigh waves. (a). period at 100 s; (b). Period at 200 s.

For short period Rayleigh waves, the results are similar to the Love wave results and show clear correlation with surface plate tectonics. When the period increases, Rayleigh waves are sensitive to deeper structure, and the correlation with tectonics decreases. The main features of the inversion results are consistent with previous global and local studies (*e.g.*, Toksöz and Anderson, 1966; Nakanishi and Anderson, 1984; Woodhouse and Dziewonski, 1984; Nataf *et al.* 1986; Tanimoto and Anderson, 1985; Wong, 1989, Zhang and Tanimoto, 1989; Montagner and Tanimoto, 1990). However, because of the smaller resolution scale, the present results contain much more detail than those of previous studies. Low velocity anomalies emerged under hotspots at Iceland, the Azores, Hawaii, Tristan de Cunha, Kerguelen, and Afar. The existence of these anomalies was apparent in previous studies, but their sizes are now well constrained to be about 1,000 - 2,000 km. The low velocity anomaly at Hawaii moves slightly to the northeast as the damping parameter is increased. This is probably caused by uneven path coverage, because more paths are along the NE-SW direction than NW-SE direction. More data from the southern hemisphere are required to resolve accurately the position of the Hawaii low velocity anomaly. It should also be noted that some hotspots fall in faster than average velocity areas (for example, Bermuda, Cape Verde, Eifel, Yellowstone and central Africa). For the Pacific, Atlantic and Indian Oceans, the surface wave velocities show an increase with plate age, which will be discussed later.

Figure 4.4, (a). Resolution at latitude and longitude coordinates $(44.0^0, 63.0^0)$. The 3D figure is plotted in the upper part, and the 2D figure is in the lower part. Dark regions are positive and white are negative. The contours are plotted in 0.2 percent interval. (b). Resolution at coordinates $(-42.0^o, 126.0^o)$. (c). Resolution at coordinates $(21.0^o, 203.0^o)$. Since more paths propagate in the NE-SW direction than in the NW-SE direction at this place, the resolution also elongates in NE-SW direction. (d). Resolution at coordinates $(-41.0^o, 244.0^o)$. There is a little spreading of the resolution because there are only a few stations in this area, and path coverage is worse than other places.

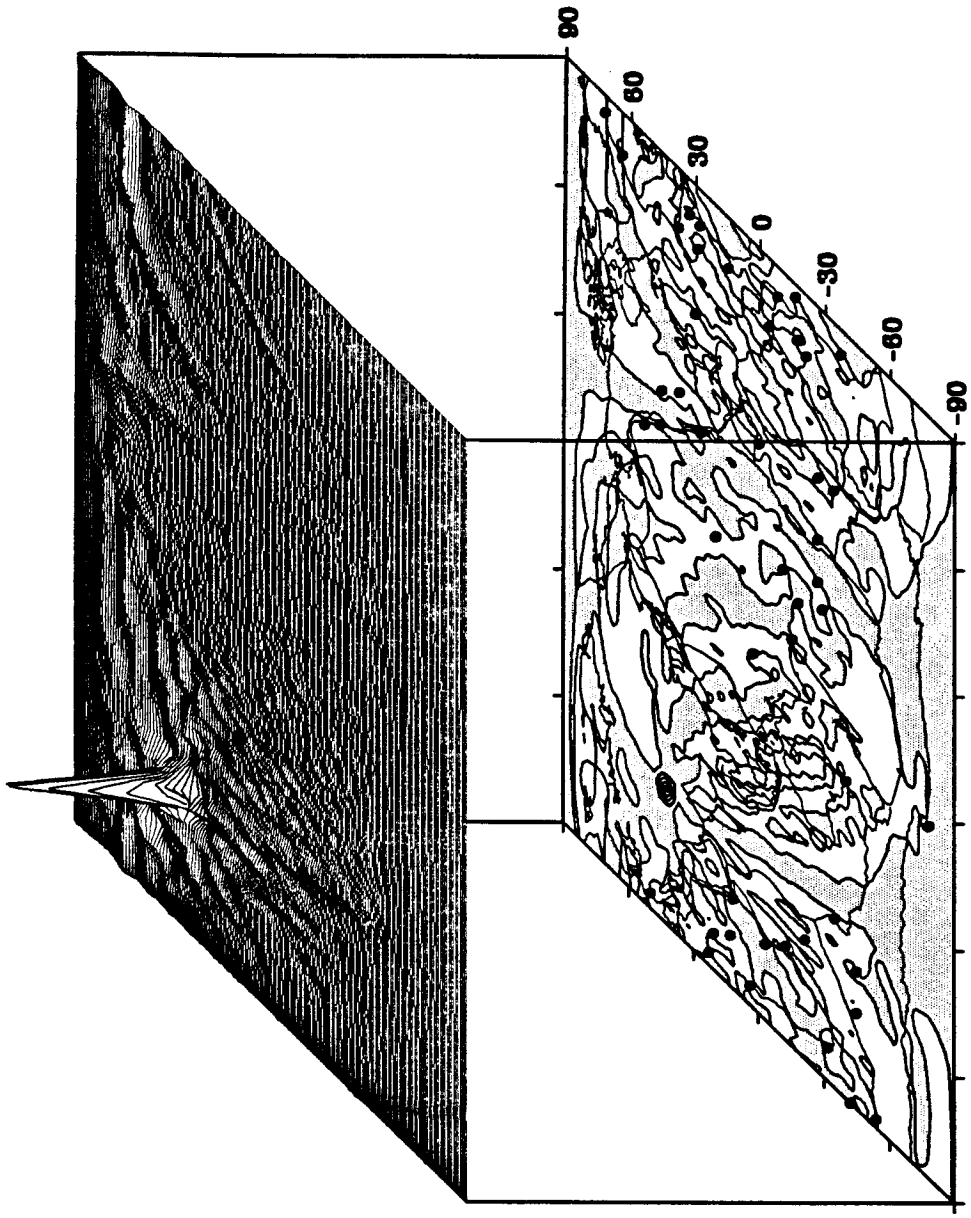

(a) LAT = 44.0, LON = 63.0, PERIOD = 100.0

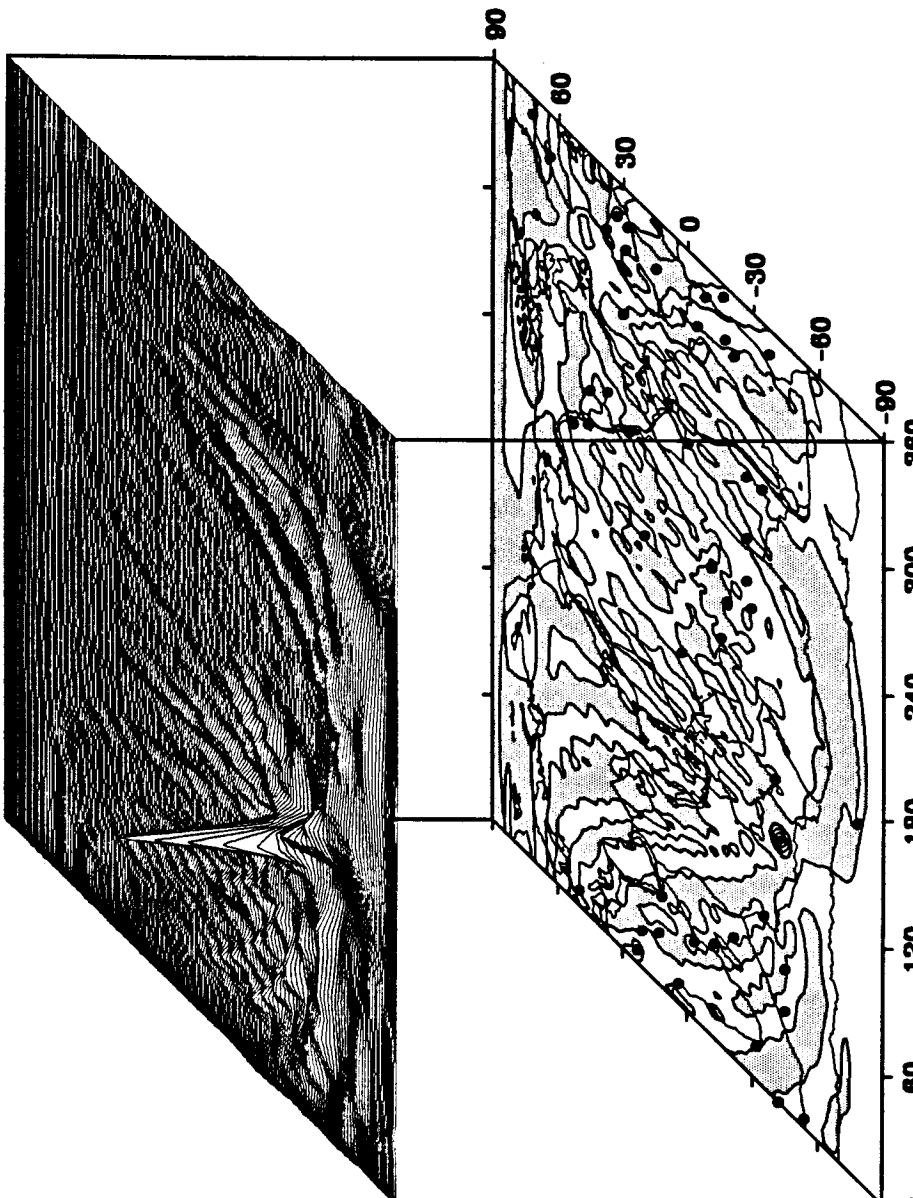

(b) LAT = -42.0, LON = 126.0, PERIOD = 100.0

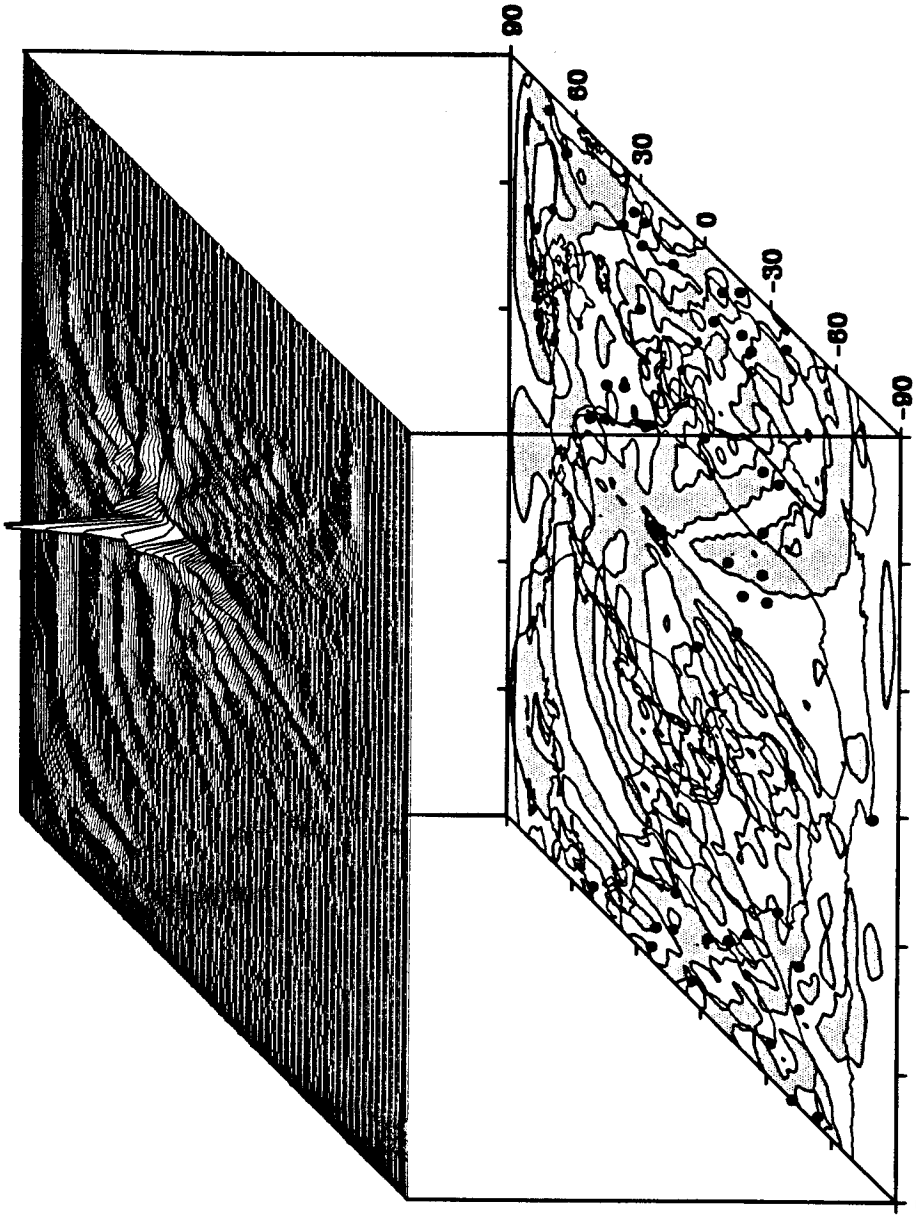

(c) LAT = 21.0, LON = 203.0, PERIOD = 100.0

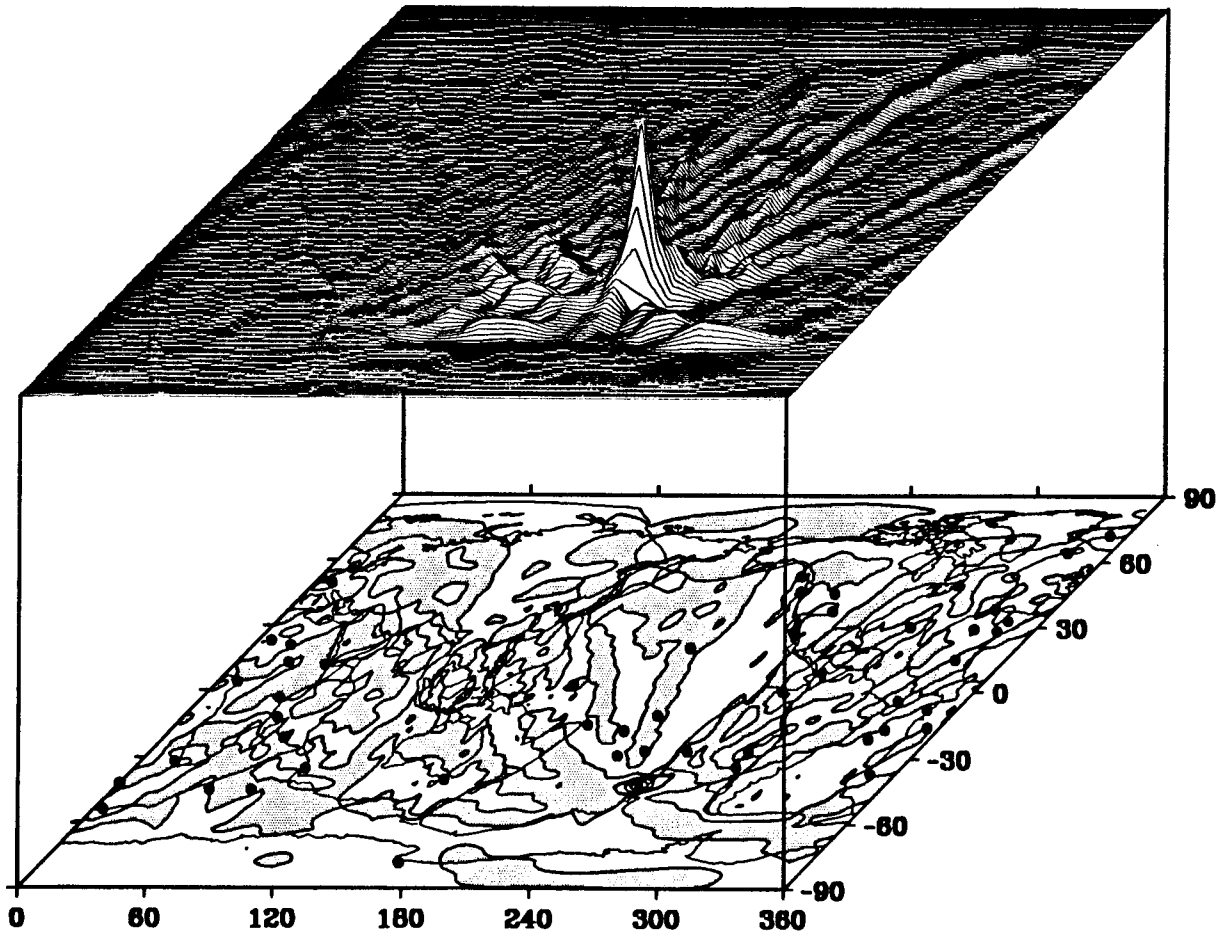

(d) LAT = -41.0, LON = 244.0, PERIOD = 100.0

4.2.2 Resolution, error and stability

Since the surface of the Earth was divided into 1628 blocks, the full resolution matrix has approximately 2.65×10^6 elements, which would be impossible to display in its entirety. An alternate approach is to sample the resolution matrix at a few selected places. Figures 4.4a - 4.4d show the resolution at latitude and longitude coordinates (44.0^o, 63.0^o), (-42.0^o, 126.0^o), (21.0^o, 203.0^o) and (-41.0^o, 244.0^o), respectively at a period of 100 s. These resolution kernels are plotted in 3-D figure in the upper figure, and in ordinary 2-D in the lower map. The dark regions represent positive anomalies, and the contour interval is 0.2 percent.

The path coverages at these four targets were different (see Figure 2.2), resulting in various resolution features. At (44.0^o, 63.0^o) and (-42.0^o, 126.0^o), there were good azimuthal coverage, and the resolution kernels were sharp. The path coverage was good at (21.0^o, 203.0^o) near Hawaii, but many more paths were in the NE-SW direction than in the NW-SE direction. The resolution here showed elongation in NE-SW direction, but the main kernel (amplitude $\geq$ 0.4 percent) was near the center target point. The path coverage in the southeast Pacific ocean was poorer than that in other areas, because there are only a few stations in that area. The resolution kernel is a little spread out, showing this effect. Overall, however, the resolution kernels in this study have fairly sharp peaks at the target locations with a resolution wavelength of about 1000 kilometers.

Figures 4.5a-b show error maps for Love waves at period of 100.0 and 200.0 seconds, respectively. In these figures, contours are drawn at each 0.1 percent interval and patterns change every 0.2 percent. We have calculated the standard deviation for each period and assumed that every path shares the

same error of one standard deviation. The error maps were estimated by using the covariance matrix $<\Delta X\ \Delta X^T>$. Figures 4.5a-b show that most areas are associated with an error of less than 0.5 percent. A few place at 200 seconds have maximum error between 0.6 and 0.7 percent. Figures 4.6a-b are the same as Figure 4.5a-b, except for Rayleigh waves. The error estimate maps for Rayleigh waves have similar features to the Love wave maps. It is clear from Figures 4.5a-b and 4.6a-b that any velocity anomalies smaller than about 0.5 (or 0.7) percent are not reliable features in the lateral phase velocity variation maps.

We also show two previous separate inversion results, 10 degrees by 10 degrees near the equator in the equal area block discretization inversion for Love waves in Figures 4.7a and 4.7b. Each inversion included about 400 events and 3500 paths and used data entirely independent from each other, the events and stations both situated only in the northern or southern hemisphere. It should be borne in mind that the full data set was chosen to maximize the global path coverage, and in a number of cases, only a few events and station pairs were available in a given region; thus, each inversion would be incomplete, especially near the equator. Figures 4.7a and 4.7b show the phase velocity variations at a period of 100 seconds in the northern hemisphere and the southern hemisphere, respectively. Figure 4.7a is a view from above, centered at the North Pole. Figure 4.7b is a similar projection with the center at the South Pole and viewed from below. World maps are given on the left hand side for reference and phase velocity maps are on the right hand side. Black dots are locations of hotspots. These maps have features similar to the global results in the present study, indicating that the patterns we observed are reliable and are not strongly dependent upon the choice of data.

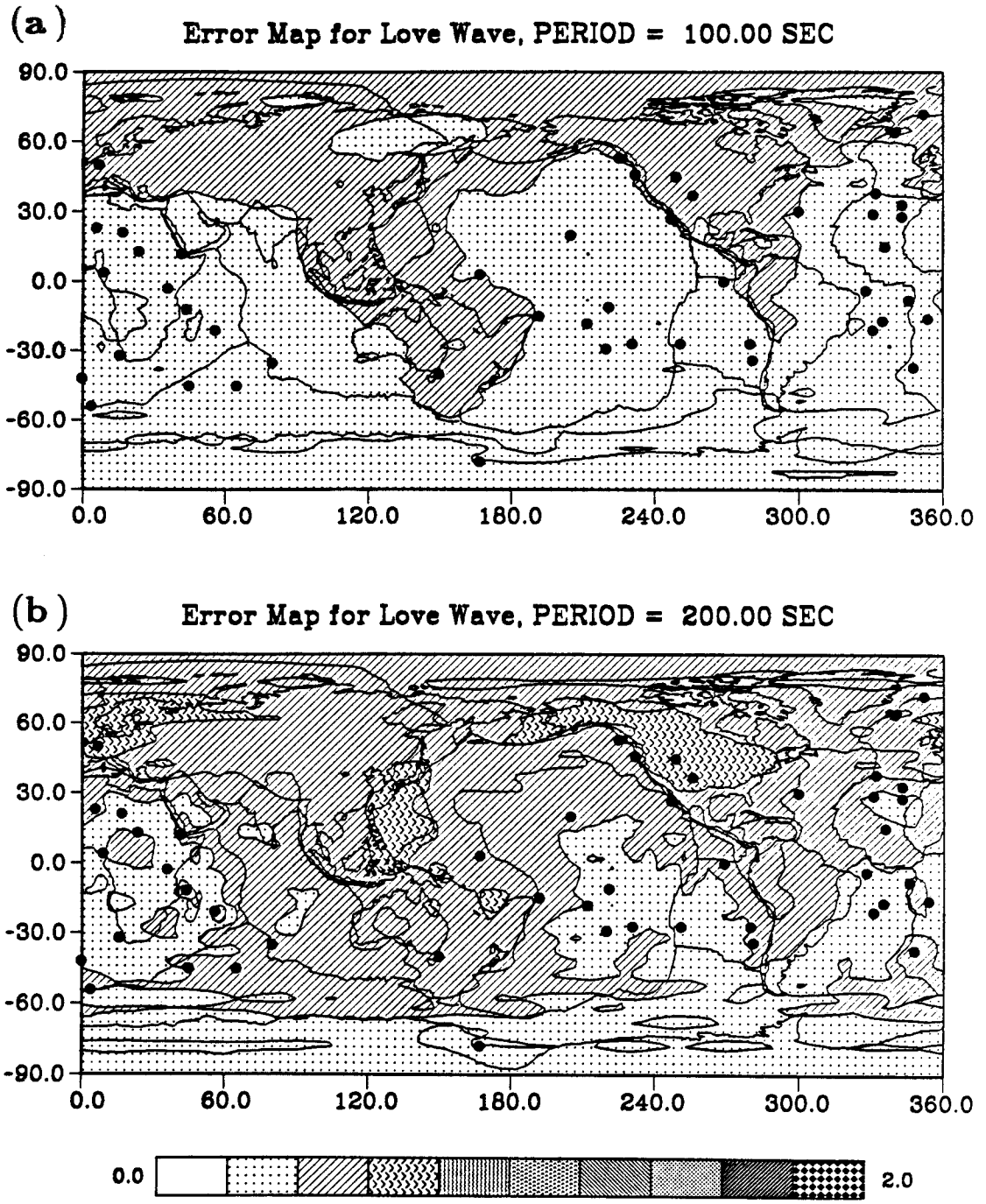

Figure 4.5, Error maps estimated for Love waves at periods of 100 and 200 seconds. The contour intervals are in 0.1 percent and the patterns change every 0.2 percent. (a). Period at 100 s; (b). Period at 200 s.

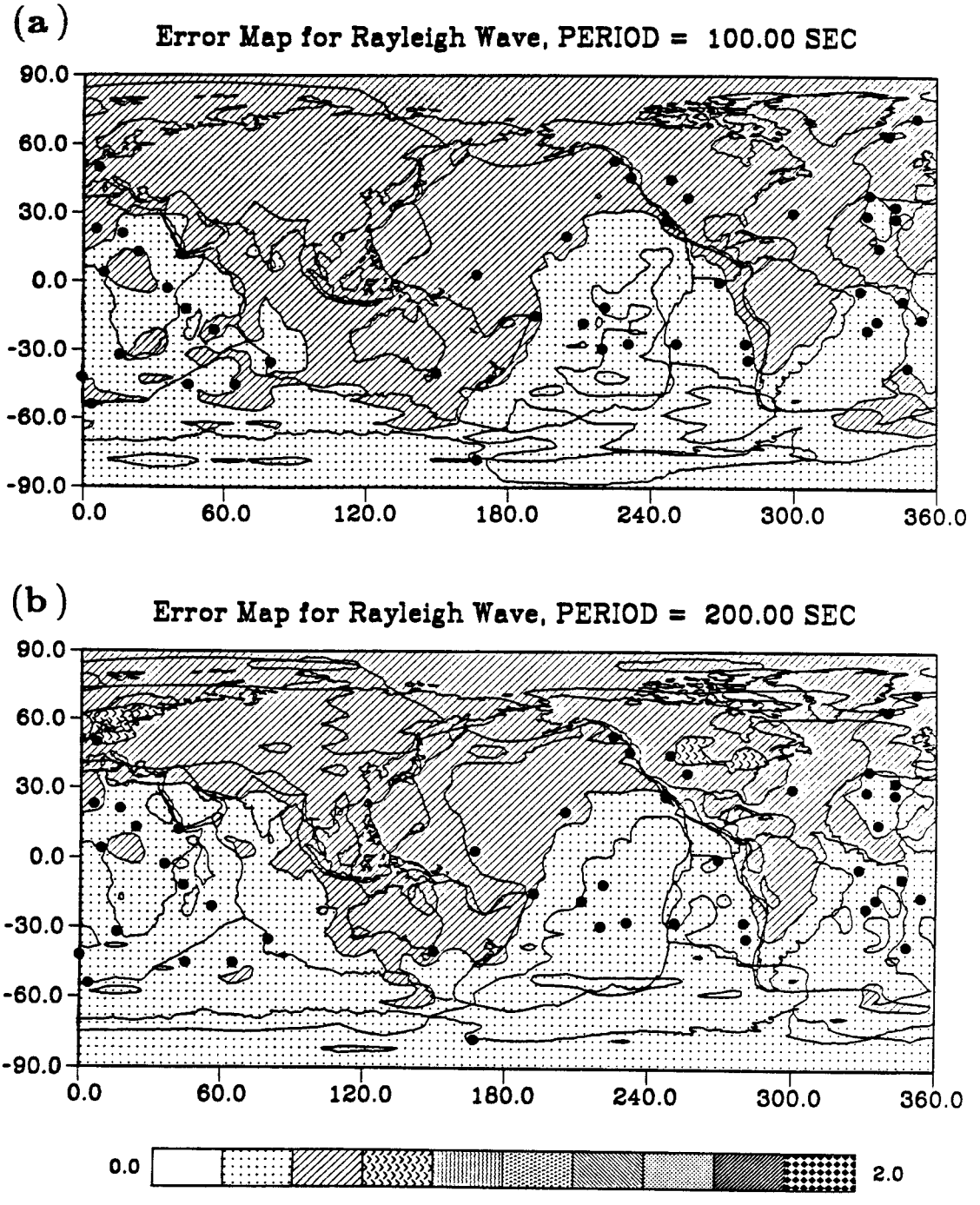

Figure 4.6, Same as Figure 4.5, but for Rayleigh waves.

Figure 4.7, (a). The results of inversion by using independent data and 10×10 degree blocks near the equator in the equal area block approach. The left side is a map of the northern hemisphere viewed from above. The north pole is at the center and equator is the perimeter. The right side shows Love wave phase velocity variation in the northern hemisphere at a period of 100 s. White regions indicate the slow velocity anomalies, dark regions are for the fast velocity anomalies and black dots represent hotspots. The contour interval is in 0.5 percent. (b). Same as Figure 4.7a except for southern hemisphere and viewed from below.

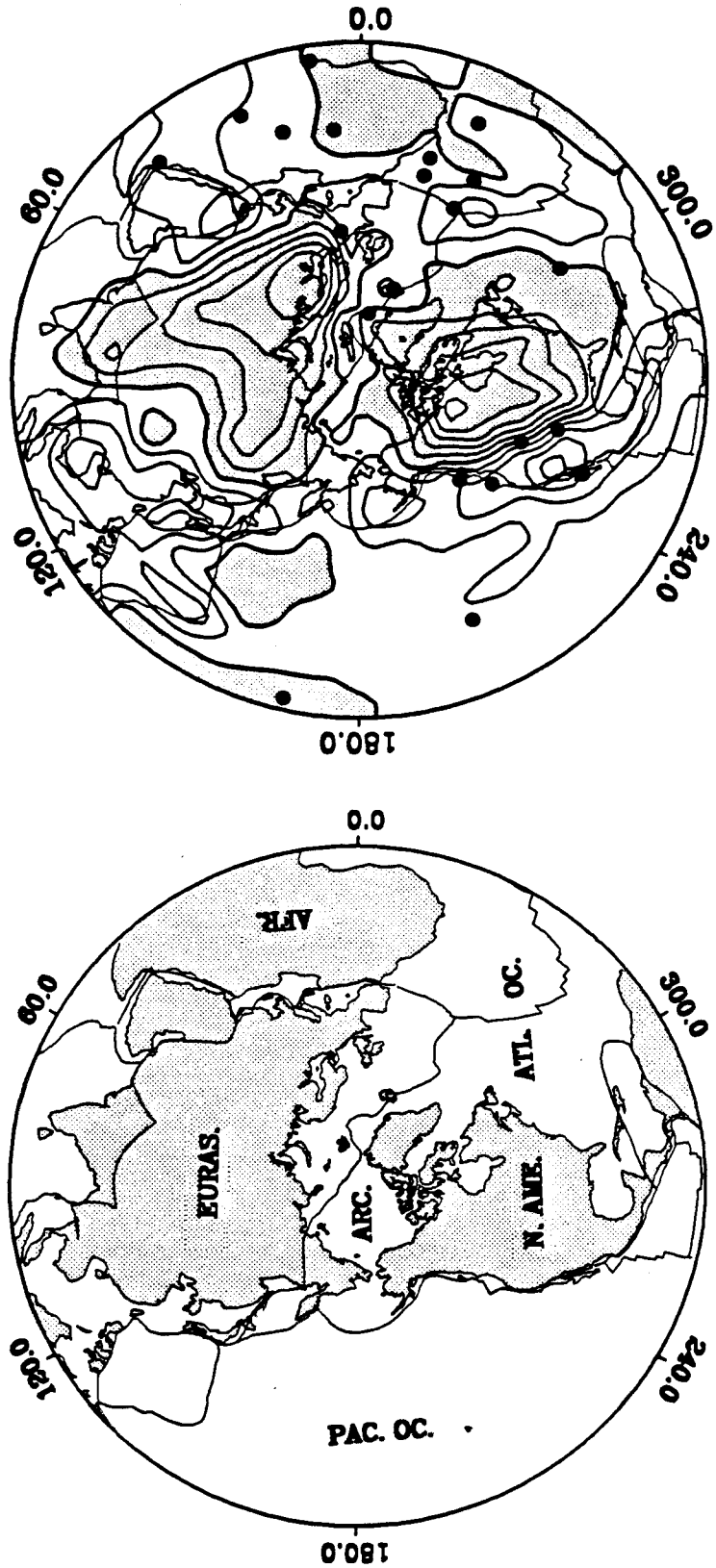
(a)
G1, WITH CORRECTION, PERIOD = 100.00 SEC
0.0
60.0
120.0
180.0
240.0
300.0
AFR.
EURAS.
ARC.
OC.
ATL.
N. AME.
PAC. OC.
LATITUDE FROM 90.0 TO 0.0

(b)

G1, WITH CORRECTION, PERIOD = 100.00 SEC

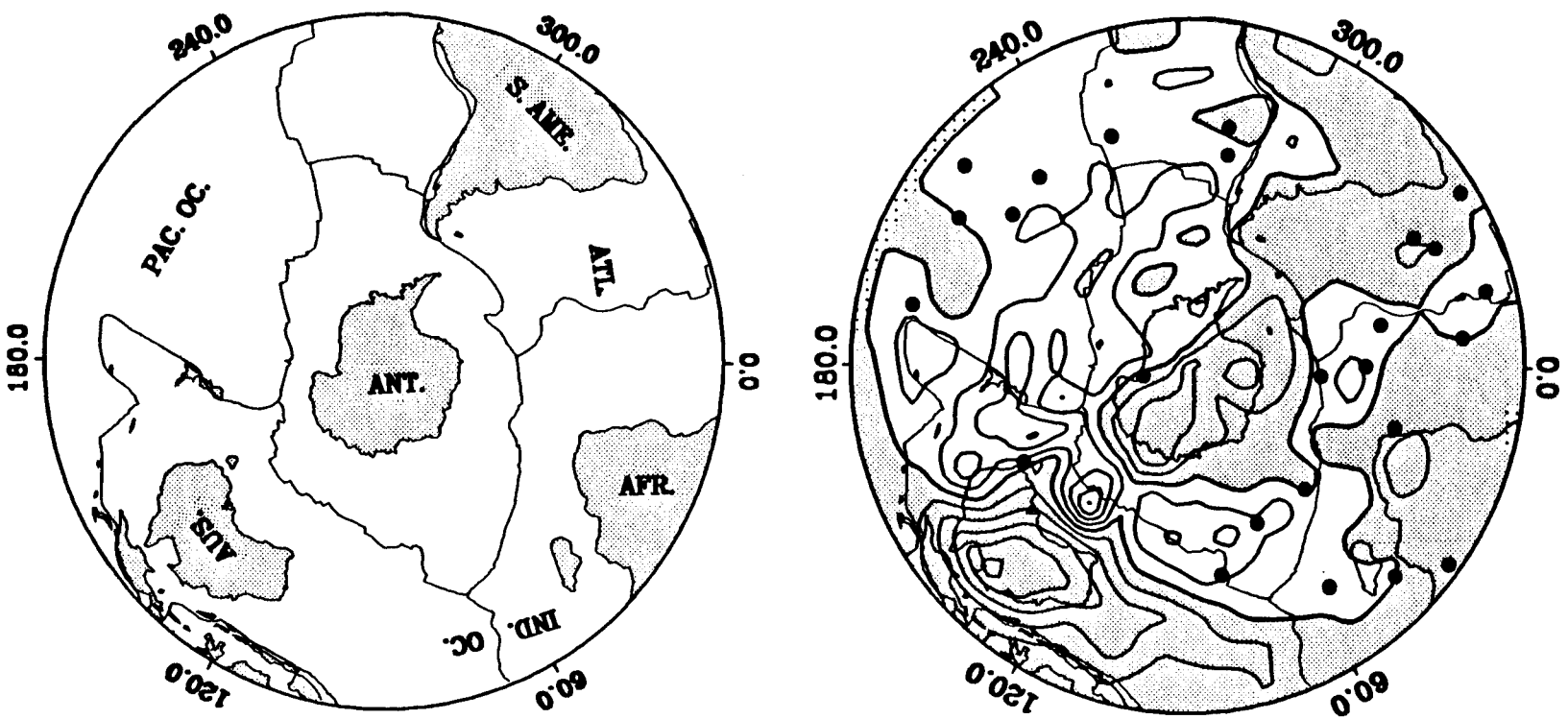

LATITUDE FROM -90.0 TO 0.0

4.3 3-D Modeling Upper Mantle S-Wave Velocity Structure

4.3.1 Theory

In the preceding section, global phase velocity variations have been measured at fixed periods. We will use these results to invert for the upper mantle S-wave velocity structure at fixed wavelength. Therefore, it is logical and necessary to convert the phase velocities from a propagation wave to a standing wave. To perform this kind of conversion, we designed the following method:

Using all of the phase velocity results and the Spline interpolation method, we build a smooth, continuous dispersion curve. We pick up phase velocity variations at equivalent periods for normal modes. The picked results are now for fixed periods of a propagation wave; we convert them into standing normal mode wave by the formula,

$$(\frac{\delta\omega}{\omega})_L = \frac{U}{C}(\frac{\delta C}{C})_T \ , \tag{4.1}$$

where C is phase velocity, U is group velocity, and ω is angular frequency. The subscript L is for fixed wavelength (or fixed wavenumber), and the subscript T is for fixed period (or fixed frequency). This conversion is important, and it will cause at least a 20 percent variation.

In the last decade, there have been many studies that show the Earth is anisotropic (*e.g.*, Forsyth, 1975; Tanimoto and Anderson, 1985; Montagner and Tanimoto, 1990). On the basis of the present data, the resolution is not good enough to justify the use of anisotropy terms, and they are dropped in this study. The perturbation in angular frequency of a mode can be expressed by

$$(\frac{\delta\omega}{\omega})_i = \int_0^a dr(R_i \frac{\delta\rho}{\rho} + P_i \frac{\delta\alpha}{\alpha} + S_i \frac{\delta\beta}{\beta}), \tag{4.2}$$

where R_i, P_i, and S_i are appropriate kernels of the ith mode, and a is the radius of the Earth.

We used only long period fundamental modes in the present study. The continuous presentations of the unknown function for density, P-wave velocity and S-wave velocity variations, like some previous studies (*e.g.*, Woodhouse and Dziewonski, 1984; Nataf *et al.* 1986; Zhang and Tanimoto, 1989), were not used. We used 33 knots in the vertical direction, located about every 20 km from the surface of the Earth to 670 km depth. We believe that this kind of regularization gives a better approximation to the real structure of the Earth than the continuous presentation, which are like the numerical tests we did in Chapter 2. Thus, the Equation (4.2) is:

$$(\frac{\delta\omega}{\omega})_i = \sum_j \Delta r_j R_{ij} (\frac{\delta\rho}{\rho})_j + \sum_j \Delta r_j P_{ij} (\frac{\delta\alpha}{\alpha})_j + \sum_j \Delta r_j S_{ij} (\frac{\delta\beta}{\beta})_j. \tag{4.3}$$

We rewrite Equation (4.3) as

$$Y = A\,X\,, \tag{4.4}$$

for convenient use in a later section, where

$$Y = \left[(\frac{\delta\omega}{\omega})_1, \ldots, (\frac{\delta\omega}{\omega})_n \right]^T,$$

$$X = \left[(\frac{\delta\rho}{\rho})_1, (\frac{\delta\alpha}{\alpha})_1, (\frac{\delta\beta}{\beta})_1, \ldots, (\frac{\delta\rho}{\rho})_m, (\frac{\delta\alpha}{\alpha})_m, (\frac{\delta\beta}{\beta})_m \right]^T,$$

and the elements of matrix A are $\left[R_{ij}\Delta r_j, P_{ij}\Delta r_j, S_{ij}\Delta r_j \right]$, where $(i = 1, \ldots, n;\ j = 1, \ldots, m)$.

The Equation (4.4) is a linear equation. We solve this equation by using the *Akaike Bayesian information Criterion (ABIC).* The details of this method are described in Chapter 3.

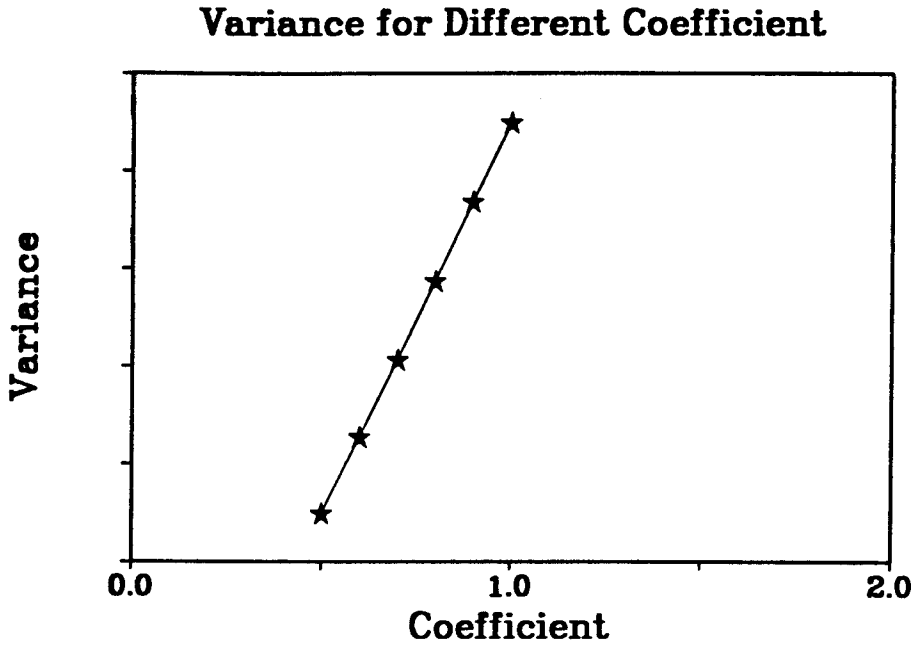

Figure 4.8, The variance vs scaling coefficient. Showing here are the results for experiment 2. The variance increases when the scaling coefficient increases. We have chosen a scaling coefficient of 0.5 in this study. The variances are in relative scale and the unit is not given.

4.3.2 Models of 3-D Structure

In this study, we have performed four different experiments in inverting for the upper mantle structure. The starting reference model is PREM (Dziewonski and Anderson, 1981). In the first experiment, we dropped the density and P-wave velocity terms, because the data set does not have sufficient resolution for these terms, and they are not important in this fundamental mode related study. In the second experiment, the velocity variation is approximated due to temperature change, and then the P-wave velocity variation is assumed to vary systematically with the S-wave velocity variation.

$$\frac{\delta\alpha}{\alpha} = \epsilon\left(\frac{\delta\beta}{\beta}\right),$$

where ϵ is a scaling coefficient. The unknown parameters in this experiment are the density and S-wave velocity variations in different layers. The scaling coefficient has been discussed in many previous studies (*e.g.*, Anderson *et al.* 1968; Master *et al.*, 1982; Woodhouse and Dziewonski, 1984; Tanimoto, 1988; Davis, 1990), but the values in these studies are different. In this study, we have used scaling coefficients from 0.5 to 1.0. In comparing with the first experiment, the variance is significantly reduced, but there are still differences for different scaling coefficients. Figure 4.8 shows the variance variations for different scaling coefficients. The variances are in relative scale, and their units are not given in Figure 4.8. Each star represents the scaling coefficient versus the possible variance. It is clear that the variance decreases as the scaling coefficient decreases.

Figure 4.9, S-wave velocity resolution kernel and trade-off between S-wave velocity and density at 38, 150 and 410 km, respectively. The horizontal axis is for the depth from the surface to 700 km deep. The resolution kernel widens as depth increases. The trade-off effect occurs at all depths, but is small.

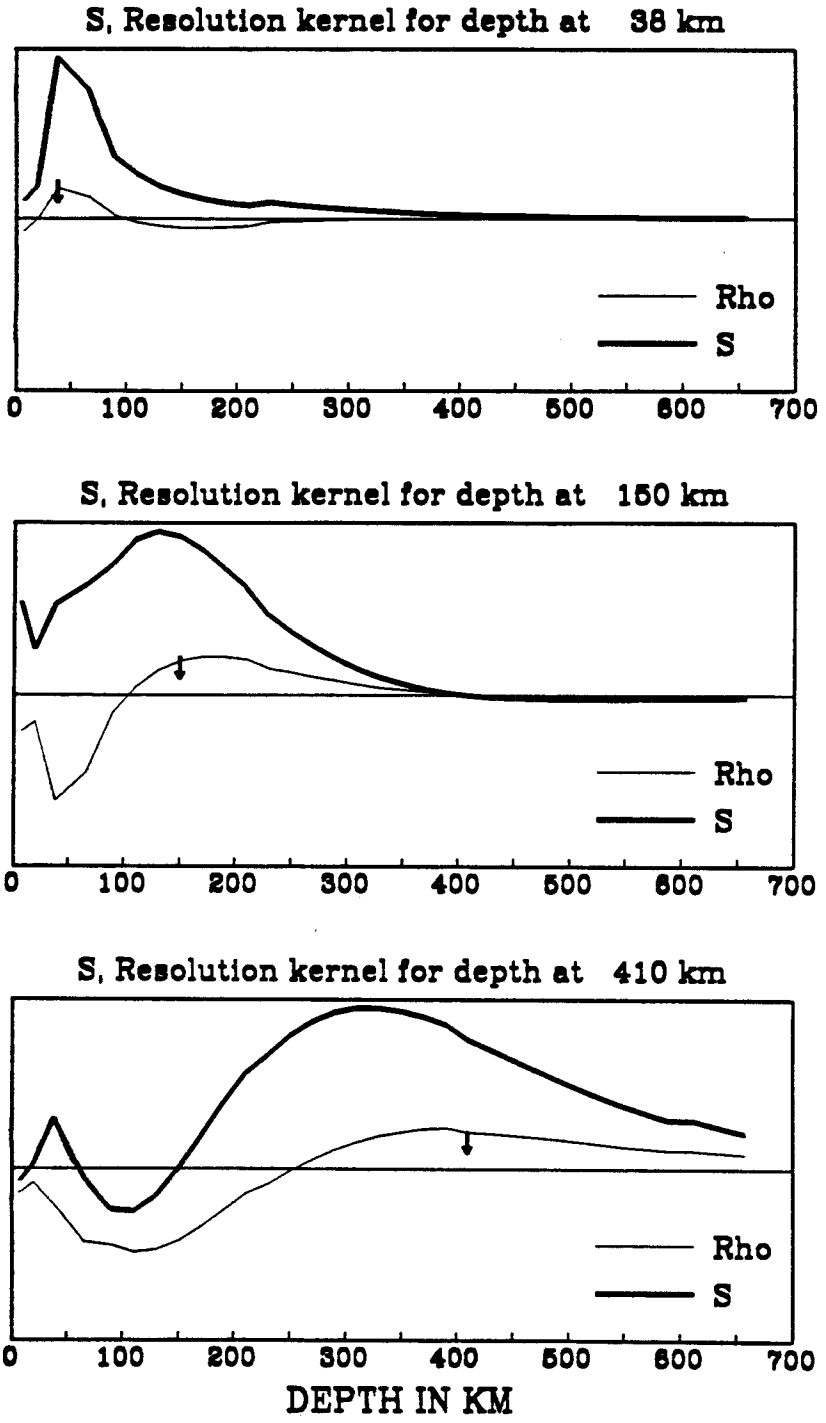
S, Resolution kernel for depth at 38 km
Rho
S
0
100
200
300
400
500
600
700
S, Resolution kernel for depth at 150 km
Rho
S
0
100
200
300
400
500
600
700
S, Resolution kernel for depth at 410 km
Rho
S
0
100
200
300
400
500
600
700
DEPTH IN KM

The possible scaling coefficient for density and S-wave velocity was tested in experiment 3. We also did another kind of inversion in experiment 4, in which the density, P-wave and S-wave velocities are independent parameters. Nevertheless, these experiments led to only very minor differences for the S-wave velocity structure from the results of experiment 2. We found that the present data set does not have enough resolution for density, P-wave velocity, and the relationship between the density and S-wave velocity is not clear. The preferred model of heterogeneity, which we designate MS5.5, is the result obtained in experiment 2 with the scaling coefficient $\epsilon = 0.5$.

Before presenting the 3-dimensional S-wave velocity structure, it is necessary to examine the resolution at a different depth from the data set. As we invert for different parameters (ρ, α, β), the resolution tells us what kind of resolving power we have for a given parameter and what leakage from other parameters comes in. Figure 4.9 shows the resolution kernels for the second experiment at 38, 150 and 410 km, respectively. The thick line is the resolution kernel for S-wave velocity, and the thin line is the trade-off of S-wave velocity with density. Ideally, we would like to obtain a delta function centered on the target (marked by an arrow) and a zero trade-off with other parameters.

It is clear that the resolution kernel broadens as target depth increases, and contamination from density occurs in all cases. By comparison with other studies (*e.g.*, Nataf *et al.*, 1986; Tanimoto, 1986a; Zhang and Tanimoto, 1989), a fairly well resolution of S-wave velocity is obtained throughout most of the upper mantle. The leakage from density is quite small. The S-wave velocity is not well resolved in the crust and below 500 km because of the limitations in the data, and there is a mirror image of shallow structure for S-wave velocity below 500 km.

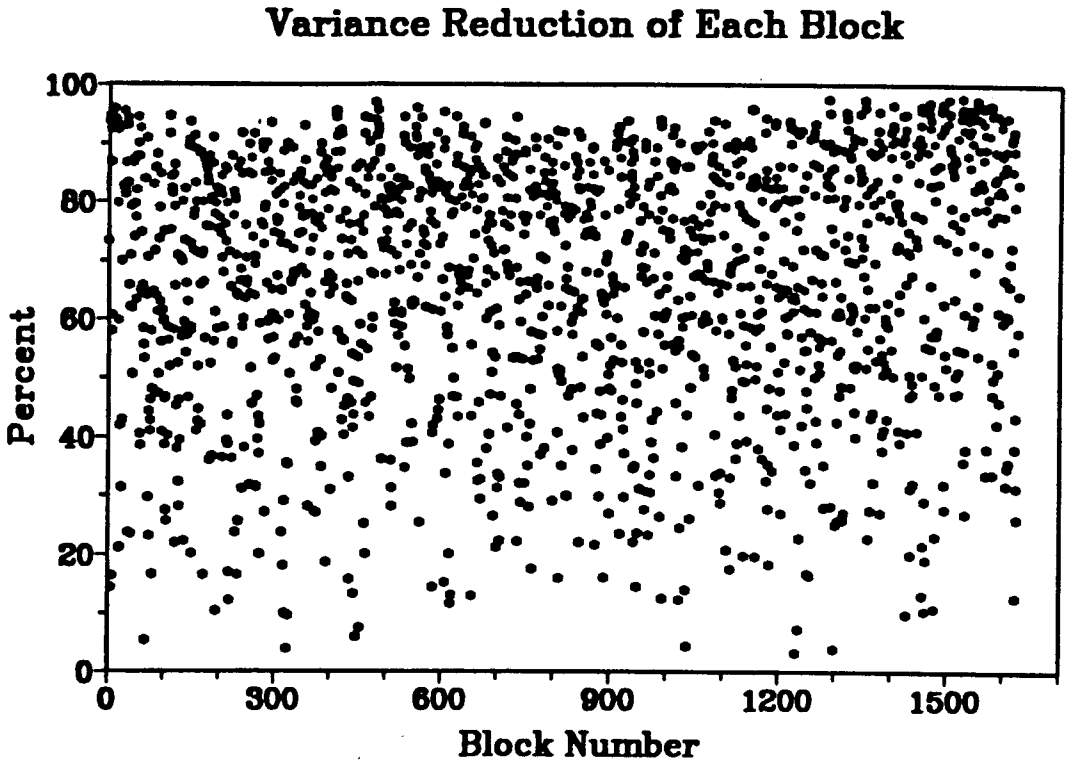

Figure 4.10, Variance reduction of each block after inversion. Each star represents variance reduction in percent at one block. The horizontal axis is the serial number of each block.

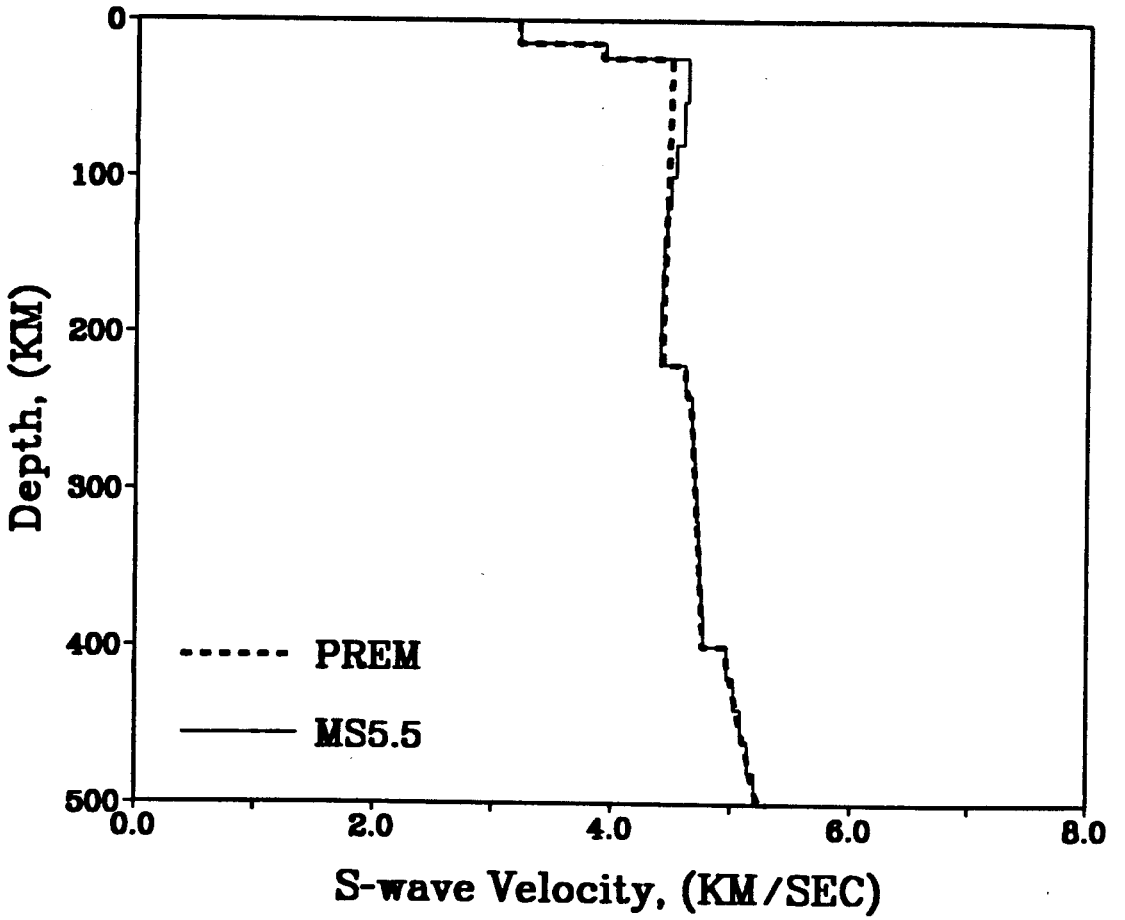

Figure 4.11, Average velocity at different depths for MS5.5. The dash line is the velocity model PREM.

Figure 4.12, (a). S-wave velocity variation at depth 38.3 km. The same conventions as in Figure 4.2 have been used. (b). S-wave velocity variation at depth 110.0 km. (c). S-wave velocity variation at depth 210.0 km. (d). S-wave velocity variation at depth 310.0 km. (e). S-wave velocity variation at depth 410.0 km. (f). S-wave velocity variation at depth 510.0 km.

(a)

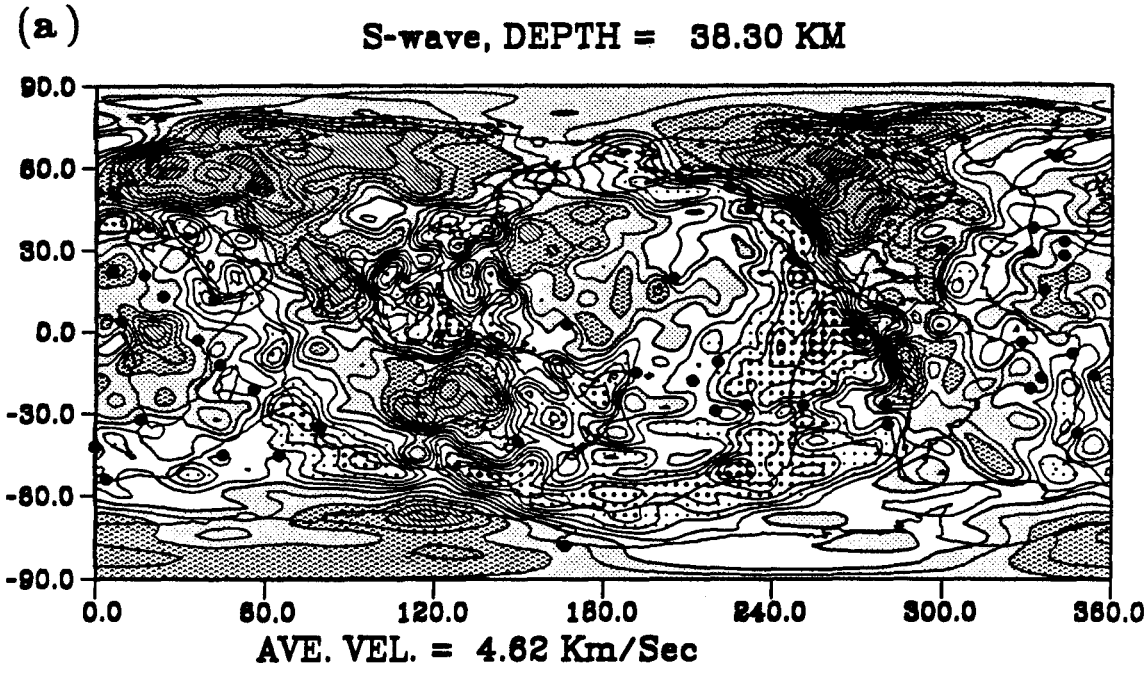
S-wave, DEPTH = 38.30 KM
90.0
60.0
30.0
0.0
-30.0
-60.0
-90.0
0.0
60.0
120.0
180.0
240.0
300.0
360.0
AVE. VEL. = 4.62 Km/Sec

(b)

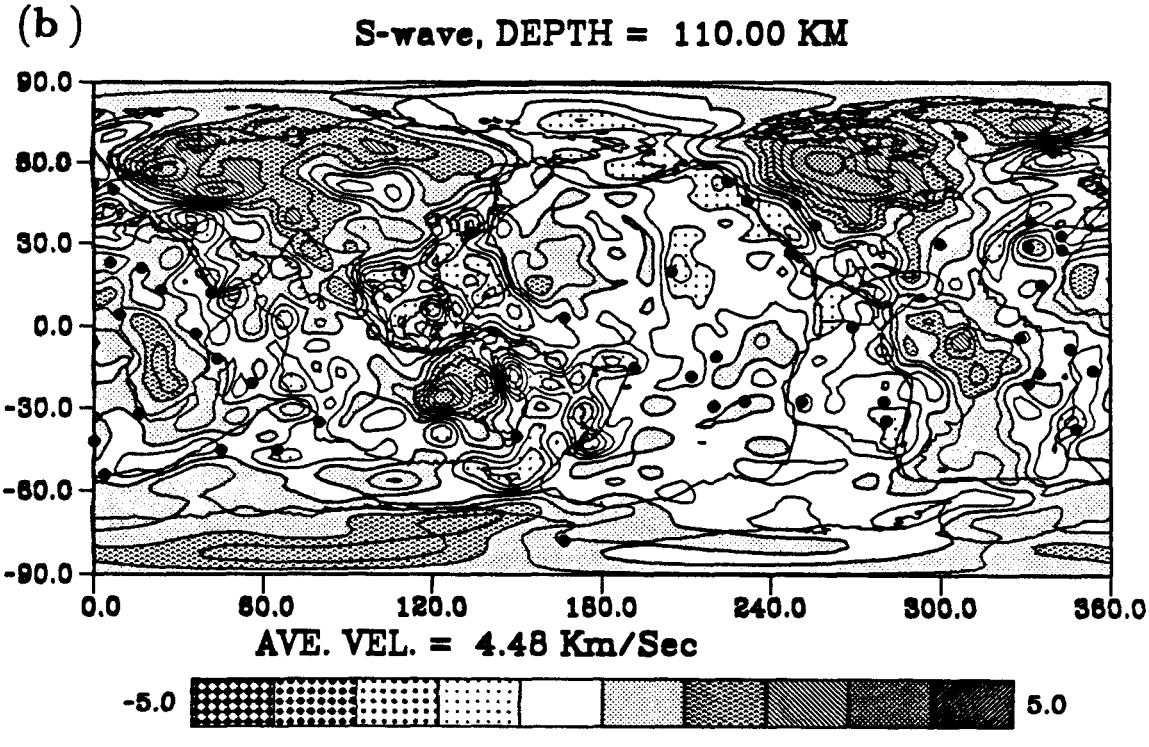
S-wave, DEPTH = 110.00 KM
90.0
60.0
30.0
0.0
-30.0
-60.0
-90.0
0.0
60.0
120.0
180.0
240.0
300.0
360.0
AVE. VEL. = 4.48 Km/Sec
-5.0
5.0

(c)

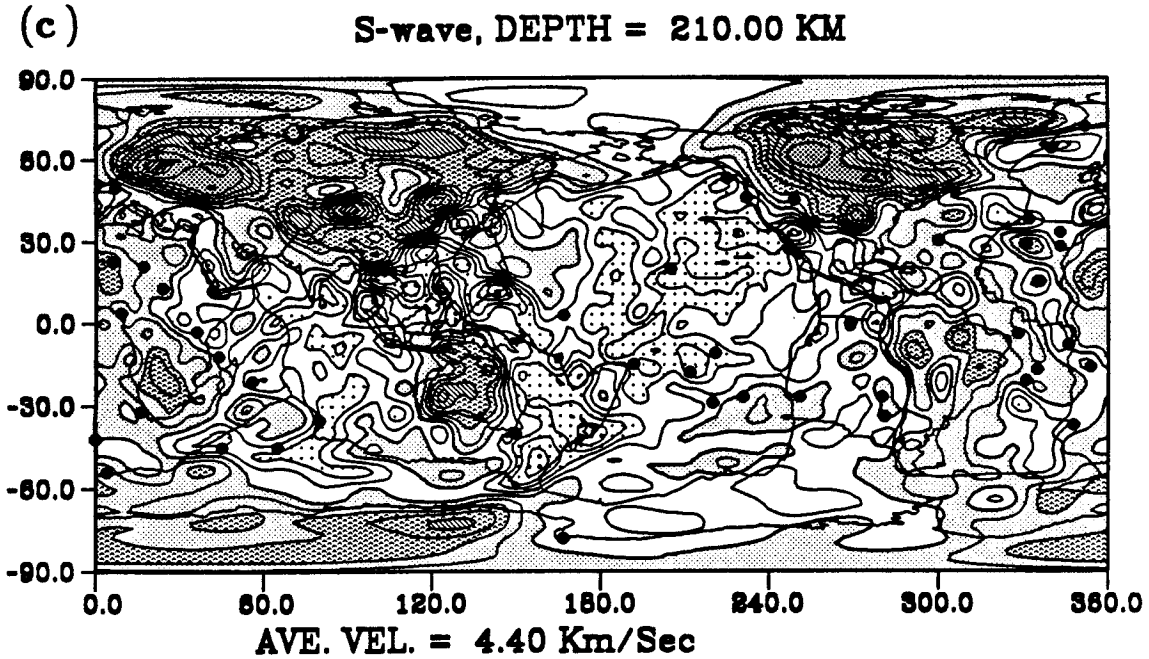
S-wave, DEPTH = 210.00 KM
90.0
60.0
30.0
0.0
-30.0
-60.0
-90.0
0.0
60.0
120.0
180.0
240.0
300.0
360.0
AVE. VEL. = 4.40 Km/Sec

(d)

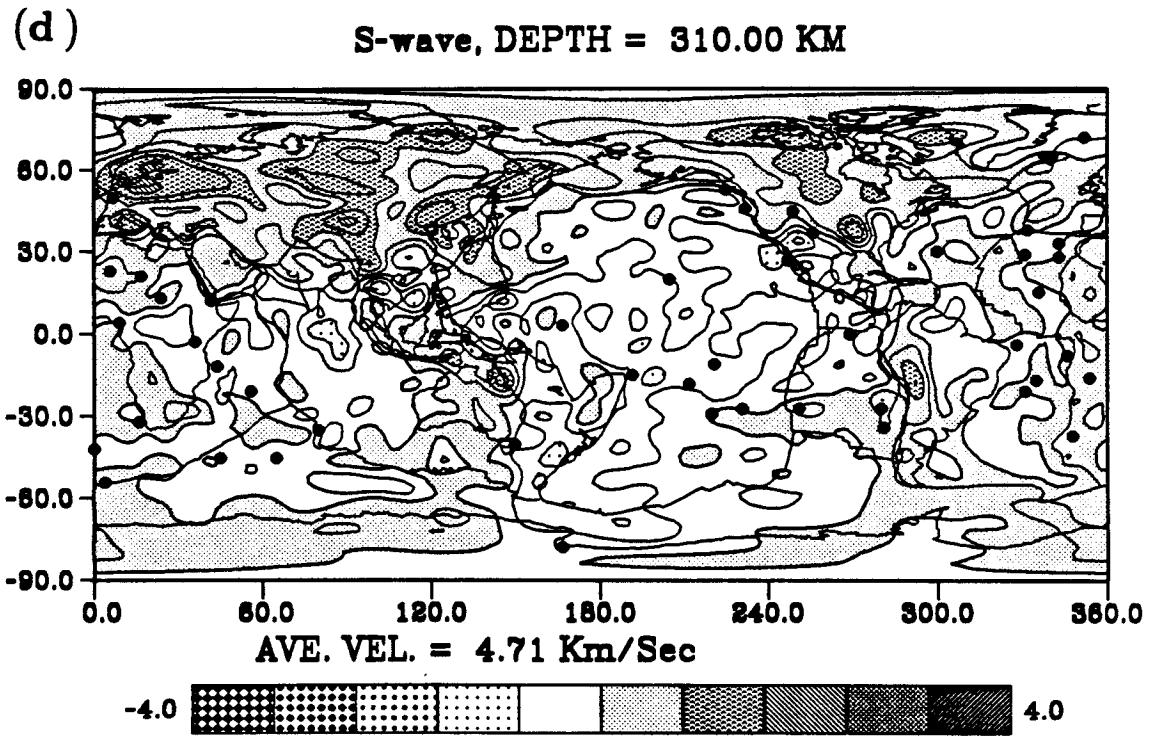
S-wave, DEPTH = 310.00 KM
90.0
60.0
30.0
0.0
-30.0
-60.0
-90.0
0.0
60.0
120.0
180.0
240.0
300.0
360.0
AVE. VEL. = 4.71 Km/Sec
-4.0
4.0

(e)

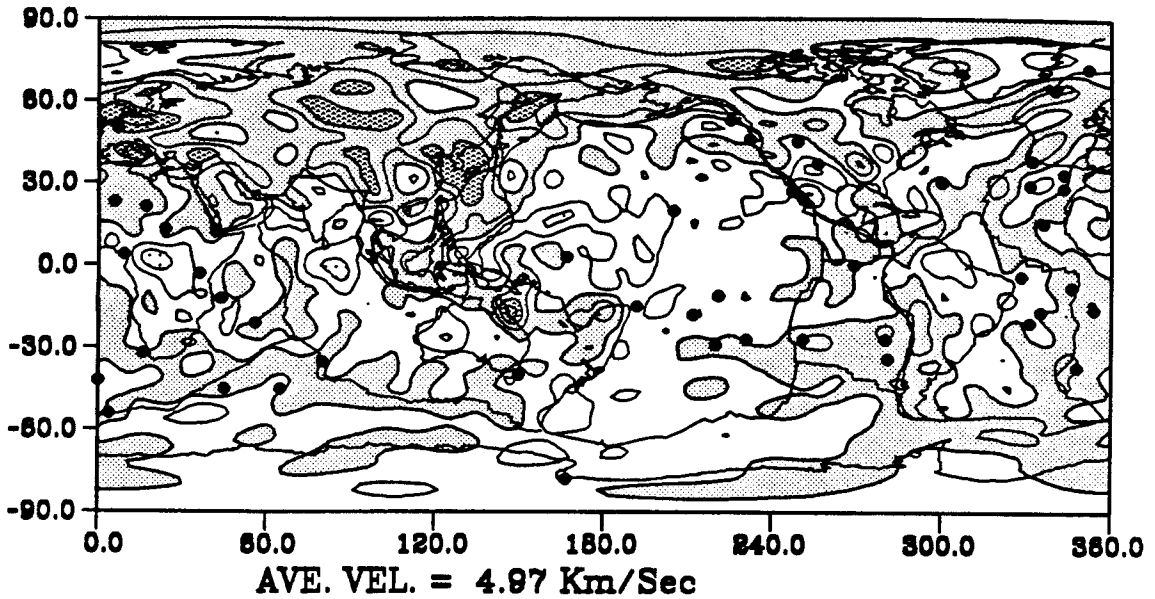
S-wave, DEPTH = 410.00 KM
90.0
60.0
30.0
0.0
-30.0
-60.0
-90.0
0.0
60.0
120.0
180.0
240.0
300.0
360.0
AVE. VEL. = 4.97 Km/Sec

(f)

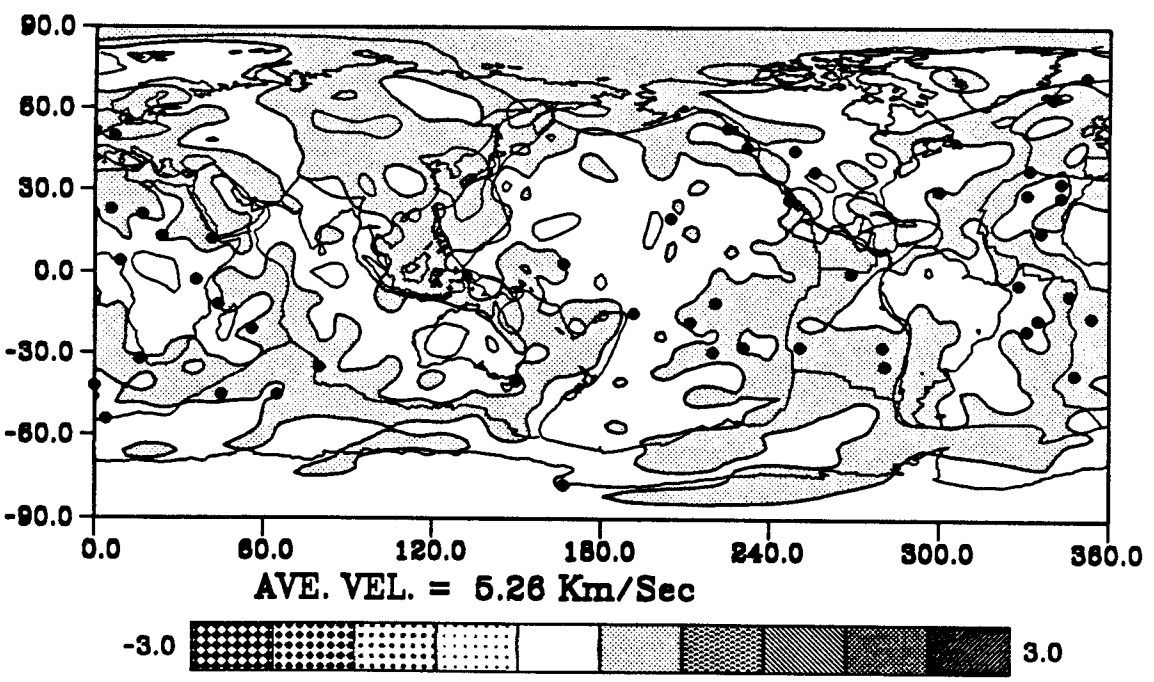
S-wave, DEPTH = 510.00 KM
90.0
60.0
30.0
0.0
-30.0
-60.0
-90.0
0.0
60.0
120.0
180.0
240.0
300.0
360.0
AVE. VEL. = 5.26 Km/Sec
-3.0
3.0

Figure 4.10 shows the variance reduction of each block in experiment 2. The vertical scale gives the reduction of variance in terms of percentage and the horizontal scale gives the serial number of each block. The variance reduction is calculated by $(\sigma_0^2 - \sigma_a^2)/\sigma_o^2$, where σ_0^2 and σ_a^2 are the variances for each block before and after the inversion. Each star represents a variance reduction in one block. Figure 4.10 shows that most blocks have a variance reduction between 60-95 percent, a few lower than 20 percent. The average variance reduction is about 75 percent.

Figure 4.11 shows the average S-wave velocity at different depths for model MS5.5. The reference period is 1 second. The velocity for PREM at same depth is also plotted as a reference. There is no large difference between these two models except from depth 50 to 100 km. The velocity at that depth in our model is higher than that of the PREM. Figures 4.12a-f show maps of S-wave velocity variations at 38.3, 110, 210, 310, 410 and 510 km for MS5.5. The same convention as in Figure 4.2 and 4.3 is used in these maps, but the contour intervals are different. The magnitude of heterogeneity decreases with depth, which is consistent with previous studies (*e.g.*, Dziewonski and Anderson, 1981; Woodhouse and Dziewonski, 1984; Nataf *et al.* 1986; Tanimoto, 1986a,b, 1990; Zhang and Tanimoto, 1989; Montagner and Tanimoto, 1990). We find fast velocity associated with stable continental shield areas (Canadian, Baltic, Siberian, Antarctic, Australian, South American and South African) and old oceanic regions (northwest Pacific Ocean, east and west of middle Atlantic Ocean, west of south Atlantic Ocean and Wharton basin in the Indian Ocean); and low velocities in younger oceans near the ridges (East Pacific Rise, Chile Rise, Mid-Atlantic Ridge, Mid-Indian Ocean Ridge, and Southeast Indian Ocean Ridge). Other low velocity anomalies are at tectonically active

continental regions, back-arc basins and subduction zones, such as west of North American, Peru-Chile trench, Aleutian trench, Japan trench, Philippine trench, Tonga trench, Java trench, Red Sea and Gulf of Aden.

The Australia-Antarctic Discordance is associated with a low velocity anomaly down to 100 km deep. This area has been studied by many researchers (Weissel and Hayes, 1971, 1974; Anderson *et al.*, 1980; Vogt *et al.* 1983; Klein *et al.*, 1988) because of its peculiarities in ocean floor depth, geoid low and distinct geochemical differences between east and west. At present, however, we do not understand why the low velocity anomaly emerges there, and future study in this area is needed.

We find good correlation between S-wave velocity and plate tectonic features for shallow depths, but this correlation decreases with depth. Figures 4.13a-e are vertical sections along different great circles. The location of each great circle is shown in the middle of the top world map, which is plotted in Lambert cylindrical equal-area projection. The great circles pass through the East Pacific Rise and the Pacific-Antarctic Ridge in Figures 4.13a-c. It shows that the ridges are associated with low velocity anomalies in the top 100 km, and the minimum velocities are at about 50 km. The magnitudes of the low velocity anomalies decrease vastly and/or vanish below 100 km. We will discuss this feature more in Chapter 6. There is about 7 percent difference in S-wave velocity between the tectonic active west North American and stable Canadian shield in Figure 4.13a, which is consistent with Grand and Helmberger's (1984) S-wave results and Grand's (1987) body wave tomography results.

Figure 4.13d is a vertical section that passes through the Pacific ocean from ridge to oldest region. Among the features of interest are that the velocity increases with the age in the top 80 (or 100) km. The lowest velocity is at

ridges, and the fastest velocity is in the old northwest Pacific ocean. Similar features cannot be found below 100 km. We believe that this is further evidence to prove that the thickness of the oceanic lithosphere is about 100 km. There is a low velocity anomaly near Hawaii island between 100 and 200 km, which is associated with the hotspot there.

The velocity structures of old oceanic areas and continental shields shown in Figures 4.13a-e are different; the stable continental shields are associated with a larger magnitude of fast velocity anomaly than the old oceanic area. The velocity structures under different stable shields are also different. The velocity structure under Australian, Baltic, Canadian, and Siberian shields are associated with strong fast velocity anomalies, which penetrate to about 400 km. But under other shields (*e.g.*, South African shield, Brazil shield, Indian shield and Antarctic shield), the fast velocity anomalies are smaller in magnitude and penetrate to about 200 km or slightly more. The velocity difference between the stable shields probably suggests that these continents have undergone a different evolution. The fast velocity anomaly under the Australian, Baltic, Canadian, and Siberian shields down to 400 km are consistent with the results of Lerner-Lam and Jordan (1987) and Grand (1987). Lerner-Lam and Jordan (1987) interpret that the deep fast velocity anomaly is connected with deep continental roots (Jordan, 1975, 1981; Jordan *et al.*, 1988). However, Anderson and Bass (1984), Anderson (1990) explain that the fast velocity anomalies under stable shields between 200 and 400 km are attributed to the absence of an appreciable melt phase rather than to a continental root that extended deeper than about 200 km. It is difficult to determine what causes the deep, fast velocity anomaly under the present conditions, and future study is needed.

Figure 4.13, (a). Vertical section for a great circle slice passing through the East Pacific Rise. The location of the great circle is shown in the middle of the top world map, which is plotted in Lambert Cylindrical Equal-area projection. The contours are at 0.5 percent intervals and patterns change every percent. (b). Vertical section for a great circle slice passing through the Pacific-Antarctic Ridge. (c). Vertical section for a great circle slice passing through the Equator. (d). Vertical section for a great circle slice passing through the Pacific Ocean. (e). Vertical section for a great circle slice passing through the Hawaiian Island and Iceland.

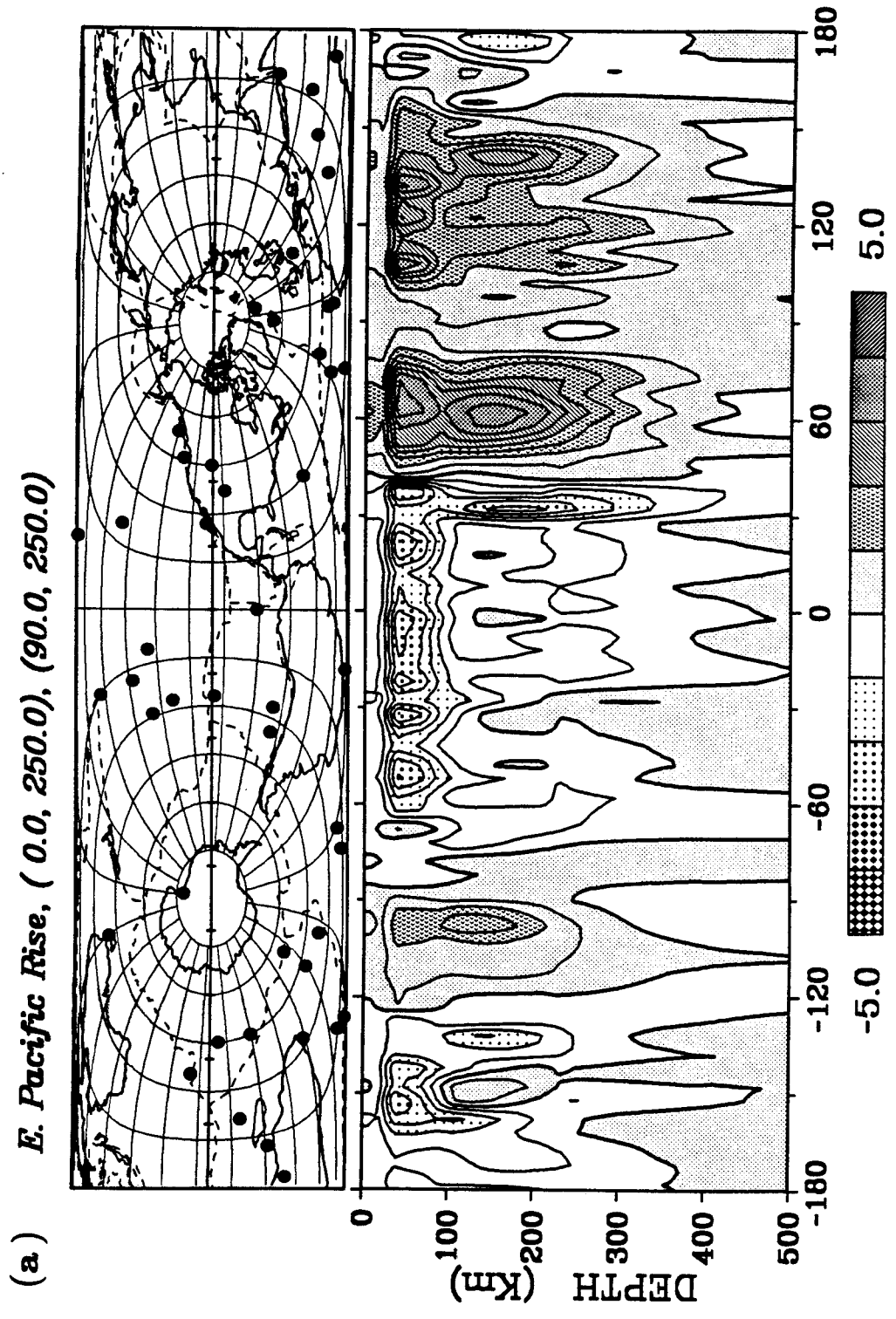
(a)
E. Pacific Rise, (0.0, 250.0), (90.0, 250.0)
DEPTH (Km)
0
100
200
300
400
500
-180
-120
-60
0
60
120
180
-5.0
5.0

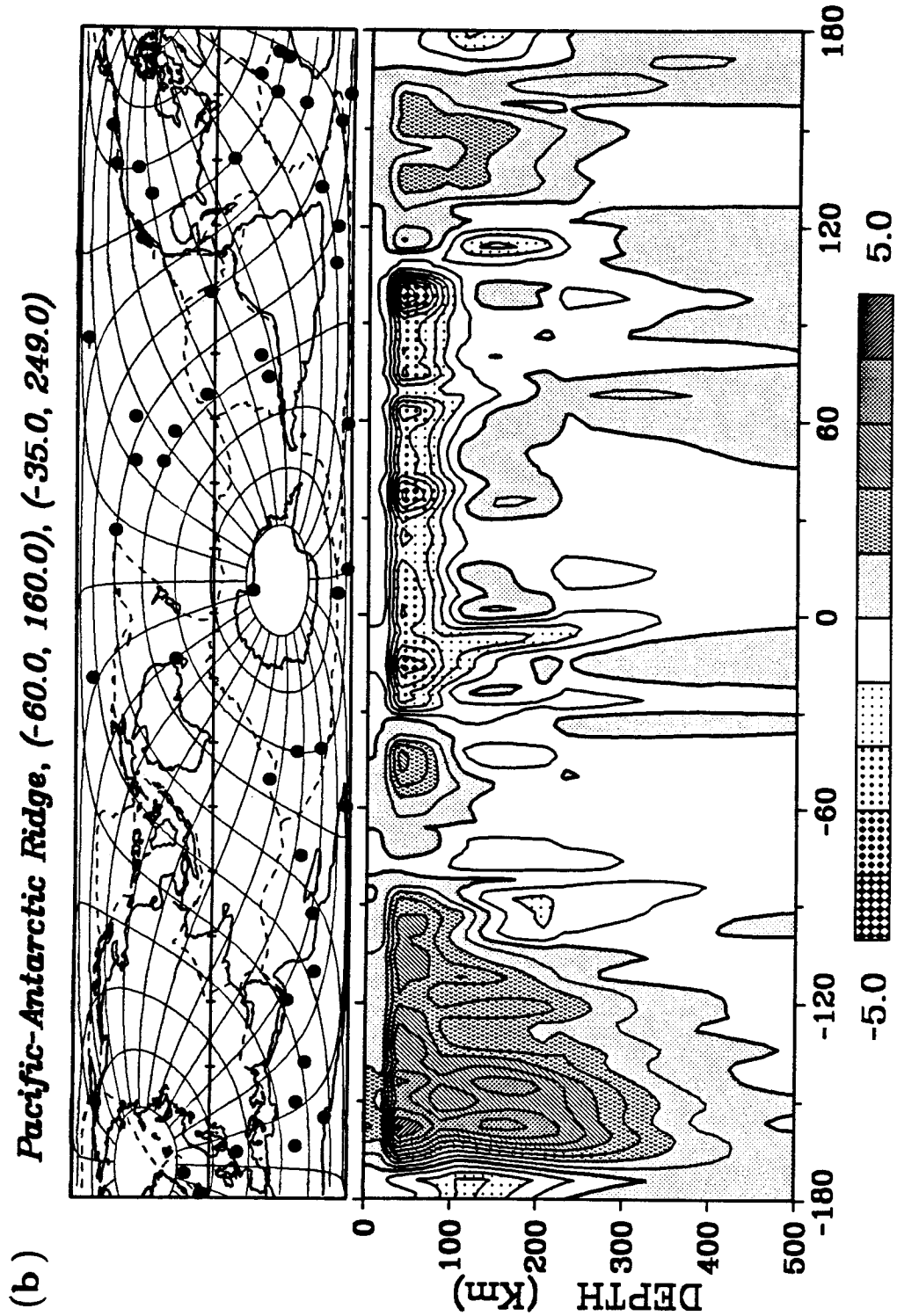
(b)
Pacific-Antarctic Ridge, (-60.0, 160.0), (-35.0, 249.0)
DEPTH (Km)
0
100
200
300
400
500
-180
-120
-60
0
60
120
180
-5.0
5.0

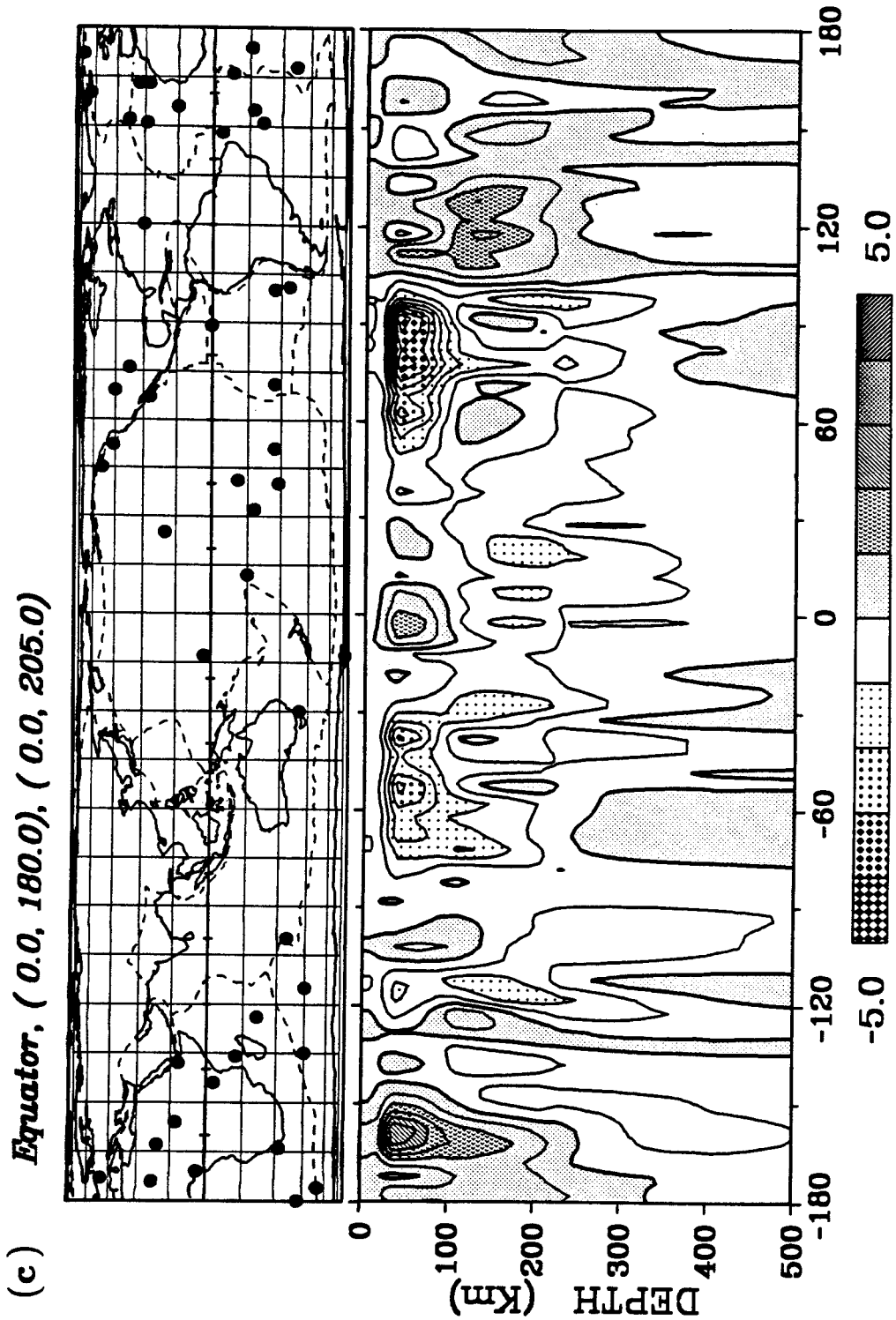
(c)
Equator, (0.0, 180.0), (0.0, 205.0)
DEPTH (Km)
0
100
200
300
400
500
-180
-120
-60
0
60
120
180
-5.0
5.0

(d) *Pacific Ocean, (-5.0, 256.0), (25.0, 149.0)*

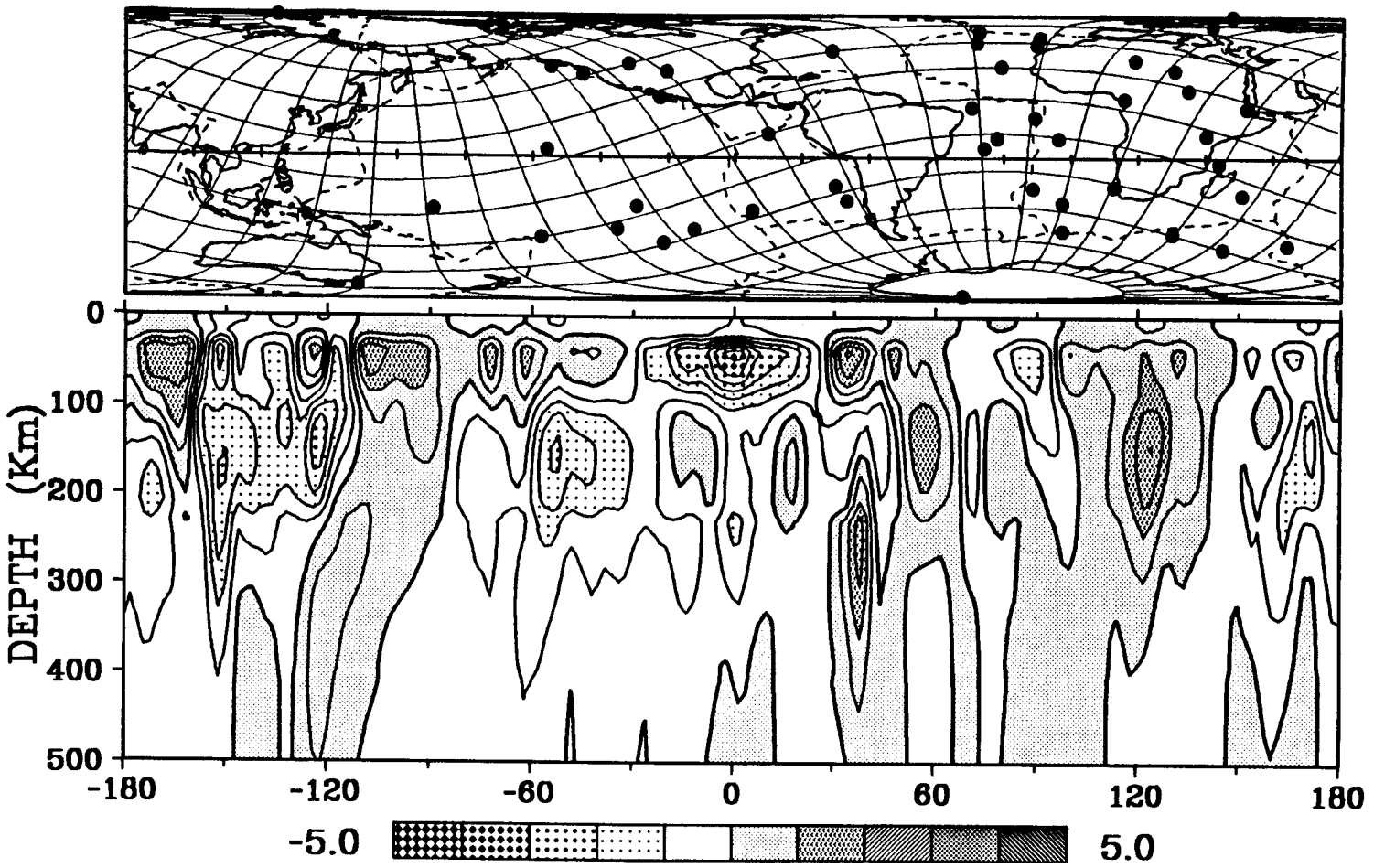

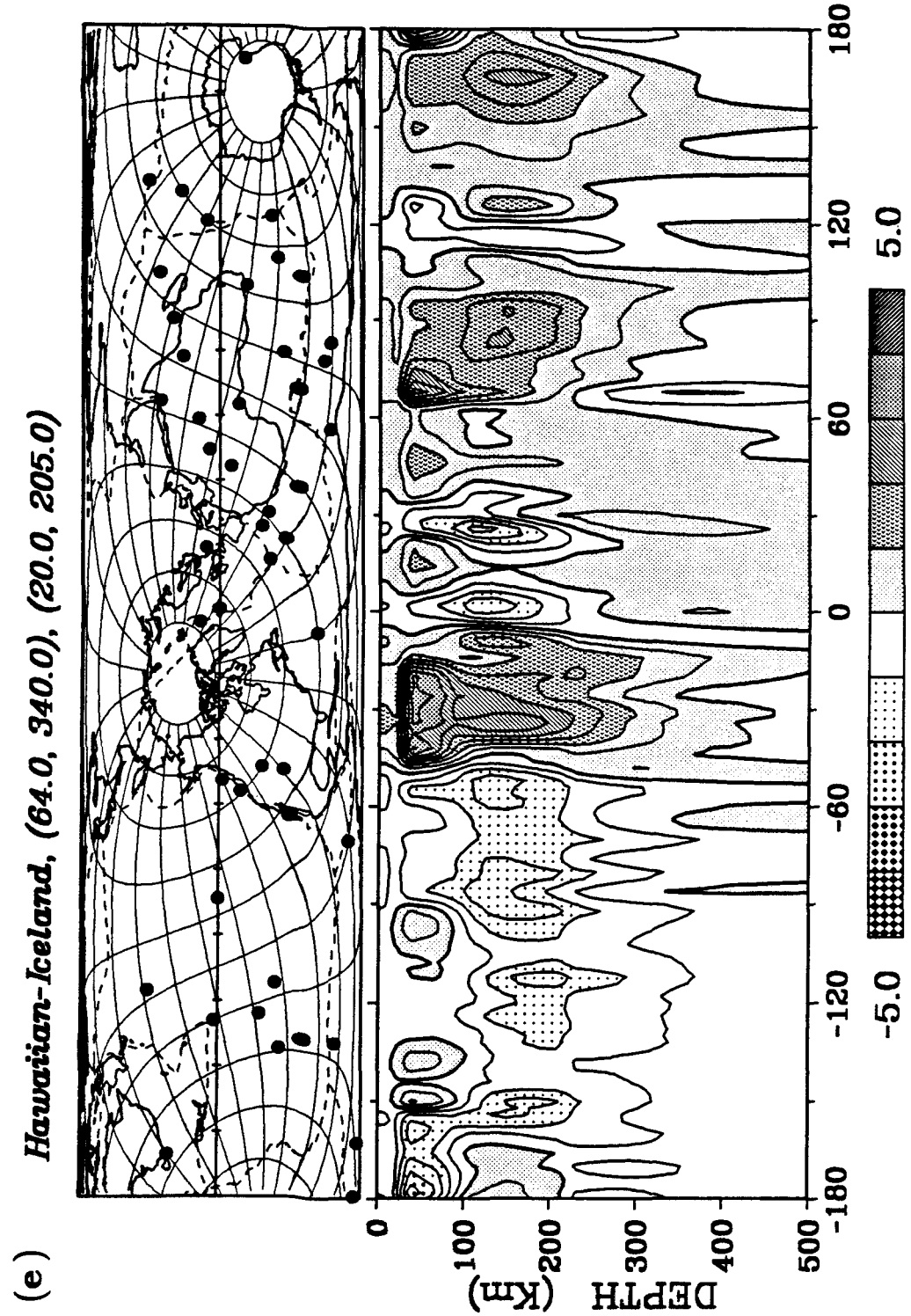
(e)
Hawaiian-Iceland, (64.0, 340.0), (20.0, 205.0)
DEPTH (Km)
0
100
200
300
400
500
-180
-120
-60
0
60
120
180
-5.0
5.0

In the present study, several major hotspots (such as Hawaii, Iceland Tristan de Cunha and the Azores) are found associated with low velocity anomalies between 80 and 200 km (Figure 4.12, Figure 4.13). The depth of these low velocity anomalies are different from that of the ridges. A clear example is in figure 4.13d. The low velocity under the East Pacific rise is confined to the top 100 km, which is different from the Hawaii hotspot. This feature supports the view that passive, upwelling upper mantle at the edges of separating plates form mid-ocean ridges, and active upwelling plumes under hotspots are creating low velocity anomalies under the lithosphere. This point we will discuss further in later chapters.

Figure 4.14, (a). Comparison of Nakanishi and Anderson's Love wave phase velocity variation and our Love wave phase velocity variation. Both are at period of 100.0 s and the spherical harmonic degree $0 \leq L \leq 6$. (b). Comparison of Woodhouse and Dziewonski's Love wave phase velocity variation at 139 s and our Love wave phase velocity variation at 100 s with spherical harmonic degree $0 \leq L \leq 8$. (c). Comparison of Tanimoto's Love wave phase velocity variation at 150 s and our Love wave phase velocity variation at 151 s with spherical harmonic degree $0 \leq L \leq 10$. (d). Comparison of Wong's Love wave phase velocity variation at 156 s and our Love wave phase velocity variation at 151 s with spherical harmonic degree $0 \leq L \leq 12$.

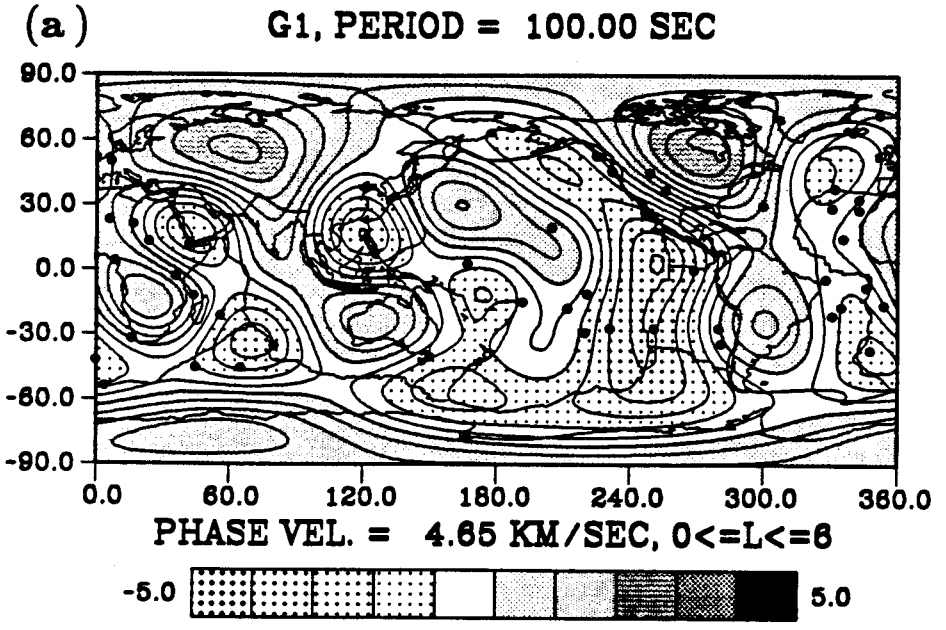
(a)
G1, PERIOD = 100.00 SEC
90.0
60.0
30.0
0.0
-30.0
-60.0
-90.0
0.0
60.0
120.0
180.0
240.0
300.0
360.0
PHASE VEL. = 4.65 KM/SEC, 0<=L<=6
-5.0
5.0

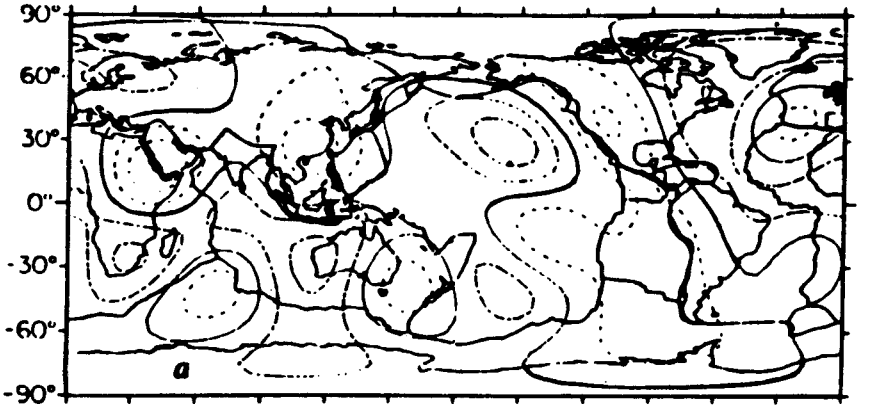
90°
60°
30°
0°
-30°
-60°
-90°
a

(b)

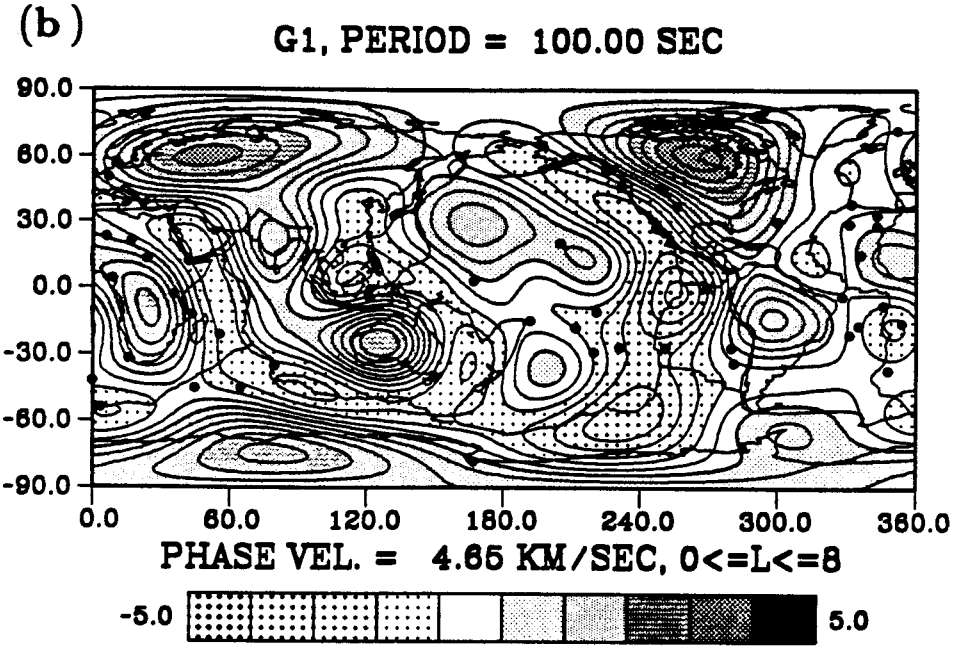
G1, PERIOD = 100.00 SEC
90.0
60.0
30.0
0.0
-30.0
-60.0
-90.0
0.0
60.0
120.0
180.0
240.0
300.0
360.0
PHASE VEL. = 4.65 KM/SEC, 0<=L<=8
-5.0
5.0

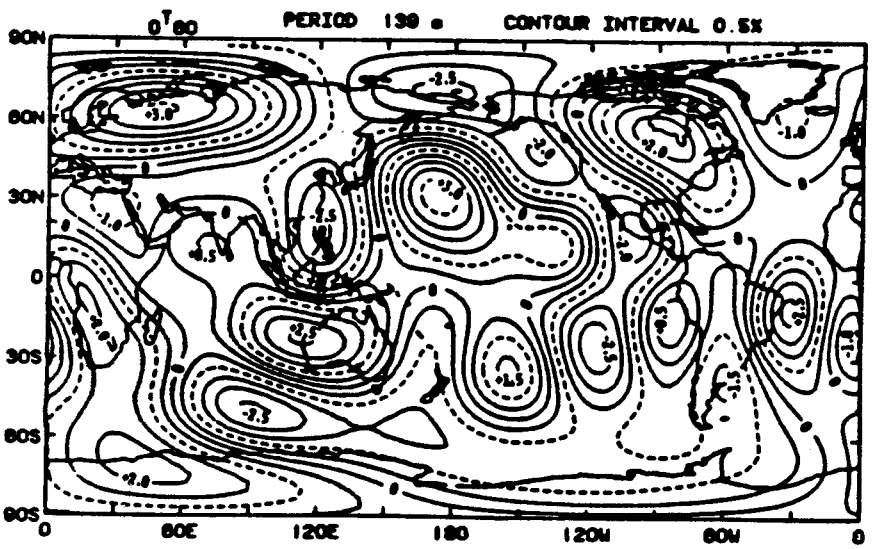
0°80
PERIOD 130 s
CONTOUR INTERVAL 0.5%
90N
60N
30N
0
30S
60S
90S
0
60E
120E
180
120W
60W
0

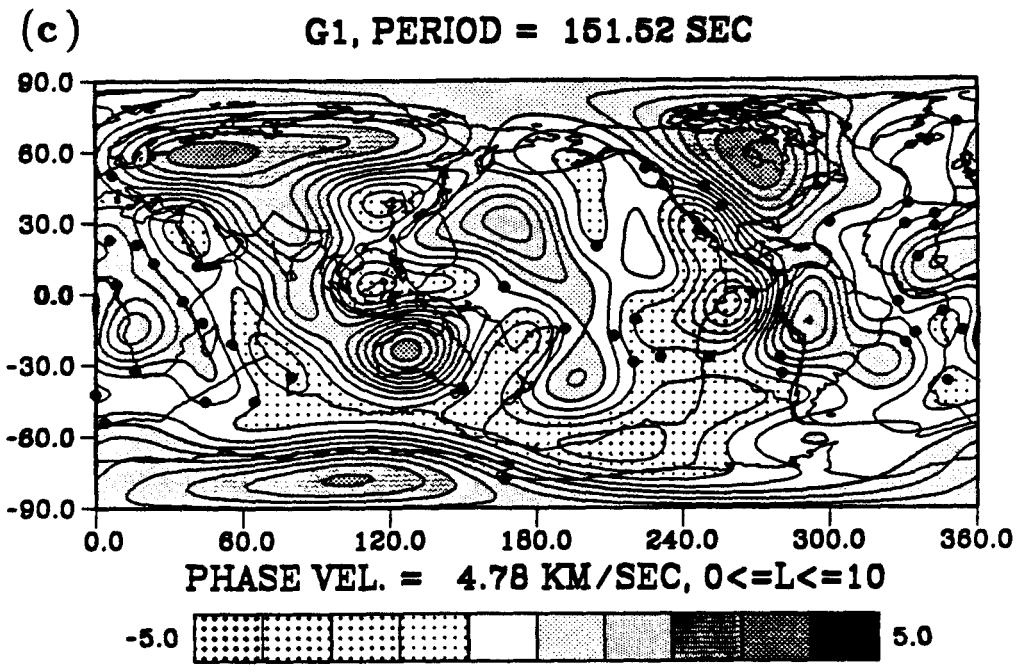
(c)
G1, PERIOD = 151.52 SEC
90.0
60.0
30.0
0.0
-30.0
-60.0
-90.0
0.0
60.0
120.0
180.0
240.0
300.0
360.0
PHASE VEL. = 4.78 KM/SEC, 0<=L<=10
-5.0
5.0

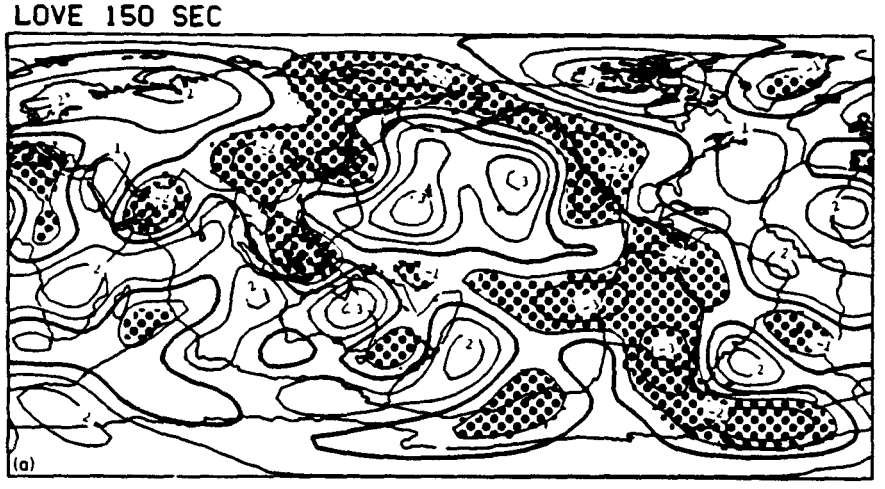
LOVE 150 SEC
(a)

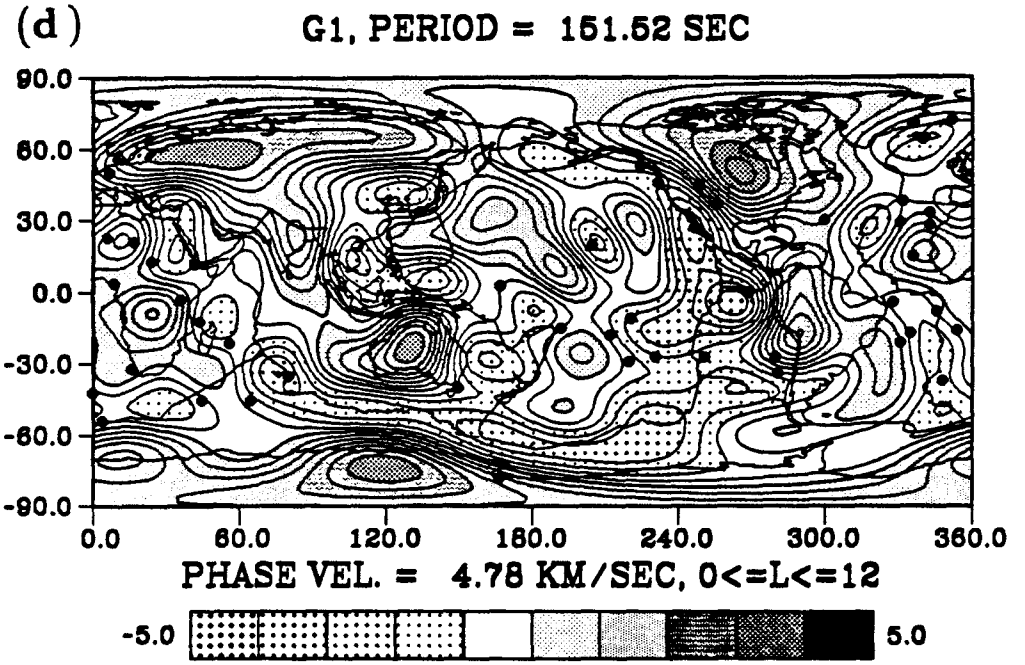
(d)
G1, PERIOD = 151.52 SEC
90.0
60.0
30.0
0.0
-30.0
-60.0
-90.0
0.0
60.0
120.0
180.0
240.0
300.0
360.0
PHASE VEL. = 4.78 KM/SEC, 0<=L<=12
-5.0
5.0

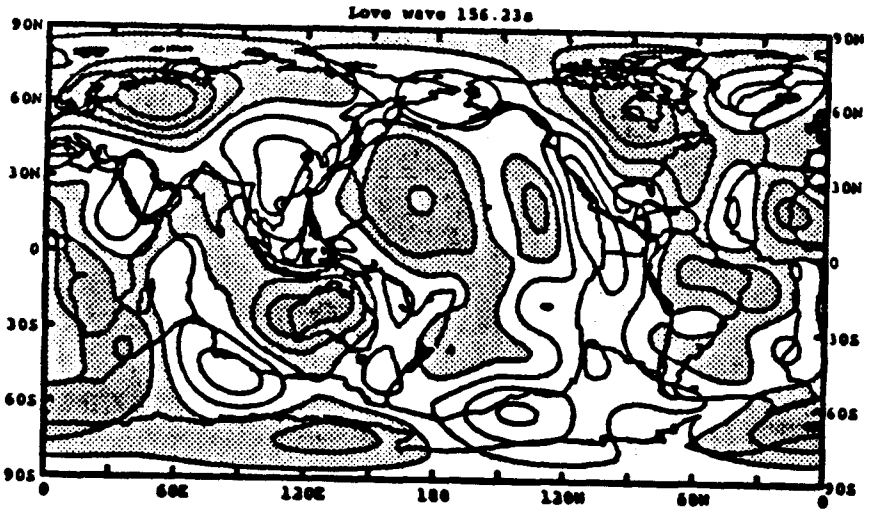
Love wave 156.23s
90N
60N
30N
0
30S
60S
90S
0
60E
120E
180
120W
60W
0

4.4 Discussion

There have been a lot of upper mantle studies (*e.g.*, Nakanishi and Anderson, 1984; Woodhouse and Dziewonski, 1984; Nataf *et al.*, 1986; Tanimoto, 1986a,b; Montagner and Tanimoto, 1990). Different authors have used different data sets, different techniques and different parametrizations. We would like to compare our results with these results, and find the differences between the various studies. Our results are first expanded up to the spherical harmonic degree 36, which is equivalent to the $5^0 \times 5^0$ block approach. And then the maps, which correspond to different spherical harmonic degrees, are calculated and compared with previous studies.

Figures 4.14a-d are the comparison of our Love wave phase velocity variations with Nakanishi and Anderson (1984, Fig. 2a, $l_{max}=6$), Woodhouse and Dziewonski (1984, Fig. 8b, $l_{max}=8$), Tanimoto (1985, Fig. 5a, $l_{max}=10$) and Wong (1989, Fig. 5.3, $l_{max}=12$). Figures 4.15a-d are the comparison of our Rayleigh wave phase velocity variations with Nakanishi and Anderson (1984, Fig. 3a, $l_{max}=6$), Woodhouse and Dziewonski (1984, Fig. 8a, $l_{max}=8$), Tanimoto (1985, Fig. 6a, $l_{max}=10$) and Wong (1989, Fig. 5.2, $l_{max}=12$). The period for each map is shown at the top. Because these results come from different studies, the periods do not match each other exactly. We tried to make the period difference as small as possible. Our results shown here are associated with the optimal damping parameter at the $5^o \times 5^o$ approach, so there are some minor differences from the results we presented before.

Figure 4.15 (a). Comparison of Nakanishi and Anderson's Rayleigh wave phase velocity variation at 153 s and our Rayleigh wave phase velocity variation at 151 s with spherical harmonic degree $0 \leq L \leq 6$. (b). Comparison of Woodhouse and Dziewonski's Rayleigh wave phase velocity variation at 153 s and our Rayleigh wave phase velocity variation at 151 s with spherical harmonic degree $0 \leq L \leq 8$. (c). Comparison of Tanimoto's Rayleigh wave phase velocity variation at 150 s and our Rayleigh wave phase velocity variation at 151 s with spherical harmonic degree $0 \leq L \leq 10$. (d). Comparison of Wong's Rayleigh phase velocity variation at 155 s and our Rayleigh wave phase velocity variation at 151 s with spherical harmonic degree $0 \leq L \leq 12$.

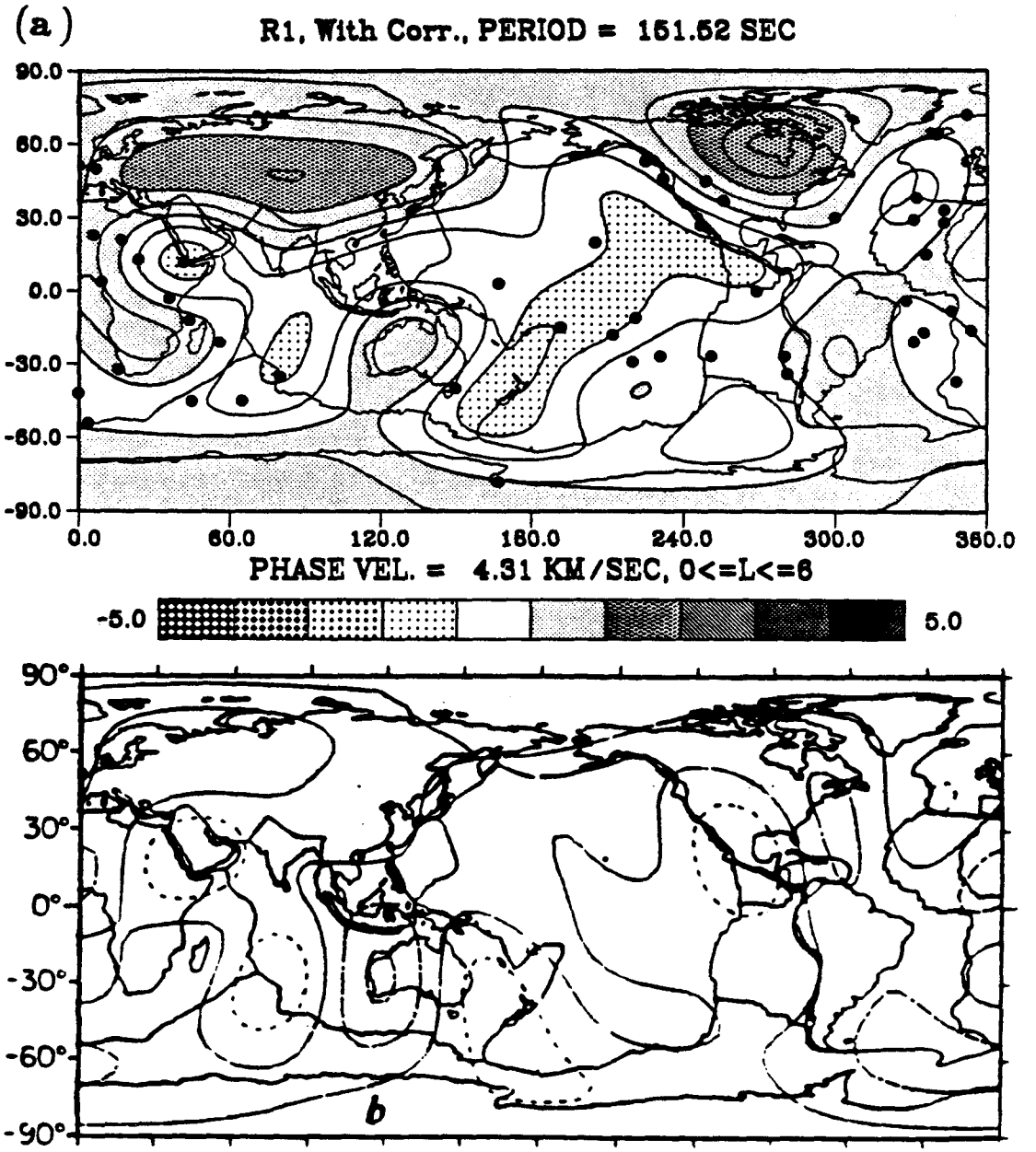
(a)
R1, With Corr., PERIOD = 151.52 SEC
90.0
60.0
30.0
0.0
-30.0
-60.0
-90.0
0.0
60.0
120.0
180.0
240.0
300.0
360.0
PHASE VEL. = 4.31 KM/SEC, 0<=L<=6
-5.0
5.0
90°
60°
30°
0°
-30°
-60°
-90°
b

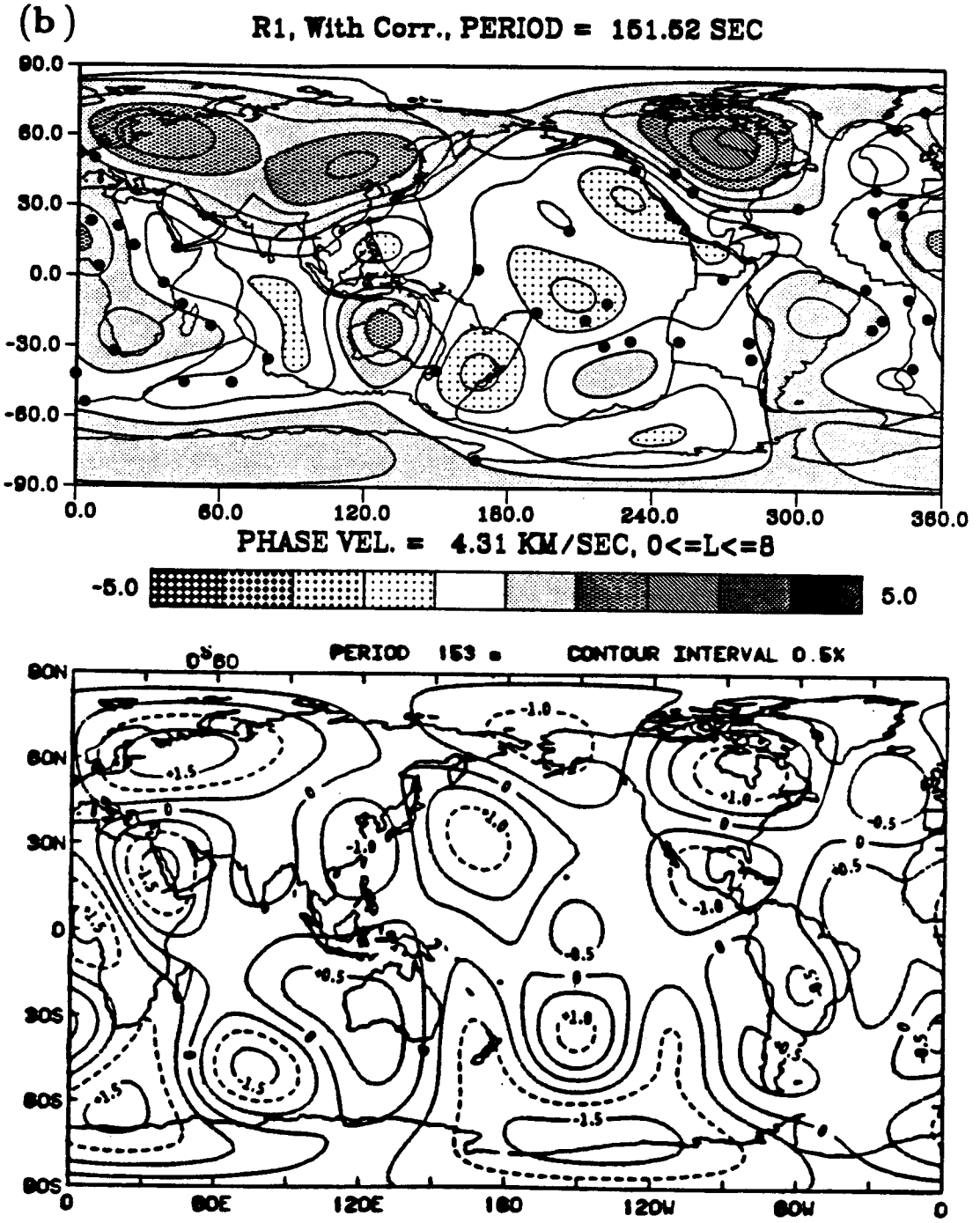
(b)
R1, With Corr., PERIOD = 151.52 SEC
90.0
60.0
30.0
0.0
-30.0
-60.0
-90.0
0.0
60.0
120.0
180.0
240.0
300.0
360.0
PHASE VEL. = 4.31 KM/SEC, 0<=L<=8
-5.0
5.0
PERIOD 153 s
CONTOUR INTERVAL 0.5%
0°&360
90N
60N
30N
0
30S
60S
90S
0
60E
120E
180
120W
60W
0

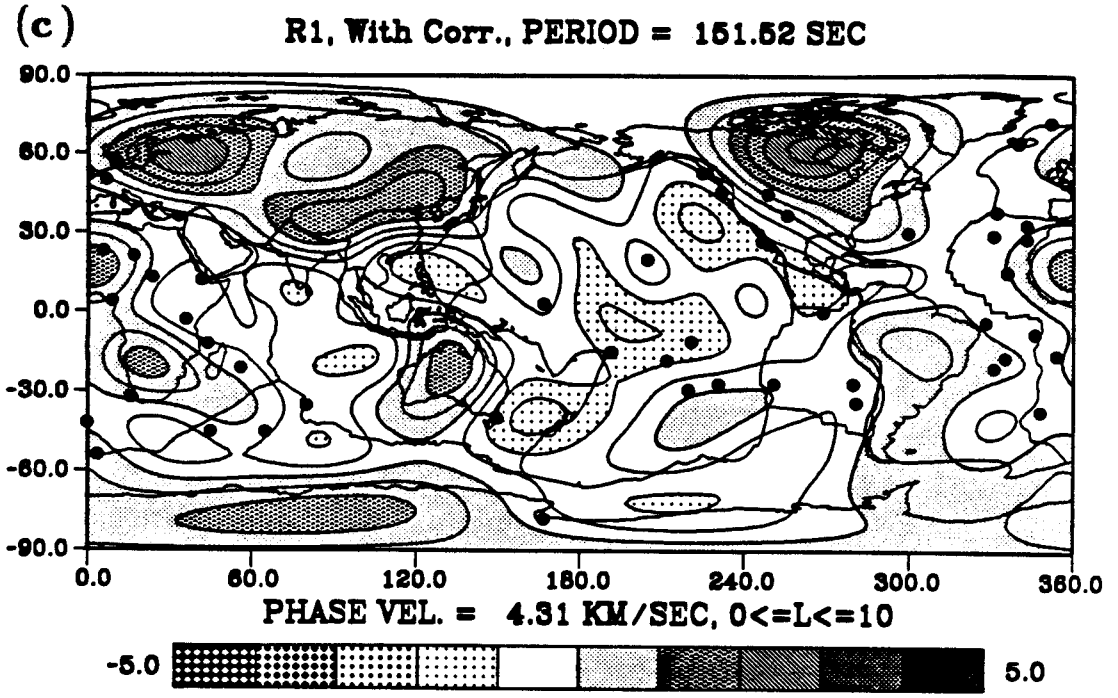
(c)
R1, With Corr., PERIOD = 151.52 SEC
90.0
60.0
30.0
0.0
-30.0
-60.0
-90.0
0.0
60.0
120.0
180.0
240.0
300.0
360.0
PHASE VEL. = 4.31 KM/SEC, 0<=L<=10
-5.0
5.0

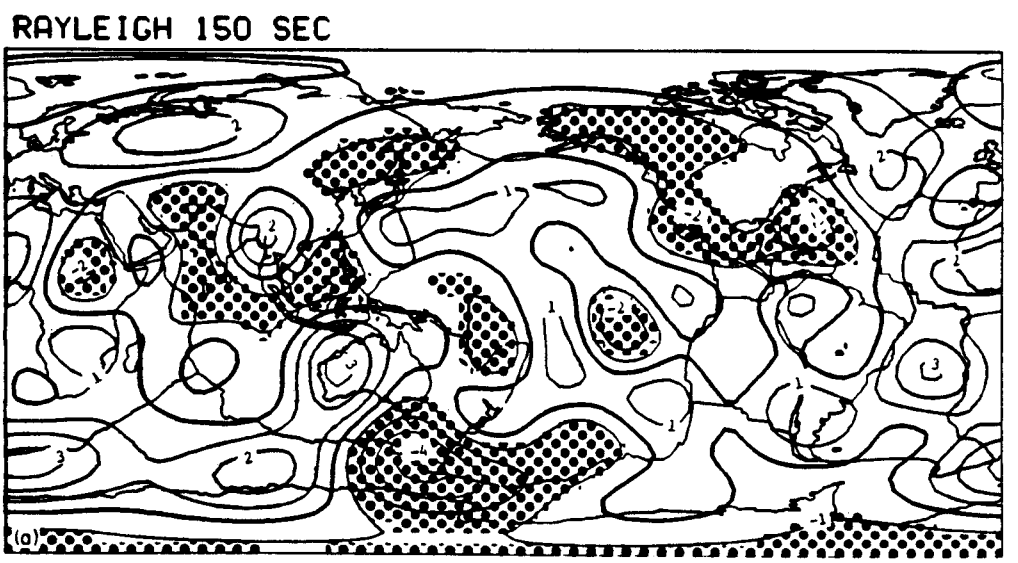
RAYLEIGH 150 SEC

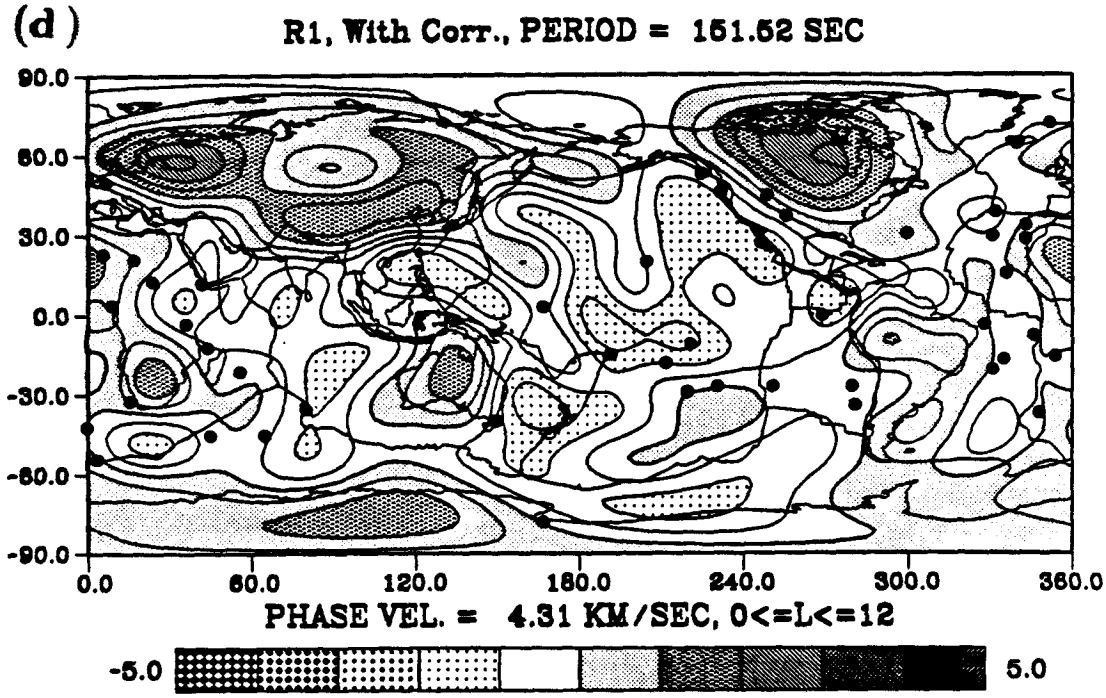
(d)
R1, With Corr., PERIOD = 151.52 SEC
90.0
60.0
30.0
0.0
-30.0
-60.0
-90.0
0.0
60.0
120.0
180.0
240.0
300.0
360.0
PHASE VEL. = 4.31 KM/SEC, 0<=L<=12
-5.0
5.0

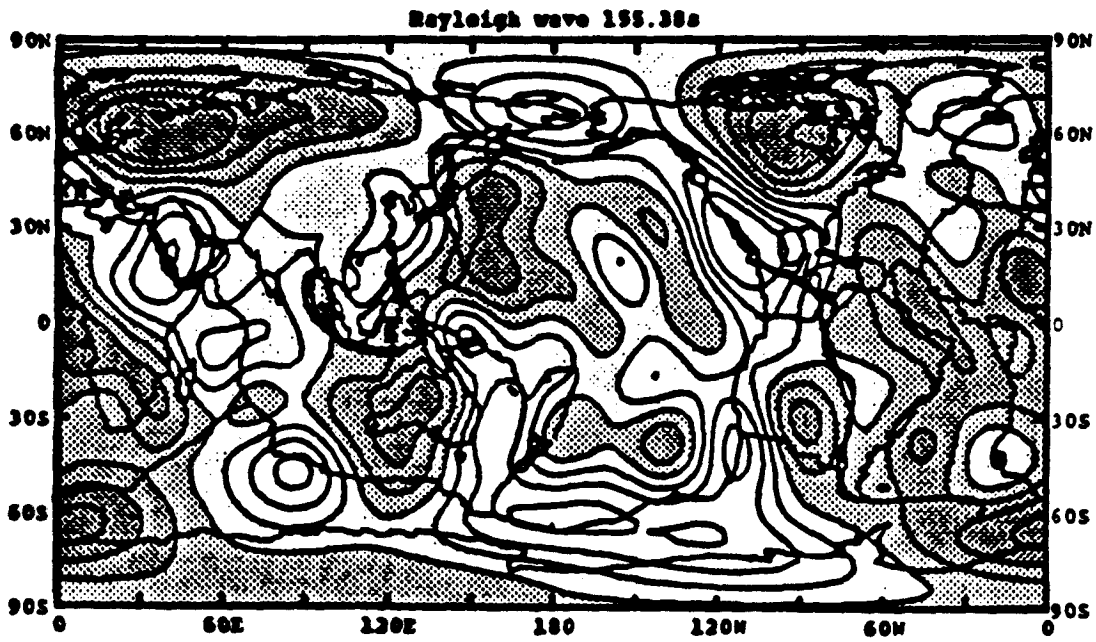
Rayleigh wave 155.38s
90N
60N
30N
0
30S
60S
90S
0
60E
120E
180
120W
60W
0

An interesting point is that our results are quite similar to previous results. For example, our Love wave $l_{max}=8$, 12 results are almost the same as Woodhouse and Dziewonski's (1984) and Wong's (1989) results, both in velocity pattern and magnitude. There are minor differences in the different studies because of different data sets and different techniques. From these comparisons, we conclude that all of previous studies are consistent. In the present study, we have vastly increased the data set and improved the inversion technique, which allowed us to get more detailed and reliable results than in previous studies.

The spectral amplitude (calculated by Equation 2.12) distributions as a function of the spherical angular order l at different depth are shown in Figure 4.16. These distributions are plotted in logarithmic scale. The spectrum amplitude distributions of topography and Moho depth are also plotted in Figure 4.16 as references, and they are normalized by the maximum value equal to 1.0. All of the spherical amplitudes at different depths are normalized at the same level. It is clear from the figure that the heterogeneity decreases with depth. One important point is that all of the spherical amplitude curves are approximate to the l^{-1} curve (the diagonal dash line in the figure) from $l=1$ to $l=36$. A similar feature is also found in Inoue *et al.*'s (1990) mantle P-wave velocity tomography results. The l^{-1} dependence of the spectrum amplitude on spherical harmonic degree explains why previous studies with low l_{max} did not suffer very much from aliasing and why they produced consistent results with different data set and different approaches. It is obvious that the large-scale heterogeneity is predominantly inside of the Earth. It also provides an important constraint for constructing a theoretical mantle model for the Earth.

Figure 4.16, The spherical amplitude distributions as a function of the spherical angular order l for S-wave velocity at different depths, topography and Moho depth. These distributions are plotted in logarithmic scale. One important feature is that all of the spherical amplitude curves are approximate to the l^{-1} from $l = 1$ to 36.

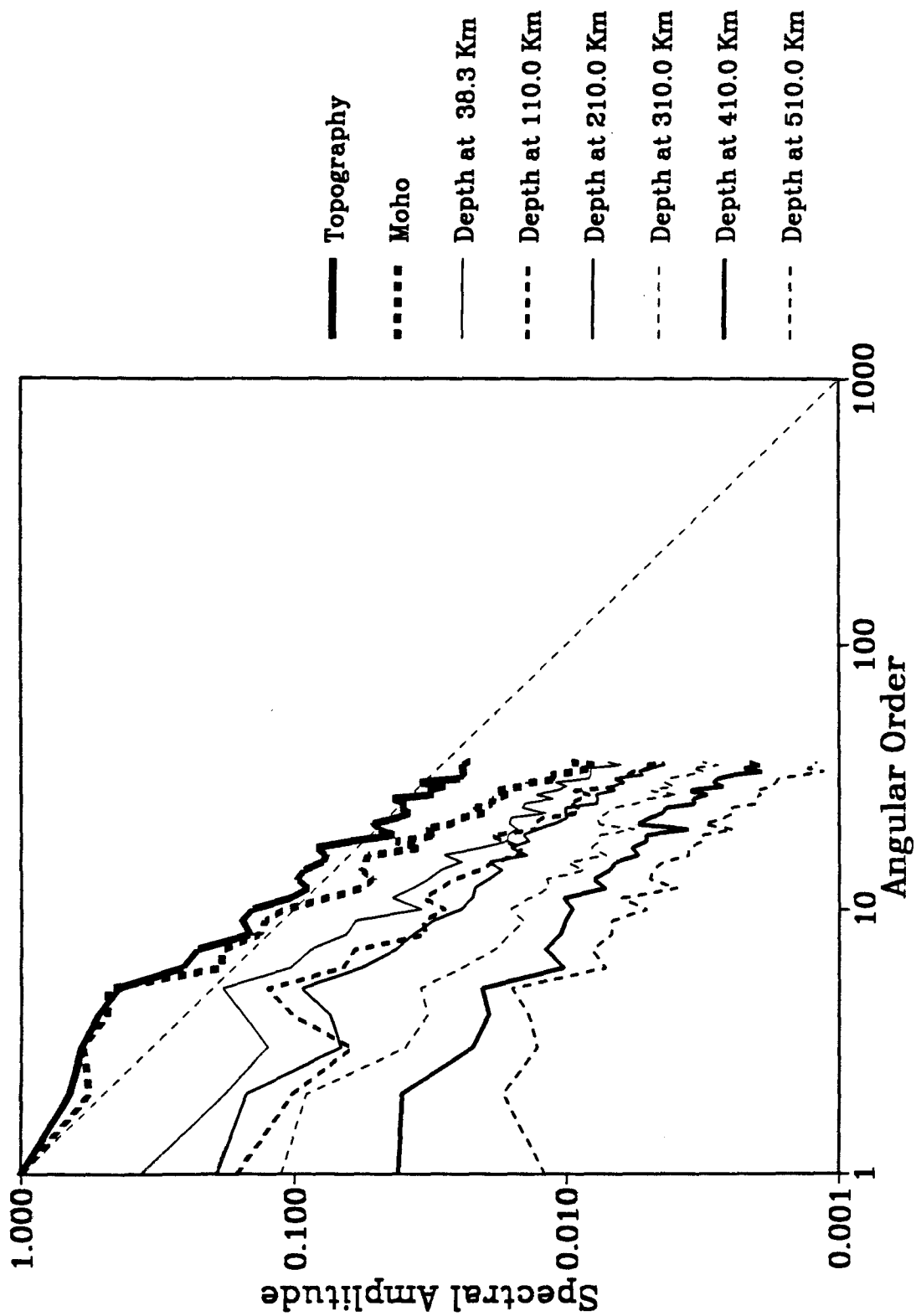
Topography
Moho
Depth at 38.3 Km
Depth at 110.0 Km
Depth at 210.0 Km
Depth at 310.0 Km
Depth at 410.0 Km
Depth at 510.0 Km
Spectral Amplitude
1.000
0.100
0.010
0.001
1
10
100
1000
Angular Order

Figures 4.17a-c show the correlation between topography and geoid, and topography and S-wave velocity variation at depths 38.3 km and 110 km. The geoid model comes from GEM-T1 (Marsh *et al.* 1988). The correlation coefficients between any two spherical harmonic functions are given by the ratio of covariance to variance at each harmonic degree

$$r = \frac{\sum_{m=0}^{l} (C_l^m A_l^m + S_l^m B_l^m)}{\left[\sum_{m=0}^{l} (C_l^{m^2} + S_l{}^{m^2})\right]^{\frac{1}{2}} \left[\sum_{m=0}^{l} (A_l^{m^2} + B_l^{m^2})\right]^{\frac{1}{2}}}, \qquad (4.5)$$

where $A_l{}^m, B_l{}^m, C_l{}^m, S_l{}^m$ are the coefficients of the spherical harmonic expansion. The dashed lines in the figure are confidence limits, calculated by the method of Eckhardt (1984). The corresponding number of each level is shown in the upper right side of the figure. A confidence level of 0.99 implies only one percent chance that the correlation is random.

Figure 4.17a verifies that there is consistent correlation between topography and the geoid for high degrees, for example, $l > 10$, and no consistent correlation for $l < 10$. The short wavelength geoid is mainly due to the topography, bathymetry variations (Haxby and Turcotte, 1978; Chase and McNutt, 1982; Richards and Hager, 1988). If the relationship $d\ln\rho/d\ln\beta = 0.4$ (Anderson *et al.*, 1968; Masters *et al.*, 1982; Woodhouse and Dziewonski, 1984) exists, the high degree of shallow-layer velocity variation should positively correlate with the topography. Figures 4.17b,c show that the correlation for high-degrees does not exist. This result made us choose density and S-wave velocity as independent parameters in the present study, although future study regarding this relationship is needed.

Figure 4.17, (a). The correlation between topography and geoid. The dashed lines are the confidence level, and the corresponding number of each level is shown in the upper right of the figure. (b). The correlation between topography and S-wave velocity at 38.3 km. (c). The correlation between topography and S-wave velocity at 110.0 km.

(a)

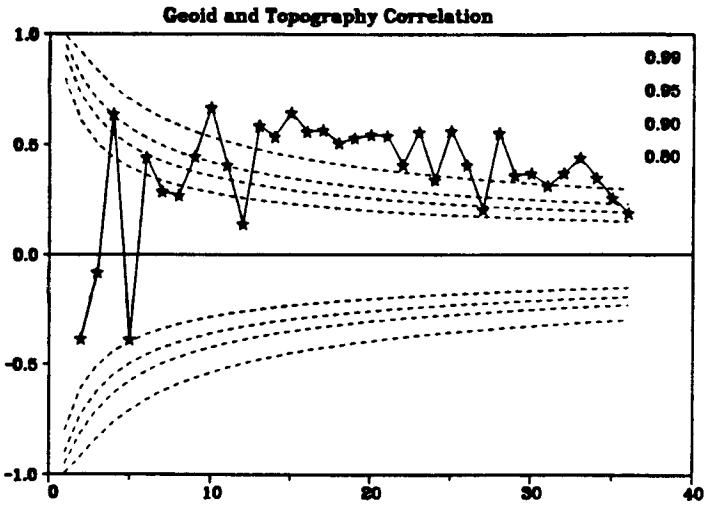
Geoid and Topography Correlation
0.99
0.95
0.90
0.80
1.0
0.5
0.0
-0.5
-1.0
0
10
20
30
40

(b)

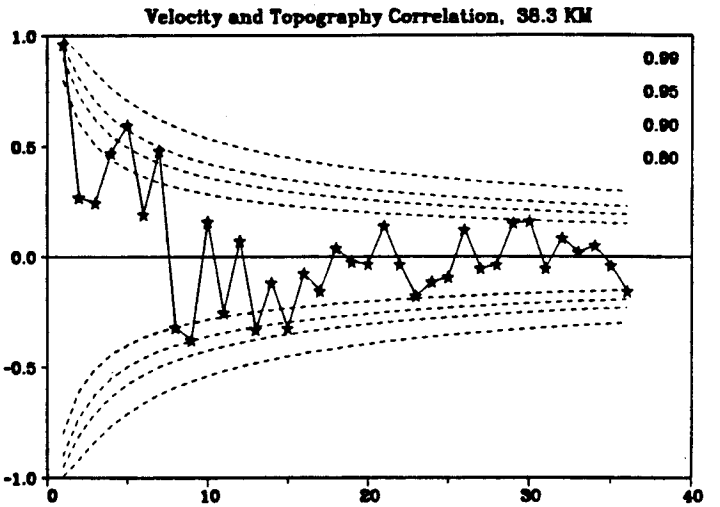
Velocity and Topography Correlation, 38.3 KM
0.99
0.95
0.90
0.80
1.0
0.5
0.0
-0.5
-1.0
0
10
20
30
40

(c)

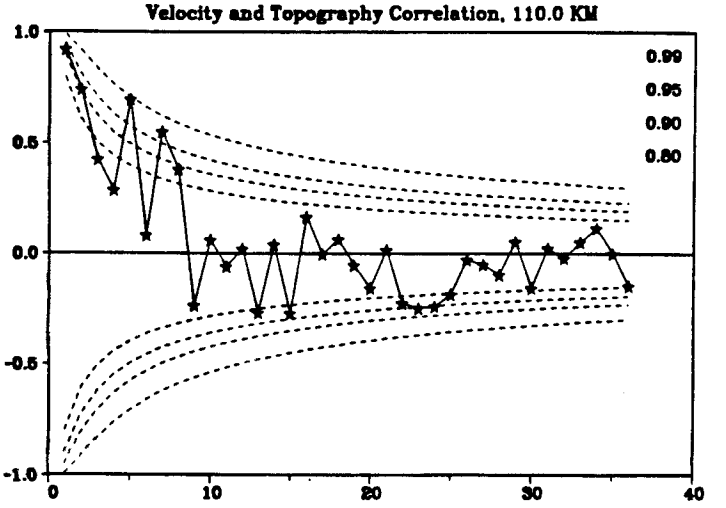
Velocity and Topography Correlation, 110.0 KM
0.99
0.95
0.90
0.80
1.0
0.5
0.0
-0.5
-1.0
0
10
20
30
40

Figures 4.18a-b show the fit of seismograms before and after the inversion for Love and Rayleigh waves, respectively. The events are at (-17.31, 289.35) and (-1.45, 126.76). The station is located at (44.55, 285.47) and (36.54, 59.65), respectively. In each case, the upper figure gives the data and synthetic seismogram for PREM (Dziewonski and Anderson, 1981), and the lower figure indicates the data and synthetic seismograms after the heterogeneity correction. In both examples, the waveform obtained after correction fits the observed seismograms much better than those before inversion.

Figure 4.18, (a). Fitting test of synthetic seismograms before and after inversion for Love waves. The thick line is the observed waveform, and the thin line is the calculated synthetic seismogram. The upper figure is before inversion and low layer is after inversion. (b). The same as Figure 4.18a, but for Rayleigh waves.

(a) Before Inversion /84/02/26/ G1, RSNY

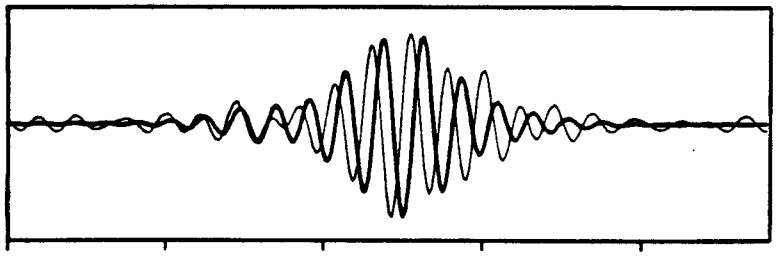

After Inversion /84/02/26/ G1, RSNY

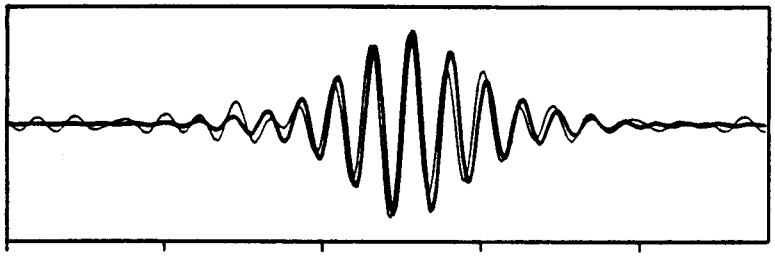

(b) Before Inversion /86/04/10/ R1, MAJO

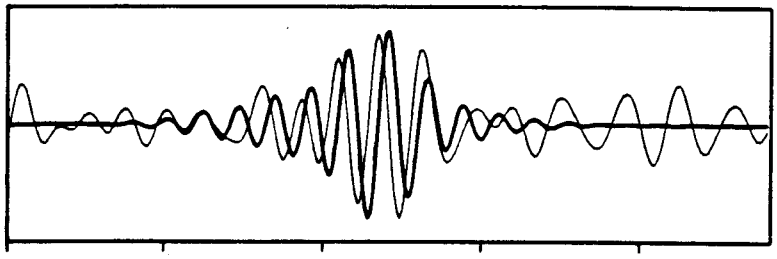

After Inversion /86/04/10/ R1, MAJO

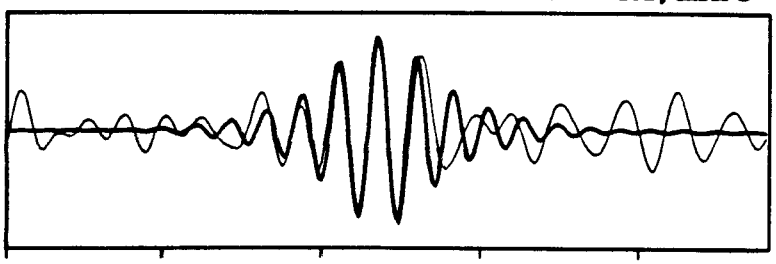

4.5 Summary

Using a large data set, 18,000 seismograms associated with 971 earthquakes ($M \geq 5.5$) for Love and Rayleigh waves between 1980 and 1987, global Love and Rayleigh wave phase velocities are analyzed, and the three-dimensional upper mantle model MS5.5 is constructed. The principal conclusions of this chapter are contained in the maps of heterogeneity for MS5.5. Fast velocities are centered on stable shields and older oceanic areas, and slow velocities are in younger oceans near ridges, tectonically active continental regions, back-arc basins, and subduction zones. Some of the major hotspots, such as the Iceland, Azores, Hawaii, Tristan de Cunha, Kerguelen and Afar were mapped as distinct low phase velocity anomalies. Some of the lower velocity regions are associated with triple-junctions.

The fast velocity anomalies under the Australian, Baltic, Canadian, and Siberian shields penetrate down to 400 km, but only about 200 km deep under other stable shields, which indicate differences between these shields. Ridges are associated with low velocity in the top 100 km, while the major hotspots are associated with the low velocity anomalies between 80-200 km. The difference between ridges and hotspots supports the idea that ridges are shallow, passive features, and the hotspots are connected with an active upwelling plume.

Comparison of our results with several previous studies at different scales, leads us to believe that most of previous studies are consistent and improve our understanding of the Earth. A number of consistency, reproducibility and comparison tests give us confidence that the present results are, indeed, a smoothed and detailed representation of three-dimensional earth structure in the upper mantle.

Appendix 4.1, Love and Rayleigh waves phase velocity inversion results without topography and Moho depth correction.

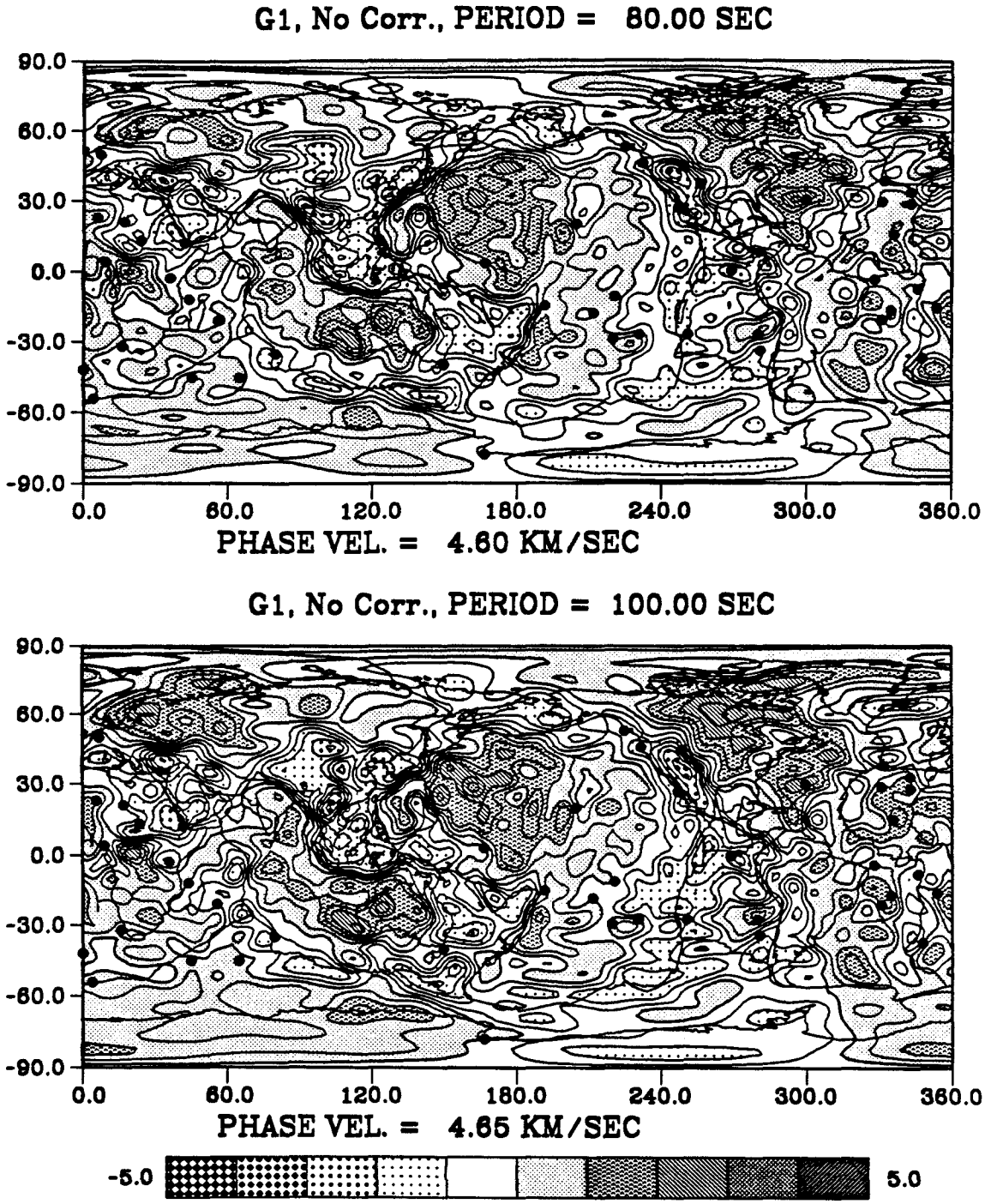
G1, No Corr., PERIOD = 80.00 SEC
90.0
60.0
30.0
0.0
-30.0
-60.0
-90.0
0.0
60.0
120.0
180.0
240.0
300.0
360.0
PHASE VEL. = 4.60 KM/SEC
G1, No Corr., PERIOD = 100.00 SEC
90.0
60.0
30.0
0.0
-30.0
-60.0
-90.0
0.0
60.0
120.0
180.0
240.0
300.0
360.0
PHASE VEL. = 4.65 KM/SEC
-5.0
5.0

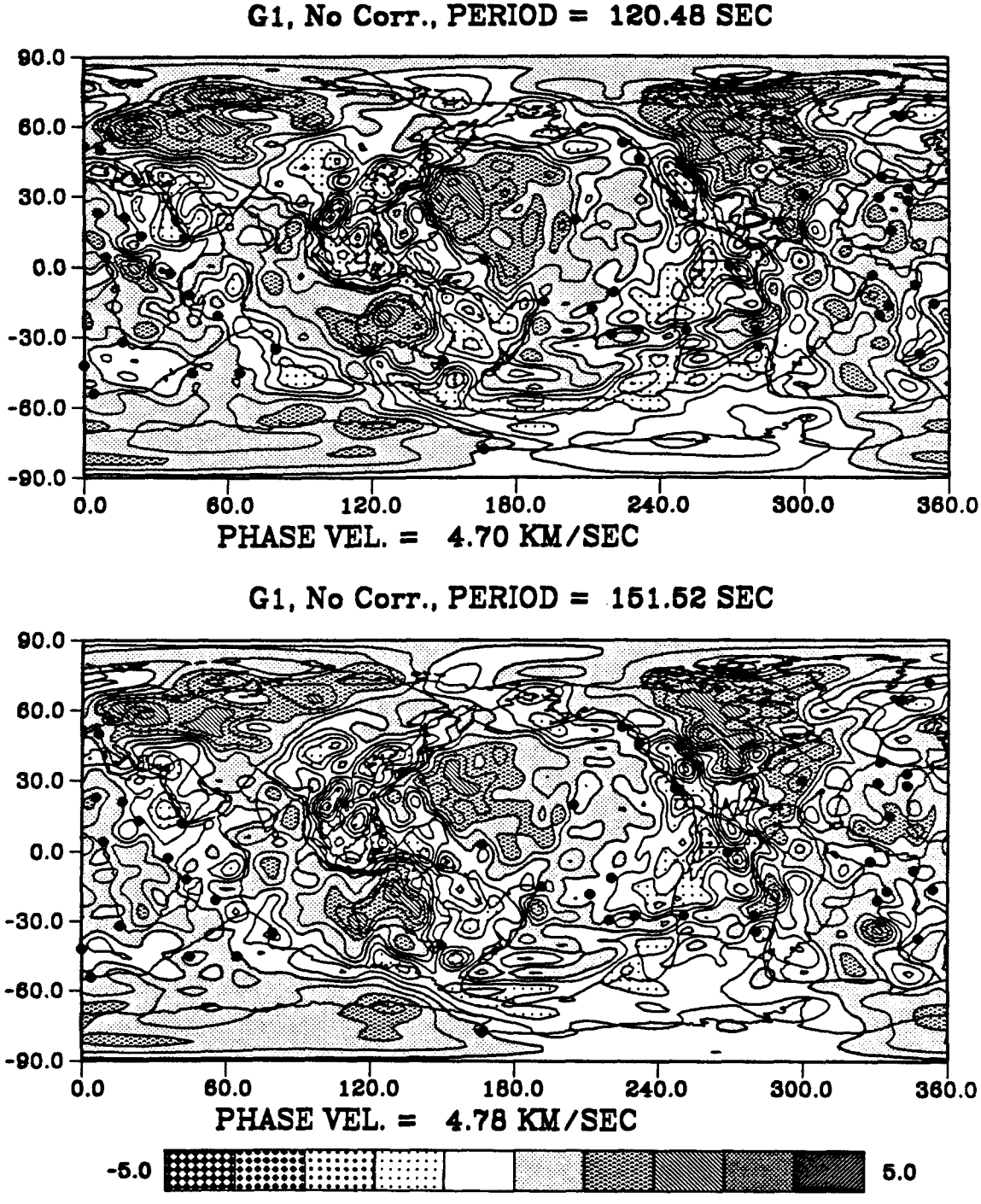
G1, No Corr., PERIOD = 120.48 SEC
90.0
60.0
30.0
0.0
-30.0
-60.0
-90.0
0.0
60.0
120.0
180.0
240.0
300.0
360.0
PHASE VEL. = 4.70 KM/SEC
G1, No Corr., PERIOD = 151.52 SEC
90.0
60.0
30.0
0.0
-30.0
-60.0
-90.0
0.0
60.0
120.0
180.0
240.0
300.0
360.0
PHASE VEL. = 4.78 KM/SEC
-5.0
5.0

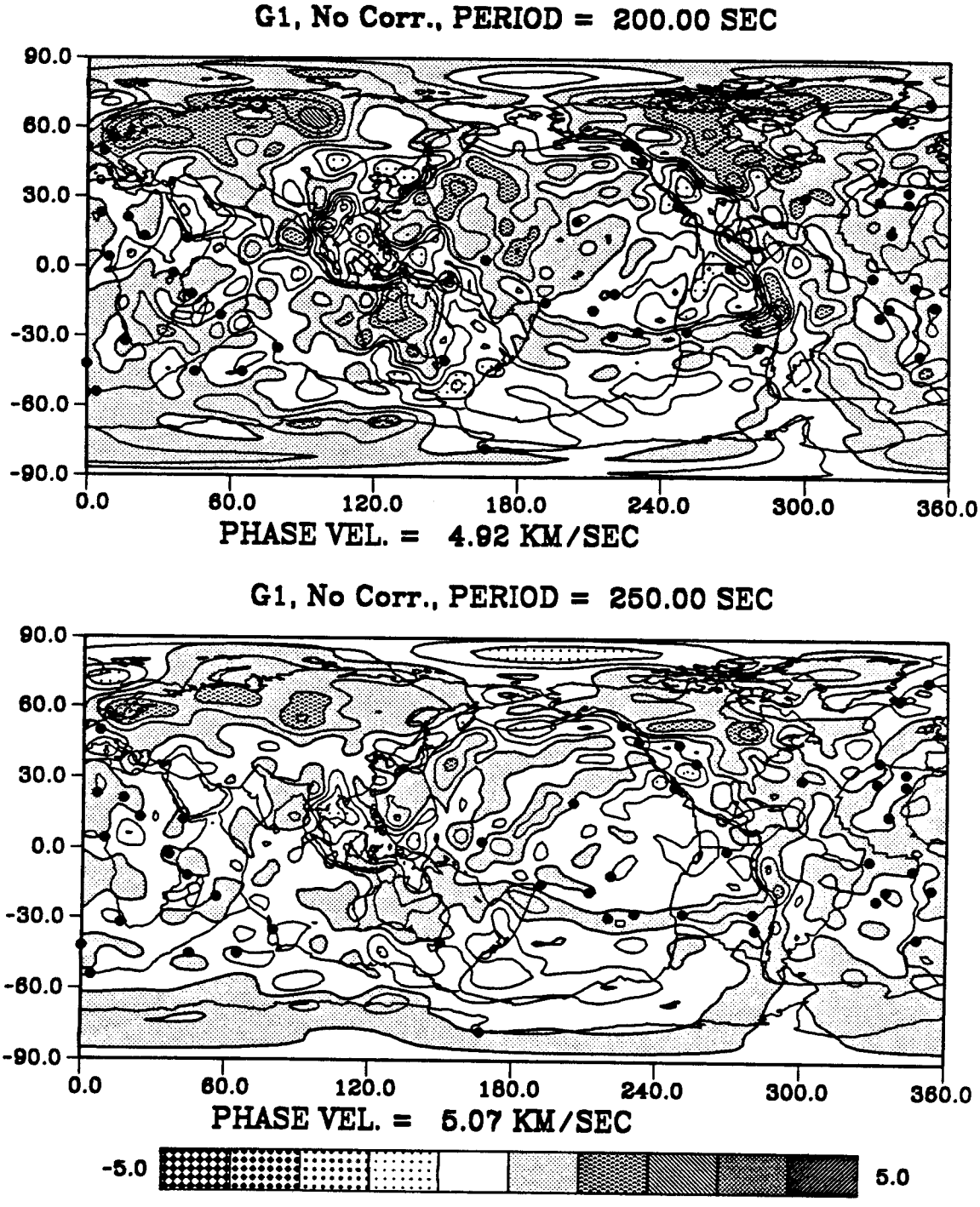
G1, No Corr., PERIOD = 200.00 SEC
90.0
60.0
30.0
0.0
-30.0
-60.0
-90.0
0.0
60.0
120.0
180.0
240.0
300.0
360.0
PHASE VEL. = 4.92 KM/SEC
G1, No Corr., PERIOD = 250.00 SEC
90.0
60.0
30.0
0.0
-30.0
-60.0
-90.0
0.0
60.0
120.0
180.0
240.0
300.0
360.0
PHASE VEL. = 5.07 KM/SEC
-5.0
5.0

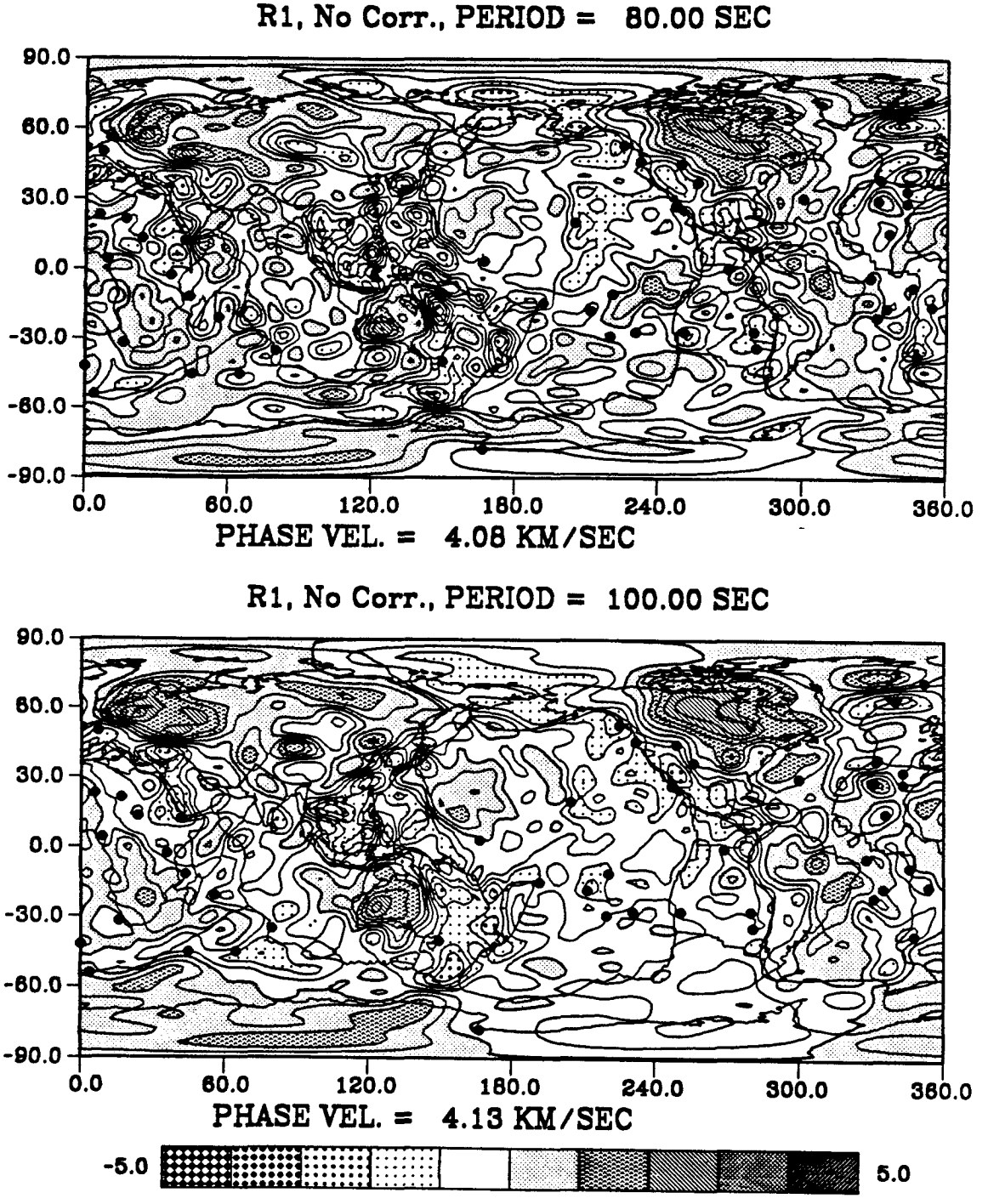
R1, No Corr., PERIOD = 80.00 SEC
90.0
60.0
30.0
0.0
-30.0
-60.0
-90.0
0.0
60.0
120.0
180.0
240.0
300.0
360.0
PHASE VEL. = 4.08 KM/SEC
R1, No Corr., PERIOD = 100.00 SEC
90.0
60.0
30.0
0.0
-30.0
-60.0
-90.0
0.0
60.0
120.0
180.0
240.0
300.0
360.0
PHASE VEL. = 4.13 KM/SEC
-5.0
5.0

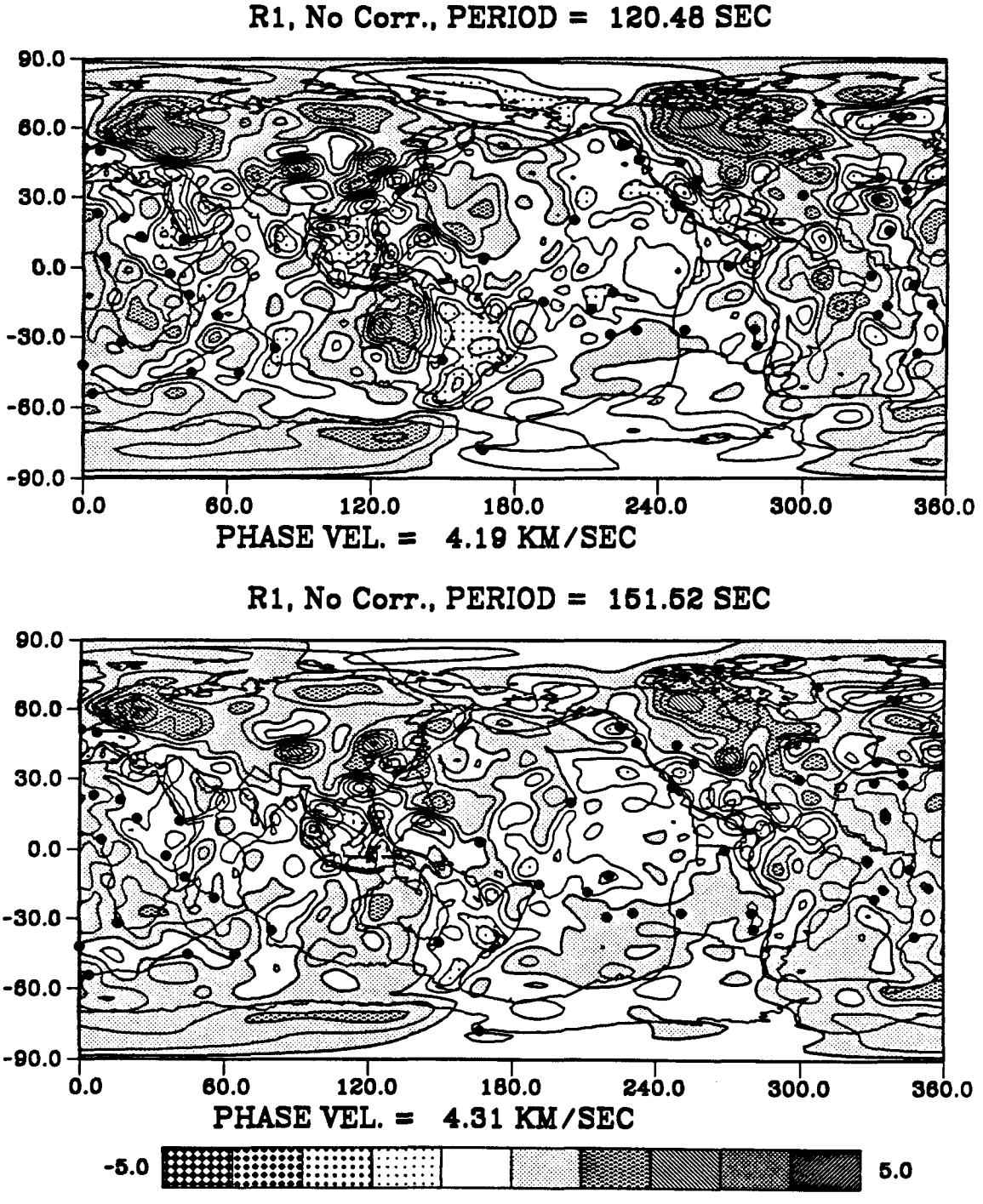
R1, No Corr., PERIOD = 120.48 SEC
90.0
60.0
30.0
0.0
-30.0
-60.0
-90.0
0.0
60.0
120.0
180.0
240.0
300.0
360.0
PHASE VEL. = 4.19 KM/SEC
R1, No Corr., PERIOD = 151.52 SEC
90.0
60.0
30.0
0.0
-30.0
-60.0
-90.0
0.0
60.0
120.0
180.0
240.0
300.0
360.0
PHASE VEL. = 4.31 KM/SEC
-5.0
5.0

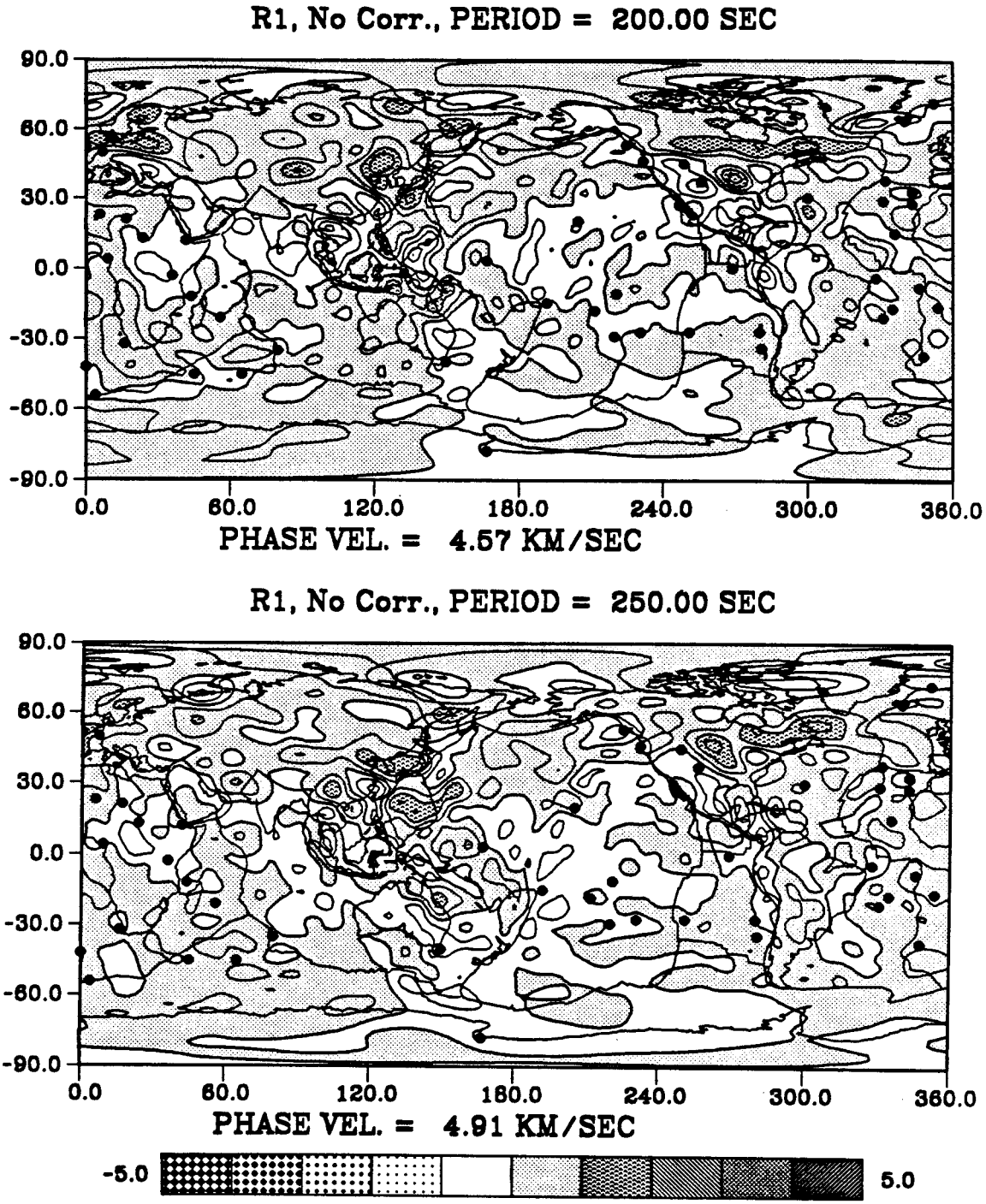
R1, No Corr., PERIOD = 200.00 SEC
90.0
60.0
30.0
0.0
-30.0
-60.0
-90.0
0.0
60.0
120.0
180.0
240.0
300.0
360.0
PHASE VEL. = 4.57 KM/SEC
R1, No Corr., PERIOD = 250.00 SEC
90.0
60.0
30.0
0.0
-30.0
-60.0
-90.0
0.0
60.0
120.0
180.0
240.0
300.0
360.0
PHASE VEL. = 4.91 KM/SEC
-5.0
5.0

Appendix 4.2, Love and Rayleigh waves phase velocity inversion results with topography and Moho depth correction.

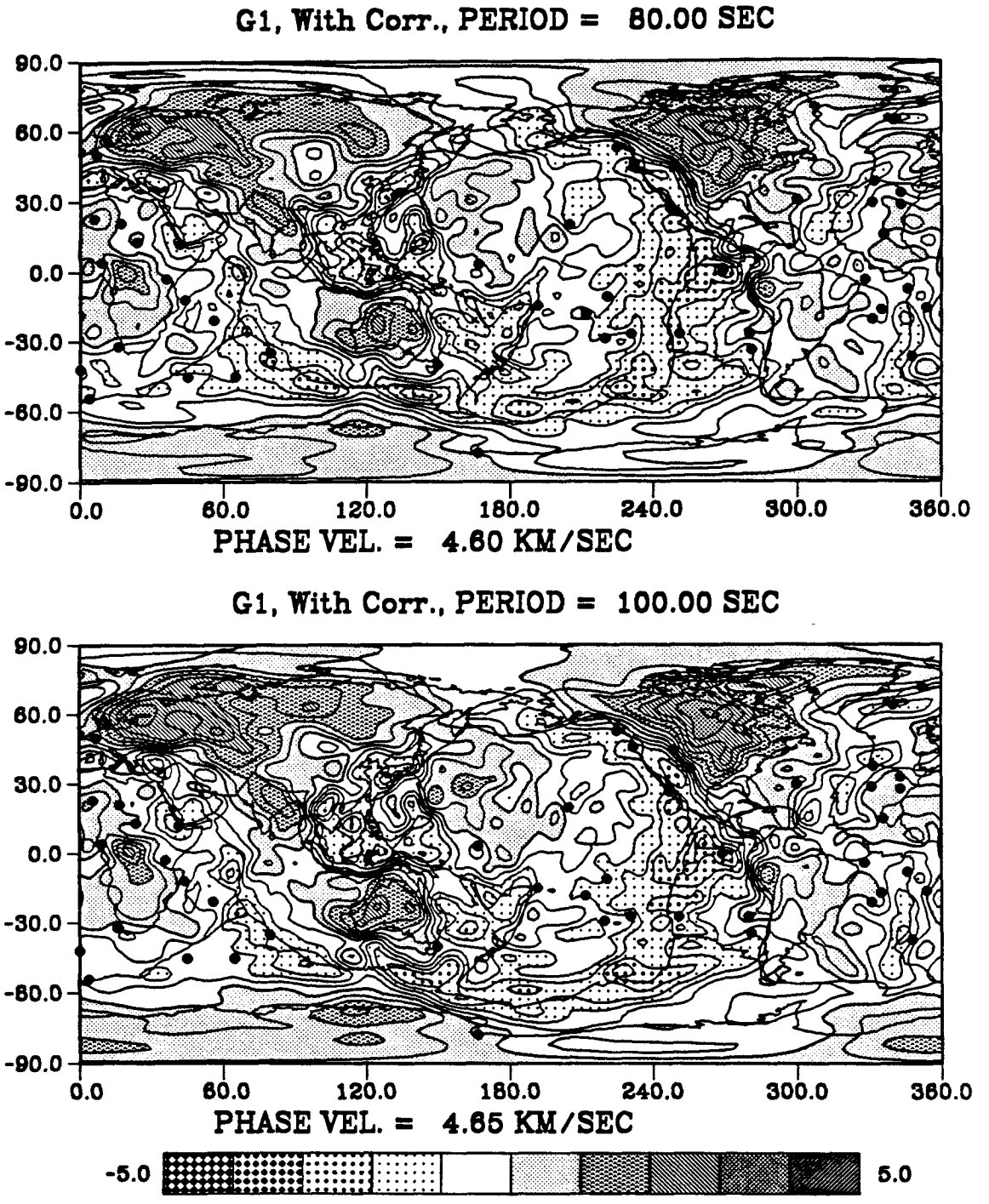
G1, With Corr., PERIOD = 80.00 SEC
90.0
60.0
30.0
0.0
-30.0
-60.0
-90.0
0.0
60.0
120.0
180.0
240.0
300.0
360.0
PHASE VEL. = 4.60 KM/SEC
G1, With Corr., PERIOD = 100.00 SEC
90.0
60.0
30.0
0.0
-30.0
-60.0
-90.0
0.0
60.0
120.0
180.0
240.0
300.0
360.0
PHASE VEL. = 4.65 KM/SEC
-5.0
5.0

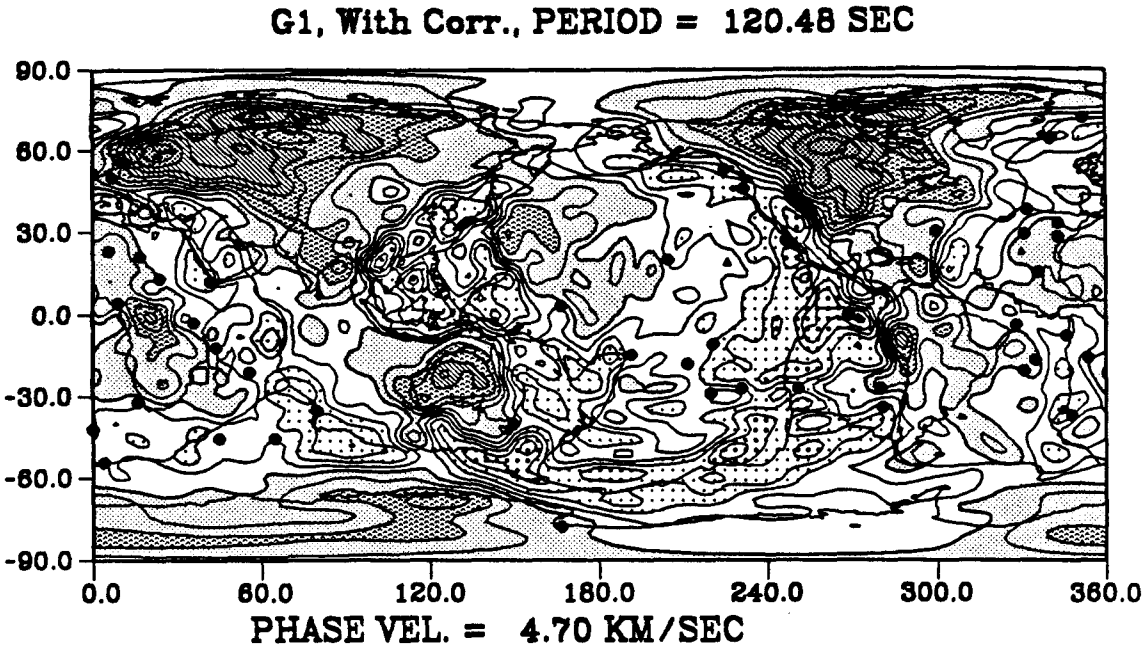
G1, With Corr., PERIOD = 120.48 SEC
90.0
60.0
30.0
0.0
-30.0
-60.0
-90.0
0.0
60.0
120.0
180.0
240.0
300.0
360.0
PHASE VEL. = 4.70 KM/SEC

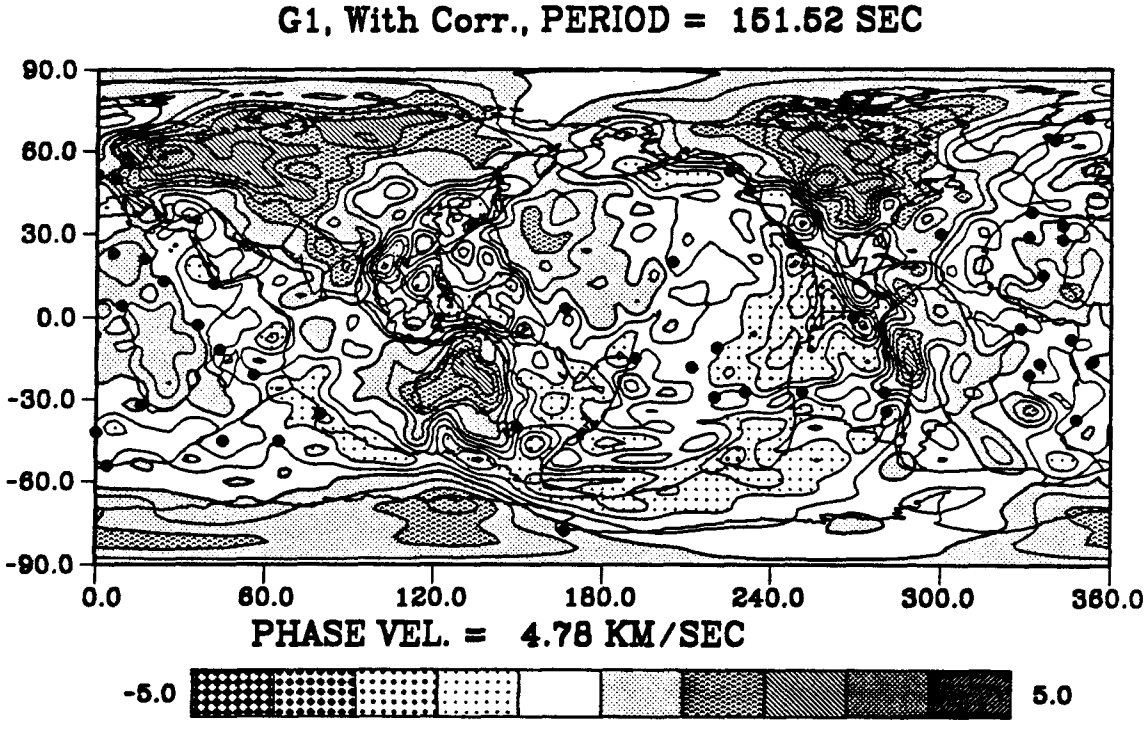
G1, With Corr., PERIOD = 151.52 SEC
90.0
60.0
30.0
0.0
-30.0
-60.0
-90.0
0.0
60.0
120.0
180.0
240.0
300.0
360.0
PHASE VEL. = 4.78 KM/SEC
-5.0
5.0

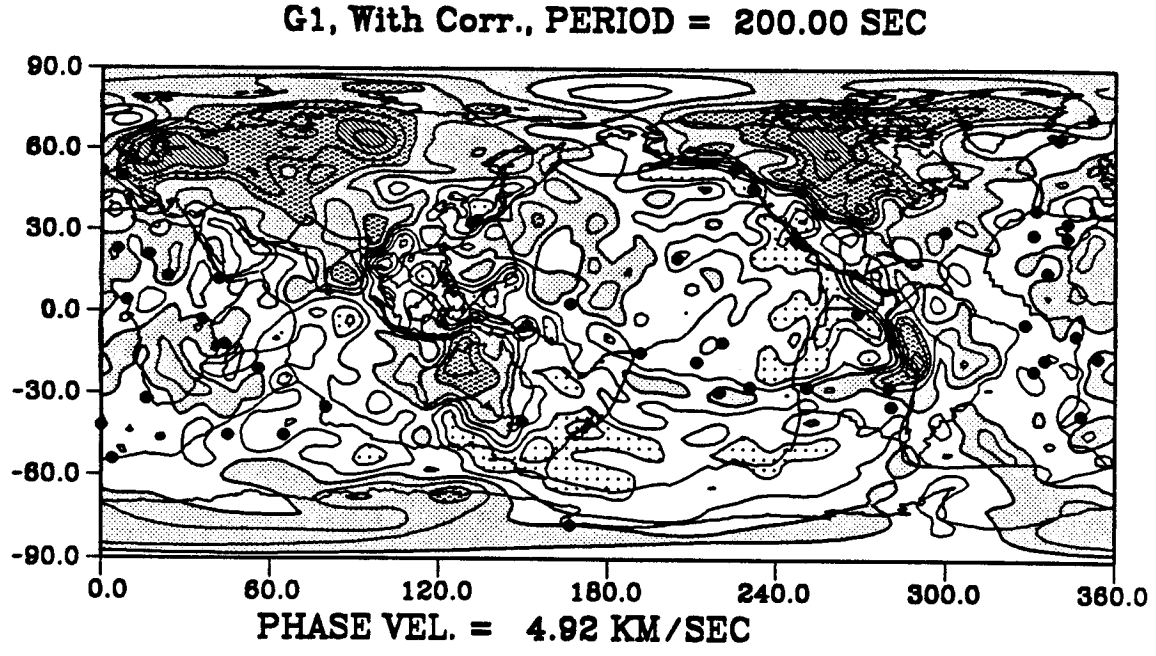
G1, With Corr., PERIOD = 200.00 SEC
90.0
60.0
30.0
0.0
-30.0
-60.0
-90.0
0.0
60.0
120.0
180.0
240.0
300.0
360.0
PHASE VEL. = 4.92 KM/SEC

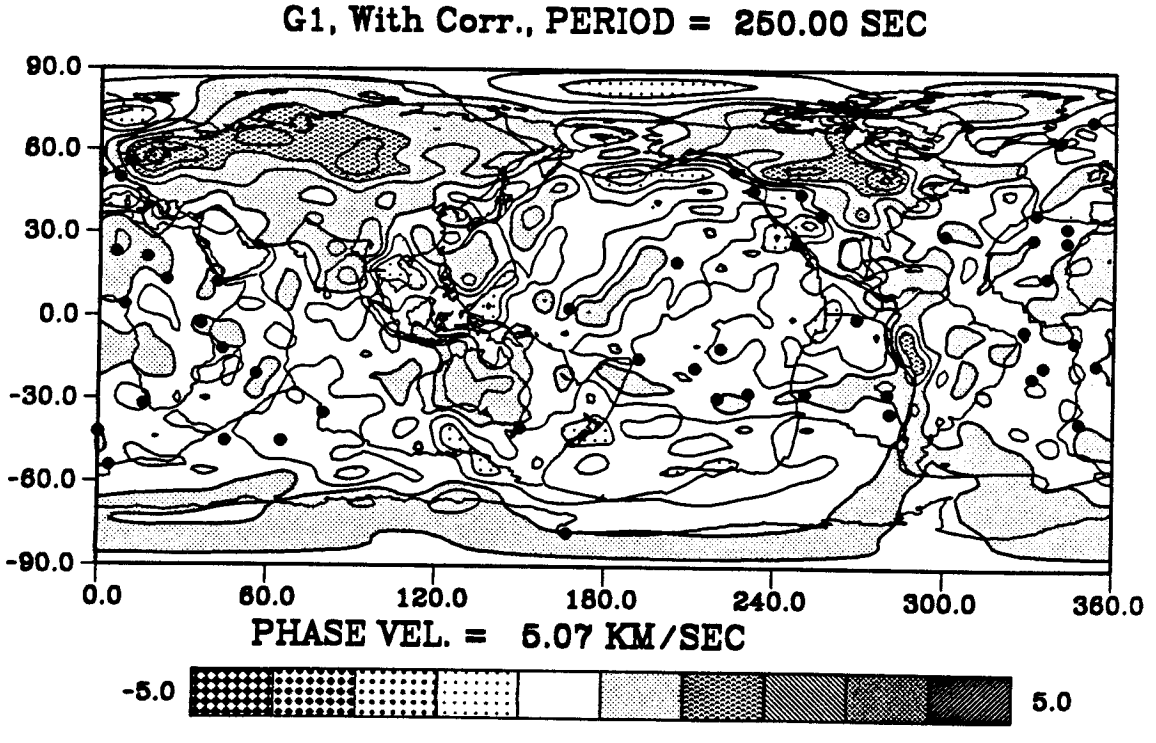
G1, With Corr., PERIOD = 250.00 SEC
90.0
60.0
30.0
0.0
-30.0
-60.0
-90.0
0.0
60.0
120.0
180.0
240.0
300.0
360.0
PHASE VEL. = 5.07 KM/SEC
-5.0
5.0

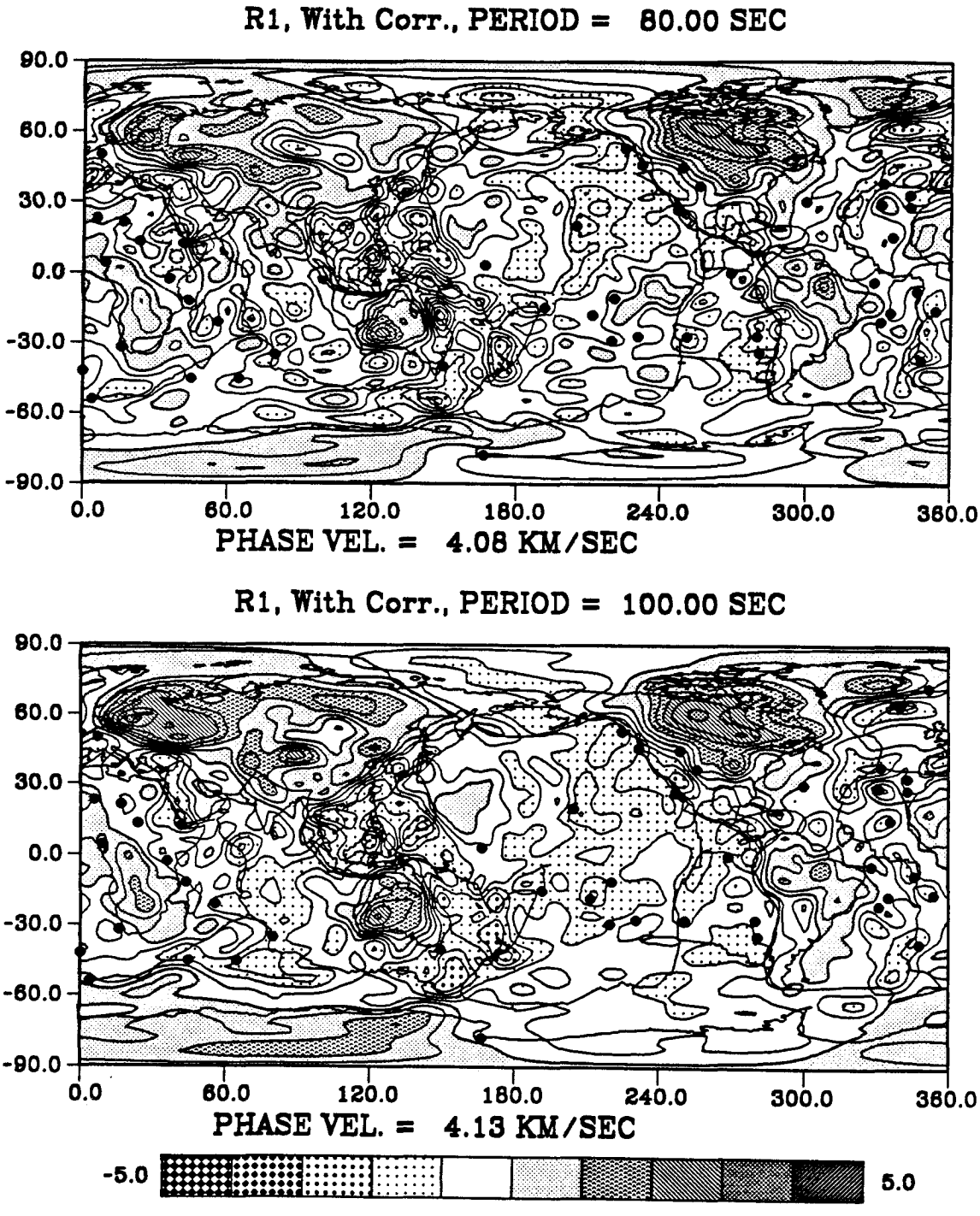
R1, With Corr., PERIOD = 80.00 SEC
90.0
60.0
30.0
0.0
-30.0
-60.0
-90.0
0.0
60.0
120.0
180.0
240.0
300.0
360.0
PHASE VEL. = 4.08 KM/SEC
R1, With Corr., PERIOD = 100.00 SEC
90.0
60.0
30.0
0.0
-30.0
-60.0
-90.0
0.0
60.0
120.0
180.0
240.0
300.0
360.0
PHASE VEL. = 4.13 KM/SEC
-5.0
5.0

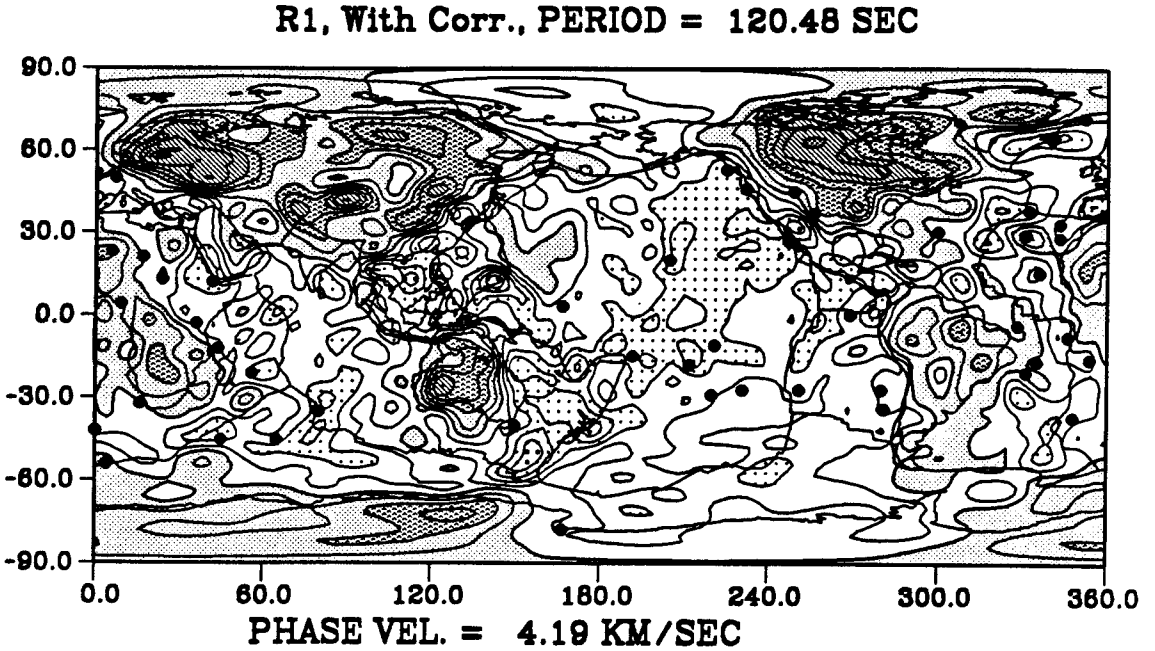
R1, With Corr., PERIOD = 120.48 SEC
90.0
60.0
30.0
0.0
-30.0
-60.0
-90.0
0.0
60.0
120.0
180.0
240.0
300.0
360.0
PHASE VEL. = 4.19 KM/SEC

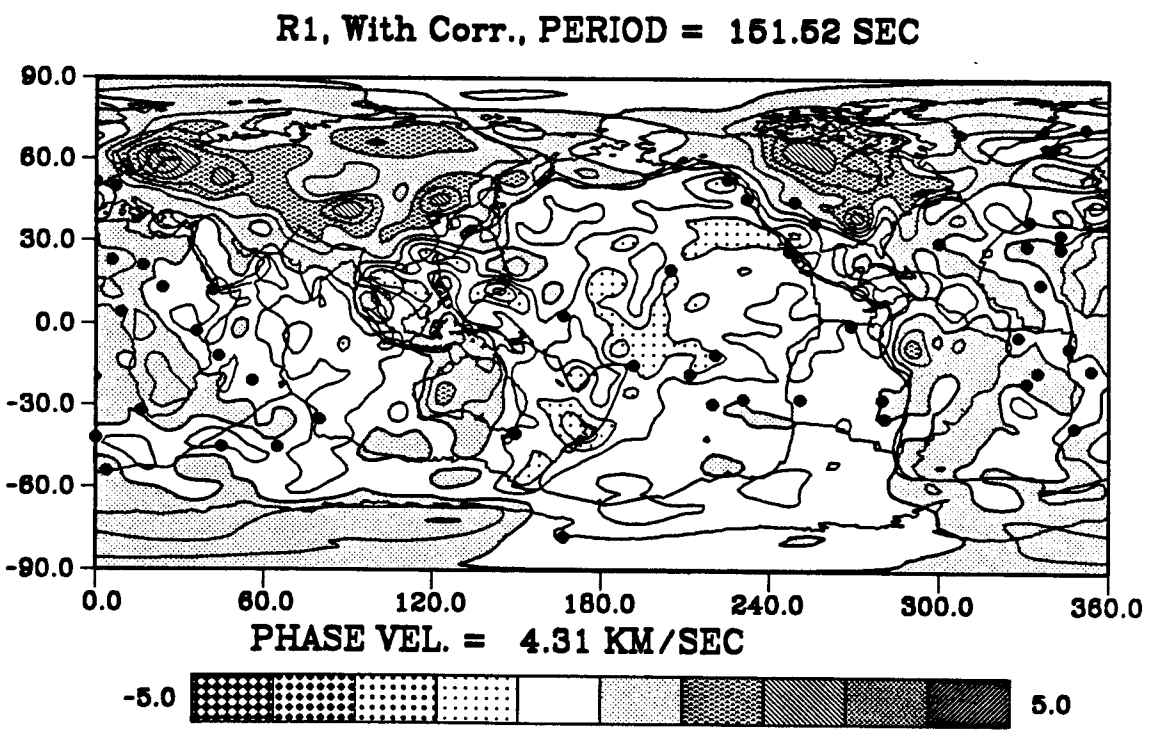
R1, With Corr., PERIOD = 151.52 SEC
90.0
60.0
30.0
0.0
-30.0
-60.0
-90.0
0.0
60.0
120.0
180.0
240.0
300.0
360.0
PHASE VEL. = 4.31 KM/SEC
-5.0
5.0

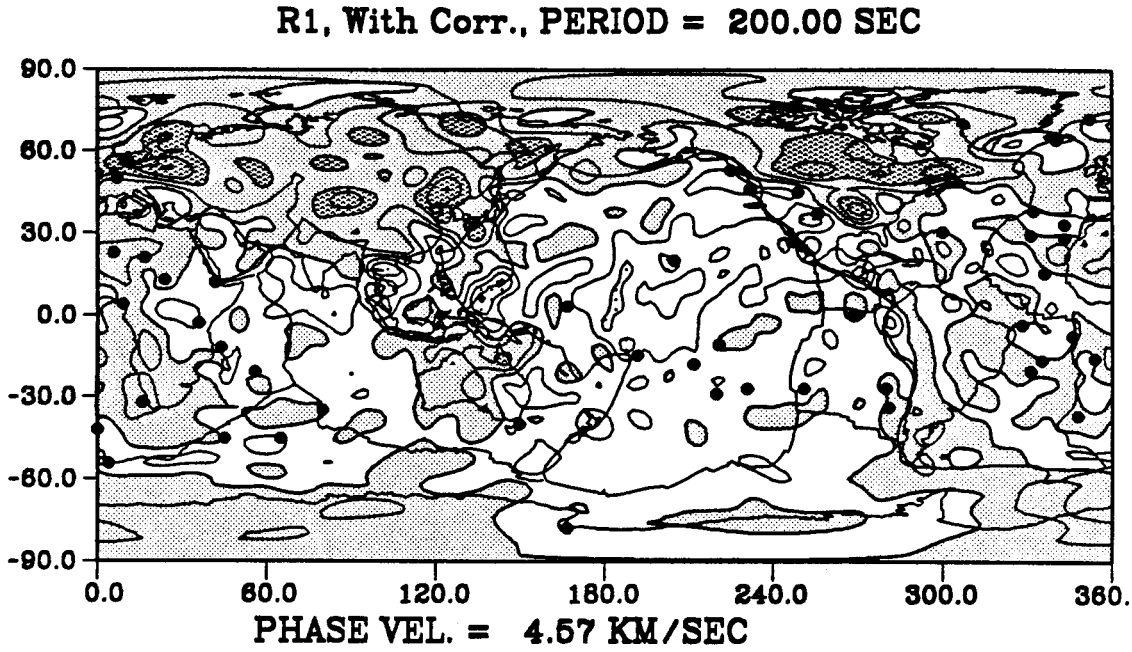
R1, With Corr., PERIOD = 200.00 SEC
90.0
60.0
30.0
0.0
-30.0
-60.0
-90.0
0.0
60.0
120.0
180.0
240.0
300.0
360.0
PHASE VEL. = 4.57 KM/SEC

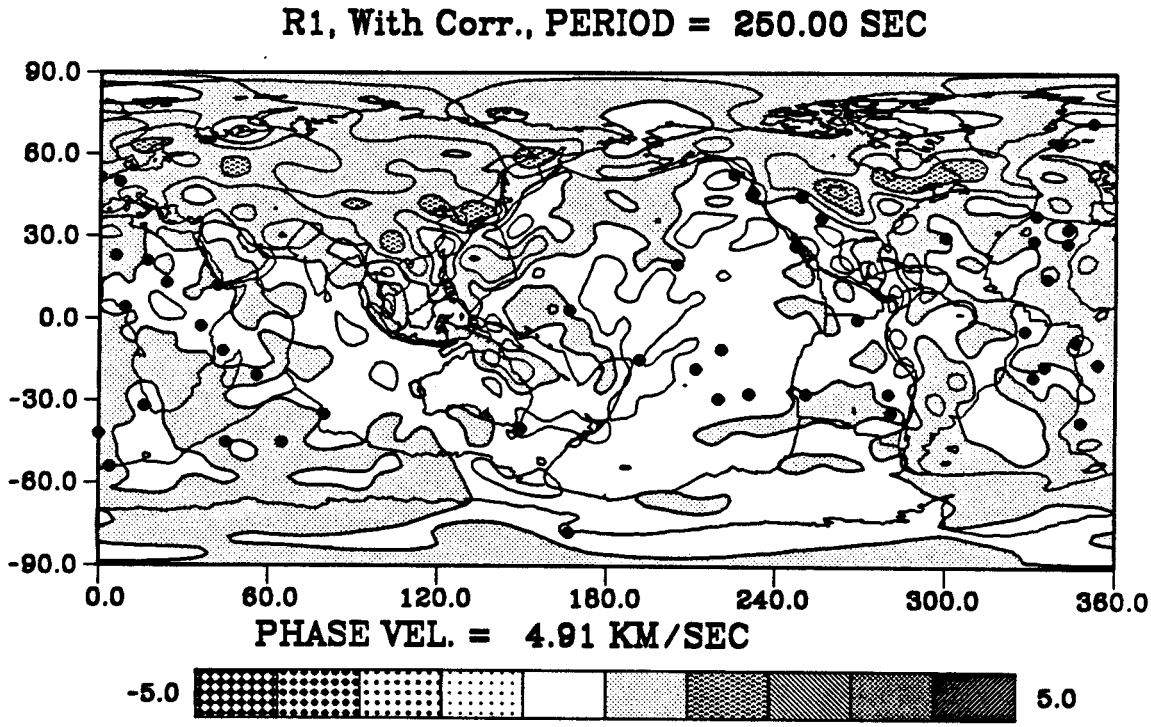
R1, With Corr., PERIOD = 250.00 SEC
90.0
60.0
30.0
0.0
-30.0
-60.0
-90.0
0.0
60.0
120.0
180.0
240.0
300.0
360.0
PHASE VEL. = 4.91 KM/SEC
-5.0
5.0

Chapter 5

Oceanic Lithosphere

5.1 Introduction

The establishment of the theory of plate tectonics in the late 1960s has improved our understanding of the Earth. The most widely accepted oceanic plate model can be summarized as follows: Adjacent plates seperate, hot mantle ascends and generates new lithosphere at a midocean ridge; the plates cool, subside and thicken as they move away from the ridge; and the lithosphere approximates to a stable state at 60 - 80 Ma (*e.g.*, Parsons and McKenzie, 1978; Sclater *et al.*, 1980, Turcotte and Schubert, 1982). This model has been examined by heat flow and bathymetry data (Parsons and Sclater, 1977; Lister, 1977; Sclater and Wixon, 1986; Renkin and Sclater, 1988), and also by seismological data (Leeds *et al.*, 1974; Forsyth, 1975; Yoshii, 1975; Mitchell and Yu, 1980; Regan and Anderson, 1984). Because of the limitations of seismic station distribution, previous seismic studies are constrained to restricted areas. There is no systematic seismic study examining all oceanic data in a uniform manner. One of the aims of this chapter is to reexamine this model in light of our new phase velocity results. Our results, perhaps for the first time, allow us to

perform a systematic analysis, since all oceanic results are obtained simultaneously in global inversion.

Average phase velocities are obtained every 10 million years along oceanic plates; then the age-Love wave phase velocity relations for the Pacific, Atlantic and Indian Oceans are established separately. One of the features for different oceans is that the phase velocity shows a smooth increase with plate age up to about 150 Ma, disagreeing with previous ocean depth and heat flow data, which exhibit slope changes at about 60-80 and 90-100 million years (Parsons and Sclater, 1977; Renkin and Sclater,1988), respectively. Another important feature is that the age-phase velocity relation is different from one ocean to another, suggesting a violation of the universal scaling law derived in previous studies (Turcotte and Oxburgh, 1967; Parker and Oldenburg, 1973).

Weissel and Hayes (1971) found asymmetric spreading along the South-East Indian Ocean Ridge, but other ridges, such as the East Pacific Rise and Mid-Atlantic Ridge, are thought to exhibit symmetric spreading (*e.g.*, Minster and Jordan, 1978; Vogt, 1986). A recent study by Hayes (1988) indicated asymmetric subsidence in the southeast Indian Ocean and the south Atlantic Ocean. In order to understand the differences on either side of ridges, we have also examined the age-phase velocity relations on both sides, and found asymmetric velocity variations. There are probably a wide variety of differences in the thermal state of the lithosphere, resulting perhaps in different lithosphere thickening rates.

As we know, there are prominent features that cannot be directly explained by plate tectonics, for example, hotspots and thermal anomalies (Morgan, 1972; Detrick and Crough, 1978; Crough, 1983; Smith *et al.*, 1989). Parsons and McKenzie (1978) suggested that the development of secondary

small scale convection below the lithosphere causes the oceanic plate thickness to remain constant after 60-80 Ma. On the other hand, Heestand and Crough (1981) and Schroeder (1984) argued that the flattening of the ocean floor depth with age is the effect of hotspot swell on old ocean floor. In order to understand mantle heterogeneity which is unrelated to plates, we subtracted the average age-phase velocity relations from phase velocity maps and produced "residual" maps. In these "residual" maps, we find large-scale low velocity anomalies in the south Pacific, the so-called "superswell region" (Smith *et al.*, 1989; McNutt and Judge, 1990), and in southern parts of the Indian Ocean; high velocity anomalies east of the East Pacific Rise, and in the northeastern Indian Ocean.

In Section 5.2, we describe the continuous thickening of oceanic lithosphere beyond 100 Ma in three oceans. The failure of scaling laws from the thermal boundary layer model is discussed in Section 5.3. In Section 5.4, the asymmetric thickening on different sides of the ridges is analyzed. The "residual" of Love wave phase velocity maps and thermal anomalies under the oceanic plate are described in Sections 5.5 and 5.6, respectively. The main conclusions are given in Section 5.7.

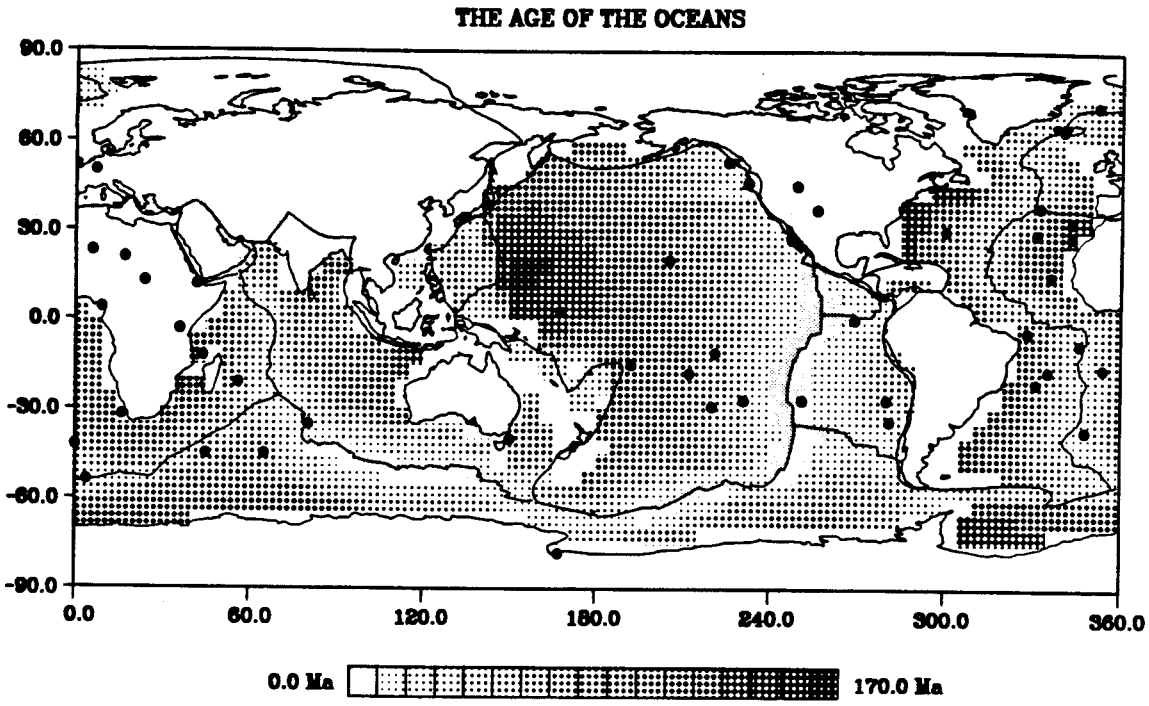

Figure 5.1, The age of the oceans. Original values are come from Sclater et al. (1981). The correction is also applied based on the resolution at each location.

Figure 5.2, (a). Velocity distributions in the Pacific Ocean for periods from 80 s to 200 s. (b). Velocity distributions in the Atlantic Ocean for periods from 80 s to 200 s. (c). Velocity distributions in the Indian Ocean for periods from 80 s to 200 s.

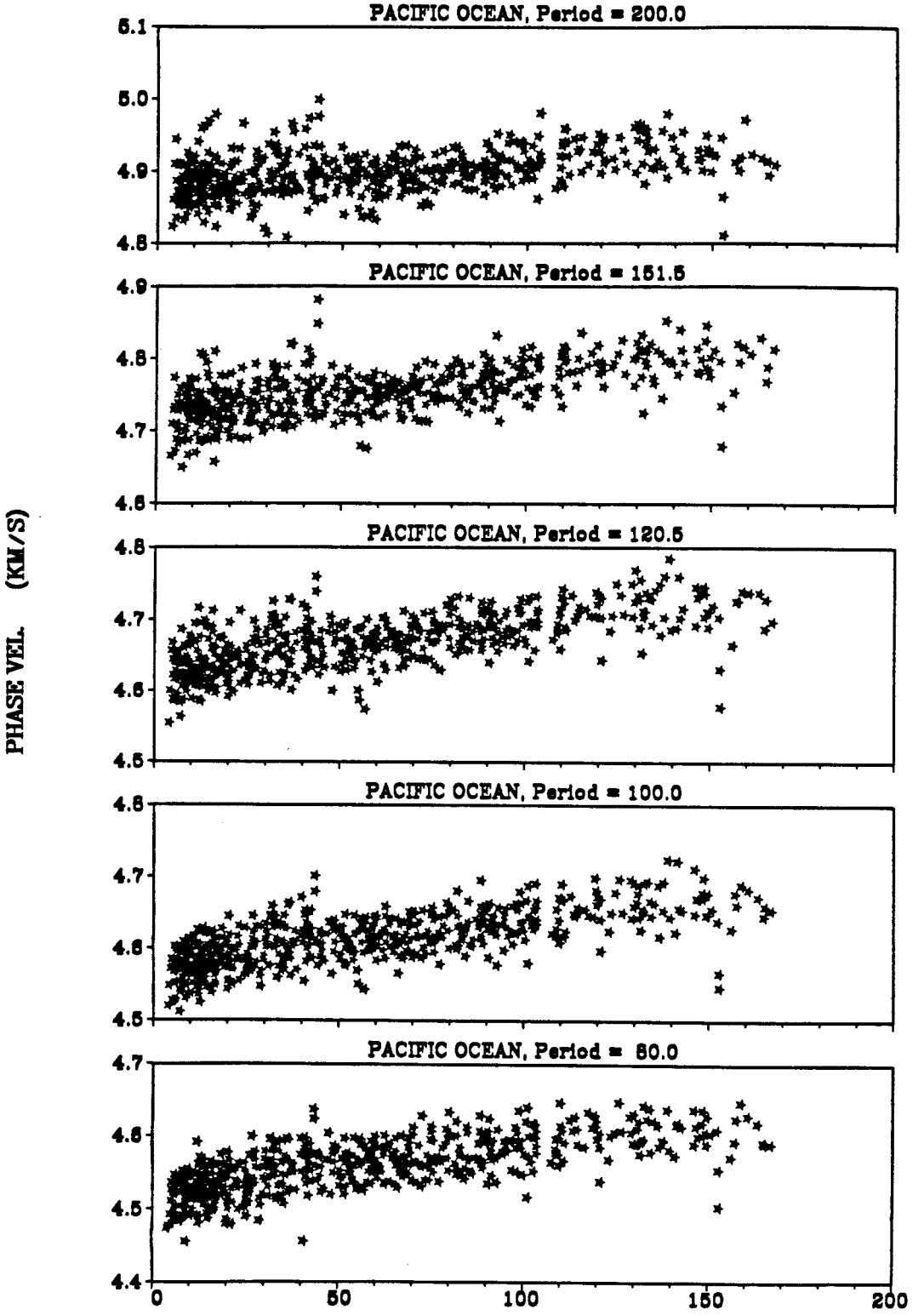
PACIFIC OCEAN, Period = 200.0
PACIFIC OCEAN, Period = 151.5
PACIFIC OCEAN, Period = 120.5
PACIFIC OCEAN, Period = 100.0
PACIFIC OCEAN, Period = 80.0
PHASE VEL. (KM/S)
AGE (Ma)
0
50
100
150
200

(a)

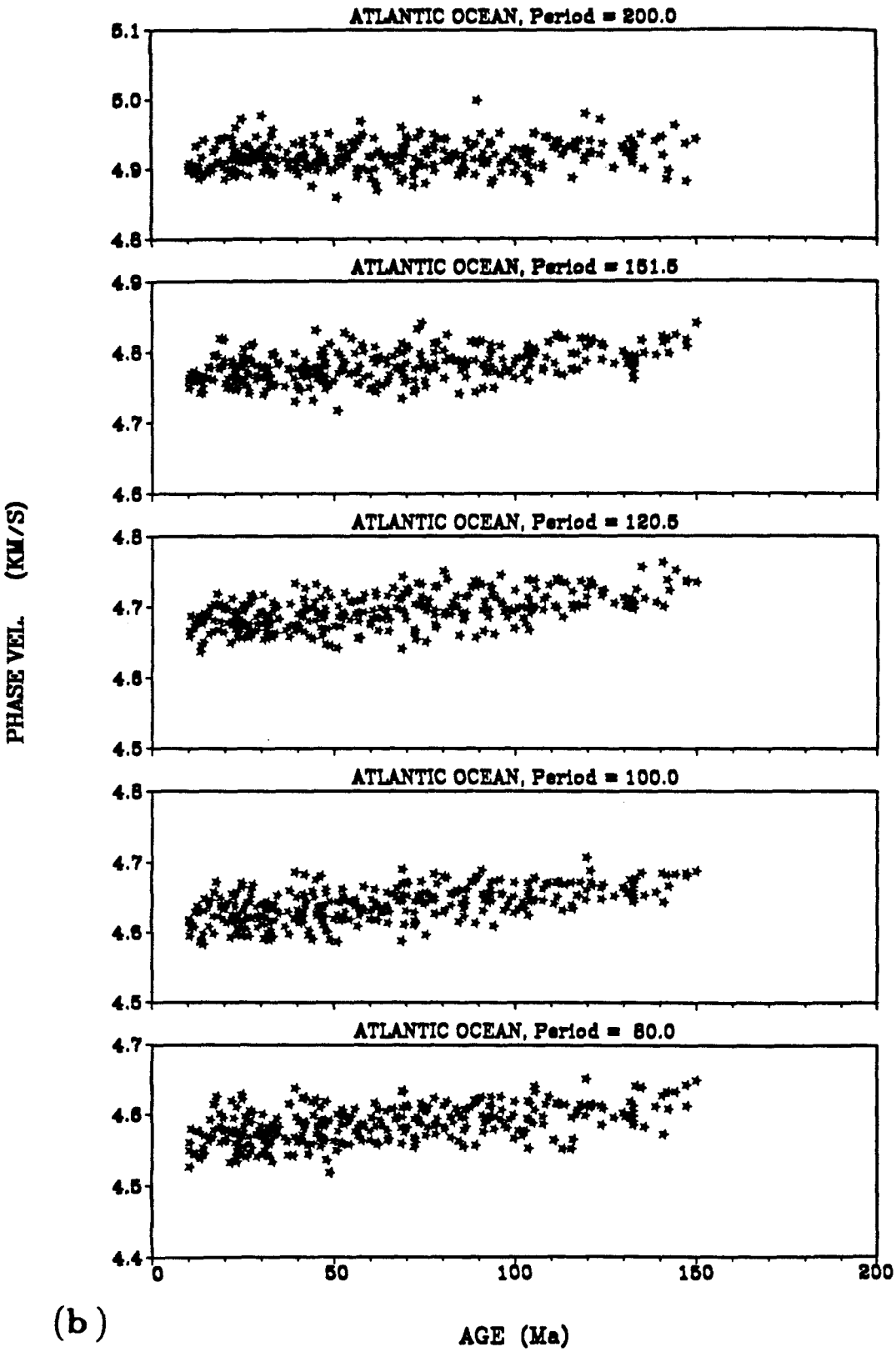
ATLANTIC OCEAN, Period = 200.0
ATLANTIC OCEAN, Period = 151.5
ATLANTIC OCEAN, Period = 120.5
ATLANTIC OCEAN, Period = 100.0
ATLANTIC OCEAN, Period = 80.0
PHASE VEL. (KM/S)
AGE (Ma)
0
50
100
150
200

(b)

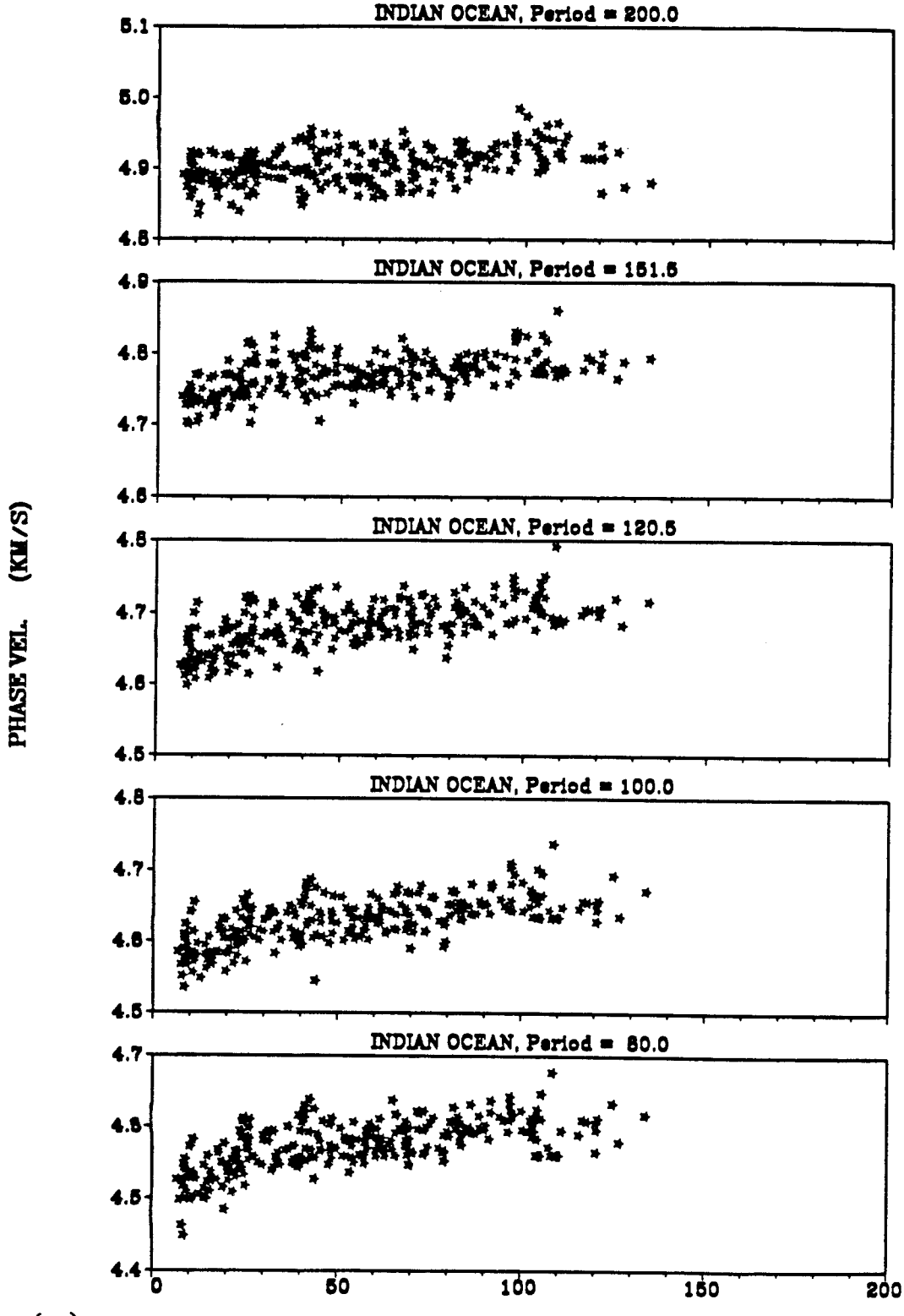
INDIAN OCEAN, Period = 200.0
INDIAN OCEAN, Period = 151.5
INDIAN OCEAN, Period = 120.5
INDIAN OCEAN, Period = 100.0
INDIAN OCEAN, Period = 80.0
PHASE VEL. (KM/S)
AGE (Ma)
0
50
100
150
200

(c)

5.2 Continuous thickening of oceanic lithosphere

Using the age map of Sclater *et al.* (1981), we assigned an age to each 5 degrees by 5 degrees block in the Pacific, Atlantic and Indian oceans. We also corrected the age map based on the resolution kernel at each block, because the obtained phase velocity result at one block contains not only the contribution from that block (see Figure 4.4 resolution kernel), but also some contributions from adjacent blocks. The oceanic age map thus obtained is presented in Figure 5.1; continental areas were not examined. The age versus phase velocity distributions for different periods and oceans are plotted in Figures 5.2a, 5.2b and 5.2c, which are based on the age map and the velocity variation maps in Appendix 4.2. There is some scatter in the data, but the increase of phase velocity with age is apparent.

The average phase velocities at ten million year intervals were calculated and plotted in Figures 5.3a, 5.3b, and 5.3c. One standard deviation was also shown in the figures. The number in parentheses at the bottom of Figures 5.3a-c is the number of blocks for a given age interval. A smooth increase of phase velocity to plates older than 100 Ma are shown in Figures 5.3a-c. The corresponding values are given in Table 5.1. In the conventional model, plates are believed to cool, subside and thicken during the first 60-80 Ma, but the development of secondary small scale convection (Parsons and McKenzie, 1978) or viscous shear stress heating (Schubert *et al.*, 1976) below the lithosphere causes plate thickness to remain constant (*e.g.*, Sclater *et al.*, 1980; Sclater and Wixson, 1986). On the contrary, our results indicate a smooth increase of surface wave phase velocity for all oceans from ridges to older than 100 Ma.

Figure 5.3, (a). Average phase velocity at every ten million year intervals with one standard deviation for the Pacific Ocean. The number in brackets at bottom is the number of blocks for a given age interval. Solid lines are theoretical phase velocity curves for a model that has increased lithosphere thickness with age t by $h = A + B\sqrt{t}$, where thickness h is in kilometers and t is in million years. The values of a and b are listed in Table 5.2. (b). Same as Fig. 5.3a but for the Atlantic Ocean. (c). Same as Fig. 5.3a but for the Indian Ocean.

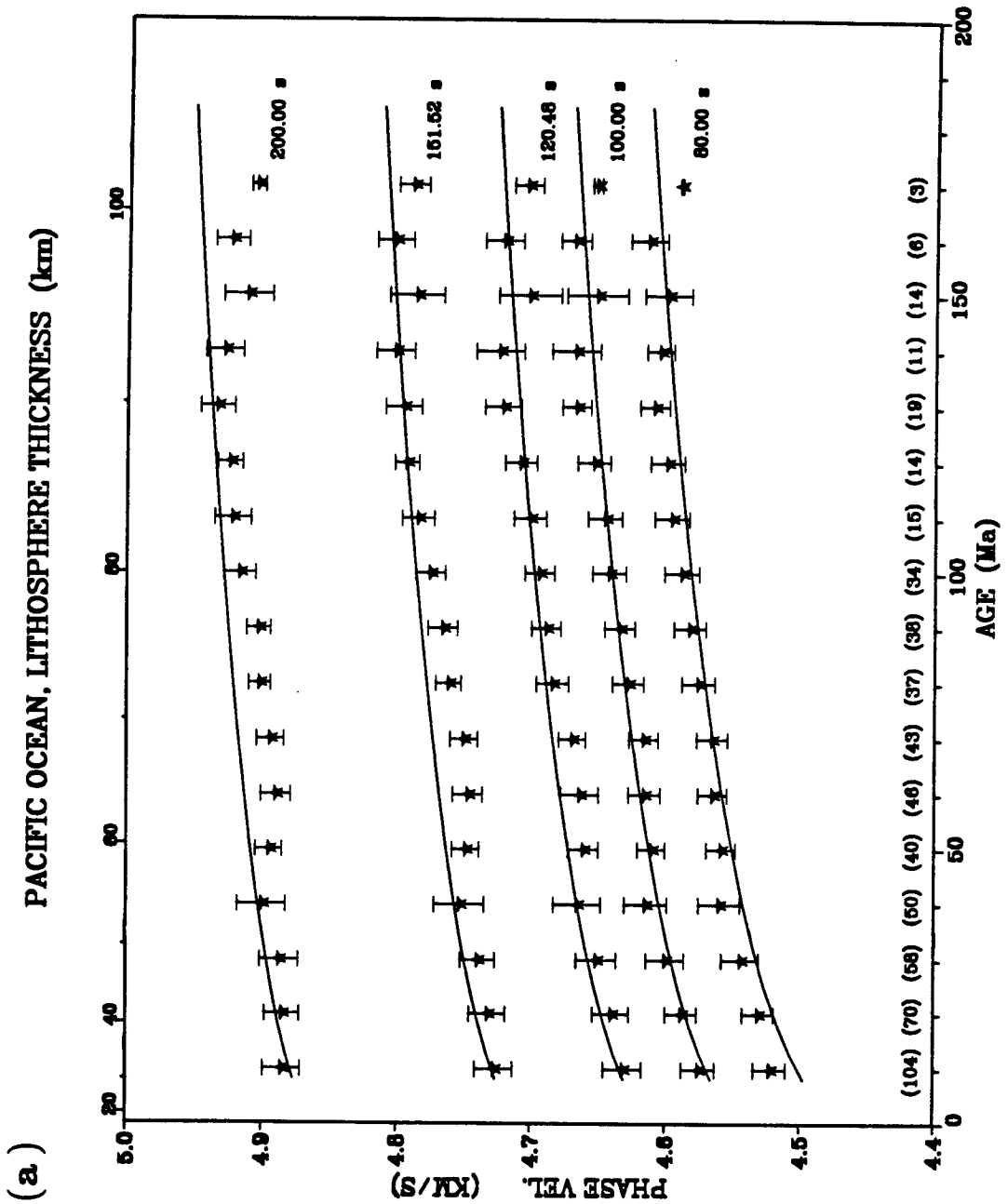
(a)
PACIFIC OCEAN, LITHOSPHERE THICKNESS (km)
200.00
161.62
120.48
100.00
80.00
PHASE VEL. (KM/S)
AGE (Ma)
(104) (70) (58) (50) (40) (46) (43) (37) (38) (34) (16) (14) (19) (11) (14) (6) (3)

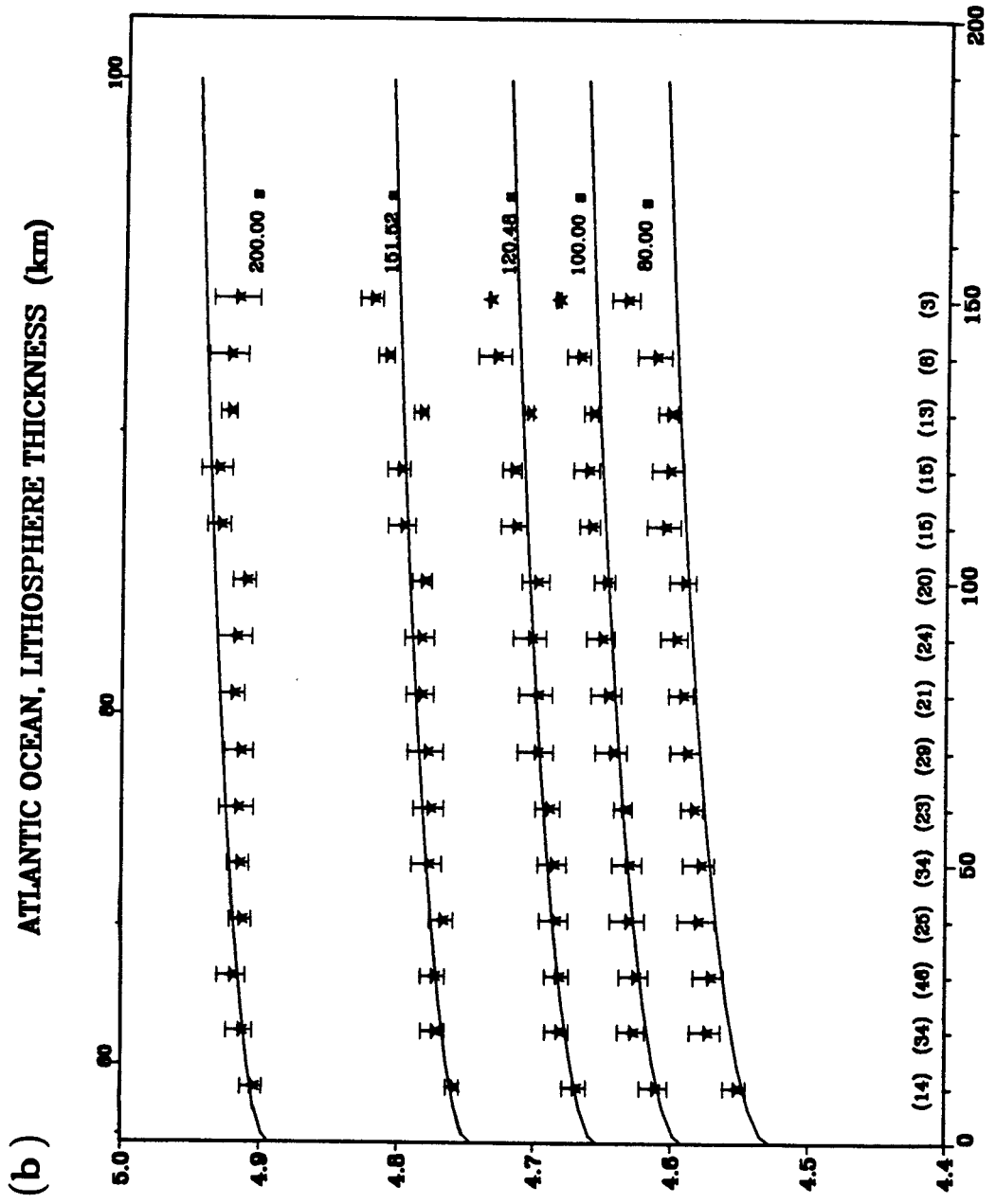
(b) ATLANTIC OCEAN, LITHOSPHERE THICKNESS (km)
200.00 m
161.62 m
120.48 m
100.00 m
80.00 m
(14) (34) (46) (26) (34) (23) (29) (21) (24) (20) (15) (15) (13) (8) (3)
5.0
4.9
4.8
4.7
4.6
4.5
4.4
60
80
100
0
50
100
150
200

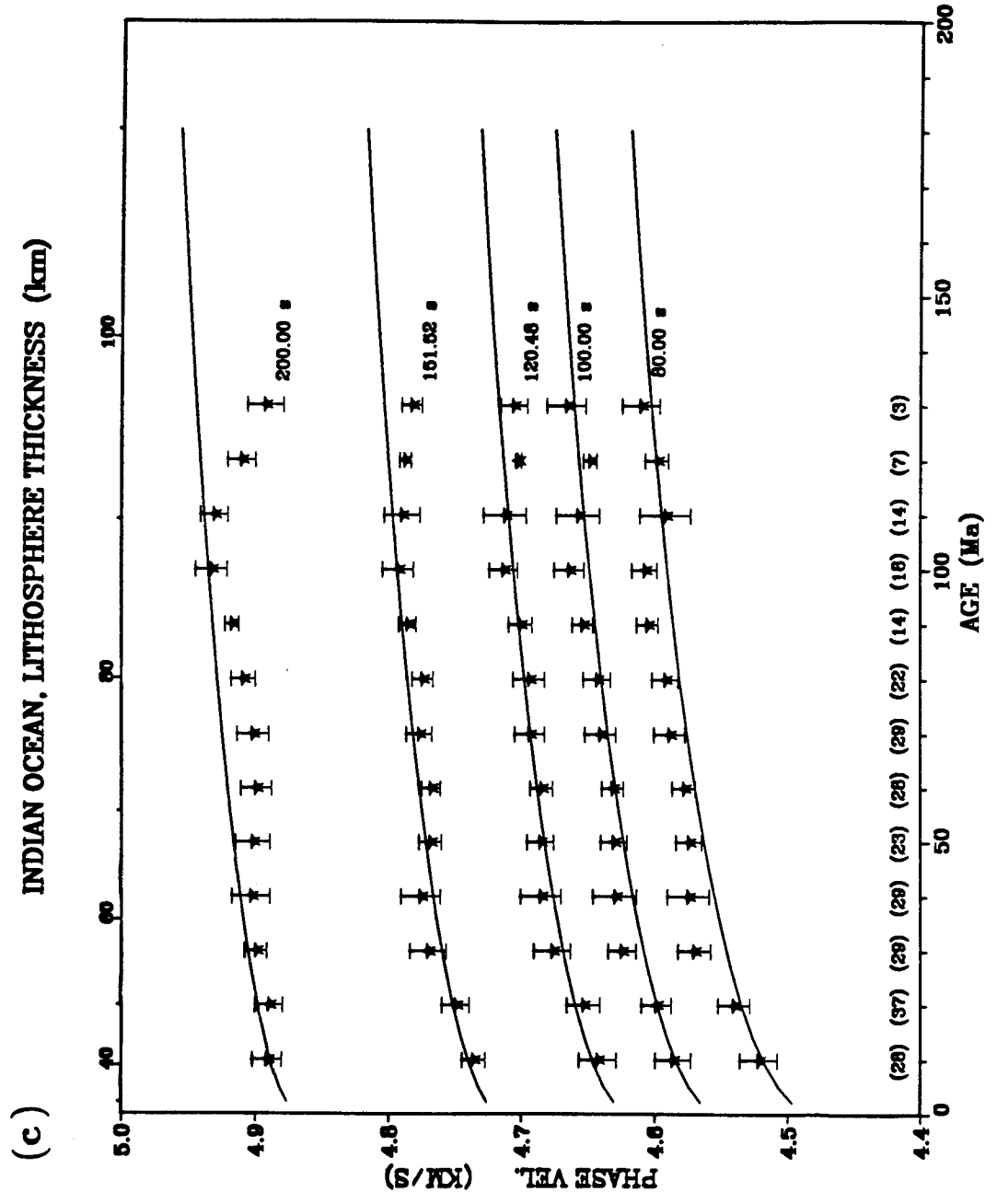
(c)
INDIAN OCEAN, LITHOSPHERE THICKNESS (km)
200.00
151.52
120.48
100.00
80.00
PHASE VEL. (KM/S)
AGE (Ma)
(28) (37) (29) (29) (23) (28) (29) (22) (14) (16) (14) (7) (3)

Using PREM (Dziewonski and Anderson, 1981) as a starting model, we calculated theoretical phase velocity dispersion curves, and attempted to fit the observations by varying the thickness of the lithosphere and the S-wave velocities of different layers. The final model for the Pacific Ocean is shown in Figure 5.4. The corresponding velocities of different layers are also given in the figure. Topography and crustal corrections are included in the analysis. The models for the Atlantic and Indian Oceans are similar to that for the Pacific Ocean, and are not presented here. The velocity at a given depth may change as the age increases, and anisotropy may also change with the age (Regan and Anderson, 1984), but we believe that it is a good enough approximation to assume a constant velocity in each layer. Theoretical phase velocity variation curves are plotted by solid lines in Figures 5.3a-c, and the corresponding thicknesses of the lithosphere are given on top of the figures.

We adopted the formula, $h = A + B\sqrt{t}$, where the thickness h is in kilometers and the age t is in million years for the relationship between the thickness of the lithosphere and the age. The parameter A represents the initial thickness under a ridge, and B is a constant. We varied A and B to fit dispersion curves for different oceans. The final fitting parameters A and B are shown in Table 5.2, and are different for different oceans. Figures 5.3a-c suggest that the lithosphere continuously thicken with age up to about 150 million years, and does not stop thickening at 60-80 Ma.

TABLE 5.1 PHASE VELOCITY IN DIFFERENT OCEANS

PERIOD = 80 SECONDS

AGE	PACIFIC OCEAN		ATLANTIC OCEAN		INDIAN OCEAN	
(Ma)	V	σ	V	σ	V	σ
10	4.522	0.024	4.553	0.017	4.522	0.028
20	4.528	0.022	4.575	0.026	4.541	0.024
30	4.540	0.025	4.572	0.022	4.570	0.024
40	4.552	0.026	4.581	0.027	4.575	0.031
50	4.555	0.020	4.579	0.023	4.574	0.019
60	4.564	0.022	4.585	0.016	4.578	0.017
70	4.565	0.023	4.590	0.021	4.589	0.023
80	4.576	0.024	4.593	0.017	4.592	0.020
90	4.582	0.023	4.598	0.019	4.605	0.016
100	4.588	0.026	4.592	0.019	4.607	0.019
110	4.596	0.026	4.607	0.024	4.592	0.038
120	4.599	0.025	4.604	0.023	4.598	0.017
130	4.609	0.022	4.604	0.014	4.610	0.028
140	4.605	0.020	4.614	0.025		
150	4.600	0.035	4.636	0.020		
160	4.614	0.027				
170	4.590	0.001				

PERIOD = 100.0 SECONDS

AGE	PACIFIC OCEAN		ATLANTIC OCEAN		INDIAN OCEAN	
(Ma)	V	σ	V	σ	V	σ
10	4.575	0.025	4.612	0.021	4.586	0.027
20	4.586	0.021	4.629	0.020	4.599	0.023
30	4.595	0.025	4.627	0.021	4.624	0.021
40	4.605	0.025	4.632	0.025	4.630	0.033
50	4.607	0.019	4.632	0.022	4.631	0.020
60	4.615	0.024	4.635	0.013	4.631	0.016
70	4.616	0.022	4.644	0.023	4.640	0.023
80	4.628	0.023	4.648	0.022	4.643	0.021
90	4.634	0.023	4.652	0.020	4.654	0.015
100	4.642	0.025	4.649	0.015	4.664	0.023
110	4.646	0.025	4.661	0.015	4.658	0.032
120	4.654	0.024	4.663	0.019	4.648	0.010
130	4.667	0.022	4.660	0.010	4.666	0.029
140	4.668	0.036	4.670	0.017		
150	4.652	0.045	4.685	0.003		
160	4.669	0.022				
170	4.653	0.007				

PERIOD = 120.5 SECONDS

AGE	PACIFIC OCEAN		ATLANTIC OCEAN		INDIAN OCEAN	
(Ma)	V	σ	V	σ	V	σ
10	4.631	0.029	4.670	0.017	4.643	0.028
20	4.638	0.025	4.683	0.017	4.653	0.025
30	4.646	0.027	4.683	0.018	4.677	0.028
40	4.656	0.028	4.685	0.021	4.685	0.030
50	4.657	0.022	4.687	0.021	4.686	0.020
60	4.663	0.028	4.690	0.018	4.685	0.017
70	4.669	0.020	4.699	0.026	4.694	0.023
80	4.684	0.024	4.699	0.024	4.694	0.024
90	4.689	0.022	4.704	0.024	4.701	0.018
100	4.694	0.022	4.700	0.020	4.714	0.021
110	4.702	0.024	4.716	0.019	4.713	0.032
120	4.709	0.024	4.718	0.014	4.702	0.004
130	4.722	0.027	4.706	0.007	4.706	0.020
140	4.725	0.036	4.731	0.024		
150	4.703	0.046	4.736	0.001		
160	4.722	0.029				
170	4.705	0.021				

PERIOD = 151.5 SECONDS

AGE	PACIFIC OCEAN		ATLANTIC OCEAN		INDIAN OCEAN	
(Ma)	V	σ	V	σ	V	σ
10	4.727	0.029	4.759	0.009	4.736	0.017
20	4.730	0.024	4.774	0.017	4.750	0.021
30	4.736	0.022	4.774	0.018	4.770	0.027
40	4.742	0.026	4.768	0.017	4.776	0.030
50	4.744	0.018	4.778	0.022	4.769	0.017
60	4.746	0.022	4.777	0.022	4.768	0.014
70	4.750	0.020	4.780	0.026	4.777	0.019
80	4.762	0.019	4.784	0.020	4.774	0.015
90	4.766	0.022	4.784	0.021	4.786	0.013
100	4.775	0.022	4.783	0.014	4.793	0.023
110	4.785	0.024	4.798	0.020	4.790	0.027
120	4.793	0.018	4.800	0.017	4.788	0.009
130	4.796	0.027	4.785	0.010	4.783	0.015
140	4.802	0.028	4.810	0.012		
150	4.787	0.040	4.822	0.017		
160	4.803	0.027				
170	4.790	0.022				

PERIOD = 200.0 SECONDS

AGE	PACIFIC OCEAN		ATLANTIC OCEAN		INDIAN OCEAN	
(Ma)	V	σ	V	σ	V	σ
10	4.885	0.028	4.906	0.016	4.891	0.022
20	4.883	0.023	4.914	0.019	4.890	0.020
30	4.883	0.024	4.921	0.020	4.900	0.016
40	4.891	0.028	4.914	0.016	4.903	0.028
50	4.891	0.018	4.916	0.016	4.902	0.025
60	4.888	0.022	4.917	0.025	4.899	0.023
70	4.894	0.020	4.915	0.021	4.902	0.024
80	4.902	0.016	4.920	0.018	4.909	0.018
90	4.903	0.017	4.919	0.025	4.917	0.011
100	4.917	0.024	4.912	0.016	4.933	0.024
110	4.922	0.027	4.931	0.017	4.931	0.020
120	4.924	0.019	4.933	0.022	4.910	0.021
130	4.934	0.025	4.924	0.012	4.893	0.027
140	4.929	0.027	4.925	0.029		
150	4.912	0.036	4.919	0.033		
160	4.924	0.024				
170	4.905	0.010				

The units for V and σ are Km/Sec.

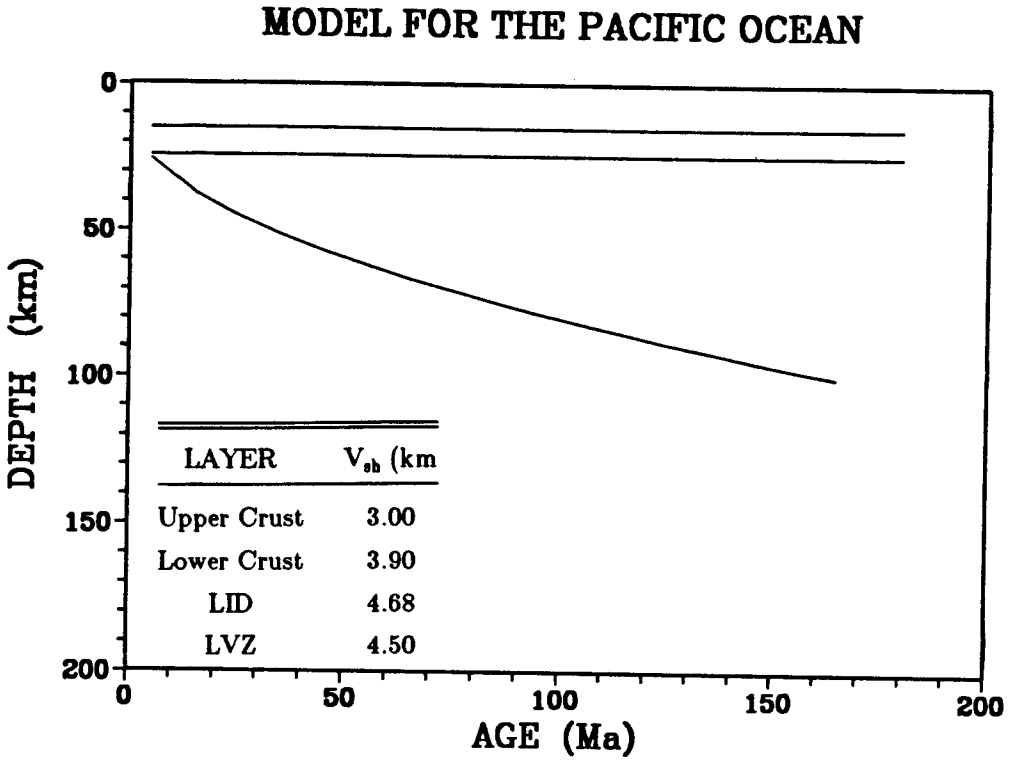

Figure 5.4, Model for the Pacific plate in calculating the phase velocity variation. The thickness of the lithosphere is proportional to the square root of the age. The corresponding velocities for each layer are also given in the figure.

TABLE 5.2 PARAMETER

OCEAN	A	B
PACIFIC	10.0	7.0
INDIAN	20.0	6.7
ATLANTIC	45.0	4.0

Heestand and Crough (1981) and Schroeder (1984) have examined the continuous thickening model by compiling seafloor topography data, avoiding areas that may be influenced by hotspots. They concluded that the age-depth curve does not flatten if the data near hotspot swells are removed. Yoshii *et al.* (1976) deduced similar continuous thickening of the lithosphere from gravity residual anomalies. These studies disagree with other heat flow and sea floor topography studies, but are consistent with our phase velocity results. There are advantages to using seismic data over heat flow and ocean depth data. One of them is the lack of sensitivity to shallow sediment thickness, for which correction is required for ocean depth data. It also has much less scatter than the heat flow data (Davis, 1989). The major obstacle to using seismic data has been poor path coverage, which can now be overcome with digital data.

Figure 5.5, (a). Average phase velocity and one standard deviation in every ten million year intervals for three oceans. These are the results at a period of 100 s. There are systematic differences in younger ages and convergence for age beyond 100 Ma. (b). Same as Fig. 5.5a but for a period of 151.52 s. (c). Same as Fig. 5.5a but for a period 200.00 s.

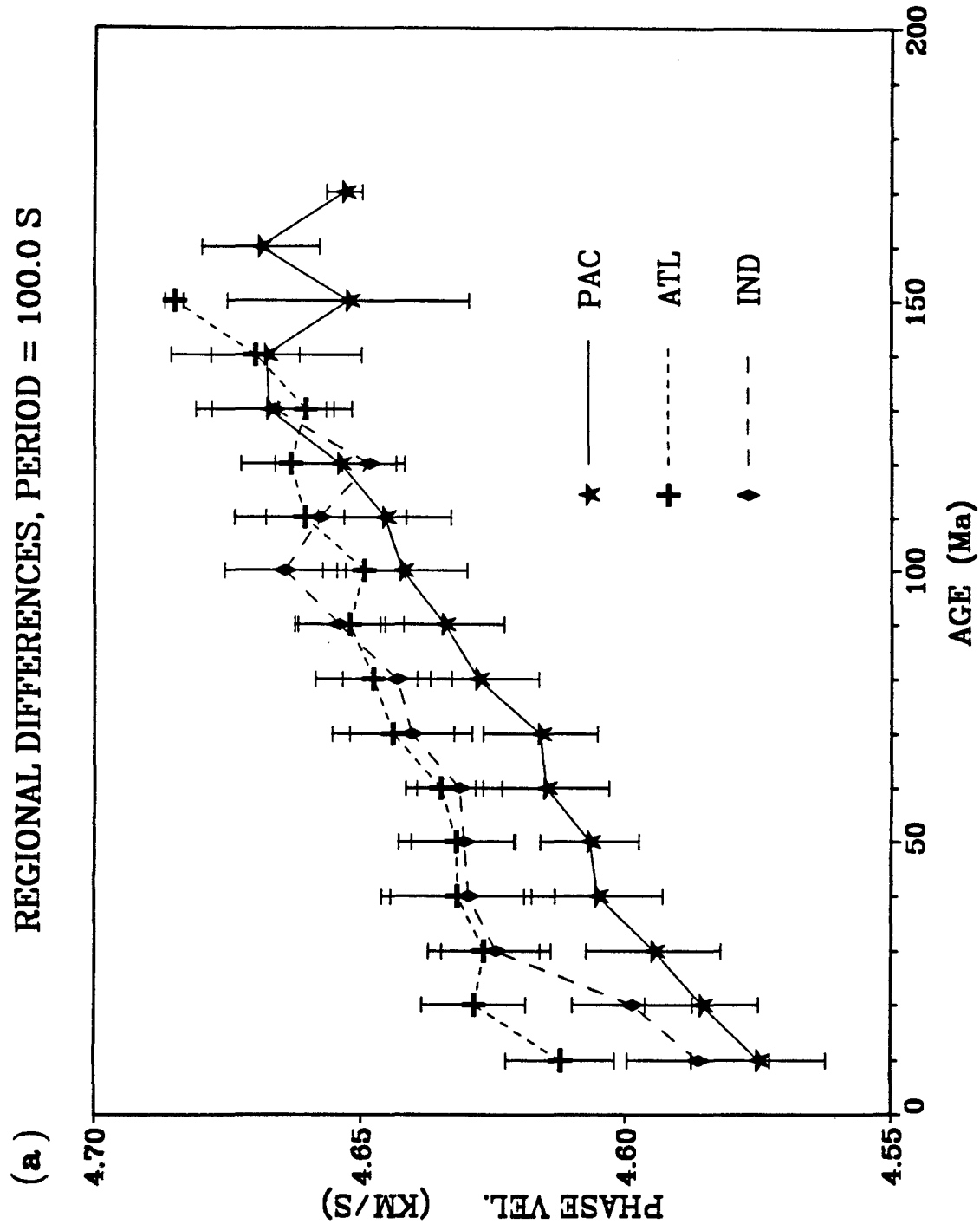
(a)
REGIONAL DIFFERENCES, PERIOD = 100.0 S
PHASE VEL. (KM/S)
4.70
4.65
4.60
4.55
0
50
100
150
200
AGE (Ma)
PAC
ATL
IND

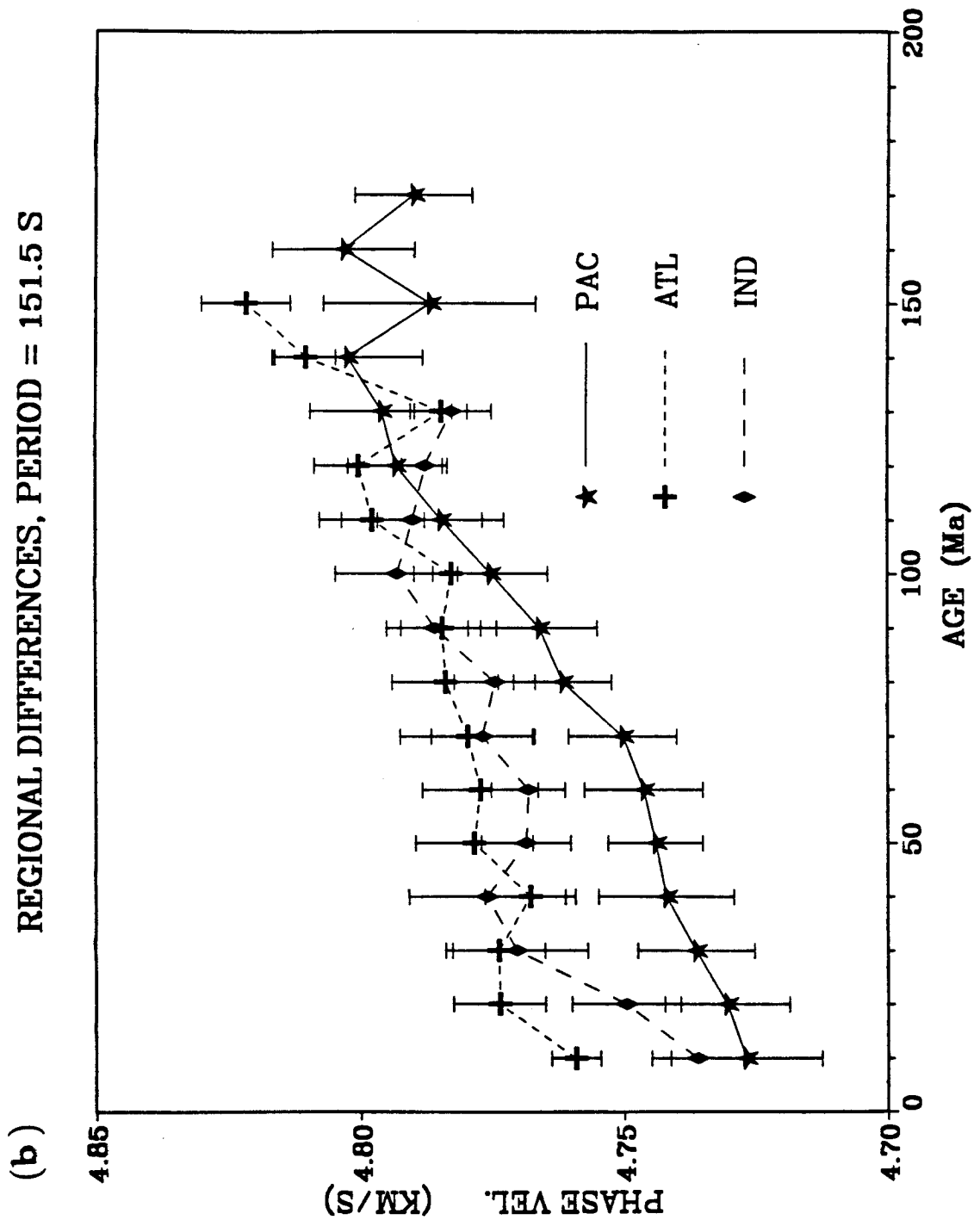
(b)
REGIONAL DIFFERENCES, PERIOD = 151.5 S
PAC
ATL
IND
PHASE VEL. (KM/S)
4.85
4.80
4.75
4.70
0
50
100
150
200
AGE (Ma)

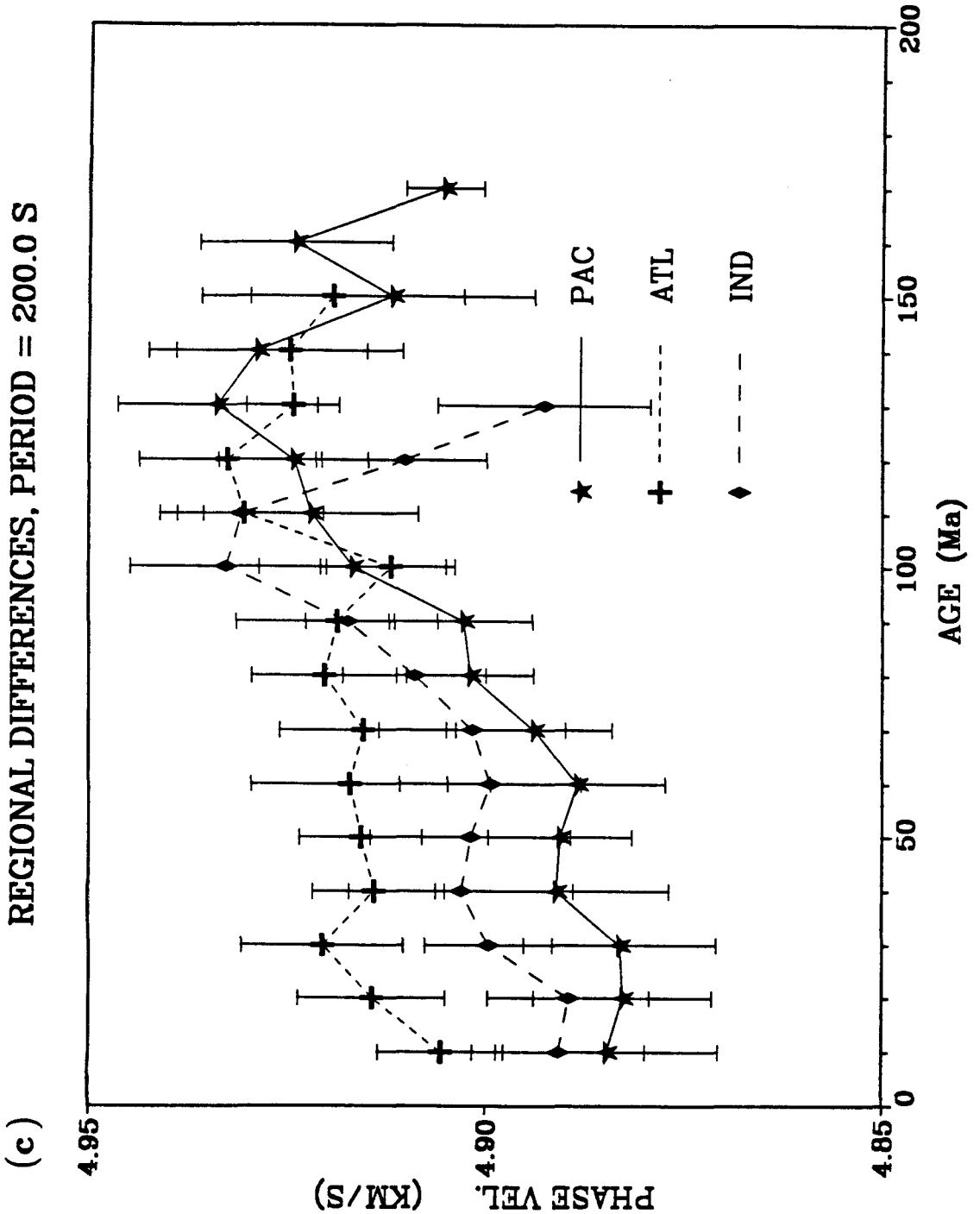
(c)
REGIONAL DIFFERENCES, PERIOD = 200.0 S
PAC
ATL
IND
PHASE VEL. (KM/S)
4.95
4.90
4.85
0
50
100
150
200
AGE (Ma)

5.3 Failure of scaling law

A simple, thermal boundary layer theory has been successfully used to explain thickening of oceanic lithosphere (Turcotte and Oxburgh, 1967; Parker and Oldenburg, 1973). In this model, temperature distribution with respect to depth z at age t is given by the error function:

$$T(z,t) = T_s \, erf \left[\frac{z}{2\sqrt{\kappa t}} \right],$$

where κ is the thermal diffusivity, T_s is the initial temperature and $t = x/u$, with x being the distance from the ridge and u the spreading velocity. The thickness of lithosphere h is

$$h = \beta\sqrt{\kappa t} \ ,$$

where the coefficient β is decided by the ratio $T_s/T(z,t)$.

The above formulas suggest that thermal structure, and thus the phase velocity, should be scaled by only two parameters, T_s and t, independent of spreading rate u. Age-phase velocity curves for the Pacific, Atlantic and Indian Oceans are plotted together in Figures 5.5a-c for each frequency, and the values are given in Table 1. There are two distinct features in these curves: (1) convergence of phase velocities for plates older than 100 Ma, and (2) systematic differences in plates of younger ages.

The convergence of phase velocities beyond 100 Ma probably means that the lithospheric thicknesses for different oceans are approximately the same for old ages. The previous forward modeling (Figures 5.3a-c) also showed that the thicknesses of the lithosphere at the oldest age for the Pacific, Atlantic and Indian Oceans are between 90 and 100 km. There may be some correlation

between phase velocity variations and spreading rates, since the faster spreading ocean has smaller phase velocity at younger ages (Figure 5.5). Canas and Mitchel (1981) studied Q_β in the Pacific and Atlantic Oceans, and found that Q_β^{-1} under the Mid-Atlantic Ridge at a depth of 100 km from the surface is much smaller than that under the East Pacific Rise. This is consistent with the present results, which show that the Atlantic Ocean has a larger phase velocity and a smaller growth rate than the Pacific Ocean at younger ages.

The heat flow data (Anderson and Skilbeck, 1981) have shown differences in the young region ($<$ 80 Ma) of the Pacific, Indian and Atlantic Oceans. Average heat flow decreased from the Pacific Ocean to the Indian Ocean, and then to the Atlantic Ocean. This order is also consistent with Love wave phase velocity differences in different oceans. Previously, the differences in heat flow data were mainly explained by hydrothermal circulation, but our surface wave results indicate that thermal differences in the mantle are required.

It is clear that a simple thermal boundary model cannot explain these differences. The above evidence, in addition to the observations we describe in the next sections, seems to indicate that there is a great variation of differences in the thermal states of the lithosphere.

Figure 5.6, (a). Age-Love wave phase velocity curves on both sides of the Southeast Indian Ocean Ridge. The velocity gradients are different on each side. (b). Same as Fig. 5.6a, except for the East Pacific Rise. (c). Same as Fig. 5.6a, except for the Mid-Atlantic Ridge. The difference of the curve for the Mid-Atlantic ridge is clearest in these three cases.

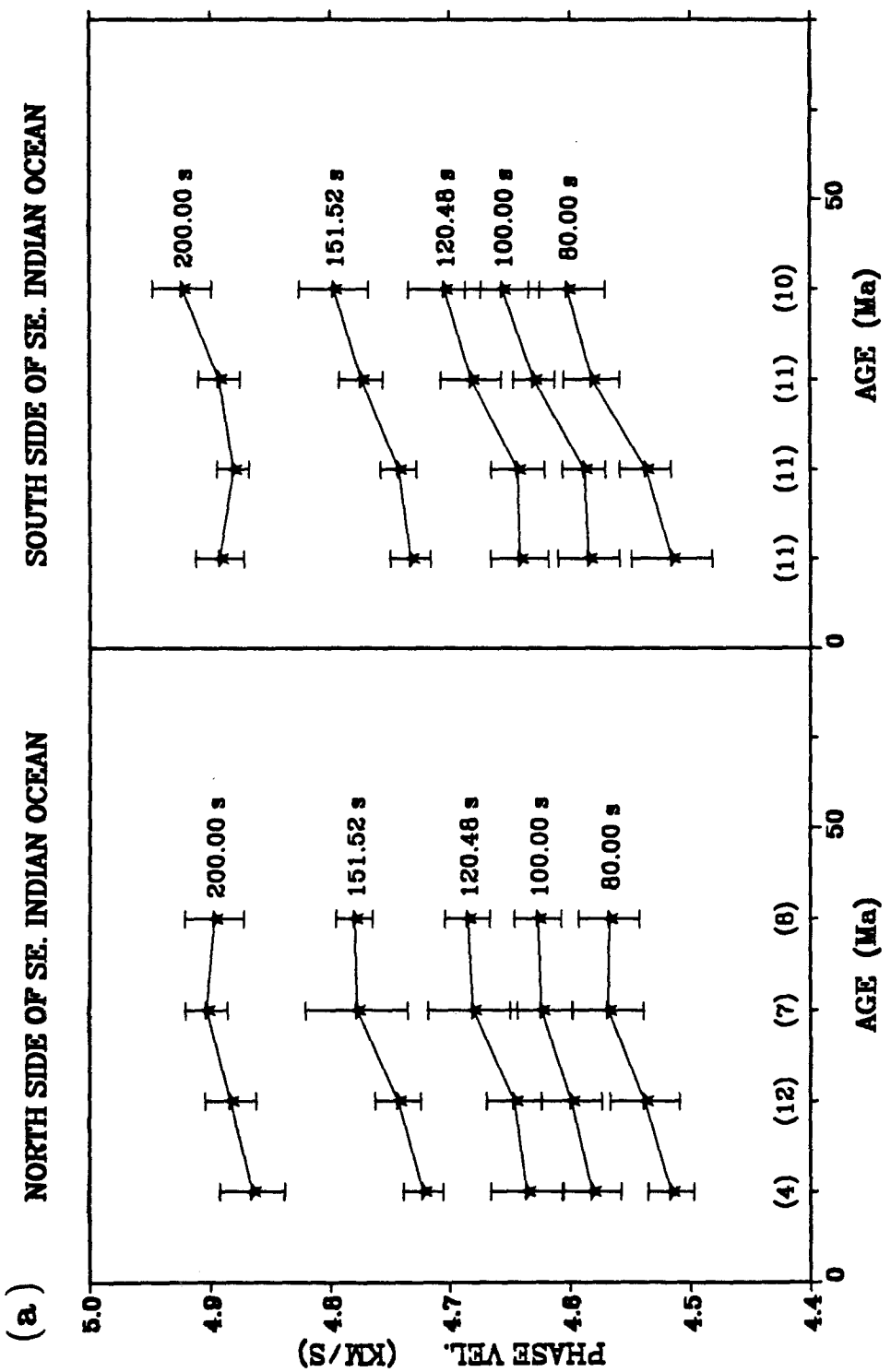
(a)
NORTH SIDE OF SE. INDIAN OCEAN
SOUTH SIDE OF SE. INDIAN OCEAN
PHASE VEL. (KM/S)
AGE (Ma)
200.00 s
151.52 s
120.48 s
100.00 s
80.00 s
(4) (12) (7) (8)
(11) (11) (11) (10)

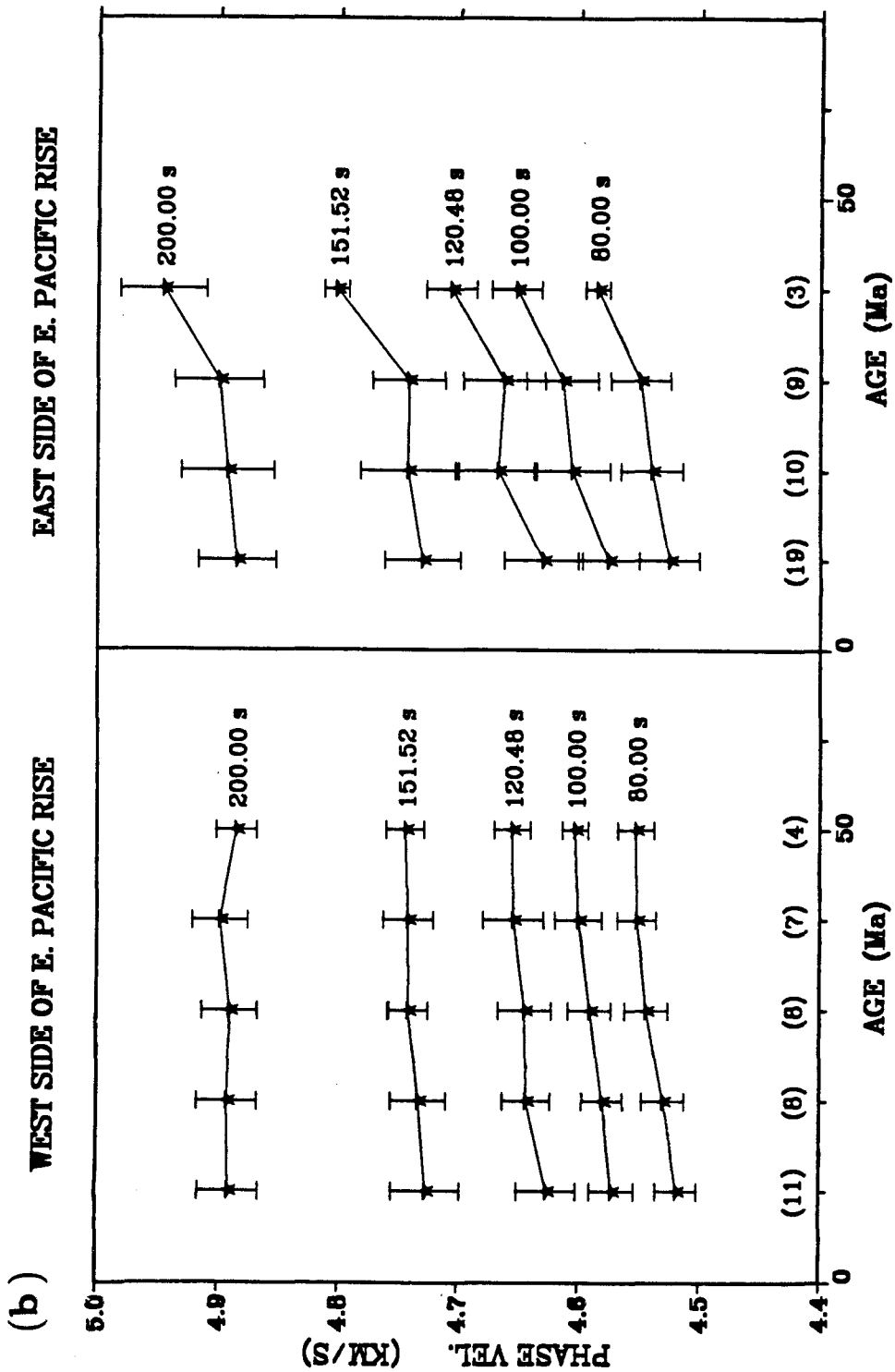
(b)
WEST SIDE OF E. PACIFIC RISE
EAST SIDE OF E. PACIFIC RISE
PHASE VEL. (KM/S)
AGE (Ma)
200.00 s
151.52 s
120.48 s
100.00 s
80.00 s
(11) (8) (8) (7) (4)
(19) (10) (9) (3)

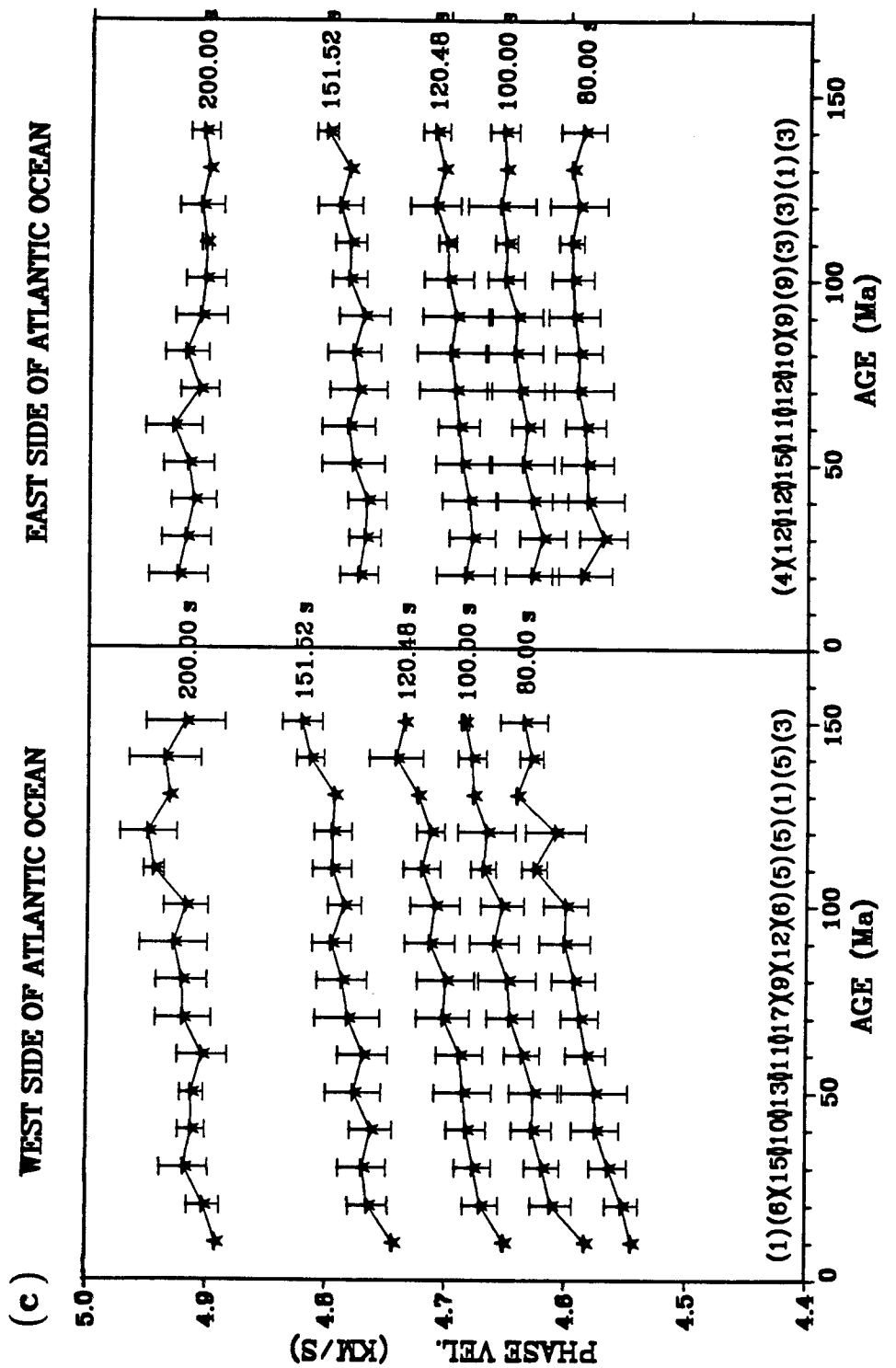
(c)
WEST SIDE OF ATLANTIC OCEAN
EAST SIDE OF ATLANTIC OCEAN
PHASE VEL. (KM/S)
AGE (Ma)
200.00 s
151.52 s
120.48 s
100.00 s
80.00 s
(1)(6)(15)(10)(13)(11)(17)(9)(12)(6)(5)(5)(1)(5)(3)
(4)(12)(12)(15)(11)(12)(10)(9)(9)(3)(3)(1)(3)

TABLE 5.3 PHASE VELOCITY ON EACH SIDE OF THE SOUTHEAST INDIAN OCEAN RIDGE

PERIOD = 80.0 S				
AGE	NORTH SIDE		SOUTH SIDE	
(Ma)	V	σ	V	σ
10	4.516	0.019	4.515	0.033
20	4.538	0.029	4.537	0.021
30	4.568	0.030	4.581	0.023
40	4.568	0.025	4.602	0.032
PERIOD = 100.0 S				
AGE	NORTH SIDE		SOUTH SIDE	
(Ma)	V	σ	V	σ
10	4.581	0.024	4.584	0.026
20	4.599	0.025	4.588	0.018
30	4.624	0.026	4.630	0.017
40	4.627	0.020	4.656	0.031
PERIOD = 120.5 S				
AGE	NORTH SIDE		SOUTH SIDE	
(Ma)	V	σ	V	σ
10	4.636	0.030	4.642	0.024
20	4.646	0.023	4.643	0.022
30	4.681	0.037	4.682	0.025
40	4.685	0.019	4.704	0.030
PERIOD = 151.5 S				
AGE	NORTH SIDE		SOUTH SIDE	
(Ma)	V	σ	V	σ
10	4.722	0.017	4.733	0.017
20	4.743	0.019	4.743	0.015
30	4.778	0.043	4.774	0.018
40	4.780	0.015	4.797	0.029
PERIOD = 200.0 S				
AGE	NORTH SIDE		SOUTH SIDE	
(Ma)	V	σ	V	σ
10	4.865	0.027	4.892	0.020
20	4.883	0.021	4.881	0.013
30	4.903	0.017	4.893	0.017
40	4.897	0.024	4.923	0.025

The units for V and σ are Km/Sec.

TABLE 5.4 PHASE VELOCITY ON EACH SIDE OF THE EAST PACIFIC RISE

AGE	WEST SIDE		EAST SIDE	
(Ma)	V	σ	V	σ
PERIODS = 80.0 S				
10	4.518	0.017	4.525	0.025
20	4.530	0.017	4.540	0.025
30	4.544	0.018	4.549	0.025
40	4.552	0.016	4.585	0.010
50	4.552	0.015		
PERIODS = 100.0 S				
10	4.572	0.018	4.576	0.025
20	4.580	0.017	4.606	0.031
30	4.590	0.018	4.614	0.030
40	4.600	0.019	4.652	0.021
50	4.603	0.011		
PERIODS = 120.5 S				
10	4.626	0.025	4.630	0.032
20	4.643	0.020	4.668	0.032
30	4.644	0.022	4.662	0.034
40	4.654	0.025	4.706	0.021
50	4.655	0.015		
PERIODS = 151.5 S				
10	4.726	0.028	4.730	0.031
20	4.733	0.023	4.742	0.039
30	4.742	0.017	4.742	0.030
40	4.742	0.021	4.802	0.010
50	4.744	0.016		
PERIODS = 200.0 S				
10	4.891	0.025	4.885	0.032
20	4.892	0.025	4.892	0.038
30	4.890	0.023	4.899	0.037
40	4.898	0.023	4.946	0.036
50	4.885	0.017		

The units for V and σ are Km/Sec.

TABLE 5.5 PHASE VELOCITY ON EACH SIDE OF THE MID-ATLANTIC OCEAN RIDGE

PERIOD = 80.0 S

AGE	WEST SIDE		EAST SIDE	
(Ma)	V	σ	V	σ
10	4.544	0.000		
20	4.553	0.014	4.588	0.025
30	4.564	0.015	4.570	0.020
40	4.574	0.020	4.583	0.030
50	4.575	0.028	4.584	0.022
60	4.583	0.017	4.586	0.017
70	4.588	0.015	4.592	0.029
80	4.593	0.018	4.591	0.019
90	4.601	0.021	4.596	0.021
100	4.600	0.018	4.597	0.017
110	4.627	0.011	4.598	0.010
120	4.609	0.025	4.592	0.024
130	4.641	0.000	4.597	0.000
140	4.630	0.010	4.588	0.019
150	4.636	0.020		

PERIOD = 100.0 S

AGE	WEST SIDE		EAST SIDE	
(Ma)	V	σ	V	σ
10	4.583	0.000		
20	4.611	0.017	4.630	0.022
30	4.619	0.015	4.621	0.019
40	4.628	0.017	4.630	0.029
50	4.626	0.020	4.638	0.026
60	4.636	0.015	4.634	0.013
70	4.646	0.019	4.640	0.028
80	4.649	0.024	4.645	0.023
90	4.660	0.020	4.643	0.021
100	4.653	0.018	4.653	0.015
110	4.669	0.011	4.652	0.009
120	4.667	0.024	4.657	0.028
130	4.678	0.000	4.653	0.000
140	4.679	0.012	4.655	0.012
150	4.685	0.003		

PERIOD = 120.5 S

AGE	WEST SIDE		EAST SIDE	
(Ma)	V	σ	V	σ
10	4.650	0.000		
20	4.670	0.015	4.686	0.024
30	4.677	0.015	4.680	0.019
40	4.683	0.016	4.683	0.023
50	4.686	0.024	4.688	0.022
60	4.688	0.020	4.692	0.017
70	4.703	0.022	4.694	0.030
80	4.700	0.024	4.698	0.029
90	4.714	0.021	4.695	0.028
100	4.710	0.021	4.701	0.021
110	4.721	0.016	4.702	0.007
120	4.714	0.012	4.712	0.021
130	4.724	0.000	4.705	0.000
140	4.743	0.022	4.712	0.011
150	4.736	0.001		

PERIOD = 151.5 S

AGE	WEST SIDE		EAST SIDE	
(Ma)	V	σ	V	σ
10	4.743	0.000000		
20	4.764	0.017	4.775	0.016
30	4.769	0.020	4.770	0.013
40	4.762	0.018	4.768	0.016
50	4.777	0.023	4.780	0.026
60	4.769	0.021	4.784	0.022
70	4.782	0.027	4.776	0.024
80	4.787	0.021	4.780	0.022
90	4.796	0.016	4.771	0.021
100	4.786	0.014	4.784	0.014
110	4.796	0.016	4.783	0.013
120	4.796	0.016	4.792	0.019
130	4.794	0.000	4.784	0.000
140	4.815	0.011	4.803	0.009
150	4.822	0.017		

PERIOD = 200.0 S

AGE	WEST SIDE		EAST SIDE	
(Ma)	V	σ	V	σ
10	4.892	0.000		
20	4.902	0.013	4.926	0.024
30	4.919	0.020	4.920	0.021
40	4.913	0.011	4.914	0.019
50	4.913	0.010	4.918	0.021
60	4.904	0.021	4.930	0.024
70	4.920	0.023	4.909	0.016
80	4.921	0.021	4.920	0.018
90	4.929	0.028	4.908	0.021
100	4.918	0.018	4.904	0.017
110	4.945	0.008	4.904	0.004
120	4.950	0.024	4.908	0.018
130	4.932	0.000	4.902	0.000
140	4.936	0.030	4.906	0.012
150	4.919	0.033		

The units for V and σ are Km/Sec.

5.4 Asymmetric thickening on different sides of the ridges

We also focused our attention on velocity variations on different sides of ridges. The spreading rate is known to be asymmetric for the South-East Indian Ocean Ridge (Weissel and Hayes, 1971), but the East Pacific Rise and the Mid-Atlantic Ridge are thought to be symmetric (Vogt, 1986; Minster and Jordan, 1978). We examine to see whether there are differences in velocity variation.

The areas were carefully selected to determine the velocity variation on each side of the South-East Indian Ocean Ridge, East Pacific Rise and Mid-Atlantic Ridge. Only short age spans were available for the East Pacific Rise and the South-East Indian Ocean Ridge. Regions bounded by the equator and 35°S for the East Pacific Rise were used in order to avoid effects from adjacent perpendicular ridges and the Eltanin fracture zone. For the Mid-Atlantic Ridge, we added data from all areas of the Atlantic Ocean. Figures 5.6a-c show age-phase velocity curves for the three ridges, respectively. The corresponding values are given in Tables 5.3, 5.4 and 5.5. The phase velocity gradients of these curves are different for each side in all three cases, and are clearest for the Mid-Atlantic Ridge.

Hayes (1988) recently showed that the subsidence rate of plates in the south-east Indian Ocean and the south Atlantic Ocean can vary along the strike of ridges and coined the phrase "tectonic corriders," which are striped regions along the directions of spreading. He also suggested asymmetric subsidence curves, although he did not develop a physical model to explain this observation. As a result, we now have two independent data sets, surface wave data and ocean depth data, to support asymmetry at ridges. Different hotspot concentration is one possible explanation for the asymmetry. There are different

thermal thermal states on different sides of ridges, resulting perhaps in different lithospheric thickening rates.

5.5 The "residual" maps

In order to understand the thermal state below oceanic plates, we subtracted the average phase velocity, which was based on the age-phase velocity relation, from the velocity variation maps (Figure 5.2a-c), and then the "residual" maps for different periods were constructed. Figures 5.7a-c show these "residual" maps. Because we applied age-phase velocity relations only for oceanic areas, continental areas are hatched.

Almost 80 percent of hotspots in oceanic plates are located in or near relatively low velocity areas in Figures 5.7a-c, which probably indicates that hotspots are associated with high temperature and/or partial melting. The low velocity anomaly near the Hawaii hotspot is now more obvious than that in phase velocity variation maps (Figure 4.2). Low velocity anomalies are found in the south Pacific Ocean superswell region (Smith *et al.*, 1989; McNutt and Judge, 1990), and the west and south of the Indian Ocean; fast velocity anomalies are found in the northeast Indian Ocean. In the area east of the Azores, several hotspots (Azores, Maderia, Canary Islands and New England Seamounts) are located, and low velocity shows up. It seems that hotspots are an important factor there. West of the Azores, fast velocities appear. Because the thermal state of oceanic lithosphere is complicated, there apparently is not a single factor that controls everything; for example, there are fast velocity anomalies along the longitude at about 30^0S latitude near the East Pacific Rise, although several hotspots are there.

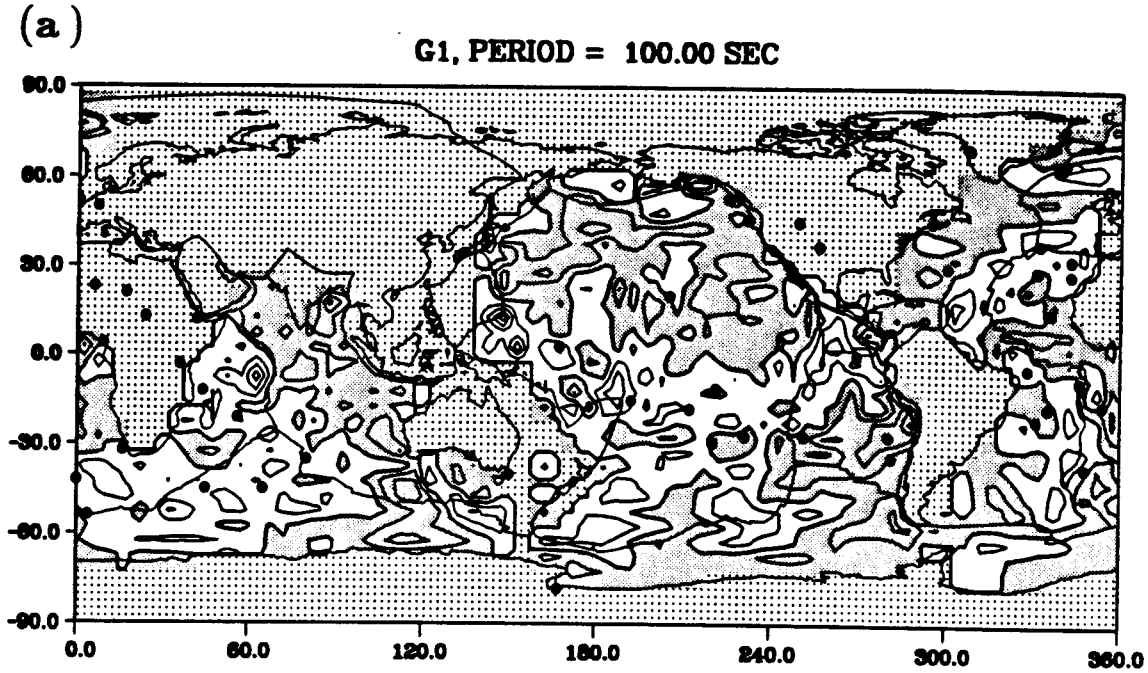

Figure 5.7, (a). "Residual" map for oceanic area at a period of 100.00 s. This "residual" map is produced by subtracting average phase velocity for a given age from the phase velocity map (Figure 4.2). The same format as Figure 4.2 is used. (b). Same as Fig. 5.7a but for a period of 151.52 s. (c). Same as Fig. 5.7a but for a period of 200.00 s.

(b)

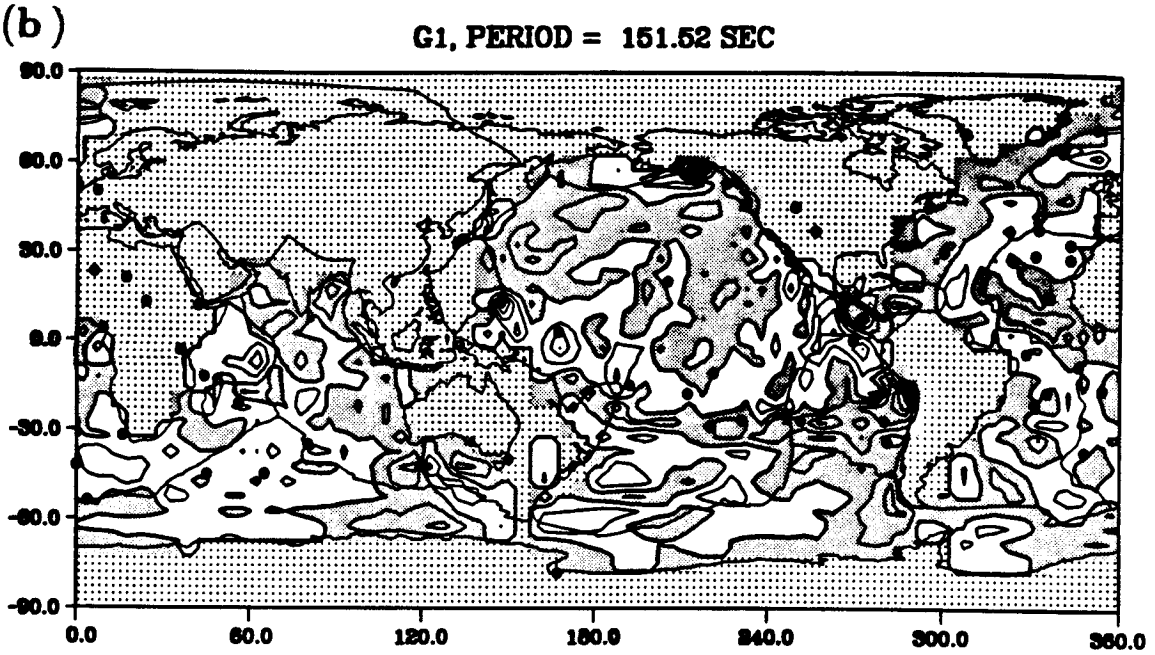
G1, PERIOD = 151.52 SEC
90.0
60.0
30.0
0.0
-30.0
-60.0
-90.0
0.0
60.0
120.0
180.0
240.0
300.0
360.0

(c)

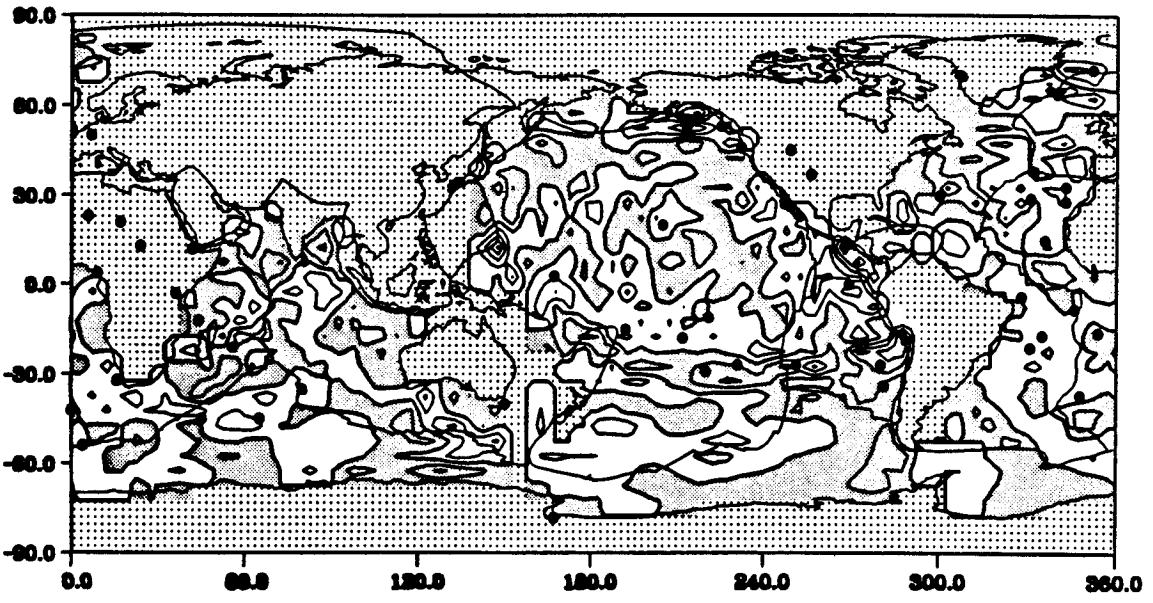
G1, PERIOD = 200.00 SEC
90.0
60.0
30.0
0.0
-30.0
-60.0
-90.0
0.0
120.0
180.0
240.0
300.0
360.0

The low velocity anomalies on the west side of the East Pacific Rise, the north side of the South-East Indian Ocean Ridge, and the west side of the south mid-Atlantic Ridge probably reflect different thermal states on each side of the ridges, and may also explain why there is asymmetric velocity variation (Figure 5.6). There are low velocity anomalies under the north-west Pacific plate at an age older than 120 Ma (Figures 5.7a-c). These anomalies get larger in the longer period maps. It suggests an existence of low velocity anomalies below some old oceanic plates. Since the low velocity anomalies are distinct within the fast velocity zone, the viscous heating model is not a preferred explanation. They may be caused by upwelling of deeper, small scale convection. But further study is needed to confirm the nature of these low velocity anomalies.

5.6 Thermal anomalies under the oceanic plate

This study showed that thermal states on each side of ridges are different. One possible cause is the existence of hotspots on one side of a ridge. In the case of the East Pacific Rise, the so-called superswell region is found on the western side. These hotspots will cause the western side of the East Pacific Rise to have higher temperature than the eastern side, and will reduce the Love wave phase velocity variation rate. This explanation may also be applied to the Mid-Atlantic Ocean, which shows a flatter growth rate on the east side, and thus higher temperature there. Hotspots on the eastern side, such as the Canary islands, may be the cause of this feature. Canas (1980) performed a surface wave study of the Atlantic Ocean and found that shear attenuation (Q_β^{-1}) is about a factor of two smaller on the eastern side than on the western side at depths of about 100 km. This is consistent with slower growth of plates on the eastern side.

Another possible cause of asymmetry is ridge migration. Burke and Wilson (1976) discussed the possible westward migration of the Mid-Atlantic Ridge based on geological surface observations, and Stein *et al.* (1977) studied the possible relationship between ridge migration and asymmetric spreading. Many upper mantle studies (Nataf *et al.* 1984, 1986; Woodhouse and Dziewonski, 1984; Tanimoto, 1986a,b) showed that low velocity anomalies associated with ridges can be traced to depths of about 300-400 km. Our S-wave velocity inversion results (Chapter 4) also showed that the lowest velocity region is near the surface, 100 km deep. At greater depths, the magnitude of low velocity anomaly decreases quickly, and it changes into a fast velocity anomaly at the 300 or 400 km depth. If ridges migrate, which is presumably a shift of shallow regions with respect to deeper regions, asymmetry in thermal states can occur

at the deeper regions. According to this model, the growth rate of lithosphere, and thus the gradient of phase velocity curves, should be higher on the west side than on the east side of the mid-Atlantic Ridge. However, it is difficult to assess its validity of this model, because the direction of ridge migration is not clear at this moment.

5.7 Summary

Using phase velocities measured from 971 earthquakes occurring between 1980 and 1987, global lateral Love wave phase velocity variations were analyzed. The most significant results are the age-phase velocity relations for the Pacific, Atlantic and Indian Oceans. The observation of phase velocity variation and simple forward modeling showed a continuous thickening of lithosphere with age up to about 150 Ma, disagreeing with conventional oceanic plate tectonic models (*e.g.* McKenzie, 1967; Sclater *et al.*, 1971) which changed variations at about 60-80 Ma. The age-phase velocity relations are different from one ocean to another, suggesting a violation of the scaling law derived from the thermal boundary layer model (*e.g.* Turcotte and Oxburgh, 1967; Parker and Oldenburg, 1973). Also, an initial lithosphere depth under ridges may correlate with the spreading rate of ridges.

Age-phase velocity relations on each side of ridges were also examined. Asymmetric velocity variations were found, which indicate complex thermal anomalies in the mantle. Several possible reasons were discussed in this paper, although further studies are needed to clarify the situation.

For the Pacific, Atlantic and Indian Oceans, the "residual" maps were obtained by subtracting the average velocity from the phase velocity maps. About 80 percent of the hotspots are located in or near upper mantle low velocity areas, which indicats higher temperatures and/or partial melting associated with these hotspots. The low velocity anomalies on the west side of the East Pacific Rise, the north side of the South-East Indian Ocean Ridge and the west side of the Mid-Atlantic Ridge were shown in these maps. A low velocity anomaly was found in the northwest Pacific region at an age older than 120 Ma, and became more distinct for longer period maps.

Chapter 6

Ridges, Hotspots, and Rifts

6.1 Introduction

The spreading of the oceanic plates, the formation of new oceanic lithosphere at mid-ocean ridges, the hotspot distribution over the world and the continental rifts are essential features of plate tectonics. Most understanding of these features is from surface observations and constructions of theoretical models based on simple physical principles and our knowledge of the gross structure and evolution of the mantle (*e.g.* Le Pichon, 1968; Parker and Oldenburg, 1973; Turcotte and Ahern, 1978; Turcotte and Oxburgh, 1978; Cochran, 1979; Craig and McKenzie, 1986; Morgan 1987; Spiegelman and McKenzie, 1987; Richards and Hager, 1988; Scott and Stevenson, 1989; White and Mckenzie, 1989; Chen and Morgan, 1990a, 1990b). Seismology provides a direct procedure for understanding these features, but because of the limitation of earthquake distribution, seismic observation station distribution and present technology, the detailed structures under mid-ocean ridges and hotspots have not been obtained until recently. The development of global networks of digital seismographs in the last decade has permitted the acquisition and processing of

unprecedented amounts of seismic data, and has improved the resolution wavelength in global tomography to a level of about 1000 km. It allowed us to obtain seismic velocity structure under global mid-ocean ridges and hotspot swells simultaneously. The aim of this chapter is to study hotspots and ridges in light of our new S-wave velocity results. The complete analysis of the original data set, and the inversion of S-wave velocity structure are presented in Chapters 2, 3, and 4. We will use the results directly in Chapter 4 as our new data set, and will continue our study in this chapter.

At mid-ocean ridges, when adjacent plates diverge, hot, partially melted mantle rock flows upward to fill the gap, then, cools and forms new lithospheric plates. The global mid-ocean ridge show different morphology, bathymetry and gravity variations with spreading rates (Macdonald *et al.*, 1984; Macdonald, 1986, Small and Sandwell, 1989). At slow spreading rate sites, a deep rift valley marks the axis, the bathymetry is rough and faulted, and gravity is low. At intermediate rate sites, the rift valley is less pronounced, and the bathymetry and gravity are relatively smooth. At fast spreading rate sites, a triangle-shaped peak is observed at the ridge axis, and gravity is locally high. In our seismic surface wave study, the low velocity anomalies are associated with the global mid-ocean ridge (Figure 4.12), which is consistent with a geodynamic explanation, but the low velocity anomaly is limited to the top 100 km, and the minimum velocity is shallower than 50 km. The widths of the low velocity anomalies, which cross over ridges, increase with spreading rates. We also find that seismic velocities are strongly correlated with the spreading rate for shallow results, but correlation decreases for deeper results and almost disappears below 100 km. This is the first time that seismic velocity structure over the global mid-ocean ridge, and the relationship with the spreading rate

have been obtained simultaneously. The variations in the seismic velocity structure, the bathymetry and gravity with spreading rates give us important information for understanding the global mid-ocean ridge. Theoretically, any ridge model should satisfy these constraints.

Hotspots are interior plate volcanos (*e.g.*, Hawaii, Yellowstone), or the inferred locations of volcanos, except at island arcs or mid-ocean ridges, unless the exceptionally large (*e.g.*, the Azores, Iceland, Tristan de Cunha). Mantle plume hypothesis (*e.g.*, Morgan, 1972; Turcotte and Oxburgh, 1978; Courtney and White, 1986; White and McKenzie, 1989) gives a possible explanation for the forming of hotspots. In the present study, the low-velocity anomalies are associated with major hotspots with a magnitude of about 1-2 percent and a diameter of more than 1000 km. But the depths of the low-velocity anomalies are different from those of ridges, indicating different mechanisms between ridges and hotspots. Possible explanations are discussed in this chapter.

From the study of ridges and hotspots, we make the following conjecture: The depth of the low velocity anomaly can serve as a criterion for distinguishing passive or active upwelling. A passive mechanism is suggested as associating with a shallow low velocity anomaly while a deep anomaly suggests an active mechanism. The East African Rift is associated with a deep low velocity anomaly. The shape of the low velocity anomaly indicates that the material may be fed by hotspots at Afar and in northeastern African. The velocity under the Baikal Rift (also called Baykal Rift Valley) is clearly different from that of African Rift Valley. It is associated with a low velocity anomaly at a depth of about 100 km and did not penetrate deeply. The seismic result suggests that the Baikal Rift is connected with a passive rift.

Two numerical tests are given in Section 6.2 to make us confident about the present results. In Section 6.3, we discuss the seismic velocities under ridges, and the relationship with the spreading rates. The seismic velocities under hotspots are shown in Section 6.4, In Section 6.5, the seismic velocities under the Red Sea and Baikal Rift Valley are described. And the main conclusions are given in Section 6.6

Figure 6.1, (a). Synthetic test result. The total height (including both dark and light colors) at each column is the original anomaly magnitude. The light color column is the inversion result, and the dark column is the lost part associated with a damping parameter of 100. The locations of each block on the surface of the Earth are also shown in the figure. (b). Same as Figure 6.1b, but with a damping parameter of 1000.

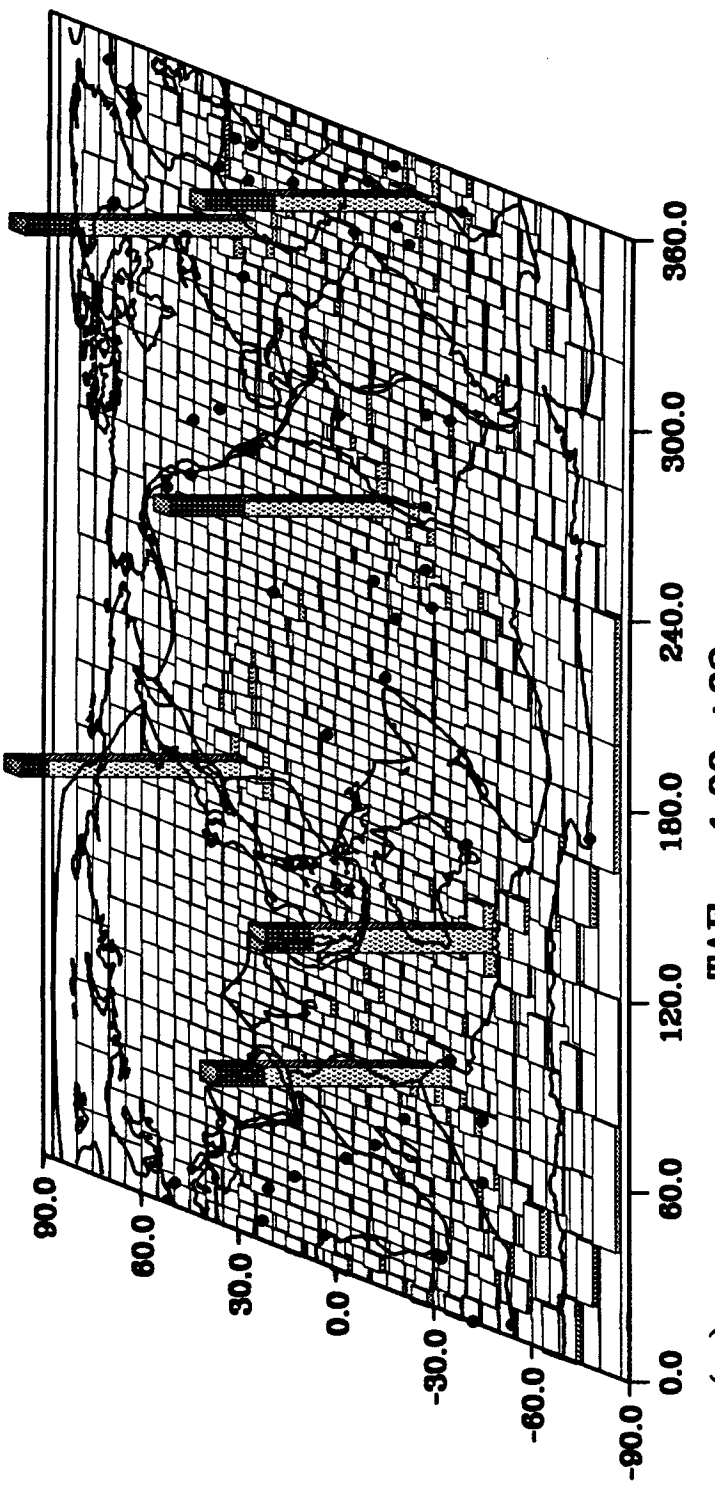
90.0
60.0
30.0
0.0
-30.0
-60.0
-90.0
0.0
60.0
120.0
180.0
240.0
300.0
360.0
TAF = 1.00e+02
(a)

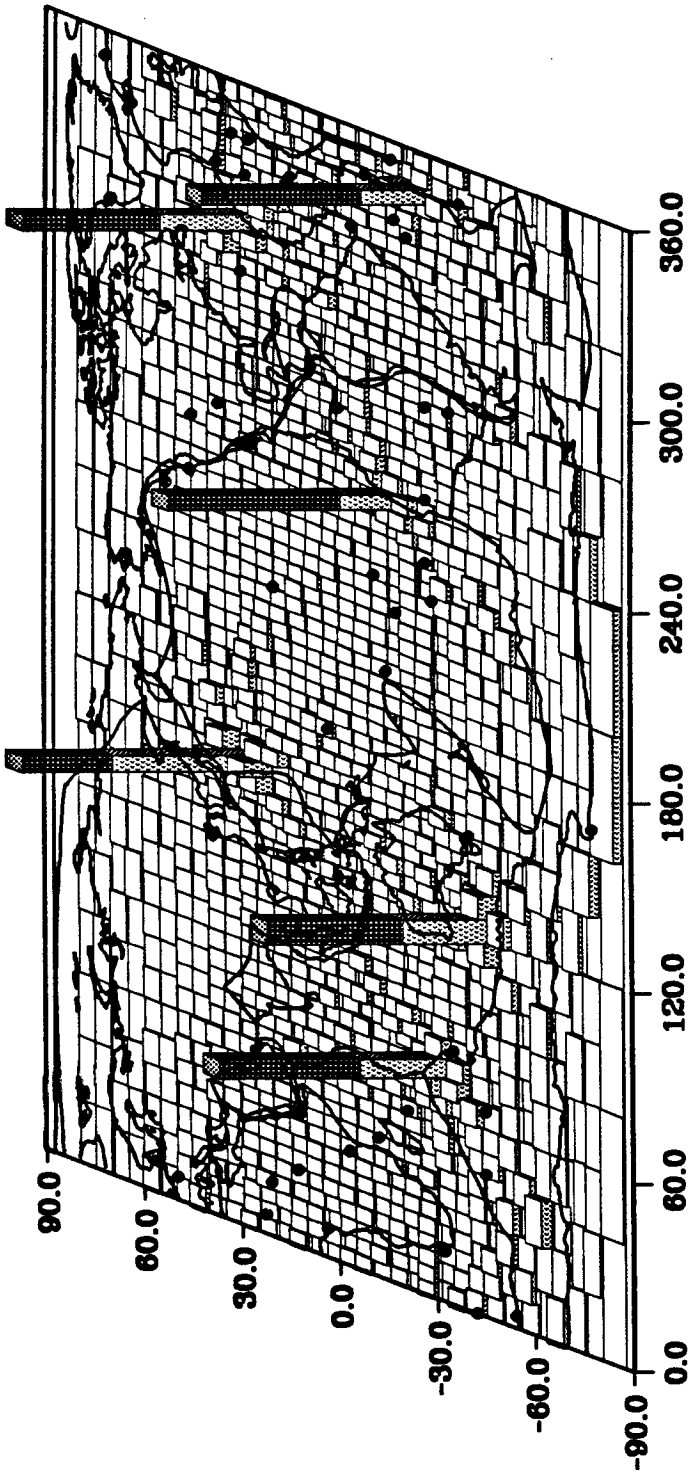
90.0
60.0
30.0
0.0
-30.0
-60.0
-90.0
0.0
60.0
120.0
180.0
240.0
300.0
360.0
TAF = 1.00e+03

(b)

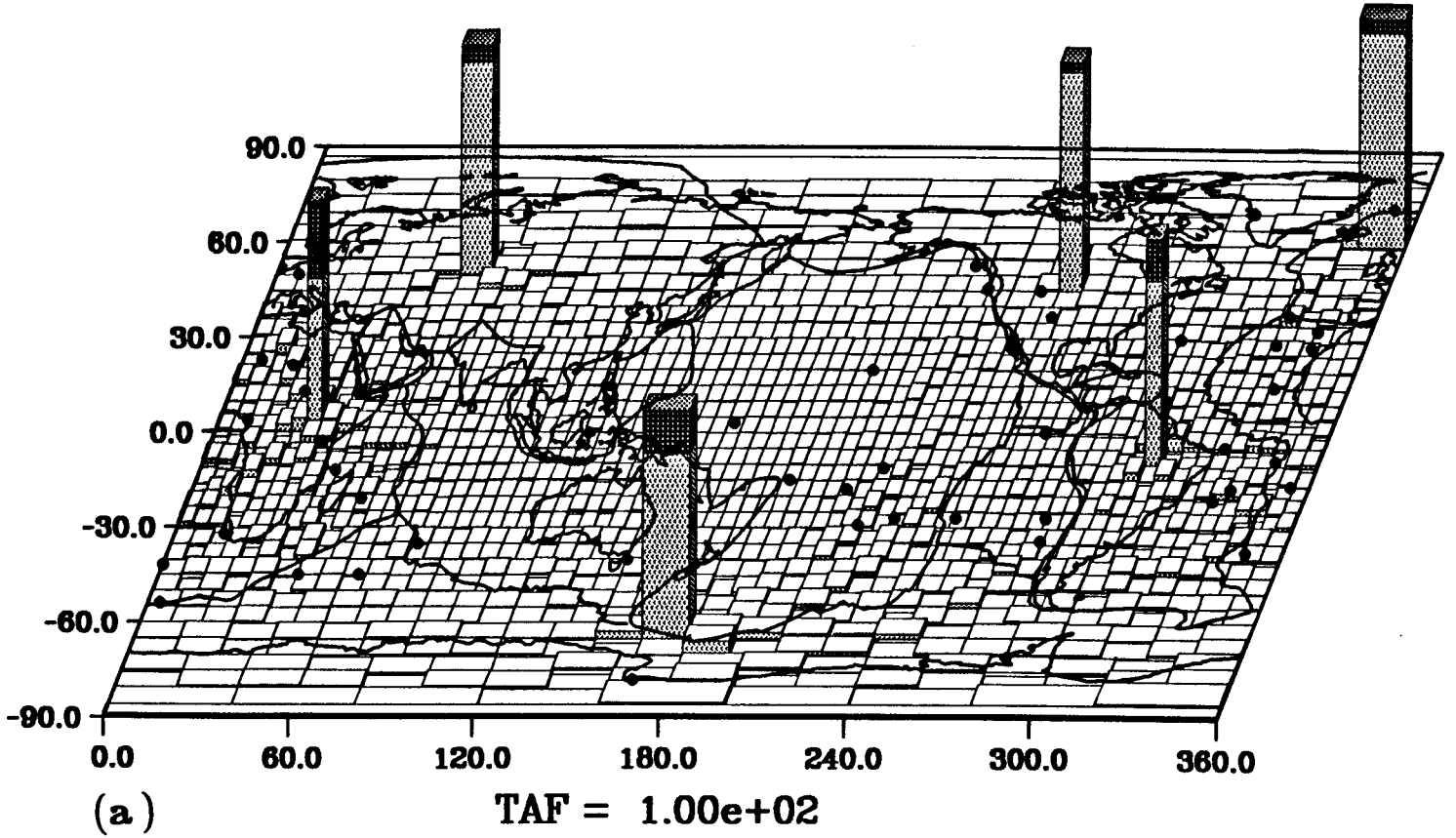

Figure 6.2, (a). Same as Figure 6.1a, but with different block locations. (b). Same as Figure 6.2a, but with a damping parameter of 1000.

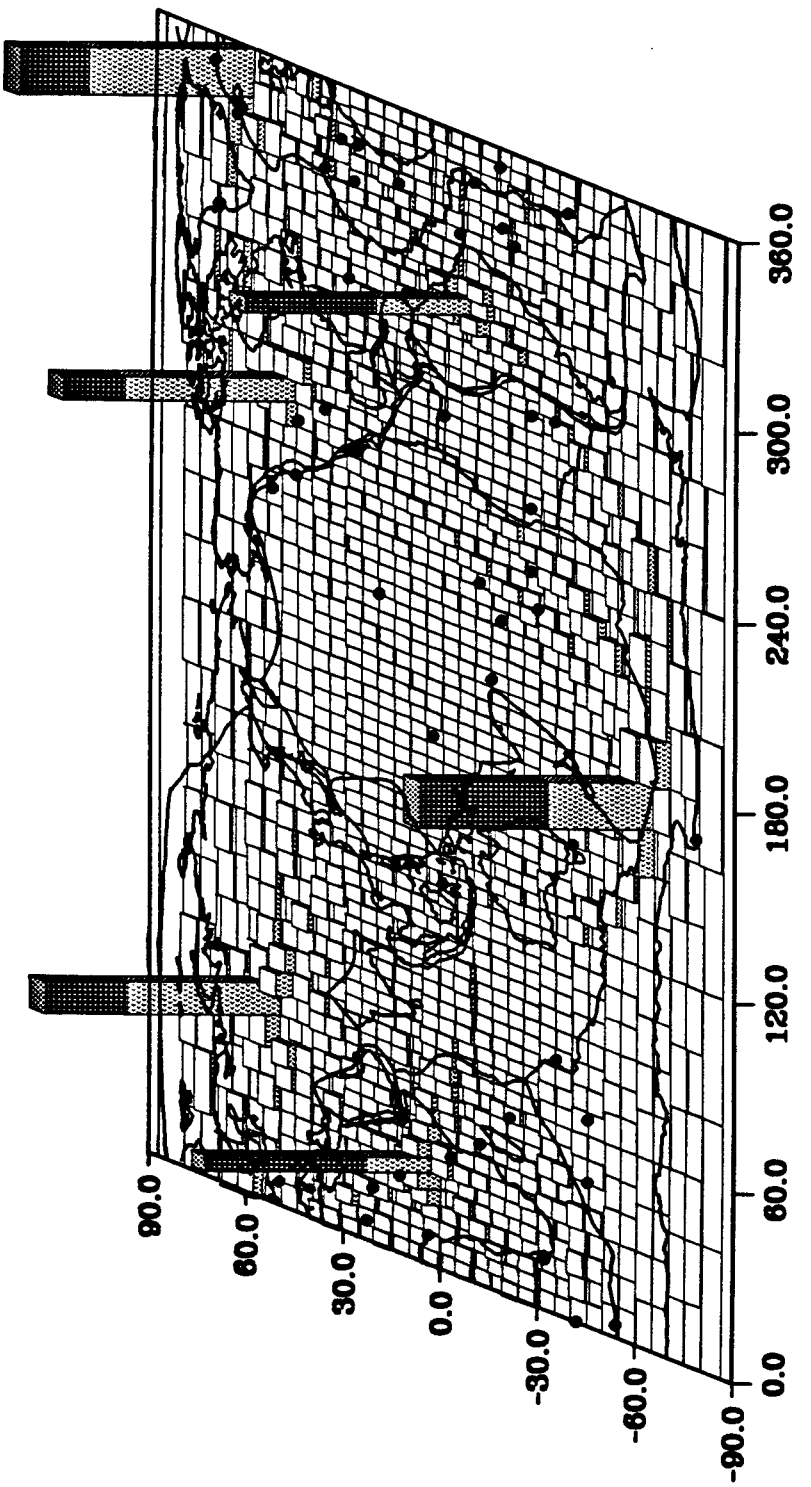
90.0
60.0
30.0
0.0
-30.0
-60.0
-90.0
0.0
60.0
120.0
180.0
240.0
300.0
360.0
TAF = 1.00e+03
(b)

6.2 Numerical examination

Before examining seismic velocities under mid-ocean ridges, hotspots and rifts, some obvious questions arise. Are the inversion results reliable or not? Do our seismic velocity results have enough resolution to allow us to study the detailed structure? In order to answer these questions, we have done some numerical tests. In these tests, several anomalies are put in different blocks, and theoretical travel time residuals are computed for the path coverage in Figure 2.2. Then velocity variations associated with various damping parameters are solved.

Figures 6.1a-b and 6.2a-b show two synthetic test results. They are plotted in three-dimensions. Continental plates, ridges, trenches and active hotspots are also shown in the figures. In Figures 6.1a-b and 6.2a-b, the total columns (including both dark and light colors) are the original anomaly, the light columns are the inversion results, and the dark columns are the lost parts. The synthetic results shown here are associated with damping parameters 100 and 1000, respectively, because the real damping parameter for different periods in Chapter 4 are between 100 and 1000. Figures 6.1a-b and 6.2a-b show that the results are quite reliable, and that contaminations from other blocks are negligiblely small, even for a damping parameter of 1000. These synthetic results make us confident about the present inversion results, and we continue our study in the basis of these results.

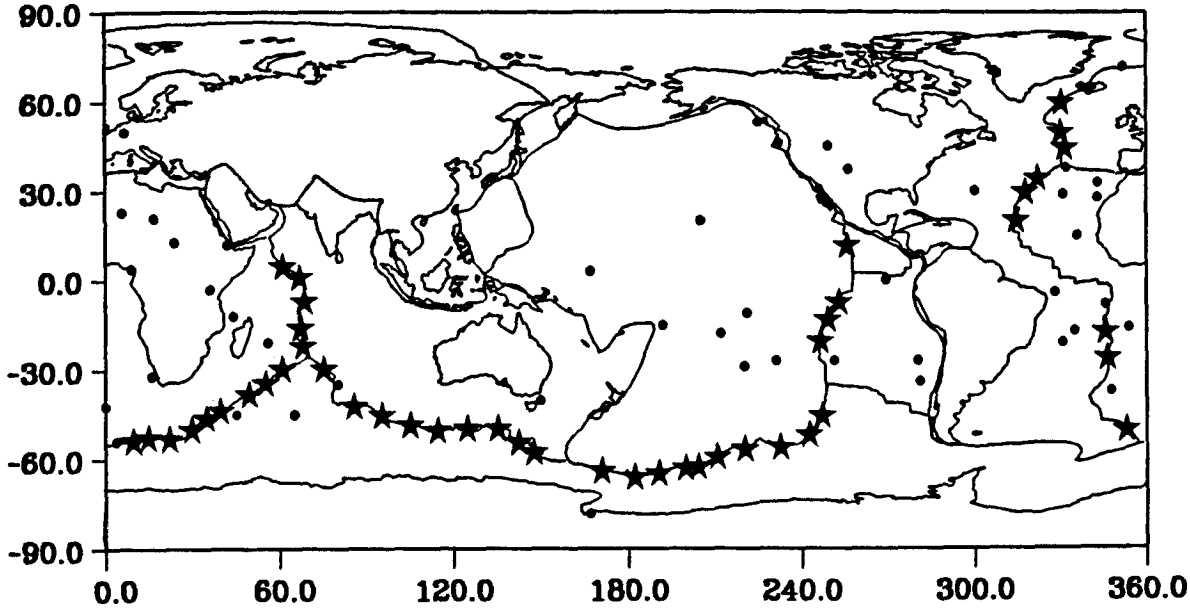

Figure 6.3, The data point distribution over the global mid-ocean ridge used in this study. A total of 46 points have been selected, and possible contaminations from hotspots, triple-junctions and fracture zones are avoided.

TABLE 6.1. Ridge Axis Data

Ridge	Plate Pair	Latitude deg	Longitude deg	Direction deg	Distance deg	Spreading Rate mm yr^{-1}
SW Indian	af-an	-53.45	9.65	37.94	71.84	13.74
SW Indian	af-an	-52.30	14.90	32.89	73.76	13.88
SW Indian	af-an	-52.80	22.25	26.60	77.89	14.13
SW Indian	af-an	-29.40	60.80	0.01	101.45	14.17
SW Indian	af-an	-49.80	29.80	19.85	81.04	14.28
SW Indian	af-an	-46.10	34.80	15.50	83.11	14.35
SW Indian	af-an	-34.30	55.15	2.20	96.74	14.36
SW Indian	af-an	-43.40	39.70	11.72	85.86	14.42
SW Indian	af-an	-37.90	49.40	5.28	92.34	14.44
Mid-Atlantic	af-na	60.20	330.25	97.93	56.90	20.49
Mid-Atlantic	af-na	34.40	321.85	103.55	53.72	22.41
Mid-Atlantic	af-na	50.10	330.10	97.15	66.93	22.51
Mid-Atlantic	af-na	44.85	331.60	97.62	72.00	23.27
Mid-Atlantic	af-na	29.80	317.50	102.92	59.04	23.84
Mid-Atlantic	af-na	20.25	314.30	101.94	68.99	25.95
Central-Indian	in-af	5.10	60.95	33.87	36.31	28.31
Mid-Atlantic	af-na	-49.85	353.15	74.05	115.28	32.17
Central Indian	in-af	1.40	66.60	34.09	43.06	32.64
Central Indian	au-af	-6.70	68.40	45.88	26.58	32.84
Mid-Atlantic	af-na	-16.95	346.05	78.44	81.94	35.23
Mid-Atlantic	af-na	-25.80	346.65	78.30	90.72	35.58
Central Indian	au-af	-15.60	67.10	57.60	32.82	39.78
Central Indian	au-af	-21.90	68.00	60.78	38.67	45.86
Pac. Anta	an-pa	-63.40	170.90	144.16	148.90	52.26
Pac. Anta	an-pa	-65.75	182.35	141.45	146.40	56.00
Pac. Anta	an-pa	-64.30	190.50	135.73	142.86	61.09
SE Indian	au-an	-29.35	74.95	44.94	55.39	62.23
Pac. Anta	an-pa	-62.60	199.70	129.79	138.83	66.62
Pac. Anta	an-pa	-62.10	204.10	127.32	137.16	68.80
SE Indian	au-an	-57.10	147.70	350.79	111.61	70.30
SE Indian	au-an	-41.80	85.40	40.55	70.07	71.08
SE Indian	au-an	-53.90	142.40	356.46	108.98	71.50
SE Indian	au-an	-49.40	135.20	3.47	104.51	73.20
SE Indian	au-an	-44.95	95.00	33.45	77.53	73.83
Pac. Anta	an-pa	-58.90	210.65	122.43	132.70	74.37
SE Indian	au-an	-49.25	124.70	11.29	97.71	74.93
SE Indian	au-an	-48.20	104.90	26.16	85.04	75.33
SE Indian	au-an	-49.90	114.50	18.88	91.50	75.59
Pac. Anta	an-pa	-56.20	220.20	117.00	127.82	79.93
Pac. Anta	an-pa	-55.60	232.50	111.22	124.46	83.44
Pac. Anta	an-pa	-51.55	242.50	105.84	118.74	88.72
Pac. Anta	an-pa	-45.10	246.80	103.17	111.78	93.96
Cocos	co-pa	11.90	255.70	81.89	25.20	98.94
E. Pac. Rise	nz-pa	-7.25	252.80	100.61	64.43	142.44
E. Pac. Rise	nz-pa	-13.05	248.75	102.46	70.91	149.22
E. Pac. Rise	nz-pa	-20.25	246.40	103.29	78.43	154.69

The first plate moves counterclockwise relative to the second plate. Direction is the spreading direction, which is measured clockwisely from north. Distance means the great circle distance between the pole and the selected point. Plate abbreviations: pa, Pacific; na, North America; sa, South America; af, Africa; co, Cocos; nz, Nazca; an, Antarctica; au, Australia.

6.3 S-wave velocity under mid-ocean ridges

It is generally believed that mid-ocean ridges are passive features that are caused by adjacent plates moving away. But another explanation suggests that mid-ocean ridges are caused by plumes from deep below. In order to understand the global mid-ocean ridge system, we selected 46 points on mid-ocean ridge axes which are based on the spreading rates and spatial distribution. Figure 6.3 shows the location of these points. Table 6.1 gives the coordinates, the great circle distances from poles, the spreading directions, and the spreading rates at different sites. These points provide an almost uniform distribution of spreading rates between 13.7 and 155.0 mm/yr. The spreading rates and directions were calculated by using the NUVEL-1 model (DeMets *et al.*, 1990). All spreading rates given are full spreading rates. The spatial distribution of these points covers every major spreading center, and the possible contaminations from hotspot, triple-junction and fracture zone are avoided.

S-wave velocity variations at four depths under mid-ocean ridge axes as a function of spreading rate are shown in Figure 6.4. The depths vary from 36 to 100 km. Because the resolution wavelength in the present study is about 1,000 km, we cannot obtain velocity structure exactly at each point. Each symbol in Figure 6.4 is a stacked result for every 10 degrees along ridges with a centered location. Triangles, stars and solid circles indicate the locations of data in the Pacific, Indian and Atlantic Oceans, respectively. All of the points are associated with low velocity anomalies, a fact is consistent with other studies (*e.g.*, Nakanishi and Anderson, 1984, 1986; Woodhouse and Dziewonski, 1984; Nataf *et al.* 1986; Tanimoto 1986a,b; Zhang and Tanimoto, 1989; Montagner and Tanimoto, 1990).

Figure 6.4, S-wave velocity variation at four different depths under the global mid-ocean ridge as a function of spreading rate. Triangles, stars and solid circles indicate the location of data in the Pacific, Indian and Atlantic Ocean, respectively. Each symbol is a stacked result every 10 degrees along ridges with a centered location. The spreading rates and directions are obtained by using the NUVEL-1 model.

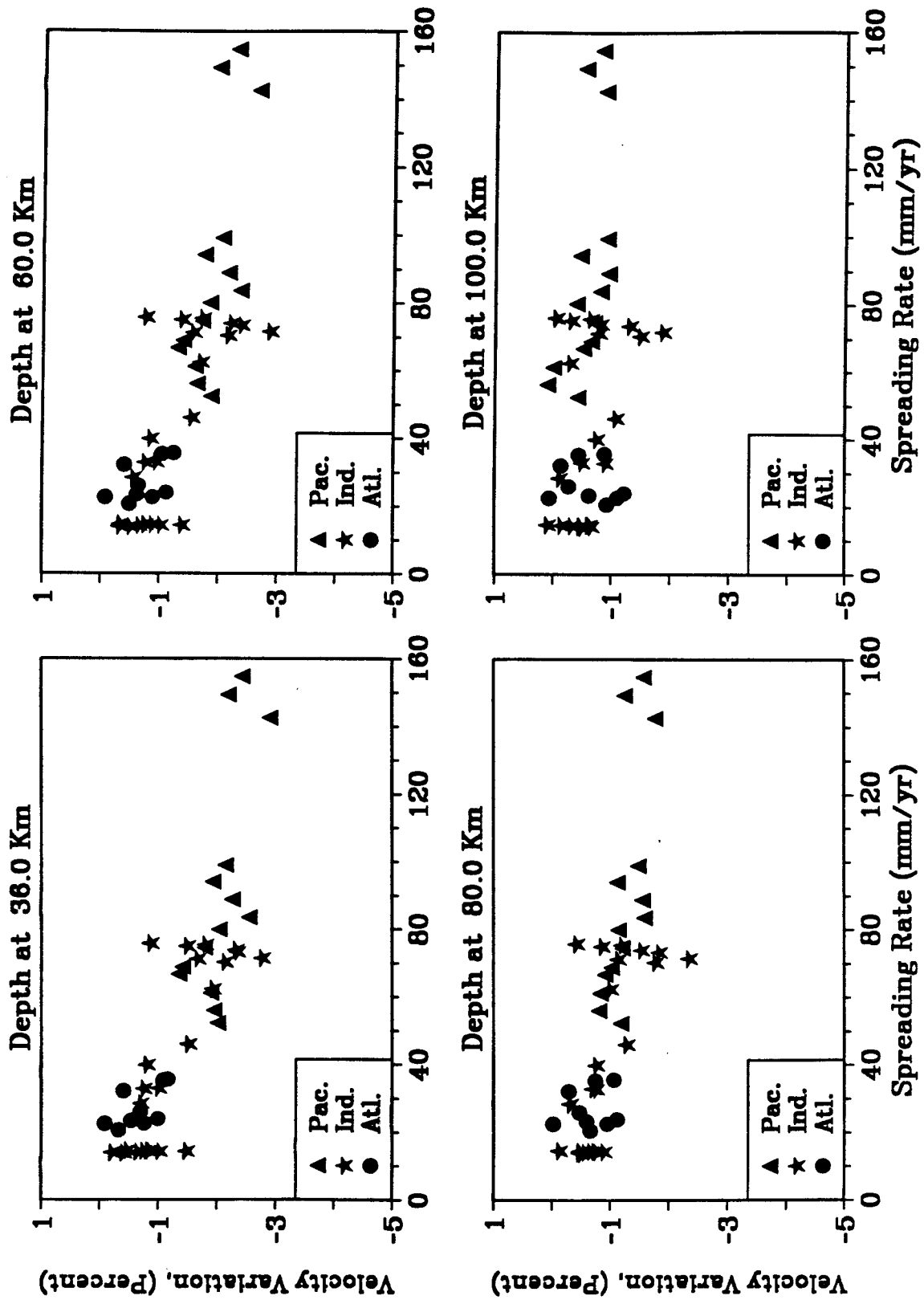
Depth at 36.0 Km
Depth at 60.0 Km
Depth at 80.0 Km
Depth at 100.0 Km
Pac.
Ind.
Atl.
Velocity Variation, (Percent)
Spreading Rate (mm/yr)
1
-1
-3
-5
0
40
80
120
160

The velocity results at shallow depths (36 and 60 km) are strongly correlated with the spreading rate of ridges. The faster the spreading rate, the slower the velocity. But the correlation decreases for deeper results and almost vanishes at 100 km. The results strongly suggest that mid-ocean ridges are shallow features. The low velocity anomaly is also consistent with geodynamic explanations. When the adjacent plates are passively stretched away, the melting temperature falls as the pressure is reduced, and then some mantle rocks under ridges will be melted. The hot, melted asthenospheric materials well up to fill the space generated by the stretching and thinning lithosphere. The slower velocity associated with the faster spreading rate can be interpreted as more melting yield that is due to the quick decrease in presure.

In order to see the average S-wave velocity under different ridges, four depth cross-sections, almost parallel to the spreading directions of the ridges, are shown in Figures 6.5a-d. These are stacked sections along the different ridge axes. The axis is aligned at the center of the figures, denoted by the arrow. The stacked section of the ridge axis is shown with stars in the top figure. For clarification, we give the azimuth of the cross line in the figure, which is measured clockwisely from north. The velocity scale (in percent) is given on the bottom of the figures. Contours are at every 0.5 percent interval and patterns change every percent.

The most notable feature in Figures 6.5a-d is the concentration of low velocity anomalies (less than -1 percent) in the top 100 km. The minimum velocity is shallower than 50 km, consistent with Figure 6.4. It should be born in mind that our collected surface wave data have periods longer than 75 seconds, and that our S-wave velocity results do not have enough resolution in the crust (less than 25 km) (see Chapter 4). That is the reason why we did not observe

low velocity anomalies near the surface. We believe our S-wave velocity results have good resolution from 25 km down to 350 km (Chapter 4), but in general we cannot see any strong low velocity anomaly deeper than 300 km, which would be associated with the active upwelling hypothesis. It strongly suggests that mid-ocean ridges are shallow, passive features, and the slow velocity anomaly, as we discussed previously, is caused by the partial melting that is due to the decompression effects. The fastest spreading East Pacific Rise does have a 0.5 percent contour that extends to more than 200 km in depth, but this could be interpreted as induced upwelling, which is due to very fast spreading.

Another notable feature in Figures 6.5a-d is that the magnitude and the size of the low velocity anomalies increase from the Mid-Atlantic Ridge with the lowest, the Southeast Indian Ocean Ridge, the Pacific-Antarctic Ridge to the East Pacific Rise with the highest. This order is consistent with the spreading rate variation for different ridges (Table 6.1). We suggest that the velocity variation is mainly caused by partial melting associated with the spreading rate. Ridges with a fast spreading rate are associated with more melted material comming out from asthenosphere, causing the lower magnitude and the larger size of low velocity anomaly than that of slow spreading ridges. This is consistent with the model predicted by Scott and Stevenson (1989); the faster the spreading rate, the more the melt fraction. The correlation decrease with depth can be explained by the partial melting fraction decrease with depth. The features shown in Figures 6.4 and 6.5a-d suggest that mid-ocean ridges are shallow, passive features.

Figure 6.5, (a). Stacked depth cross-section of S-wave velocity along the East Pacific Rise. The stars in the top figure are the locations of stacked parts. The azimuth (measured clockwisely from north) of the cross-section is 105.0 degrees. The direction of the cross-section is also labeled at the bottom of the figure. The ridge axis is aligned along the center of the figure. Contour intervals are at every 0.5 percent and patterns change every percent. (b). Same as Figure 6.5a, but for the Pacific Antarctic Ridge, and the azimuth is 115.0 degrees. (c). Same as Figure 6.5a, but for the Southeast Indian Ocean Ridge, and the azimuth is 10.0 degrees. (d). Same as Figure 6.5a, but for the South Mid-Atlantic Ridge, and the azimuth is 90.0 degrees.

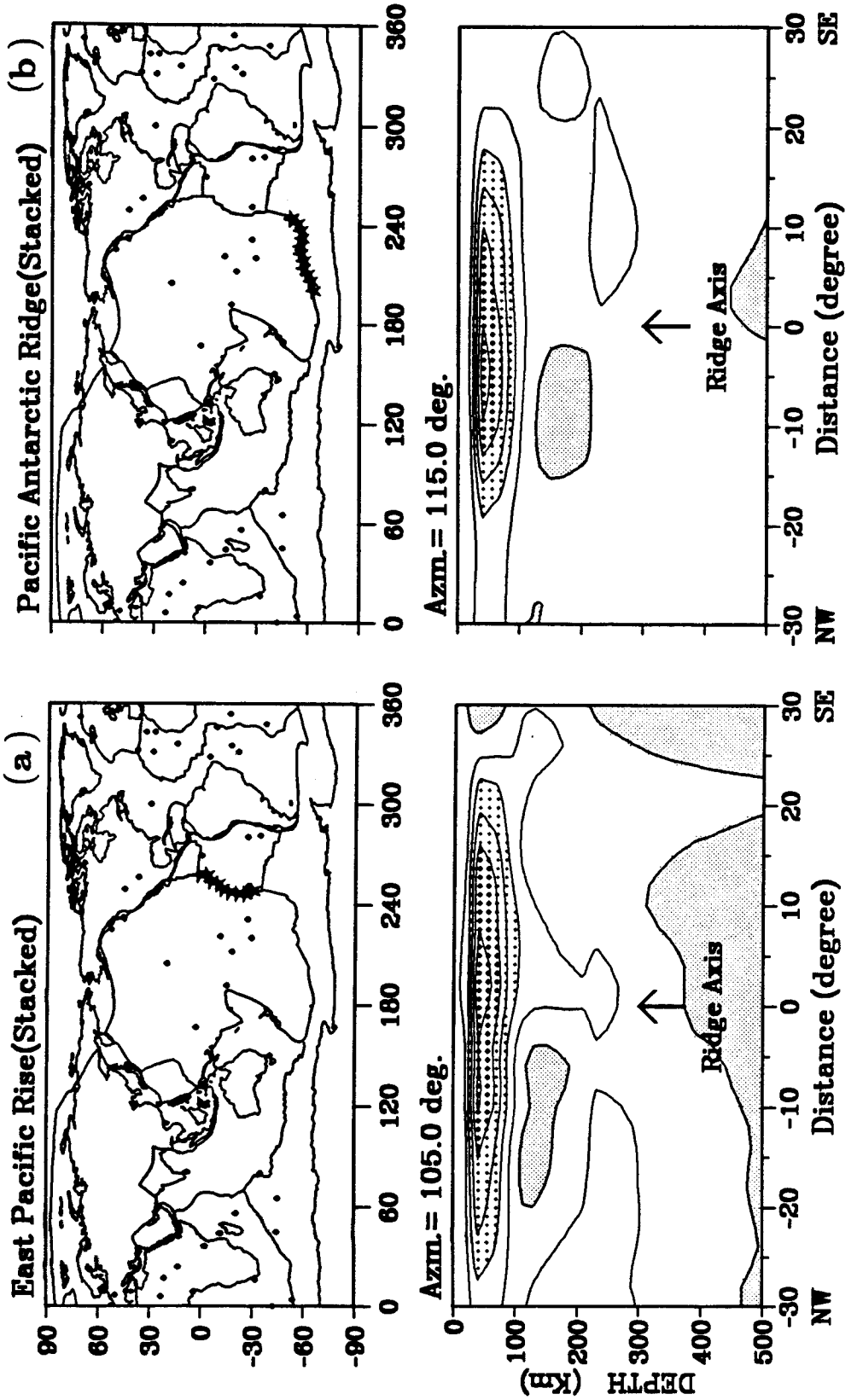
East Pacific Rise(Stacked)
(a)
Pacific Antarctic Ridge(Stacked)
(b)
90
60
30
0
-30
-60
-90
0
60
120
180
240
300
360
Azm.= 105.0 deg.
Azm.= 115.0 deg.
Ridge Axis
Ridge Axis
DEPTH (KM)
0
100
200
300
400
500
-30
-20
-10
0
10
20
30
NW
SE
Distance (degree)
-5.0
5.0

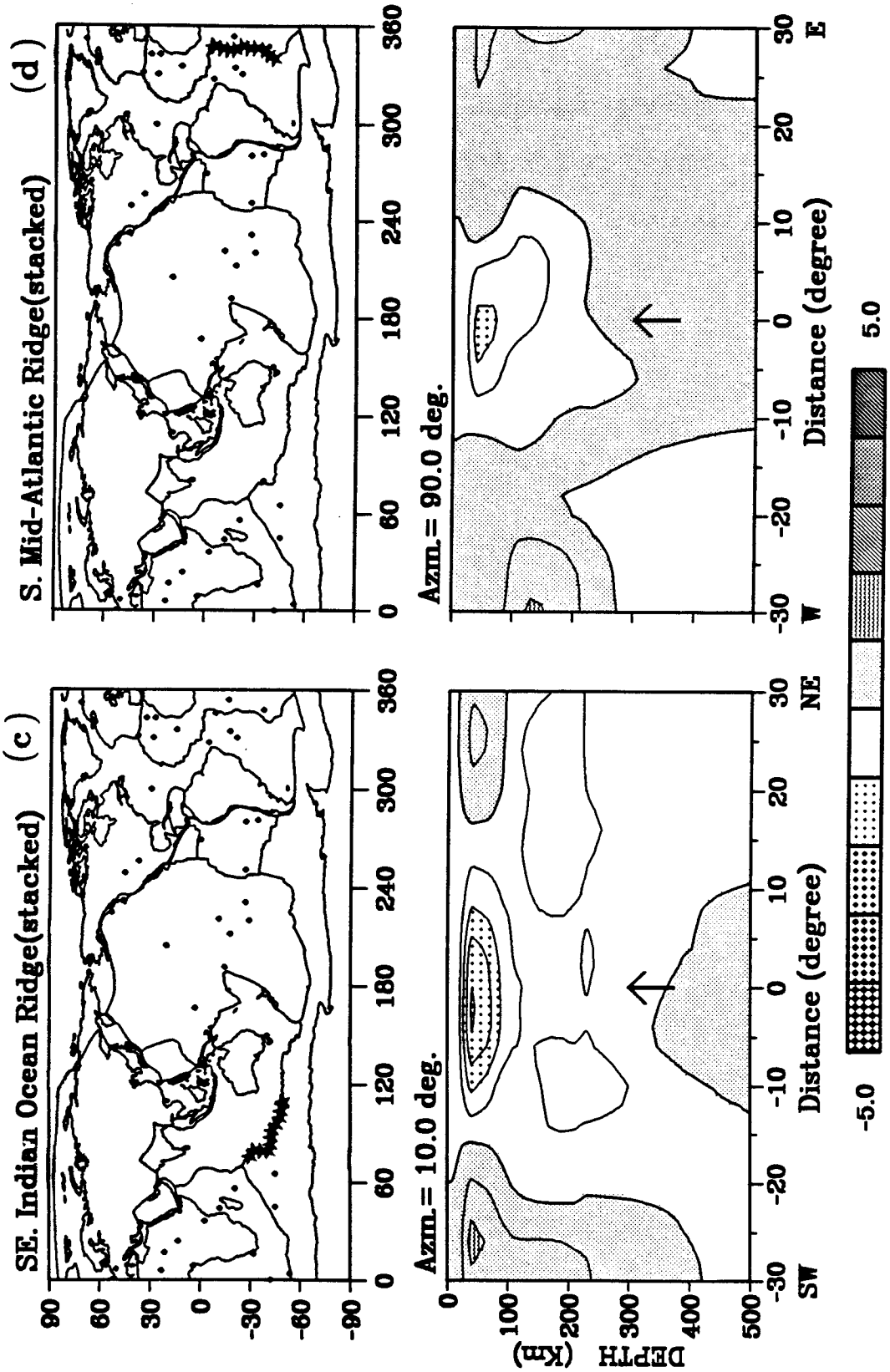
SE. Indian Ocean Ridge(stacked)
(c)
S. Mid-Atlantic Ridge(stacked)
(d)
Azm.= 10.0 deg.
Azm.= 90.0 deg.
DEPTH (Km)
Distance (degree)
SW
NE
W
E
-5.0
5.0

It is well known that the axial bathymetry and the gravity of mid-ocean ridges seem to be controlled by spreading rates (Macdonald, 1982, 1983, 1986; Small and Sandwell, 1989). We now have new information about the mid-ocean ridge, and any mid-ocean ridge model should satisfy these constraints.

6.4. Hotspots

Hotspots are different from mid-ocean ridges. They are caused by plumes generated from deep (probably at core mantle boundary), and mid-ocean ridges are passive, shallow features that are caused by adjacent plates moving away. Because of the data limitation, only recently have seismic wave results found that some major hotspots are associated with low velocity anomalies (Zhang and Tanimoto, 1987, 1989, 1991; Wong, 1989).

Figures 6.6a-d are four vertical cross-sections of the present S-wave velocity results under four major hotspots: Hawaii, Iceland, Azores and Tristan de Cunha. The total length of the cross-section is 60 degrees. The middle point is at the hotspot, denoted by an arrow. The same conventions as in Figure 6.4 have been used. For reference, the locations of the cross-sections are plotted on the top of each figure. The line with stars is the cross-section on the surface of the Earth. The cross-section at the Iceland hotspot goes from Greenland to western Europe. The section across the Hawaii hotspot follows the Hawaiian chain. The other two cross-sections are parallel to the longitude. The coordinate of the center point (hotspot) and the azimuth of the cross-section are given in the map. The direction of the cross-section is also labeled on the bottom of the figure.

Figure 6.6, (a). Depth cross-section of S-wave velocity along the Hawaiian Chain. The top figure is the location of the cross line. Hawaii hotspot is at the center. Same convention as in Figure 6.5a has been used. (b). Same as Figure 6.6a, but for the Iceland hotspot. (c). Same as Figure 6.6a, but for the Azores hotspot. (d). Same as Figure 6.6a, but for the Tristan de Cunha hotspot.

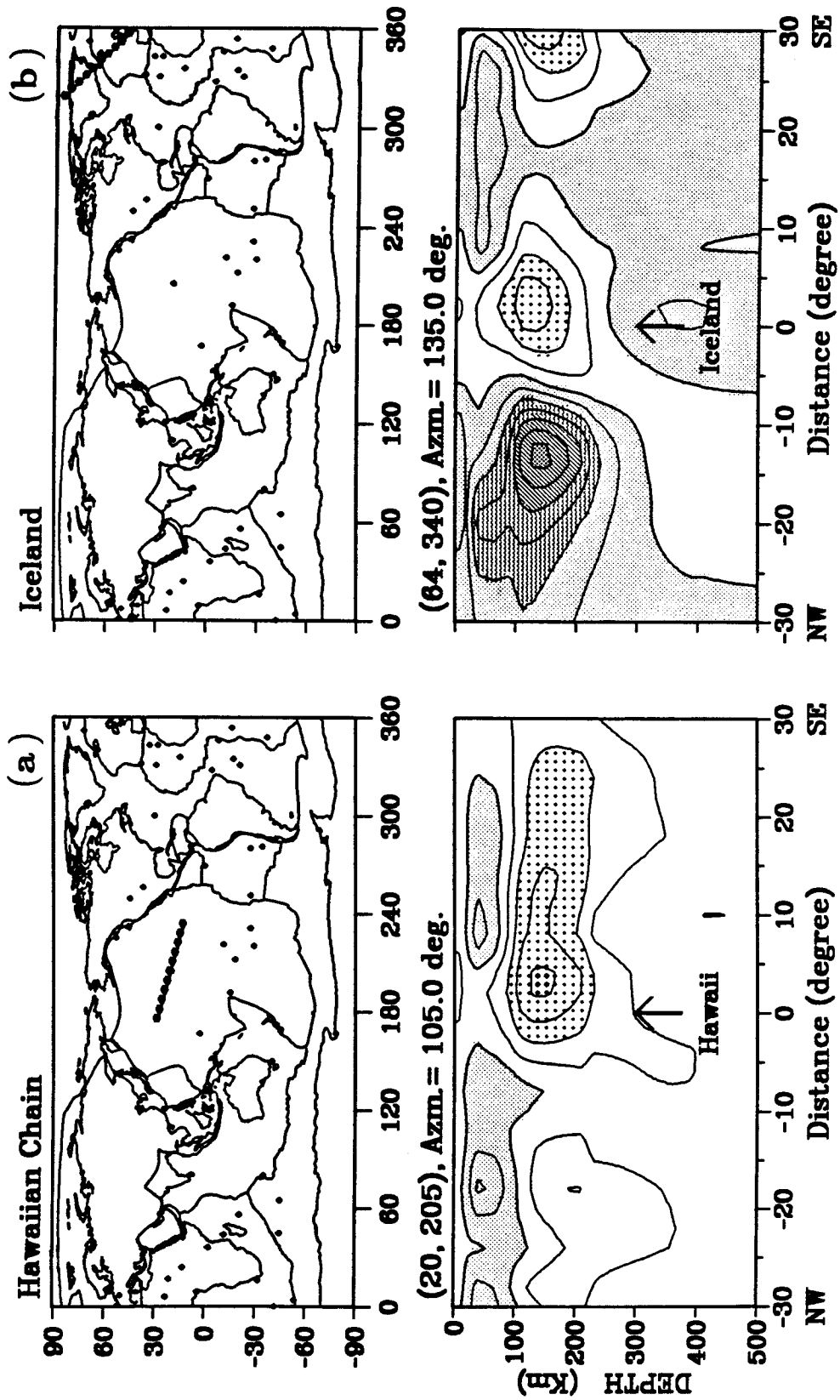
(a)
Hawaiian Chain
(b)
Iceland
(20, 205), Azm.= 105.0 deg.
(64, 340), Azm.= 135.0 deg.
Hawaii
Iceland
DEPTH (KB)
Distance (degree)
NW
SE
-5.0
5.0

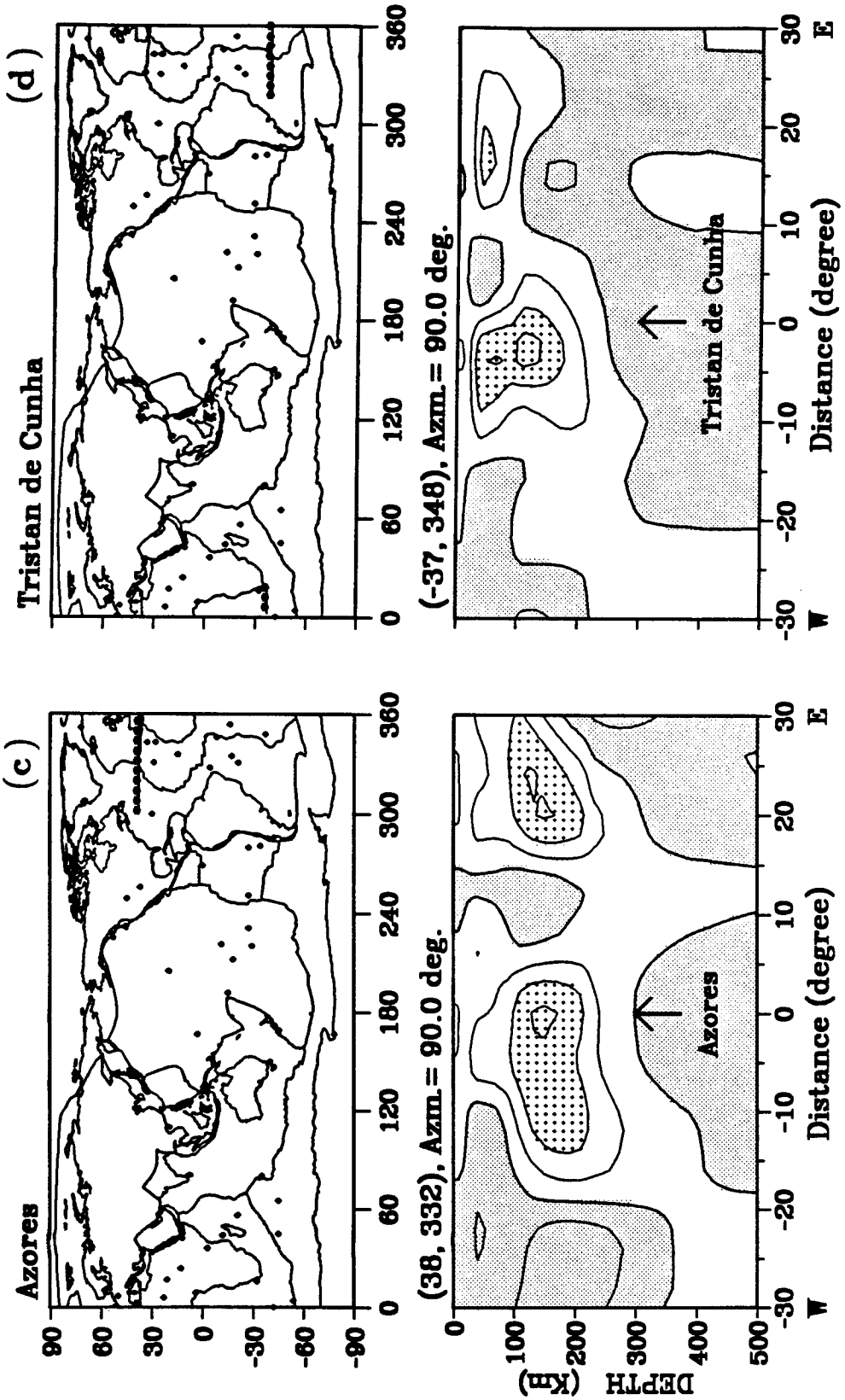
(c)
Azores
(d)
Tristan de Cunha
(38, 332), Azm.= 90.0 deg.
(-37, 348), Azm.= 90.0 deg.
DEPTH (Km)
Distance (degree)
W
E
-5.0
5.0

Figures 6.6a-d show that all of these four hotspots are connected with low velocity anomalies, and the minimum velocities (1-2 percent lower than average) are located between 100 and 200 km with horizontal lengths of about 1000 to 2000 km. This is consistent with the mantle plume hypothesis (Morgan, 1972; Turcotte and Oxburgh, 1978; Courtney and White, 1986; White and McKenzie, 1989; Duncan and Richards, 1991). A plume of about a few hundred kilometers in the horizontal dimension travels up from the deep mantle, and creates a mushroomlike head near the bottom of the lithosphere because of horizontal outward flow from its center (Figure 6.7). The plume may have partial melting and higher temperature, approximately 100-200 degrees, at the center than the surrounding mantle. Isothermal contours are elongated horizontally near the bottom of the lithosphere. We believe that the low velocities detected in the present study under these hotspots are related to the mushroom head with a diameter of more than 1000 km. The higher temperatures in the mushroom head than those of the surrounding mantle and partial melting are probably the main cause of the low velocity anomaly. Stems of plumes are presumably narrower than our resolution (about 1000 km), thus making it impossible to detect them in these plots.

Figure 6.8 shows the geoid, bathymetry and the cross-section of S-wave velocity along the Mid-Atlantic Ridge. The top part is the geoid, which is obtained from the GEM-T1 (Marsh *et al.* 1988) model, and the unit is meter. The middle part is the bathymetry, the unit is kilometer. The bottom part is the cross-section of S-wave velocity results. We have used the same convention as in Figure 6.4. The horizontal axis is along the latitude. We also marked the four hotspots, Iceland, Azores, Ascension and Tristan de Cunha, which are on/or near the Mid-Atlantic ridge.

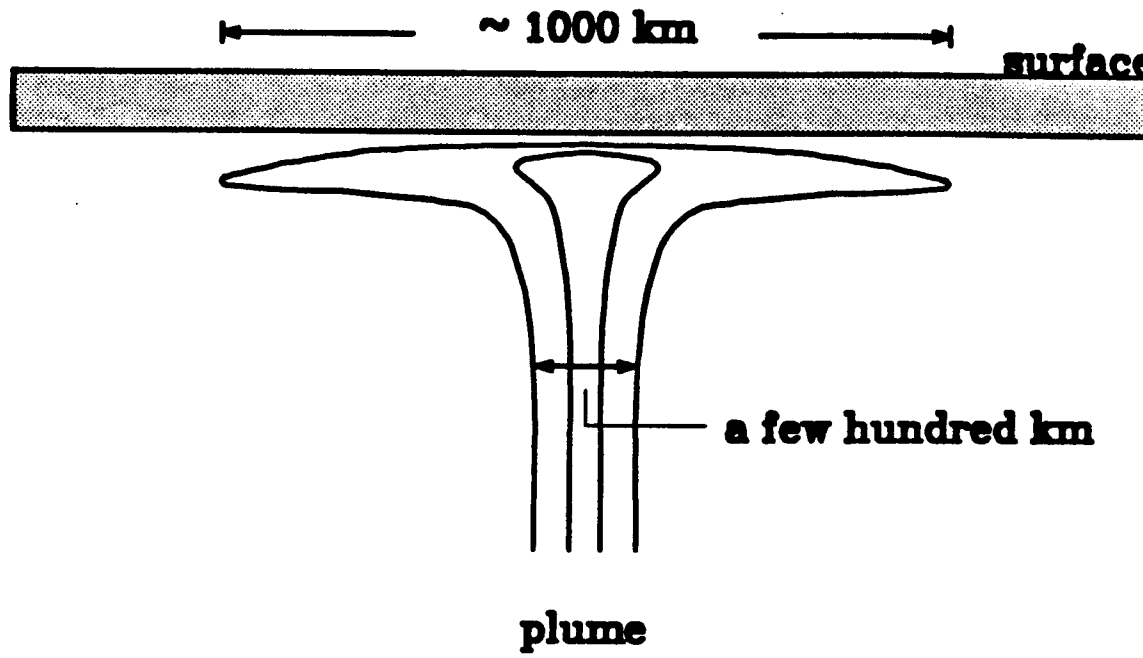

Figure 6.7, Schematic isothermal contours produced by a plume. In the interior, the horizontal size of a plume is a few hundred kilometers, but near the bottom of the lithosphere, it becomes elongated by horizontal outward flow. Temperature at the center is 100-200 degrees higher than that of the surrounding mantle

There is a clear correlation between bathymetry, geoid and seismic velocity along the north mid-Atlantic ridge. Where the geoid is high, such as over the Azores triple junction, the bathymetry is relatively high and the S-wave velocity is low; where the geoid is low, such as at 10°N, the bathymetry is low and the S-wave velocity is relatively high. However, this correlation for the south mid-Atlantic Ridge is not clear. There are clear velocity effects for the Iceland, Azores and Tristan de Cunha hotspots, consistent with Figures 6.6b-d, but there is no stronger low velocity anomaly at the Ascension hotspot. The possible explanation is that the Ascension hotspot has a small anomaly effect which is smeared in our solution.

From these observations, the differences between hotspots and global mid-ocean ridges are clear. They have different sources and different natures (passive or active upwelling), and the seismic velocities at hotspots and mid-ocean ridges are different. We would like to make the following conjecture: the depth of the low velocity anomaly can serve as a criterion for distinguishing the nature (passive or active) of upwelling. If the low velocity anomaly is shallow, a passive mechanism is suggested, while a deep, low-velocity anomaly suggests an active mechanism.

Figure 6.8, Geoid, Bathymatry and the cross-section of S-wave velocity structure along the Mid-Atlantic Ridge. Same convention as in Figure 6.5 has been used for the velocity cross-section. Four hotspots on or near the ridge are marked at the top of the figure.

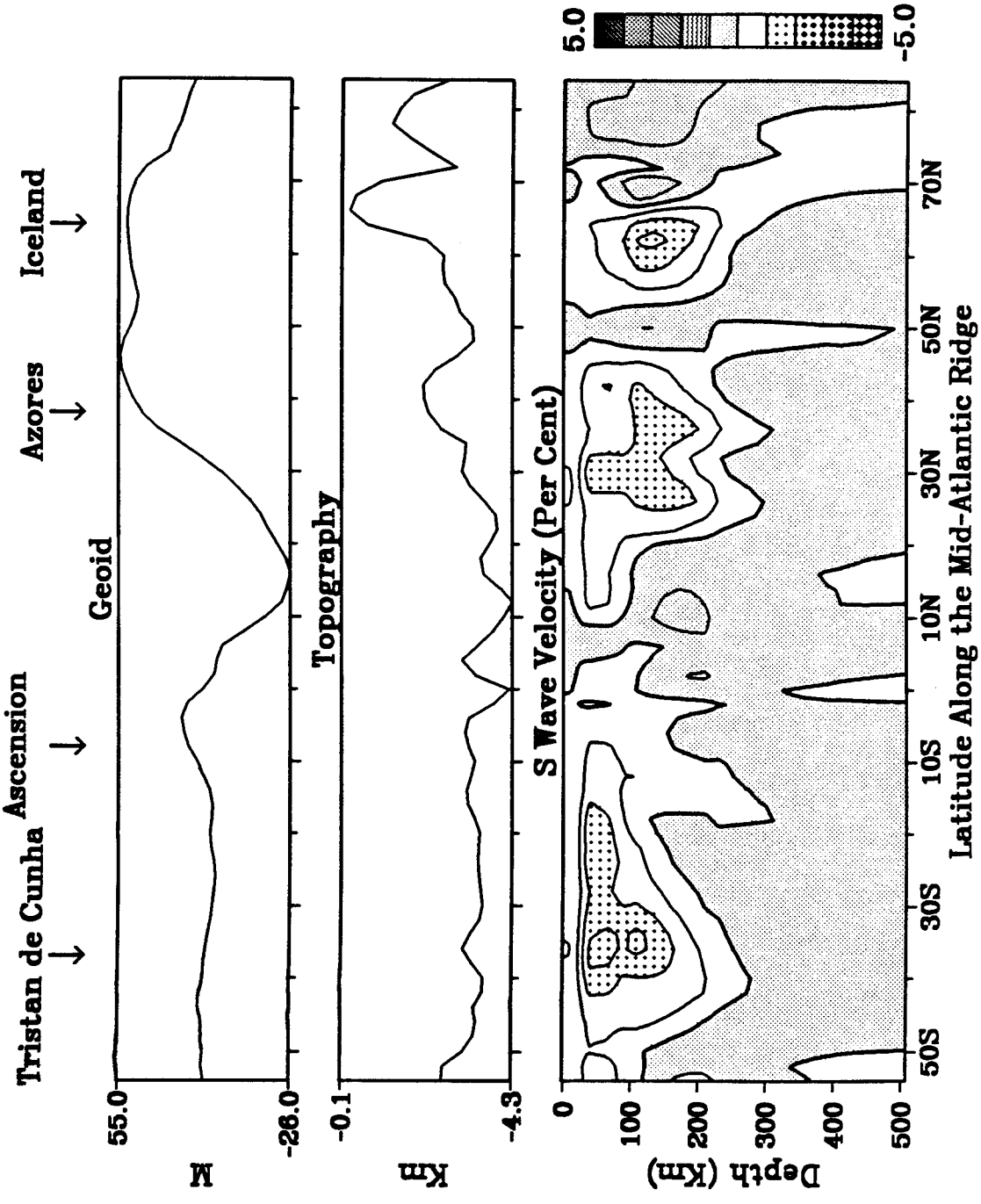
Tristan de Cunha
Ascension
Geoid
Azores
Iceland
M
55.0
-26.0
Topography
Km
-0.1
-4.3
S Wave Velocity (Per Cent)
5.0
-5.0
Depth (Km)
0
100
200
300
400
500
50S
30S
10S
10N
30N
50N
70N
Latitude Along the Mid-Atlantic Ridge

6.5. Rift Valley

Rift valleys occur in diverse tectonic environments that result from the continuous two-dimensional evolution of the multi-plate mosaic of the Earth and also from the interaction between mantle processes and the overlying lithosphere. Mechanisms of rift valley formation generally fall into two classes: active and passive. Although there have been a vast number of studies about rift valleys (Logatchev and Florensov, 1978; Sengör and Burke, 1978; Turcotte and Emerman, 1983; Crough, 1983b; Gettings *et al.*, 1986; Mcguire and Bohannon, 1989; Bohannon *et al.*, 1989), their origin is still the subject of controversy. For example, some authors (McGuire and Bohannon, 1989; Bohannon *et al.*, 1989) describe the African Rift Valley as a passive rift, but others (Sengör and Burke, 1978; Gettings *et al.* 1986, Dixon *et al.*, 1989, 1991) argue it otherwise.

All of the previous studies of the Red Sea area are based on surface observation (McGuire and Bohannon, 1989; Bohannon *et al.*, 1989; Dixon *et al.*, 1989, 1991; Dixon, 1990), and crustal structure (Gettings *et al.* 1986), and may lead us to reach different conclusions. Shown in Figures 6.9a-b are two cross-sections in the Red Sea area. One is along the Red Sea, and the other is almost perpendicular to it and crosses the East African Rift. The same conventions as in Figure 6.5 have been used. The north and south ends are denoted in the figure, as well as the locations of the cross-sections. The Red Sea is associated with a low velocity anomaly as expected, but the anomaly is clearly deeper than those for ridges (Figures 6,5a-d). Active upwelling is clearly indicated and furthermore, the shape of the low velocity anomaly suggests that material may be fed by hotspots at the southern end (Afar). The cross-section for the East African Rift also suggests an active origin, fed by a deeper low velocity

anomaly from the southwest (under Africa).

The Baikal Rift Valley is a narrow, linear feature in Central Asia, extending SW to NE for 2500 km. It has no evident structural connection with the world rift system. It has been suggested that the Baikal rift is the result of the Indian-Eurasia collision (Molnar and Tapponnier, 1975; Zonenshain and Savostin, 1981; Diament and Kogan, 1990), *i.e.*, the Baikal rift is passive. But Logatchev *et al.* (1983) claim it is caused by the development of wide asthenospheric upwellings beneath the Baikal rift. Figures 6.10a-b are two cross-sections in the Baikal Lake area. One is along the rift region and the other is perpendicular to it. Although the low seismic velocity anomalies are associated with the Baikal rift valley, these two cross-sections are different from Figures 6.9a-b. It has a small magnitude of low velocity anomaly which does not penetrate deeply. The seismic velocities on different sides are almost the same. The results suggest that the Baikal Rift is formed by stretching of the lithosphere; *i.e.*, it is passive.

Figure 6.9, (a). Same as Figure 6.6a, but for the Red Sea area. This section crosses the East African Rift Valley. (b). Same as Figure 6.9a, but along the Red Sea.

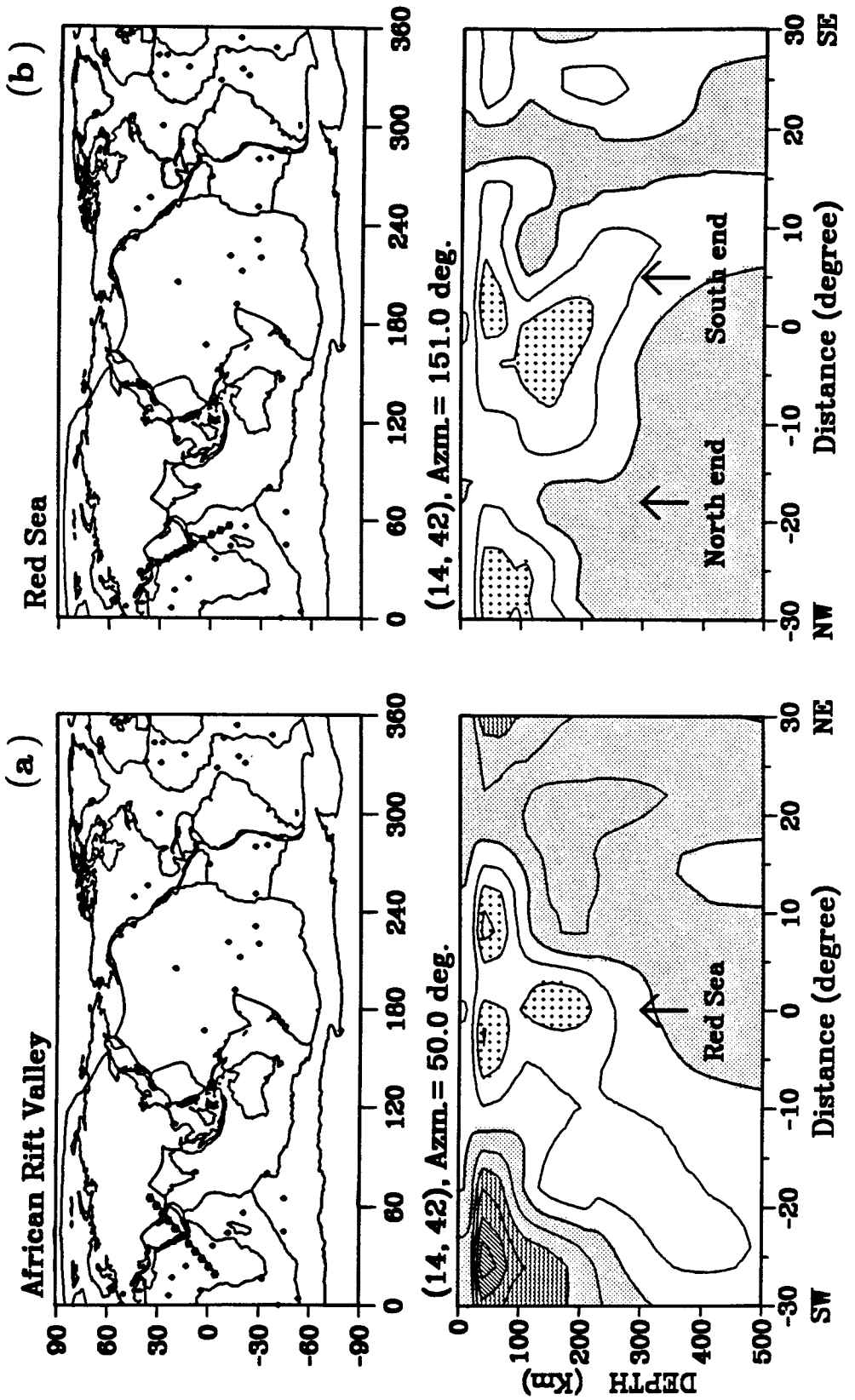
(a)
African Rift Valley
90
60
30
0
-30
-60
-90
0
60
120
180
240
300
360
(b)
Red Sea
(14, 42), Azm.= 50.0 deg.
Red Sea
SW
NE
Distance (degree)
(14, 42), Azm.= 151.0 deg.
North end
South end
NW
SE
Distance (degree)
DEPTH (Km)
0
100
200
300
400
500
-30
-20
-10
0
10
20
30
-5.0
5.0

Figure 6.10, (a). Same as Figure 6.9a, but along the Baikal Rift Valley. (b). Same as Figure 6.10b, but perpendicular to the Baikal Rift Valley.

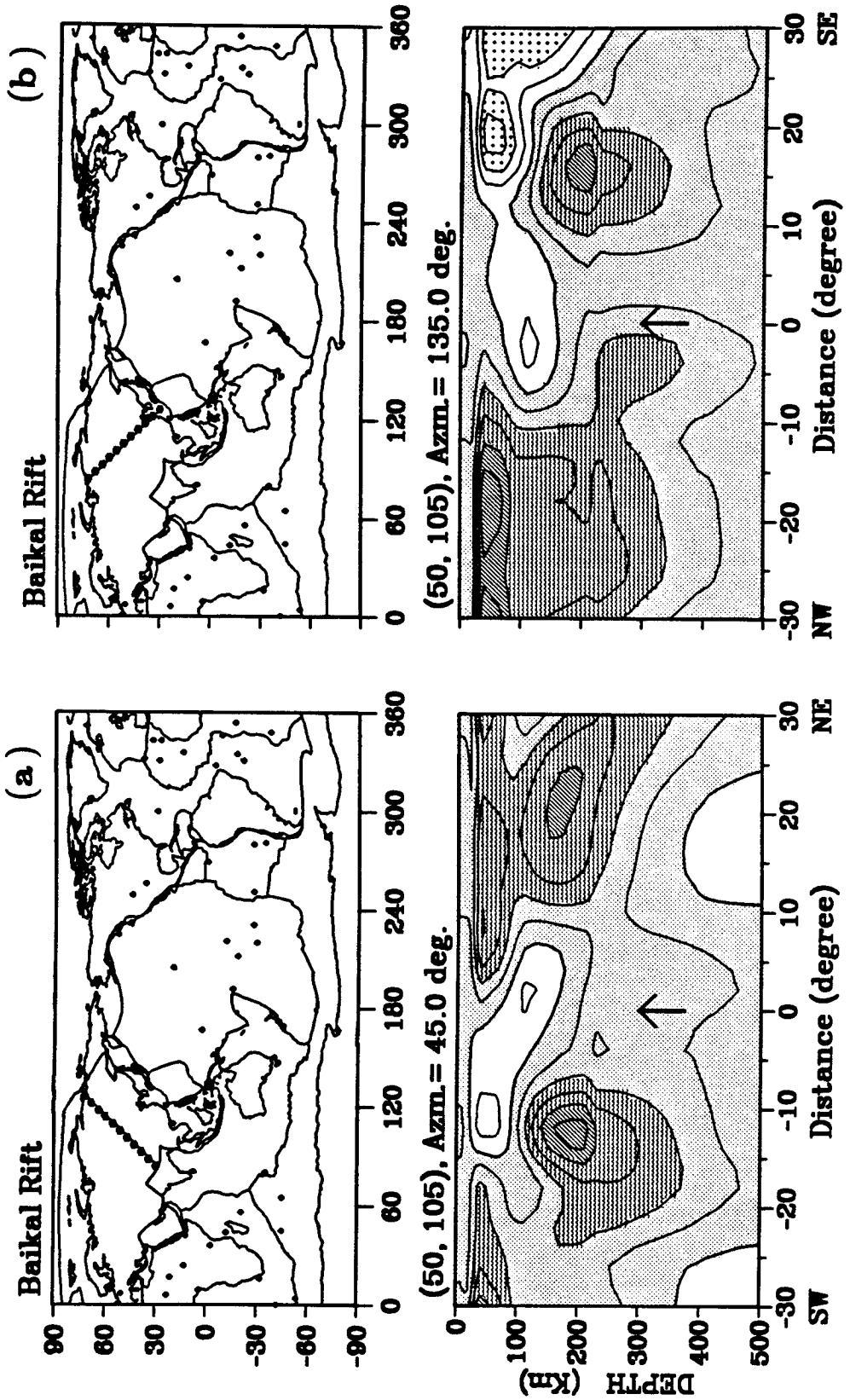
(a)
Baikal Rift
90
60
30
0
-30
-60
-90
0
60
120
180
240
300
360
(b)
Baikal Rift
(50, 105), Azm.= 45.0 deg.
(50, 105), Azm.= 135.0 deg.
DEPTH (Km)
0
100
200
300
400
500
SW
NE
NW
SE
-30
-20
-10
0
10
20
30
Distance (degree)
-5.0
5.0

6.6 Summary

Without the benefit of detailed upper mantle structure, it is impossible to study global tectonic features. The current resolution in global tomography has improved to a level of about 1000 km because of a rapid increase of digital data during the last decade. We have started seeing various important tectonic features.

S-wave velocities under the global mid-ocean ridge are strongly correlated with spreading rates at shallow depths, but the correlation decreases for depths and vanishes below 100 km. The low velocity anomalies under ridges are limited in the top 100 km, and the minimum velocity is shallower than 50 km. The width of the low velocity anomalies increases with spreading rates.

The low velocity anomalies associated with hotspots are relatively deep, and the minimum velocity is located typically between 100 and 200 km in depth. The difference in depth of low velocity anomalies suggests that mid-ocean ridges and hotspots are connected with different mechanisms. The active plume under a hotspot is creating low velocity anomalies below the lithosphere, and the mid-ocean ridge is a passive shallow feature. The partial melting that is due to decompression effects may be the main cause of the low velocity anomalies near the surface.

The cross-sections of seismic velocity at the Red Sea suggest that it is associated with active upwelling. The shape of the low velocity anomaly indicates that material may be fed by hotspots at Afar and in northeastern African. The velocity structure at the Baikal Rift suggests that it is associated with a passive mechanism.

References

Akaike, H., 1974, A new look at the statistical model identification, *IEEE Trans. Automat. Control*, AC-19, 716-723.

Akaike, H., 1979, A Bayesian extension of the minimum AIC procedure of autoregressive model fitting, *Biometrika, 66*, 237-242.

Akaike, H., 1980, Likelihood and Bayes procedure, *Bayesian Statistics,* J. M. Bernado et al. ed., University Press, Valencia, Spain, *pp*141-166.

Aki, K., Christoffersson A., and Husebye E.S., 1976 Determination of the three-dimensional seismic structures of the lithosphere. *J. Geophys. Res., 82*, 277-296.

Aki, K. and Richards P.G., 1980, *Quantitative seismology theory and methods,* Vol. II, W.H. Freeman, San Francisco.

Anderson, D. L. and Toksöz , M. N., 1963, Surface waves on a spherical Earth, *J. Geophys. Res., 68*, 3483-3500.

Anderson, D. L. and Regan J., 1983, Uppermantle anisotropy and the oceanic lithosphere, *Geophys. Res. Lett., 10*, 841-844.

Anderson, D. L. and Bass J., 1984, Mineralogy and composition of the upper mantle, *Geophys. Res. Lett., 11*, 637-640.

Anderson, D. L., 1990, Geophysics of the continental mantle: an historical perspective, in *Continental Mantle*, Menzies M.A.*ed.*, Clarendon press, Oxford, *pp*1-30.

Anderson, O. L., Schreiber E., Liebermann R. C. and Soga M., 1968, Some elastic constant data on minerals relevant to geophysics, *Rev. Geophys., 6*, 491-524.

Anderson, R. N., Spariosu D. J., Weissel J. K., and Hayes D. E., 1980, The interrelation between variations in magnetic anomaly amplitudes and basalt magnetizations and chemistry along the Southeast Indian Ridge, *J. Geophys. Res., 85,* 3883-3898.

Anderson, R. N. and Skilbeck J. N., 1981, Ocean heat flow, in *The Sea,* V.7, Wiley-Intersciences Publication, New York.

Backus, G. E., 1988, Bayesian inference in geomagnetism, *Geophys. J. Int., 92,* 125-142.

Berger, J. O., 1985, *Statistical decision theory and Bayesian Analysis,* Springer-Verlag, New York.

Bohannon, R. G., Naeser C. W., Schmidt D. L. and Zimmerman R. A., 1989, The timing of uplift, volcanism, and rifting peripheral to the Red Sea: a case for passive rifting, *J. Geophys. Res., 94,* 1683-1701.

Bonatti, E., 1990, Not so hot "hot spots" in the oceanic mantle. *Science, V. 250,* 107-111.

Box, G. and Tiao G., 1973, *Bayesian inference in statistical analysis,* Addison-Wesley, Reading, MA.

Brune, J. N., Nafe J. E., and Oliver J. E., 1960, A simplified method for the analysis and synthesis of dispersed wave trains, *J. Geophys. Res., 65,* 287-304.

Burke, K. C. and Wilson J. T., 1976, Hot spots on the Earth's surface, *Sci. Am., 235,* 46-57.

Canas, J. A., 1980, Rayleigh wave propagation and attenuation across the Atlantic Ocean, *Ph. D. thesis,* Saint Louis University.

Canas, J. A. and Mitchell B. J., 1981, Rayleigh wave attenuation and its variation across the Atlantic Ocean, *Geophys. J. R. astr. Soc., 67,* 159-176.

Chase, C. G. and McNutt M. K., 1982, The geoid: effect of compensated topography and uncompensated oceanic trenches, *Geophys. Res. Lett. 9,* 29-32.

Chen, Y. and Morgan W. J., 1990a, Rift valley/no rift valley transition at mid-ocean

ridges, *J. Geophys. Res., 95*, 17,571-17,581.

Chen, Y. and Morgan W. J., 1990b, A nonlinear rheology model for mid-ocean ridge axis topography, *J. Geophys. Res., 95*, 17,583-17,604.

Clayton., R., and Comer R., 1983, A tomographic analysis of mantle heterogeneities from body wave travel times (Abstract), *EOS, Trans. Am. Geophys. Union, 64*, 776.

Cochran, J. R., 1979, An analysis of isostasy in the world's oceans 2. Mid-ocean ridge crests, *J. Geophys. Res., 84*, 4713-4729.

Courtney, R. C. and White R. S., 1986, Anomalous heat flow and geoid across the Cape Verde Rise: evidence of Dynamic support from a thermal plume in the mantle, *Geophys. J. R. astr. Soc., 87*, 815-867.

Craig, C. H. and McKenzie D., 1986, The existence of a thin low-viscosity layer beneath the lithosphere, *Earth Planet. Sci. Lett., 78*, 420-426.

Creager, K. C. and Jordan T., 1986, Aspherical structure of the core-mantle boundary from PKP travel times, *Geophys. Res. Lett., 13*, 1497-1500.

Crough, S. T. and Jurdy D. M., 1980, Subducted lithosphere, hotspots, and the geoid, *Earth Planet Sci. Lett., 48*, 15-22.

Crough, S. T., 1983, Hotspot swells, *Ann. Rev. Earth Planet Sci., 11*, 165-193

Crough, S. T., 1983b, Rifts and swells: geophysical constraints on causality, *Tectonophysics,94*, 23-37.

Davis, E. E., 1989, Thermal aging of oceanic lithosphere, *CRC handbook of seafloor heat flow,*, Wright J. A. and Louden K. E., CRC press.

Davis, J. H., 1990, Some problems in mantle structure and dynamics. *Ph.D. thesis, California Institute of Technology.*

DeMets, C. Gordon R. G., Argus D. F. and Stein S., 1990, Current plate motions, *Geophys. J. Int., 101*, 425-478.

Detrick, R. S. and Crough S. T., 1978, Island subsidence, hot spots, and lithospheric thinning, *J. Geophys. Res., 83*, 1236-1244.

Diament M. and Kogan M., 1990, Longwavelength gravity anomalies and the deep thermal structure of the Baikal rift, *Geophys. Res. Lett., 17*, 1977-1980.

Dixon, T. H., Ivins E. R., and Franklin B. J., 1989, Topographic and volcanic asymmetry around the Red Sea: constraints on rift models. *Tectonics, 8*, 1193-1216.

Dixon, T. H., 1990, Comment on "Timing of mantle upwelling: evidence for a passive origin for the Red Sea Rift" by A.V. McGuire and R.G. Bohannon, *J. Geophys. Res., 95*, 5163-5164.

Dixon, T. H., Ivins E. R., and Franklin B. J., 1991, Reply *Tectonics, 10,* 653-656.

Dorman, J., Ewing M. and Oliver J., 1960, Study of shear-velocity distribution in the upper mantle by mantle Rayleigh waves, *Bull. Seis. Soc. Am.*, **50**, 87-115.

Duncan, R. A. and Richards M. A., 1991; Hotspots, mantle plumes, flood basalts, and true polar wander, *Rev. Geophys., 29*, 31-50.

Dziewonski, A. M. and Anderson D. L., 1981, Preliminary reference Earth model, *Phys. Earth Planet. Int., 25*, 297-356

Dziewonski, A. M., Chou T.-A. and Woodhouse J. H., 1981, Determination of earthquake source parameters from waveform data for studies of global and regional seismicity, *J. Geophys. Res., 86*, 2825-2852.

Dziewonski, A. M. and Woodhouse J. H., 1983, An experiment in systematic study of global seismicity: Centroid-moment tensor solutions for 201 moderate and large earthquakes of 1981, *J. Geophys. Res., 88*, 3247-3271.

Dziewonski, A. M., 1984, Mapping the lower mantle: Determination of lateral heterogeneity in P velocity up to degree and order 6, *J. Geophys. Res., 89*, 5929-5952.

Eckhardt, D. H., 1984, Correlations between global features of terrestrial fields, *Math. Geol., 16*, 155-171.

Forsyth, D. W., 1975, The early structural evolution and anisotropy of the oceanic upper mantle, *Geophys. J. R. astr. Soc., 43*, 103-162.

Forsyth, D. W., 1977, The evolution of the upper mantle beneath mid-ocean ridges. *Tectonophysics, 38*, 89-118.

Forte, A. M. and Peltier W. R., 1991, Mantle convection and core-mantle boundary topography: explanations and implications, *Tectonophysics, 187*, 91-116.

Gettings, M. D., Blank H. R., Mooney W. D., and Healey J. H., 1986, Crustal structure of southwestern Saudi Arabia, *J. Geophys. Res., 91*, 6491-6512.

Giardini, D., Li X.-D., and Woodhouse J. H., 1988, Splitting functions of long period normal modes of the Earth, *J. Geophys. Res., 93*, 13716-13742.

Gilbert, F. and Dziewonski A. M., 1975, An application of normal mode theory to the retrieval of structural parameters and source mechanisms from seismic spectra, *Phil. Trans. R. Soc. Lond., A, 278*, 187-269.

Grand, S. and Helmberger D. V., 1984, Upper mantle shear structure of North America. *Geophys. J. R. astr. Soc., 76*, 399-438.

Grand, S., 1987, Tomographic inversion for shear velocity beneath the North American plate, *J. Geophys. Res., 92*, 14065-14090.

Gudmundsson, O., 1989, Some problems in global tomography: Modeling the core-mantle boundary and statistical analysis of travel-time data, *Ph.D. thesis, California Institute of Technology.*

Hager, B. H., Clayton R. W., Richards M., Comer R. and Dziewonski A., 1985, Lower mantle heterogeneity, dynamic topography and the geoid, *Nature, 313*, 541-545.

Hager, B. H. and Clayton R. W., 1988, Constraints on the structure of mantle convection using seismic observations, flow models, and the geoid. In *Mantle Convection*, W. R. Peltier *ed.*, New York: Gordon and Breach, *pp*657-763.

Haxby, W. F. and Turcotte D. L., 1978, On isostatic geoid anomalies, *J. Geophys. Res., 83*, 5473-5478.

Hayes, D. E., 1988, Age-depth relationships and depth anomalies in the southeast Indian Ocean and south Atlantic Ocean, *J. Geophys. Res., 93*, 2937-2954.

Heestand, R. L. and Crough S. T., 1981, The effect of hot spots on the oceanic age-depth relation, *J. Geophys. Res., 86,* 6107-6114.

Inoue, H., Fukao Y., Tanabe K., Ogata Y., 1990, Whole mantle P-wave travel time tomography, *Phys. Earth Planet. Inter. 59,* 294-328.

Jackson D. D., 1979, The use of *a priori* data to resolve non-uniqueness in linear inversion, *Geophys. J. R. astr. Soc., 57,* 135-157.

Jeffreys, H. and Bullen K. E., 1940, Seismological Tables, British Association Gray-Milne Trust.

Jobert, N., 1986, Mantle wave propagation anomalies on laterally heterogeneous global models of the Earth by Gaussian beam synthesis, *Ann. Geophys., 4,* 261-270.

Jordan, T. H., 1975, The continental tectosphere, *Rev. Geophys., 13(3),* 1-12.

Jordan, T. H., 1981, Global tectonic regionalization for seismological data analysis, *Bull. Seismol. Soc. Am., 71,* 1131-1141.

Jordan, T. H., Lerner-Lam A. L. and Creager K. C., 1988, Seismic imaging of boundary layers and deep mantle convection, In *Mantle Convection,* W. R. Peltier *ed.*, New York: Gordon and Breach, *pp*97-201.

Kanamori, H., 1970, Seismological evidence for heterogeneity of the mantle, *J. Geomag. Geoele.,* **22**, 53-70.

Kennett, B. L. N. and Engdahl E. R., 1991, Traveltimes for global earthquake location and phase identification, *Geophys. J. Int., 105,* 429-465.

Klein, E. M., Langmuir C. H., Zindler A., Staudigel H. and Hamelin B., 1988, Isotope evidence of a mantle convection boundary at the Australian-Antarctic Discordance, *Nature,* 333, 623-629.

Lay, T. and Kanamori H., 1985, Geometric effect of global lateral heterogeneity on long-period surface wave propagation, *J. Geophys. Res., 90,* 605-621.

Lay, T., Ahrens T. J., Olson P., Smyth J. and Loper. D, 1990, Studies of the earth's deep interior: goals and trends, *Physics Today,* October, 44-52.

Leeds, A. R., Knopoff L., and Kausel E., 1974, Variations of upper mantle structure under the Pacific ocean, *Science, 186*, 141-143.

Le Pichon, X., 1968, Sea-floor spreading and continental drift, *J. Geophys. Res., 73*, 3661-3697.

Lerner-Lam, A. L. and Jordan T. H., 1987, How thick are the continents? *J. Geophys. Res., 92*, 14,007-14026.

Li, X-D., 1990, The asphericity of the Earth from free oscillations, *Ph. D. thesis, Harvard University.*

Lister, C. R. B., 1977, Estimators for heat flow and deep rock properties based on boundary layer theory, *Tectonophysics, 41*, 157-171.

Logatchev, N. A. and Florensov N. A., 1978, The Baikal system of rift valleys, *Tectonophysics, 45*, 1-13.

Logatchev, N. A., Zorin Y. A, and Rogozhina V. A., 1983, Baikal rift:active or passive? - comparison of the Baikal and Kenya rift zones, *Tectonophysics, 94*, 223-240.

Macdonald, K. C., 1982, Mid-ocean ridges: fine-scale tectonic, volcanic and hydrothermal processes within the plate boundary zone, *Annu. Rev. Earth Planet. Sci., 10*, 155-190.

Macdonald, K. C., 1983, Crustal processes at spreading centers, *Rev. Geophys. Space Phys., 21*, 1441-1453.

Macdonald, K. C., Sempere J. C. and Fox P. J., 1984, The East Pacific Rise from the Siqueirors to the Orozco fracture zones: along-strike continuity of the neovolcanic zone and the structure and evolution of overlapping spreading center, *J. Geophys. Res., 89*, 6049-6306.

Macdonald, K. C., 1986, The creast of the Mid-Atlantic Ridge: models for crustal generation processes and tectonics, in *The geology of North America, vol. M, The Western North Atlantic Region*, P. R. Vogt and B. E. Tucholke *ed.*, Geological Society of America, Boulder, Colo., *pp*51-68.

Marsh, J. G., Lerch F. J., Putney B. H., Christodoulidis D. C., Smith D. E., Felsentreger T. L., Sanchez B. V., Klosko S. M., Pavlis E. C., Martin T. V., Robbins J. W., Williamson R. G., Colombo O. L., Rowlands D. D., Eddy W. F., Chandler N. L., Rachlin K. E., Patel G. B., Bhati S. and Chinn D. S., 1988, A new gravitational model for the Earth from satellite tracking data: GEM-T1, *J. Geophys. Res., 93*, 6169-6215.

Masters, G., Jordan T. H., Silver P. G., and Gilbert F., 1982, Aspherical earth structure from fundamental spheroidal-mode data, *Nature, 298*, 609-613.

McGuire, A. V. and Bohannon R. G., 1989, Timing of mantle upwelling: evidence for a passive origin for the Red Sea rift, *J. Geophys. Res., 94*, 1677-1682.

McKenzie, D., 1967, Some remarks on heat flow and gravity anomalies. *J. Geophys. Res., 72*, 6261-6273.

McNutt, M. K. and Judge A. V. 1990, The superswell and mantle dynamics beneath the south Pacific, *Science, 248*, 969-975.

Minster, J. B. and Jordan T. H., 1978, Present-day plate motions, *J. Geophys. Res., 83*, 5331-5354.

Mitchell, B. J. and Yu G.-K., 1980, Surface wave dispersion, regionalized velocity models, and anisotropy of the Pacific crust and upper mantle, *Geophys. J. R. astr. Soc., 63*,497-514.

Molnar, P. and Tapponnier P., 1975, Cenozoic tectonics of Asia: effects of a continental collision, *Science, 189*, 419-426.

Montagner, J.-P., 1986, Regional three-dimensional structure usong long-period surface waves, *Ann. Geophys., 4*, 283-294.

Montagner, J.-P., and Tanimoto T., 1990, Global anisotropy in the upper mantle inferred from the regionalization of phase velocities, *J. Geophys. Res., 95*, 4797-4819.

Morelli, A., and Dziewonski A. M. 1987, Topography of the core-mantle boundary and lateral heterogeneity of the inner core, *Nature, 325*, 678-683.

Morgan, W. J., 1972, Plate motions and deep mantle convection, *Geol. Soc. Am. Mem., 132*, 7-22.

Morgan, J. P., 1987, Melt migration beneath mid-ocean spreading centers, *Geophys. Res. Lett., 14*, 1238-1241.

Nakanishi, I., and Anderson D. L., 1982, Worldwide distribution of group velocity of mantle Rayleigh waves as determined by spherical harmonic inversion *Bull. Seismol. Soc. Am., 72,*, 1185-1194

Nakanishi, I., and Anderson D. L., 1983, Measurements of mantle wave velocities and inversion for lateral heterogeneity and anisotropy, 1. Analysis of great circle phase velocities *J. Geophys. Res., 88*, 10267-10283.

Nakanishi, I., and Anderson D. L., 1984, Measurements of mantle wave velocities and inversion for lateral heterogeneity and anisotropy, 2, Analysis of by the single station method, *Geophys. J. R. astr. Soc. 78,* 573-617.

Nataf, H.-C., Nakanishi I. and Anderson D. L., 1984, Anisotropy and shear-velocity heterogeneities in the upper mantle, *Geophys. Res. Lett., 11*, 109-112.

Nataf, H.-C., Nakanishi I. and Anderson D. L., 1986, Measurements of mantle wave velocities and inversion for lateral heterogeneity and anisotropy, 3. inversion, *J. Geophys. Res., 91*, 7261-7307.

Nishimura, C. E., and Forsyth D. W., 1989, The anisotropic structure of the upper mantle in the Pacific, *Geophys. Jour. Int., 96*, 203-229.

Parker, R. L. and Oldenburg D. W., 1973, Thermal model of ocean ridges, *Nature, 242*, 137-139.

Parsons, B. and Sclater J. G., 1977, An analysis of the variation of ocean floor bathymetry and heat flow with age, *Geophys. Jour., 82*, 5, 803-827

Parsons, B., and McKenzie D. P., 1978, Mantle convection and the thermal structure of the plates, *J. Geophys. Res., 83*, 4485-4496.

Peterson J. and Hutt C. R., 1982, Test and calibration of the Digital Worldwide Standardized Seismograph, *U. S. Geol. Surv.*, Open-file Rept.

Regan, J. and Anderson D.L., 1984, Anisotropic models of the upper mantle. *Phys. Earth. Planet. Int., 35,* 227-263.

Renkin, M. L. and Sclater J. G., 1988, Depth and age in the north Pacific, *J. Geophys. Res., 93,* 2919-2935.

Richards, M., Hager B. H. and Sleep N. H., 1988, Dynamically supported geoid highs over hotspots: Observation and theory, *J. Geophys. Res., 93,* 7690-7708.

Richards, M. and Hager B. H., 1988, The Earth's geoid and the large-scale structure of mantle convection, in *The physics of the Earth,* Runcorn S.K. *ed.*, John Wiley & Sons Ltd. *pp*247-272.

Ritzwoller, M., Masters G. and Gilbert F., 1988 Constraining aspherical structure with low frequency interaction coefficients, *J. Geophys. Res., 93,* 6369-6396.

Romanowicz, B., Cara M., Fels J. F., and Rouland D., 1984, GEOSCOPE: A French initiative on long-period three-component global networks, *EOS, Trans. Am. Geophys. Union, 65,* 753-756.

Romanowicz, B., 1990, The upper mantle degree 2: constraints and inferences from global mantle wave attenuation measurements *J. Geophys. Res., 95,* 11051-11071.

Sakamoto, Y., M. Ishiguro and G. Kitagawa, 1986, *Akaike information criterion statistics,* KTK Scientific Publishers, D. Reidel Publishing Company, Tokyo.

Schlue, J. and Knopoff L., 1977, Shear-wave polarization anisotropy in the Pacific basin, *Geophys. J. R. astr. Soc. 49,* 145-165.

Schroeder, W., 1984, The empirical age-depth relation and depth anomalies in the Pacific Ocean basin. *J. Geophys. Res., 89,* 9873-9884.

Schubert, G., Froidevaux C. and Yuen Y. A., 1976, Oceanic lithosphere and asthenosphere: thermal and mechanical structure, *J. Geophys. Res., 81,* 3525-3540.

Schwartz, S. Y. and Lay T., 1987, Effects of off great circle propagation on the phase of long-period surface waves, *Geophys. J. R. astr. Soc. 91,* 143-154.

Sclater, J. G., Anderson R. N., and Bell M. L., 1971, The elevation of ridges and the

evolution of the central eastern Pacific, *J. Geophys. Res., 76*, 7888-7915.

Sclater, J. G., Jaupart C. and Galson D., 1980, The heat flow through oceanic and continental crust and the heat loss of the earth, *Rev. Geophys. Space Phys., 18*, 269-311.

Sclater, J. G., Parsons B. and Jaupart C., 1981, Oceans and continents: similarities and differences in the mechanisms of heat loss. *J. Geophys. Res., 86*, 11535-11552.

Sclater, J. G. and Wixson L., 1986, The relationship between depth and age and heat flow and age in the western north Atlantic, *the Geology of North America, Vol. M, The Western North Atlantic Region, pp*257-270.

Scott, D. R. and Stevenson D. J., 1989, A self-consistent model of melting, magma migration and buoyancy-driven circulation beneath mid-ocean ridges. *J. Geophys. Res., 94*, 2973-2988.

Sengör, A. M. C. and Burke K., 1978, Relative timing of rifting and volvanism on Earth and its tectonic implications, *Geophys. Res. Lett., 5*, 419-421.

Small, C. and Sandwell S., 1989, An abrupt in ridge axis gravity with spreading rate, *J. Geophys. Res., 94*, 17,383-17,392.

Smith, M. L. and Dahlen F. A., 1973, The azimuthal dependence of Love and Rayleigh wave propagation in a slightly anisotropic medium, *J. Geophys. Res., 78*, 3321-3333.

Smith, W. H. F., Staudigel H., Watts A. B. and Pringle M. S., 1989, The magellan seamounts: early cretaceous record of the south Pacific isotopic and thermal anomaly, *J. Geophys. Res., 94*, 10501-10523.

Spiegelman, M., and McKenzie D. P., 1987, Simple 2-D models for melt extraction at mid-ocean ridges and island arcs., *Earth Planet. Sci. Lett., 83*, 137-152.

Stacey, F. D., 1977, *Physics of the Earth, 2nd ed.,* John Wiley, New York, *pp*319-323.

Stein, S., Melosh H. J. and Minster J. B., 1977, Ridge migration and asymmetric seafloor spreading, *Earth Planet. Sci. Lett., 36*, 51-62.

Suetsugu, D. and Nakanishi I., 1985, Tomographic inversion and Resolution for Rayleigh wave phase velocities in the Pacific ocean, *J. Phys. Earth, 33* , 345 - 368.

Tanimoto, T., 1984, Waveform inversion of mantle Love waves: the Born seismogram approach. *Geophys. J. R. astr. Soc., 78*, 641-660.

Tanimoto, T., 1985, The Backus-Gilbert approach to the three-dimensional structure in the upper mantle - I. lateral variation of surface wave phase velocity with its error and resolution, *Geophys. J. R. astr. Soc., 82*, 105-123.

Tanimoto, T., 1986a, Free oscillation in a slightly anisotropic Earth, *Geophys. J. R. astr. Soc., 82*, 105-123.

Tanimoto, T., 1986b, The Backus-Gilbert approach to the 3-D structure in the upper mantle -II. SH and SV velocity *Geophys. J. R. astr. Soc., 84*, 49-69.

Tanimoto, T., 1988, The 3-D shear-wave structure in the mantle by overtone waveform inversion. II. Inversion of X waves, R waves, and G waves, *Geophys. J. R. astr. Soc., 93*, 321-334.

Tanimoto, T., 1988, The 3-D shear-wave structure in the mantle by overtone waveform inversion. II. Inversion of X waves, R waves, and G waves, *Geophys. J. R. astr. Soc., 93*, 321-334.

Tanimoto, T., 1990, Long wavelength S-wave velocity structure throughout the mantle, *Geophys. J. R. astr. Soc., 100*, 327-336.

Tanimoto, T., and Anderson D. L., 1984, Mapping convection in the mantle, *Geophys. Res. Lett., 11*, 287-290.

Tanimoto, T., and Anderson D. L., 1985, Lateral heterogeneity and azimuthal anisotropy of the upper mantle: Love and Rayleigh waves 100-250 sec., *J. Geophys. Res., 90*, 1842-1858

Tarantola, A. and Nercessian A., 1984. Three-dimensional inversion without blocks, *Geophys. J. R. astr. Soc., 76*, 299-306.

Toksöz, N. M., and Anderson D. L., 1966, Phase velocities of long-period surface waves and structure of the upper mantle, *J. Geophys. Res., 71*, 1649-1658.

Turcotte, D. L. and Oxburgh E. R., 1967, Finite amplitude convection cells and continental drift, *J. Fluid Mech, 28*, 29-42.

Turcotte, D. L. and Oxburgh E. R., 1978, Intra-plate volcanism, *phil. Trans. R. Soc. Lond., 288*, 561-579.

Turcotte, D. L, and Ahern J. L., 1978, A porous flow model for magma migration in the asthenosphere, *J. Geophys. Res., 83*, 767-772.

Turcotte, D. L. and Schubert G., 1982, *Geodynamics, Application of continuum physics to geological problems*, John Wiley & Sons, Inc., Canada.

Turcotte, D. L. and Emerman S. H., 1983, Mechanisms of active and passive rifting, *Tectonophysics, 94*, 39-50.

Um, J., Dahlen F. A. and Park J., 1991, Normal mode multiplet coupling along a dispersion branch, *Geophys. J. Int., 106*, 11-35.

Vogt, P. R., 1981, On the applicability of thermal conduction models to mid-plate volcanism: comments on a papre bs Gass *et al., J. Geophys. Res., 86*, 950-960.

Vogt, P. R., Cherkis N. Z., and Morgan G. A., 1983, Project Investigator, Evolution of the Australia-Antarctic Discordance deduced from a detailed aeromagnetic study, in *Antarctic Earth Science*, Oliver R.L., James P.R., and Jago J.B. *ed., pp*608-613.

Vogt, P. R., 1986, Magnetic anomalies and crustal magnetization, *The Geology of North America, M. The Western North Atlantic Region*, The Geological Society of America. 229-256.

Weinstein, S. A. and Olson P. L., 1989, The proximity of hotspots to convergent and divergent plate boundaries, *Geophys. Res. Lett., 16*, 433-436.

Weissel, J. K. and Hayes D. E., 1971, Asymmetric spreading south of Australia, *Nature, 213*, 518-521.

Weissel, J. K. and Hayes D. E., 1974, The Australian-Antarctic Discordance: New results and implications, *J. Geophys. Res., 79*, 2579-2587.

White, R. S. and McKenzie D. J., 1989, Magmatism at rift zones: the generation of

volcanic continental margins and flood basalts, *J. Geophys. Res., 94, B6,* 7685-7729.

Wong, Y.-K., 1989, Upper mantle heterogeneity from phase and amplitude data of mantle waves, *Ph. D. thesis, Harvard University.*

Woodhouse, J. H. and Dziewonski A. M., 1984, Mapping the upper mantle: Three-dimensional modeling of earth structure by inversion of seismic waveforms, *J. Geophys. Res., 89, NO. B7,* 5953-5986.

Woodhouse, J. H. and Dziewonski A. M., 1986, Three dimensional mantle models based on mantle wave and long period body wave data (Abstract), *EOS, Trans. Am. Geophys. Union, 67,* 307

Yoshii, T., 1975, Regionality of group velocities of Rayleigh waves in the Pacific and thickening of the Plate, *Earth planet. Sci. Lett., 25,* 305-312.

Yoshii, T., Kono Y., and Ito K., 1976, Thickening of the oceanic lithosphere, *The geophysics of the Pacific ocean basin and its margin,* G. Sutton, M. H. Manghnani and R. Moberly, Geophysical Monograph Series *ed., Am. Geophys. Union, 19, pp*423-430.

Yu, G.-K. and Mitchell B. J., 1979, Regionalized shear velocity models of the Pacific upper mantle from observed Love and Rayleigh wave dispersion. *Geophys. J. R. astr. Soc., 57,* 311-341.

Zhang, Y.-S. and Tanimoto T., 1987, Lateral heterogeneity in the Pacific Ocean by using long-period surface waves, (Abstract), *EOS, Trans. Am. Geophys. Union, 68,* 44, 1378.

Zhang, Y.-S. and Tanimoto T., 1989, Three-dimensional modeling of upper mantle structure under the Pacific Ocean and surrounding area, *Geophys. J. R. astr. Soc., 98,* 255-269.

Zhang, Y.-S. and Tanimoto T., 1991, Global Love wave phase velocity variation and its significance to plate tectonics, *Phys. Earth. Planet. Int., 66,* 160-202.

Zonenshain, L. P. and Savostin L. A., 1981, Geodynamics of the Baikal rift zone and

plate tectonics of Asia, *Tectonophysics, 76*, 1-45.